Interface Study of Atomic Layer Deposition based Metal Oxide Charge Transport Layer on Metal Halide Perovskite

Nitin Mallik

INSTITUT POLYTECHNIQUE DE PARIS

ÉCOLE POLYTECHNIQUE

IP PARIS

NNT : 2023IPPAX117

Thèse de doctorat

Interface Study of Atomic Layer Deposition based Metal Oxide Charge Transport Layer on Metal Halide Perovskite

Thèse de doctorat de l'Institut Polytechnique de Paris
préparée à École Polytechnique

École doctorale n°626 l'Institut Polytechnique de Paris (ED IP Paris)
Spécialité de doctorat: Physique de la matière condensée

Thèse présentée et soutenue à Palaiseau, le 08/12/2023, par

NITIN MALLIK

Composition du Jury:

Guillaume Wantz Professor, Universités Bordeaux, INP, France	Président
Thomas Riedl Professor, University of Wuppertal, Germany	Rapporteur
Anass Benayad Directeur de Recherche, CEA-Grenoble, France	Rapporteur
Elise Bruhat Industrial Strategy Director, Holosolis, France	Examinatrice
Philip Schulz Directeur de Recherche, IPVF-CNRS, France	Directeur de thèse
Nathanaelle Schneider Chargée de recherche, IPVF-CNRS, France	Co-encadrante de thèse

Often, it may be said that the interface is the device.

– Nobel laureate Herbert Kroemer

Acknowledgments

I would like to express my sincere gratitude to Dr. Philip Schulz, my thesis director, for providing me with the opportunity to work in such a fascinating field at IPVF. Throughout my PhD journey, Dr. Schulz has continuously motivated and supported me in my research work and facilitated involvement in several collaborative studies. I would also like to extend my appreciation to Dr. Nathanaelle Schneider, my co-supervisor, for her support and motivation throughout this journey, especially in the development of ALD materials, which played a crucial role in shaping the experimental studies of my work.

I am grateful to Prof. Guillaume Wantz, Prof. Thomas Riedl, Dr. Anass Benayad, and Dr. Elise Bruhat, the members of the jury, for their invaluable contributions, feedback, and constructive criticism during my defense. The fruitful discussions that we had enabled me to gain fresh perspectives and insights that enhanced the quality of my research and writing.

I also acknowledge the support of our collaborators at Helmholtz-Zentrum Berlin, Dr. Roberto Félix, Elif Hüsam, Ahmed Saleh, Dr. Regan G. Wilks, and Prof. Marcus Bär, for their kind cooperation during HAXPES measurements and help in manuscript preparations. To the team at ILV, including Dr. Damien Aureu, Dr. Muriel Bouttemy, Dr. Solène Bechu, and Mathieu Frégnaux, I am grateful for imparting their extensive knowledge and expertise on photoemission spectroscopy techniques. A big thanks to Prof. Barry P Rand for hosting me in his lab at Princeton University. I also want to show my appreciation to Junnan, Hussein, Brady, and Jessy for their help and for welcoming me during my visit.

I extend my sincere appreciation to the administrative and management team of CNRS at IPVF for their invaluable support during my Ph.D. studies. I thank Claire Vialette for her excellent administrative assistance and Jean-Francois Guillemoles for his understanding and guidance as the director of CNRS UMR 9006. I am also grateful to the Chef de Pole, Nicolas Loones, Julie Goffard, and Frederique Donsanti for their support in training various equipment in IPVF.

I would also like to acknowledge all of my colleagues and friends at IPVF who shared wonderful moments with me from the beginning of my Ph.D. until the end. Special thanks to Javid, Vincent, Davide Regaldo, and Damien Cotancier for their help and training in the last three years. I would also like to thank Pilar, Shanting, Van-Son, Salim, Celia, Marion, Ashish, Huriye, Stefania, Davide C, Alexandre PY, Alexandre B, Arthur, Claire B, Karim, and others for making this the most pleasant journey.

I want to express my gratitude to my friends outside, Dinesh, Ajay, and Spandan for their constant support. I would also like to thank my parents, sister and in-laws for their continuous motivation, support, and inspiration in this academic journey. Lastly, a big thanks to my wife, Shantipriya, for her love, support, care, and motivation in my life.

Finally, I extend my appreciation to everyone who has contributed to making my Ph.D. journey a success. Your support, guidance, and encouragement have been invaluable to me, and I could not have accomplished this without you. Thank you for being a part of this journey with me.

Acronyms

ALD	Atomic layer deposition
BE	Binding energy
CB	Conduction band
CBD	Chemical bath deposition
CTL	Charge transport layer
ETL	Electron transport layer
GiXRD	Grazing incidence X-ray diffraction
HAXPES	Hard X-ray photoelectron spectroscopy
HTL	Hole transport layer
IMFP	inelastic mean free path
KP	Kelvin probe
MHP	Metal halide perovskite
NiO_X	Nickel oxide
PCBM	Phenyl-C61-butyric acid methyl ester
PCE	Power conversion effciency
PES	Photoelectron spectroscopy
PSCs	Perovskite solar cells
PTTA	Poly(triaryl amine)
PV	Photovoltaics
SEM	Scanning electron microscopy
SnO_2	Tin oxide
VB	Valence band
XPS	X-ray photoelectron spectroscopy
XRD	X-ray diffraction

Table of Contents

List of Figures

List of Tables

Introduction

In a world where technology dominates modern life and economies, the demand for energy sources and their environmental impact has become a focal point of concern. The heavy reliance on non-renewable fossil fuel sources, such as coal and natural gas, for energy needs, has put the world in the midst of an energy crisis in recent years. In particular, the geopolitical complexity that evolved around Russia and Ukraine in 2022 cascaded the forecasted energy crisis, impacting several economies and energy supplies around the world and significantly affecting the European continent. In addition, the heavy use of fossil fuel-based energy sources has a severe impact on climate through greenhouse gas emissions. Greenhouse gas emissions have been cited as the root cause of global warming and climate change. As a result, the global average surface temperature has increased by 1°C since the pre-industrial era owing to the exponential increase in human activities and the need for energy sources.[1] Although the 1°C rise seems small, considering the vast size and high heat capacity of oceans on this planet, a colossal amount of heat energy is required for a discernible increase in the Earth's surface temperature. Therefore, to limit the temperature rise, the world needs a fast transition to efficient clean, and renewable energy sources, such as wind, solar, geothermal, and hydropower. Several nations and policymakers are working together to achieve the net zero emission goal by 2050 which was formulated in the Paris climate treaty.[2] Figure 1 shows the global temperature rise since 1960 and the projected scenarios to limit warming below 1.5°C by 2050, as reported by the International Panel on Climate Change.[3] The net-zero mission includes several strategies and initiatives for sustainable development, research, and innovation in the energy sector. The research and development of efficient and cost-effective renewable energy technologies are key to the success of the net-zero mission, and most importantly, to safeguard the planet.

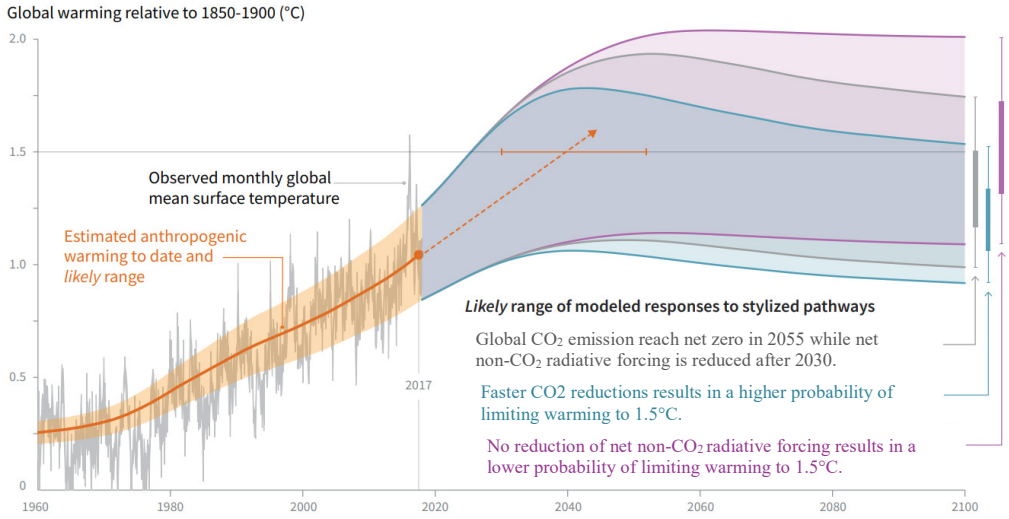

Figure 1. Change and estimated global warming by IPCC.[3]

Among the various renewable energy technologies, solar photovoltaics (PV) that convert sunlight into electricity are at the forefront due to the enormous amount of energy provided by the sun. According to a study by the National Renewable Energy Laboratory in the United States, one hour of sunlight is equivalent to the energy consumption of the world population in one year.[4] Various PV technologies have been developed, including silicon solar cells, CIGS solar cells, CdTe solar cells, GaAs solar cells, organic photovoltaics, and perovskite solar cells. Currently, silicon-based PV technology has been widely commercialized with an efficiency of approximately 24% and a lifetime of 25-30 years.[5] PV developmental research continues with the emergence of new energy materials and technologies to achieve higher efficiency, low-cost manufacturing, and ease of processing.

In recent years, novel concepts such as hybrid organic-inorganic perovskite solar cells have been developed as next-generation emerging photovoltaics. The perovskite PV, which started almost 10 years ago with an efficiency of 14.1%, has seen a rapid advancement with the current certified record efficiency of over 26% as of 2023.[4] Such extraordinary improvement of efficiency in perovskite solar cells was made possible by the growing fundamental understanding of perovskite materials and improved interface engineering. However, the long-term stability of perovskite solar cells, which is inherently affected by their interfaces, remains a key issue for widespread applications. Therefore, strategic interface and interlayer design is critical for enhancing the stability and efficiency of perovskite PV technology.[6]

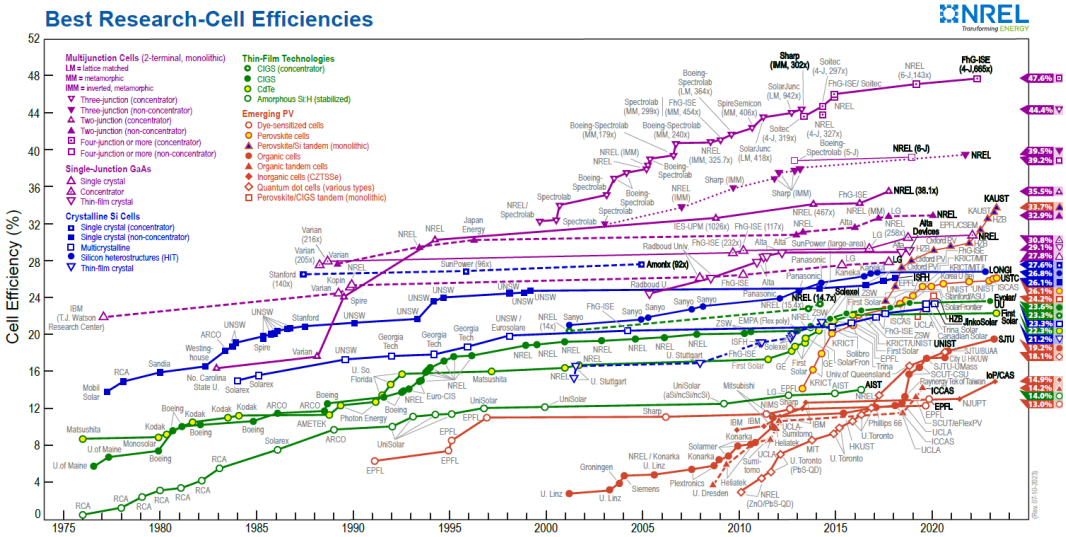

Figure 2. Solar cell technology efficiency chart by National Renewable Energy Lab.[4]

Motivation and Outline

The PhD thesis focuses on implementation atomic layer deposition (ALD) based metal oxide charge transport layer to tailor the interfaces of the perovskite solar cell. This type of interface design not only aims at making the device more efficient but also to enhance the stability by forming a protective buffer layer. One of the major concerns with the perovskite solar cell is it's limited environmental and thermal stability, especially the extensively researched $MAPbI_3$ perovskite, but also still for the more recently employed mixed-cation mixed-halide variants.[7] In this context, the ALD technique is quite promising for growing compact metal oxide layers directly on top of perovskite at a lower temperature. The compact oxide can act as protective layer for perovskite solar cells from external environmental factors as well as the internal ion migration.

The precursors used in the ALD process can chemically interact with delicate perovskite surface. Although, this new approach of interface design is promising for solving the stability issue and scalability of perovskite-based technologies, yet the lack of a precise understanding of the chemical and physical processes at the perovskite interface during ALD steps caused a roadblock to effectively utilize this approach and hence call for dedicated fundamental research. In this doctoral research work, I focus on in-depth study the chemistry, structure, morphology, and electronic band alignment of Perovskite and ALD metal oxide interface using advanced characterization techniques including X-ray photoelectron spectroscopy, synchrotron-based hard X-ray photoelectron spectroscopy, kelvin probe, X-ray diffraction, and scanning electron microscopy.

The thesis is consisting of 5 chapters with the following contents:

- Chapter 1 describes the basics of metal halide perovskites, the working principle of perovskite solar cells, charge transport layers, and stability issues. In addition, this chapter elaborates on the fundamentals of atomic layer deposition (ALD), its application in perovskite solar cells, and its challenges of direct deposition on perovskite layer. The last section of this chapter explains the fundamentals of soft and hard X-ray-based photoelectron spectroscopy.

- Chapter 2 provides details of the materials, fabrication parameters, and characterization techniques, including X-ray diffraction, scanning electron microscopy, UV-Vis spectroscopy, kelvin Probe, and X-ray photoelectron spectroscopy.

- Chapter 3 reports a synchrotron-based hard X-ray photoelectron spectroscopy (HAXPES) investigation of the interface between metal halide perovskite (MHP) and ALD-SnO_2. In addition, the effectiveness of introducing a thin interlayer of the organic electron transport material Phenyl-C61-butyric acid methyl ester (PCBM) between MHP and ALD-SnO_2 to mitigate the effect of ALD process is assessed.

- Chapter 4 reports the interface, solar cell characteristics, and operational stability of n-i-p configuration perovskite solar cells using an ALD-NiO_X hole-transport interlayer. This chapter investigates the impact of the ALD-NiO_X process on the surface of MHP using various advanced characterization techniques including HAXPES. Furthermore, a PTAA organic buffer layer was incorporated to mitigate unwanted chemical reactions between the MHP and ALD-NiO_X to fabricate stable perovskite solar cells.

- Chapter 5 reports an extension of the interface study in the previous chapter by introducing a phosphonic acid-based molecule between MHP and ALD-NiO_X in an n-i-p architecture. In this chapter, the effectiveness of this molecules in limiting unwanted interfacial reactions between the MHP surface and ALD-NiO_X precursors is discussed. This chapter also includes a HAXPES investigation to probe the buried interface to obtain the above-mentioned information.

Finally, the conclusion and perspectives, summarizes the major finding of MHP/ALD-SnO_2, MHP/ALD-NiO_X, MHP/SAM/ALD-NiO_X interface and device studies. The last part elaborates the future perspectives, focusing on use of potential buffer layer between MHP and ALD metal oxides to limit the defective interface formation without exhibiting parasitic absorptions.

■ REFERENCES

1. NASA earth observatory data, https://earthobservatory.nasa.gov/world-of-change/global-temperatures.
2. Anika, O.C., Nnabuife, S.G., Bello, A., Okoroafor, R.E., Kuang, B. and Villa, R., 2022. Prospects of low and zero-carbon renewable fuels in 1.5-degree net zero emission actualisation by 2050: A critical review. *Carbon Capture Science & Technology*, p.100072.
3. Lee, H., Calvin, K., Dasgupta, D., Krinner, G., Mukherji, A., Thorne, P., Trisos, C., Romero, J., Aldunce, P. and Ruane, A.C., 2024. CLIMATE CHANGE 2023 Synthesis Report Summary for Policymakers. *CLIMATE CHANGE 2023 Synthesis Report: Summary for Policymakers*.
4. "NREL." [Online]. Available: https://www.nrel.gov.
5. Ballif, C., Haug, F.J., Boccard, M., Verlinden, P.J. and Hahn, G., 2022. Status and perspectives of crystalline silicon photovoltaics in research and industry. *Nature Reviews Materials*, *7*(8), pp.597-616.
6. Sharif, R., Khalid, A., Ahmad, S.W., Rehman, A., Qutab, H.G., Akhtar, H.H., Mahmood, K., Afzal, S. and Saleem, F., 2023. A comprehensive review on the current progress and material advances in perovskite solar cells. *Nanoscale Advances*.
7. Zhu, H., Teale, S., Lintangpradipto, M.N., Mahesh, S., Chen, B., McGehee, M.D., Sargent, E.H. and Bakr, O.M., 2023. Long-term operating stability in perovskite photovoltaics. *Nature Reviews Materials*, pp.1-18.

Chapter 1
Background and Objectives

Preface: *This chapter contains the basics of metal halide perovskites, working principle of perovskite solar cells, charge transport layers, and stability issues. In addition, this chapter explores the fundamentals of atomic layer deposition (ALD), its application in perovskite solar cells, and challenges. In the last part, we describe soft and hard X-ray based photoelectron spectroscopy, which is used in this thesis work to study the interface between metal halide perovskites and ALD metal oxides.*

Contents

1.1. Perovskite Solar Cells: Material, Structure, and Properties

In recent years, metal halide perovskite (MHP) solar cells have attracted immense attention among researchers due to rapid advances in efficiency beyond 25% comparable to silicon-based technology.[1] Despite the discovery of perovskite in 1839 by the German mineralogist Gustrav Rose,[2] the perovskites were not utilised in solar cell technology until recently.[3] The perovskite materials have a general chemical formula of ABX_3 as shown in Figure 1.1. The crystal lattice is made up of BX_6 octahedra that are held together by the A ion in a perovskite structure. [4]

In hybrid organic-inorganic perovskites, A-site generally composed of a monovalent cation such as methylammonium, formamidinum, and cesium.[5] Furthermore, B-site consists of divalent metal cation, such as lead (Pb^{2+}) or tin (Sn^{2+}). Nevertheless, it is important to note that the Sn^{2+} cation in tin-based perovskite undergoes oxidation to Sn^{4+} state, [6] therefore the lead-based perovskites are widely used in current perovskite solar cell research due to their structural stability. Finally, X anion refers to a monovalent halide anion such as iodide, bromide and chloride.

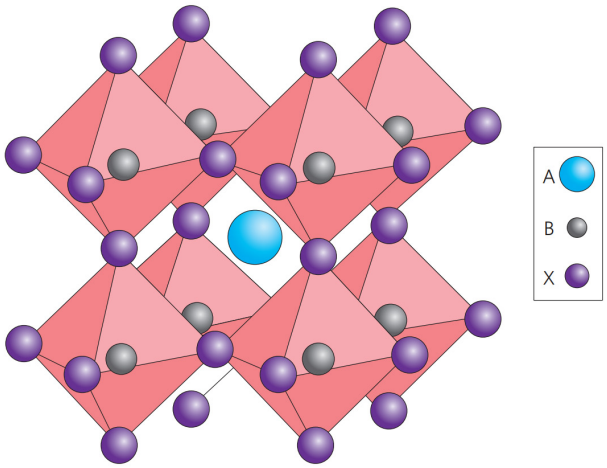

Figure 1.1. Typical crystal structure of perovskite with ABX_3 formula.[7]

In addition, multiple cation and anion can coexist in the MHP material to form alloys due to its high lattice tolerance.[8] The alloying technique is employed to produce perovskite structures that exhibit enhanced stability, while also allowing for precise control over the optoelectronic characteristics, such as the bandgap.[9-10] The crystal structure predominately can be modified by A-site alloying, which is determined by the position and size of the A cations which has direct impact on the change of the crystal lattice parameter, and defects density. [11-13] The optoelectronic properties of MHPs are significantly influenced by the B-site alloy, as the B-site cations play a direct role in the formation of the band edges of MHPs.[14] Hence, the bandgap can be adjusted by the B-site alloy within a specific range, leading to the control of the light absorption spectrum and the properties related to the movement and extraction of charge carriers in the system. Analogous to the alloying of B-site

elements, the incorporation of halide species in the X-site of MHPs enables a wide-ranging adjustment of the bandgap within the visible region by changing the stoichiometric ratios of iodine and bromine.[15-16] In general, MHP possess exceptional optoelectronic properties like outstanding light absorption (~10^4 cm^{-1}), high photoluminescence quantum yield, tunable bandgap (1.5-2.4 eV), narrow-band emission, and long diffusion length (~10 -100 μm). These properties make MHP an excellent candidate for solar cell application, leading to rapid growth in power conversion efficiency (PCE) of perovskite-based technology in the last 11 years.

1.2. Stability of Metal Halide Perovskite

MHP materials are extremely prone to degradation due to several internal and external factors, as shown in Figure 1.2. MHP materials are not chemically robust owing to the weak ionic bond and van der Waals interaction between the organic and inorganic components and can easily degrade under the influence of moisture, heat, light, and electrical bias.[17] Among external factors, MHP materials are sensitive to moisture and oxygen.[18,19] Upon exposure to moisture, MHP forms a strong hydrogen bond with the organic cation and weakens the bond between the cation and halide, causing deprotonation of the organic cations under operational bias or heat.[20] In addition, the water molecules protonate the halide, especially iodide, which forms a volatile hydroiodic acid causing complete decomposition of MHP into PbI_2.[21] When exposed to oxygen, MHP materials are generally stable in the dark; however, MHP decomposes quickly in the presence of both oxygen and light.[22] The oxygen molecules are adsorbed at the halide vacancy sites and trap the electrons in the conduction band of the MHP, forming a highly reactive superoxide that cascades an acid-base reaction with the acidic cation of the MHP, causing degradation.[23,24]Note that the creation of halide vacancies in MHP is a predominant phenomenon and occurs readily under illumination or electrical bias owing to the highly mobile nature of the halides.[25] MHP absorbers are prone to degradation at high temperatures. For example, methylammonium lead iodide decomposes rapidly at temperatures above 100°C and is completely converted to PbI_2.[26-27]

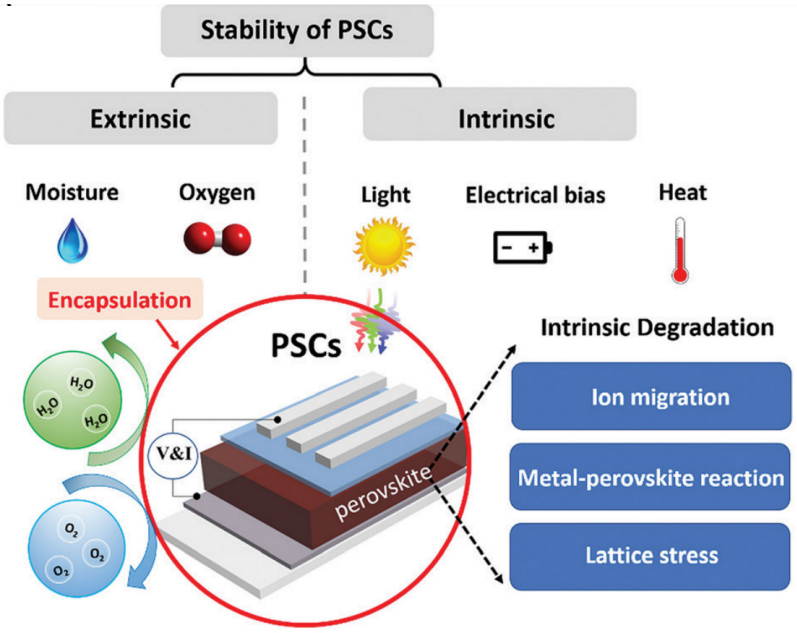

Figure 1.2. Illustration of the degradation pathways of metal halide perovskites.[28]

As discussed previously, halides in MHP tend to migrate under the influence of light or an electrical bias. Snaith et al. proposed that ion migration in MHP is one probable reason behind the hysteresis in perovskite solar cells (PSCs).[29] In addition, halide ions can diffuse through the charge-transport layer and chemically react with the metal electrode to form metal halides.[30] In another study by Kim et al., under illumination, the iodide anions in MHP were oxidized by photogenerated holes, forming neutral iodine and halide vacancies. The neutral iodide can move from the lattice and fit in the interstitial sites because of its smaller size, resulting in irreversible degradation into metallic lead.[31] This severely affects the efficiency of the PSCs.

In summary, the MHP absorber is extremely delicate, and these types of internal and external degradation of MHP are huge roadblocks to achieving long-term stability. The alloying of organic and inorganic cations has shown enhanced tolerance to heat and light moisture. [32] Specifically, the double-cation CsFA-based perovskite exhibits better stability than organic cation-only or inorganic cation-only MHPs.[33] Therefore, in this thesis work, $FA_{0.7}Cs_{0.3}Pb(I_{0.9}Br_{0.1})_3$ MHP absorber is used. Furthermore, research studies have shown various molecular, interface, and interlayer engineering strategies to limit these types of irreversible degradation in MHP devices. In a recent state of art study, Li et al., demonstrated that interface engineering using cyanoacrylic acid-based molecular additive resulting a stable PSCs retaining 95% of the initial PCE (23.5%) after 1,960 h under 1-sun illumination at 65°C (ISOS-L-2I protocol).[34] The pursuit continues to attain the enduring stability of PSCs, aiming to match the longevity of silicon technology, which can last up to 25 years.

1.3. Working Principle of Perovskite Solar Cells

A perovskite solar cell consists of an MHP absorber layer sandwiched between two charge transport layers (electron and hole transport layers), with electrodes at both ends.[35] One of the electrodes must be transparent to allow light to reach the absorber layer and generate charge carriers. These devices are typically classified as n-i-p or p-i-n architectures based on which charge transport layer (CTL) is exposed to sunlight (Figure 1.3). In n-i-p structures, sunlight passes through the electron transport layer (ETL) to reach the photo-absorber, while in p-i-n structures, light passes through the hole transport layer (HTL).[36]

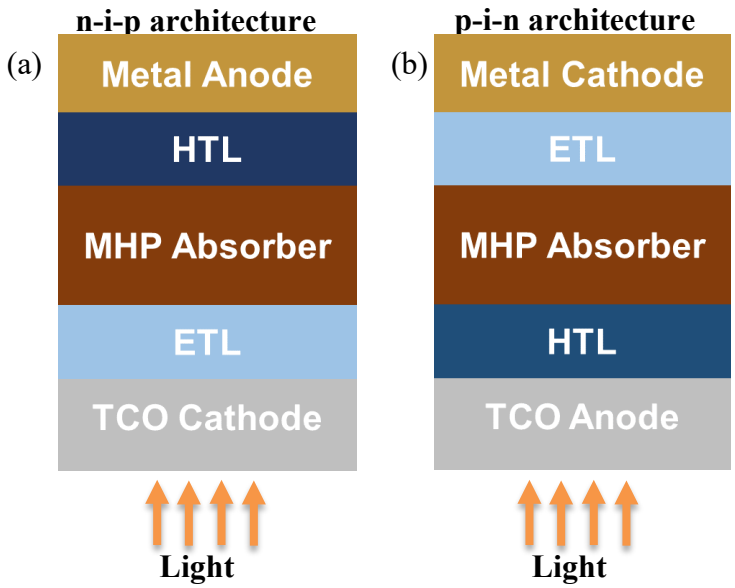

Figure 1.3. Perovskite solar cell device architecture (a) n-i-p (b) p-i-n.

When illuminating the perovskite solar cell with light energetically exceeding the band gap of the MHP, the light gets absorbed. The photon energy is utilized to excite an electron from the valence band (VB) into the conduction band(CB). This process generates electrons in the CB and holes in the VB. These charge carriers are then transported and injected to their respective CTLs and transferred through the layers before being collected at the electrodes,[37] as illustrated in Figure 1.4. The formation of a p-n junction within the device creates an intrinsic electric field that influences the separation and transport of the charge carriers. For efficient charge transport, the energy band alignment should have a downward gradient to facilitate electron transport from the conduction band of the MHP to the anode, and an upward gradient to facilitate hole transport from the valence band of the MHP to the cathode.

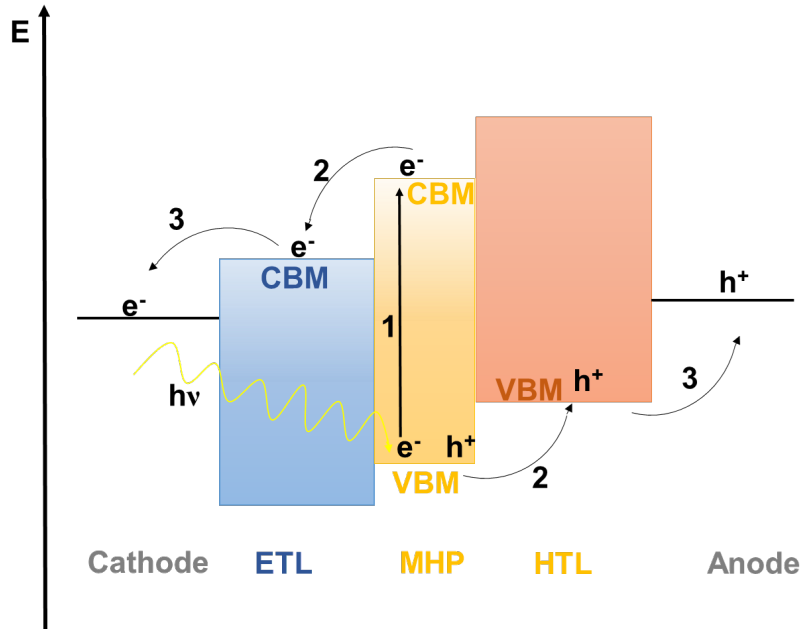

Figure 1.4. Energy level alignment and working principle PSC: (1) Absorption of photon and free charges generation; (2) Charge transport and separation; (3) Charge extraction.

PSCs contain four distinct interfaces: cathode/ETL, ETL/MHP, MHP/HTL, and HTL/anode. One key challenge in PSCs is the nonradiative recombination losses due to interface-induced recombination, which are caused by differences in the energy level alignment and surface defects.[38] Specifically, an energy-level mismatch at the ETL/MHP interface results in inefficient electron extraction, which causes significant voltage losses and introduces a hysteresis effect. [39] At the MHP/HTL interface, any limited energy barrier for holes can cause band bending, increase recombination rates, and reduce the charge collection efficiency.[40] Therefore, careful selection of CTLs and interface engineering is critical for the stability and performance of PSCs. In the next section, we elaborate on the different types of organic and inorganic CTLs used in the PSCs.

1.4. Charge Transport Layers

Charge-transporting materials play a vital role in fabricating PSCs with high efficiency and long-term operational stability.[41] Well-aligned CTLs can facilitate enhanced charge separation and reduce nonradiative recombination, which directly affects the short-circuit current (J_{SC}), fill factor, and open-circuit voltage (V_{OC}).[42] Furthermore, intrinsic stability and inertness towards MHP and electrodes are key criteria for the long-term stability of PSCs.[43] A compact CTL can inhibit the diffusion of external stressors, including moisture and oxygen, into PSCs, thereby increasing their environmental stability.[44] As discussed earlier, the ions in the MHP are highly mobile; specifically, the halides migrate under bias or photon flux, and simultaneously, the ions from the metal electrode tend to diffuse through the CTL and interact with the MHP. These internal degradations through ion migration can be suppressed using a compact CTL. Herein, we describe the current status and

development of different types of CTLs (see Figure 1.5) used in perovskite technology from the perspective of efficiency and stability.

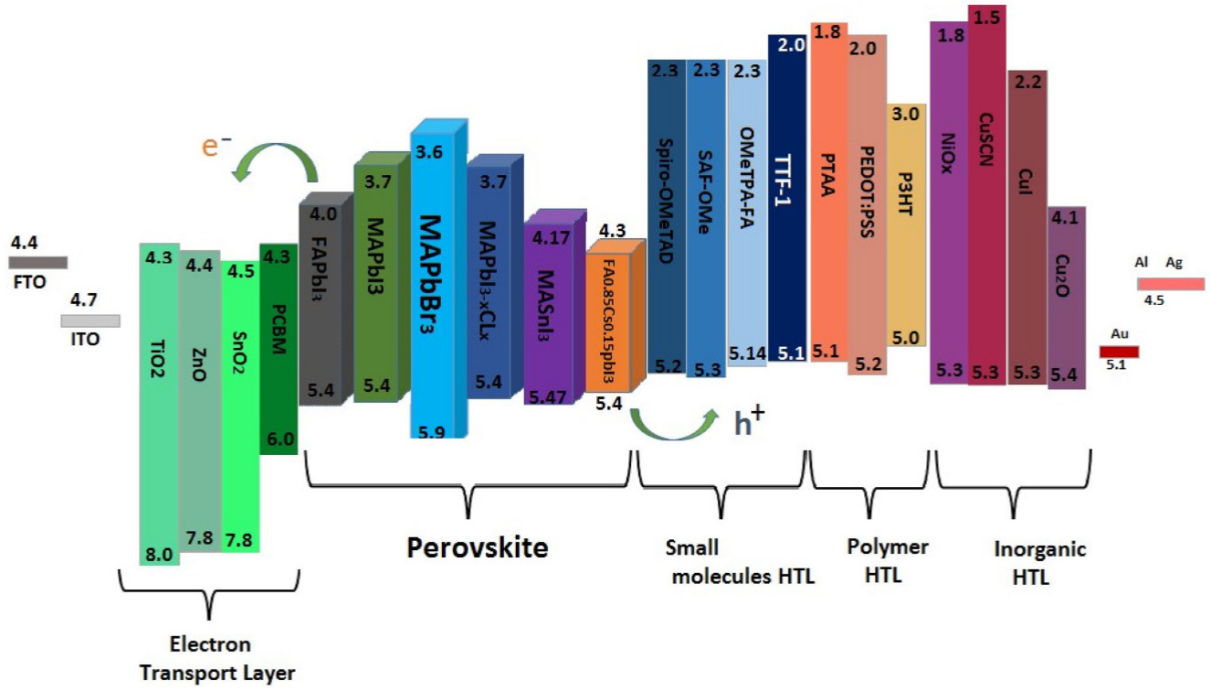

Figure 1.5. Illustration of energy level alignment of various MHP materials, ETLs and HTLs.[41]

1.4.1. Electron Transport Layers

ETLs are crucial for the electron extraction, transport, and blocking of holes in PSCs. In principle, ETL materials need to fulfill certain requirements in PSCs, including a wide bandgap for high transmission of photons, maximizing the number of photons reaching the absorber in the n-i-p architecture.[45] In addition, a suitable energy-level alignment and high mobility are necessary to facilitate efficient electron transport. Achieving a smooth morphology without any pinholes is essential for uniform MHP film growth and to avoid direct contact with electrode in the n-i-p architecture. In the p-i-n architecture, it is also crucial to have a pinhole-free, compact, and uniform ETL to protect the MHP from external stressors and limit ion migration. Furthermore, the photochemical and thermal stabilities of the ETLs can ensure the long-term stability of the devices. Low-temperature deposition of ETL is also required for the fabrication of p-i-n solar cells, as the perovskite is sensitive to temperatures higher than 100°C. ETL materials can be classified into two broad categories, organic and inorganic ETLs,[42] which are discussed in the next section.

1.4.1.1 Organic Electron Transport Layers

The organic ETLs are commonly incorporated in p-i-n configuration PSCs and among different types of organic ETL, fullerene (C60) and its derivatives such as phenyl-C61-butyric acid methylester (PCBM) are widely used (see Figure 1.6).[46] Fullerene ETLs coupled with other organic or inorganic ETLs achieve high efficiency in p-i-n PSCs. Fullerenes play a crucial role in PSCs as they form a direct interface with the MHP film. Fullerenes have high electron affinity and electron mobility (~1 $cm^2V^{-1}s^{-1}$), are well aligned with the CBM of the MHP, and their C60 cage structure expedites electron extraction and transport.[47-50] Side chains attached to the C60 cage can enhance PSC stability by improving the quality of the MHP film and mitigating MHP oxidation.[51,52] Fullerene derivatives require low-temperature processing and have high thermal and moisture resistance. [53] They also have defect-passivation [46] capabilities and can be easily functionalized for better solution processability[48]. For example, PCBM has better solubility in organic solvents than C60 does, so PCBM films are deposited by spin coating, whereas C60 materials are deposited by thermal evaporation.

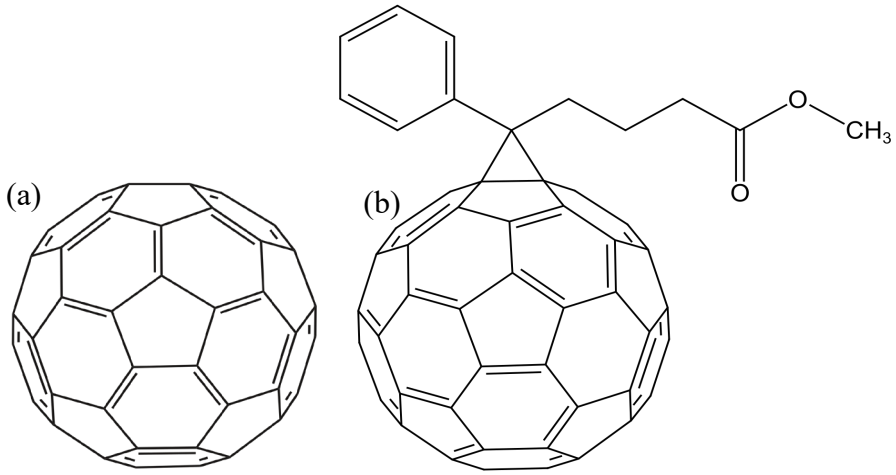

Figure 1.6. Chemical structure of (a) C60 and (b) phenyl-C61-butyric acid methylester (PCBM).

The initial study on p-i-n PSCs using PCBM as the ETL in 2013 achieved a low PCE of 3.9%.[54] This relatively low efficiency was deemed acceptable during this period because the fabrication methods for the MHP film were not yet well refined. The PCBM layer was thin, leading to an increased leakage current and, consequently, a lower PCE. Several years later, the PCE improved significantly to 20.9% when PCBM was used as the ETL.[55] Snaith et al. conducted pioneering experiments employing PCBM as an ETL to investigate the charge diffusion length in $MAPbI_3$.[56] Furthermore, Lam et al. used PCBM as an ETL to explore the factors contributing to the high performance of $MAPbI_3$ based PSCs. They discovered that PCBM played a crucial role in inhibiting halide ion migration from the perovskite layers through halide–π noncovalent interactions.[57] These

interactions promote electron transport within the ETLs, further enhancing the overall performance of the solar cells.

Further, the most efficient silicon/perovskite and perovskite/perovskite tandem solar cells ever made utilize C60 electron transport layers. Chen et al. reported a high efficiency all perovskite tandem solar cells with a PCE of 26.1%, which was achieved using C60/SnO_2 and C60/BCP for the narrow and wide band gap perovskites, respectively.[58] However, fullerenes possess some drawbacks that impede the progress of fullerene-based perovskite solar cells (PSCs). The fullerenes induce significant nonradioactive recombination MHP/ETL interface. Warby et al. reported a study of MHP/C60 interface using photoluminescence, photoelectron spectroscopy, and first principle numerical simulations that found the origin of the non-radiative recombination.[59] Their research revealed that the operational mechanism responsible for recombination across the interface involves C60 trap states. These traps can either originate from charge transfer states or result from a broadening of the density of states at the interface, effectively anchoring the lowest unoccupied molecular orbital below the conduction band of the MHP. To reduce the non-radiative recombination losses C60/MHP interface, Mariotti et al used piperazinium iodide as interlayer between MHP and C60.[60] This work resulted in a silicon-perovskite tandem solar cells with a certified PCE of 32.5%.

Despite of the high efficiency achieved with Organic ETLs, these organic materials are generally prone to aging and mechanical failure,[61] making them difficult to maintain long-term stability. Additionally, in tandem and semi-transparent PSCs, the top transparent electrode is generally deposited using sputtering. The organic ETLs surfaces are not tough enough to brace the impact of the sputtering process without suffering damage, which has huge detrimental impact on the efficiency of devices. [62] Therefore, alternative ETLs with high physicochemical stability, excellent electronic properties and high mechanical toughness are necessary for achieving long term stability of the PSCs. One of the alternative candidate for PSCs are metal oxides that are discussed in detail in the next section.

1.4.1.2 Inorganic Metal Oxide Electron Transport Layers

Metal oxides tend to exhibit excellent inherent stability to heat, light, and local environment. Among the various metal oxides, TiO_2, ZnO, and SnO_2 possess exceptional electron transport properties, and their combination of transport properties and inherent stability makes them promising candidates for PSCs.[43,45]

TiO_2 is the most researched ETL in n-i-p architecture PSCs and usually incorporated together with combination of compact and mesoporous bilayer TiO_2 film.[63,64] Alternatively, in the planar PSCs,

the compact TiO_2 layer can be prepared using atomic layer deposition (ALD) at a temperature lower than 200 ◦C, which exhibit simple structure and potential application in fabrication flexible devices.[65] There are three main crystalline phases of TiO_2 namely, anatase,[66,67] rutile,[68] and brookite[69]. Among these phases, anatase is most frequently incorporates in the n-i-p PSCs. In the aspect of depositions methods, high quality TiO_2 film can be produced using various techniques such as, spin coating, sputtering, ALD, chemical bath deposition (CBD), spray pyrolysis, and etc.[65,70-74]

Even though use of TiO_2 ETL resulted in high PCE devices, it has several disadvantages including high temperature processing greater than 450 ◦C is required for to obtain high quality mesoporous film.[75] Not only such high temperature process is energy inefficient, this also affect the resistivity of underneath TCO film (ITO).[76] TiO_2 exhibit high photocatalytic activity which is established in the field of catalysis. However, the catalytic nature of TiO_2 can create new trap states the MHP interface and decompose the MHP as well.[77] This has severe impact on the long term stability of the PSCs. Furthermore, TiO_2 film possess low electron mobility i.e.; 0.1–4 $cm^2\ V^{-1}\ s^{-1}$ and consequently limiting the electron transport.[78] Therefore, improving the surface or bulk properties of TiO_2 is crucial in achieving high-performance and stable PSCs.

Alternatively, ZnO is used as ETL in PSCs, which exhibits a much higher bulk electron mobility around 205–300 $cm^2\ V^{-1}\ s^{-1}$.[79] High quality ZnO thin film can be synthesized at low temperatures using ALD.[80] Furthermore, pre-synthesized dispersed ZnO nanoparticles can also be deposited by spin coating without any post heat treatment. This not only provides more freedom for the synthesis of ZnO nanoparticle with excellent charge transport properties but also makes the low-temperature deposition possible.[81] Therefore, ZnO ETL is used for both n-i-p and p-i-n architecture PSCs. However, the performance of PSCs based on ZnO ETL is considerably mediocre to that TiO_2, due to the unfavourable surface properties of ZnO films. The ZnO has a basic surface and that can result in proton transfer reaction with MHP causing degradation of the MHP film.[82] Moreover, the surface defects of ZnO tend to absorb moisture and oxygen that can act a centre of recombination and accelerate the degradation PSCs.[83] The efficiency and stability can be improved by introducing an interlayer between ZnO and MHP. In p-i-n PSCs, PCBM-ZnO is coupled together for achieve high PCE and also used for fabrication semi-transparent and tandem solar cells due to the tough nature of ZnO film.[84]

Among all inorganic alternatives, SnO_2 has emerged as a highly effective electron transport layer (ETL) for metal halide perovskite (MHP) solar cells. Its suitability for this role stems from its exceptional properties, including a wide bandgap (3.6–4.1 eV), high optical transmission, favorable carrier mobility (240 $cm^2V^{-1}s^{-1}$), conduction band alignment that aligns well with perovskites, and strong chemical stability. [85,86] These characteristics make SnO_2 an ideal choice for facilitating efficient electron transport within PSCs. Hanul Min et al. reported a certified high efficiency of 25.5% in single-junction PSCs by interlayer design of SnO2-based ETL.[87] In this study, the interface engineering between a SnO_2 ETL and MHP was demonstrated by coupling Cl-bonded SnO_2 with a Cl-containing perovskite precursor. This interlayer has reported to be atomically coherent, which improves charge extraction and transport from the MHP layer by defect passivation. The versatility of SnO_2 is evident in its ability to seamlessly integrate into both n-i-p and p-i-n configurations of solar cells. Additionally, various deposition methods can be employed to fabricate SnO2 layers, such as the sol-gel process, CBD, ALD, physical vapor deposition, and other applicable techniques.[88] In later part of this chapter, we comprehensively described about low temperature ALD-SnO_2 used PSCs.

1.4.2. Hole Transport Layers

The HTLs in solar cells play the role of hole transport and simultaneously block electrons at the absorber/HTL interface. As discussed earlier in a general prospect, the HTL needs to have an appropriate energy level alignment, meaning that the VBM of the HTL should be slightly shallower than the VBM of the MHP absorber to efficiently extract holes, while the CBM needs to be high enough to block electrons to suppress charge recombination. [89] Further, the HTL material needs to exhibit high hole mobility and conduction to facilitate hole transport from the MHP to the anode and eliminate charge accumulation at the interface. In addition, similar to the requirements of the ETL, HTLs must possess high chemical and thermal stability, which is crucial for the long-term stability of PSCs. HTL films require high uniformity and compactness to ensure the protection of PSCs from the external environment. Passivation properties are also a key criterion for suppressing the surface defects of MHP, thereby limiting non-radiative recombination at the HTL/MHP interface. To date, several organic and inorganic HTLs with various surface and interface passivation strategies have been used to achieve high efficiencies and long-term stability PSCs.[90] In the next section, we discuss a few widely used organic and inorganic HTL materials, their properties, and their drawbacks.

1.4.2.1 Organic Hole Transport Layers

Organic HTLs have consistently led the way in advancing the efficiency of PSC devices for nearly a decade. The highest PCE in n-i-p PSCs are often achieved using tetrakis[N,N-di(4-methoxyphenyl)amino]-9,90 spirobifluorene (spiro-OMeTAD) and poly[bis(4- phenyl)(2,4,6-trimethylphenyl)amine] (PTAA) HTLs (see Figure 1.7).[91-93] The wide popularity of spiro-OMeTAD as a HTL in PSCs can majorly be attributed to the ease of processing, good hole conductivity when doped and favourable band alignment with several MHP absorbers.[94,95] Schulz et al. reported the energy band alignment of spiro-OMeTAD using photoemission spectroscopies method.[96] The HOMO and LUMO of spiro-OMeTAD found to be located at an energy level of -5.0 eV and -1.5 eV respectively. The spiro-OMeTAD's LUMO is situated at an energy level more than 2 eV above the CBM of MHP, signifying its strong electron blocking abilities.

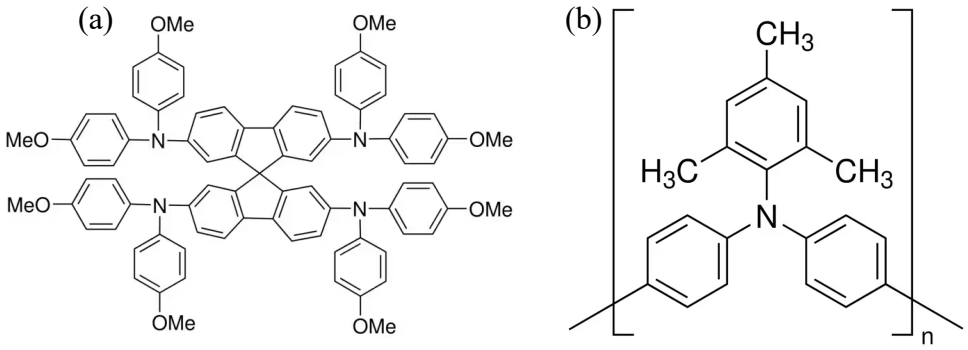

Figure 1.7. Chemical structure of (a) tetrakis[N,N-di(4-methoxyphenyl)amino]-9,90 spirobifluorene (spiro-OMeTAD) and (b) poly[bis(4- phenyl)(2,4,6-trimethylphenyl)amine] (PTAA).

Spiro-OMeTAD has been generally doped with different additives to enhance the electronic characteristics. The most frequently used additives are lithium-bistrifluoromethanesulfonimidate (LiTFSI), (tris[2-(1H-pyrazol-1-yl)-4-tert-butylpyridine)cobalt(III)tris(bis(trifluoromethylsulfonyl) imide)] (FK209), and 4-tert-butylpyridine (tBP).[97] When LiTFSI and tBP are used simultaneously in spiro-OMeTAD, there is an increase in its conductivity, improving it by two orders of magnitude, from $2.5*10^{-7}$ Scm^{-1} to $2*10^{-5}$ Scm^{-1}. Furthermore, the addition of FK209 led to further enhanced conductivity, resulting in a reduction in the series resistance from 94.7 Ω to 65.8 Ω.[98]

Despite the excellent hole transporting properties of doped spiro-OMeTAD resulting high efficiency PSCs, it's stability is a major concern. Spiro-OMeTAD is vulnerable to operational temperature and can succumb to thermal degradation.[99] The dopants used in spiro-OMeTAD are hygroscopic in nature and can accelerate the degradation process.[100] Furthermore, the dopant can cause morphological issue which can cause formation of pinholes.[95] The pinholes in the HTL opens up ion migration process between dopant, MHP and electrode ions.[101] In addition, minor deviation in

the concentration of dopant and environmental condition can significantly impact the conductivity properties of spiro-OMeTD and thereby affecting the reproducibility. Consequently, spiro-OMeTAD based PSCs suffers from low operational stability even with the exceptionally high efficiency of the fresh devices.

The PTAA HTL exhibits better inherent stability compared to spiro-OMeTAD.[102] The enduring popularity of PTAA as an HTL in PSCs is due to its favorable characteristics, such as its excellent thermal stability up to 300°C in an amorphous state, high hole mobility (3–6*10-5 $cm^2V^{-1}s^{-1}$), favorable solubility in organic solvents, and good energetic alignment with most MHP materials. PTAA is also p-doped to enhance the hole transport properties using LiTFSI and tBP.[103] The most effective concentration of dopants used in PTAA based PSCs are approximately four time lower than the concentration of LiTFSI and tBP used in spiro-OMeTAD.[104] This observation suggests either a greater efficiency in doping or a reduced ideal concentration of holes in PTAA required for optimal device performance. Although PTAA is stable at high temperatures, it still fails to protect MHP from the outer environment owing to the hygroscopic nature of the dopants, similar to spiro-OMeTAD.[105] Furthermore, the migration and evaporation of LiTFSI and tBP dopants cause several issues related to ion migration in devices.106 Therefore, exploring other p-dopants suitable for maintaining the long-term stability of PSCs is essential.

In summary, the research on spiro-OMeTAD and PTAA has resulted in record efficiency devices, and simultaneously the stability is of big concern. Hence, several other robust inorganic metal oxides HTLs have been studied for their application in PSCs. In the next section, we describe the current developments in these materials for application in PSCs.

1.4.2.2 Inorganic Metal Oxide Hole Transport Layers

Several metal oxides, such as V_2O_5, NiO_X, and CuO_X, have been used in perovskite devices as alternatives to organic HTL to enhance their stability. CuO_X as an HTL in PSCs has great potential because of its compatibility with MHP materials, ease of synthesis, and non-toxicity. CuO_X film consists of Cu_2O and CuO phases, exhibiting hole mobilities of 100 $cm^2\ V^{-1}\ s^{-1}$ and 0.129 $cm^2\ V^{-1}\ s^{-1}$, respectively.[107] The composition can be modified to tune the mobility, conductivity, and transmittance of the CuO_X HTL. Yuhui Ma et al. have reported CuO_X quantum dots-based PSCs that have demonstrated an efficiency of 19.91%.[108] This high performance is attributed to the higher crystallinity of the perovskite layer on the CuO_X quantum dot layer, which reduces the charge trap state densities, resulting in low non-radiative recombination. Similarly, VO_X is also a promising HTL candidate for PSCs owing to its tunable electrical properties, high conductivity, and thermal stability. However, because of the high resistivity of VO_X, the thickness and thin-film deposition

methods can dramatically influence device performance. In a recent study, Park et al. demonstrated a 45 °C ALD-grown VO_X on top of spiro-OMeTAD as an interlayer in n-i-p-architecture PSCs. The compact ALD-VO_X layer acted as a protective layer by blocking moisture and oxygen from the surroundings and inhibiting Au and Li-ion diffusion in the device. They reported a high efficiency of 23% with enhanced operational stability. [109]

Among the various metal oxides used in PSCs, NiO_X is the most researched and widely used owing to its chemical stability and abundance. It has achieved a maximum PCE of over 23% [110] and possesses desirable properties, such as a band gap greater than 3.6 eV, high transmittance in the near ultraviolet and visible regions, and excellent thermal, chemical, and light stability, making it a promising material for MHP technology.[111] In addition, low-cost, low-temperature, reproducible, and scalable fabrication processes are beneficial. Several methods, such as sol-gel, combustion, spin coating, electrodeposition, pulsed laser deposition, sputtering, and atomic layer deposition, have been employed to deposit NiO_X.[112] The p-i-n structure is the most commonly studied in NiO_X-based PSCs. The use of NiO_X in the n-i-p structure faces challenges because of factors such as the use of strong polar organic solvents or water as a dispersant for NiO_X and the high annealing temperatures needed for NiO_X preparation, which can degrade the MHP material, restricting its applicability in this device architecture.

In addition, stoichiometric NiO_X exhibits low intrinsic conductivity around 10^{-4} S/cm, which restricts its application in PSCs.[113,114] Undoped NiO_X typically displays p-type characteristics owing to the presence of numerous nickel vacancies with high ionization energy, causing a reduction in the total density of the holes.[115] Furthermore, the mismatch between the Fermi level of NiO_X and the VBM of the MHP weakens the built-in field of the PSCs, leading to the accumulation of holes at the MHP/NiO_X interface and hindering efficient charge extraction.[116] Additionally, the Ni^{3+} species in NiO_X can readily react with the halides present in the MHP, leading to the deterioration of the MHP film and the formation of numerous trap defects at the MHP/NiO_X interface.[117] Several strategies have been studied to improve the conductivity and hole mobility of NiO_X, as well as to decrease its reactivity with MHP materials, including interfacial modifications and doping.[112]

In summary, we discussed different organic and inorganic CTLs research by the PSCs community, their advantages, and shortcomings. In particular, metal oxide-based CTLs have great potential for use in stable PSCs because of their inherent chemical stability to various stressors. However, there are limitations in incorporating some of these metal oxide HTLs due to solvent incompatibility with the MHP material and high-temperature thermal processing, which can degrade PSCs. Hence, in this thesis, we study a low-temperature metal oxide deposition technique known as atomic layer deposition, specifically for deposition on top of an MHP. The previous sections of the chapter also cited this technique and reported some research studies demonstrating the high-stability PSCs

obtained. In the next section, we discuss the fundamental advantages and challenges of ALD techniques in the context of PSCs.

1.5. Atomic Layer Deposition based Metal-oxides for Stable PSCs

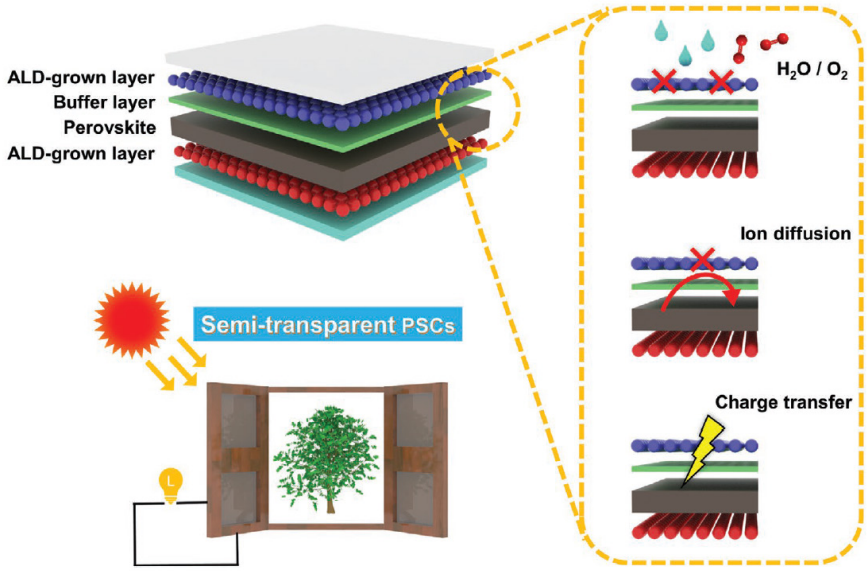

Figure 1.8. Schematics of advantages of ALD oxides in PSCs.[118]

The ALD technique is promising for growing metal oxide layers for application in PSCs due to its relatively low deposition temperature, uniform coverage, and industrial scalability.[119] Using the ALD process ultra-thin dense metal oxide film could be deposited that can act as encapsulation to the outer environment and also block internal ion migration in PSCs as illustrated in Figure 1.8.[118] In addition, several ALD grown metal oxides such as SnO_2, NiO_X possess excellent charge transport properties which are used for fabrication high performance PSCs. Moreover, this ultrathin film possesses high optical transmittance that makes it suitable interlayer for semi-transparent solar cells and top cell of tandem solar cells.

1.5.1 Fundamentals of Atomic Layer Deposition

ALD is a chemical gas-phase thin film deposition technique based on sequential, self-saturating surface reactions. In this deposition method, highly reactive precursor chemicals are injected and interact with the substrate. The precursor chemicals are introduced into the chamber separately, to restrict uncontrolled gas-phase reactions. [120]

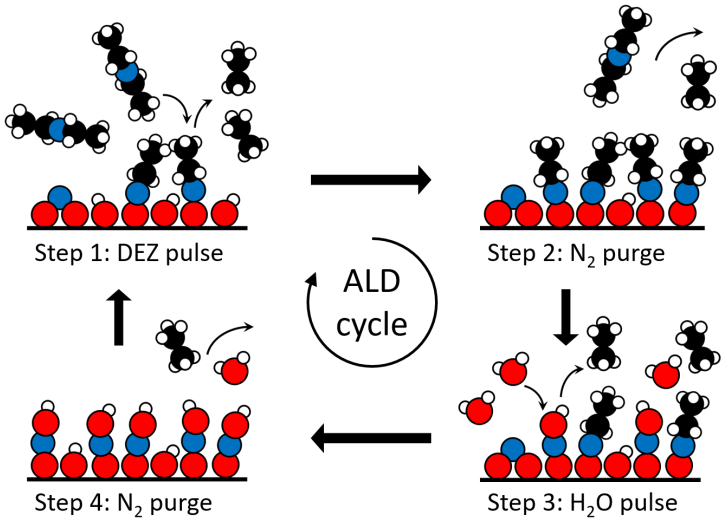

Figure 1.9. Schematics representation of ALD cycle of the deposition of ZnO with Diethyl-Zn and H_2O. [121]

A schematic of the ALD process is demonstrated in the Figure 1.9. During the ALD process, the first precursor generally an organometallic compound is pulsed into the deposition chamber where it chemisorbs to the surface of the substrate. In the next step, an inert gas such as Nitrogen is purged to remove excessive metallic precursor, followed by subsequent pulse of reactant precursor such as H_2O, H_2O_2 or Ozone. The reactant precursor chemically interacts with the surface organometallic fragment in maintained pressure and temperature forming an ultra-thin film layer. Excessing reactant precursor is similarly removed by purging inert gas into the chamber. This reaction cycle is continued to achieve a desired thickness depending upon the application. Taking the advantage of self-limit reactions are precise control over the layer thickness, and stepwise deposition of monolayers (in the range of Å), which results in very smooth, compact and conformal films in a large area which is suitable for industrial application.[122] ALD also has the advantage low temperature processing (as low as 25°C),[123] making it suitable for thermally sensitive material such as MHP or organic CTLs. Furthermore, the recent advancements in ALD technique enables the deposition at the atmospheric pressure. Additionally, the atomic scale control over thickened using ALD process facilitates precise tuning of the optoelectronic and chemical properties of the ALD grown thin films.

1.5.2 Applications of Atomic Layer Deposition in PSCs

ALD thin films are popular in the perovskite community because of their versatile properties, and are incorporated for various functionality including electrode, buffer layer, passivation, absorber, CTLs and encapsulation as shown in Figure 1.10.[124] In the following, we discuss few select examples of these functionally of ALD film.

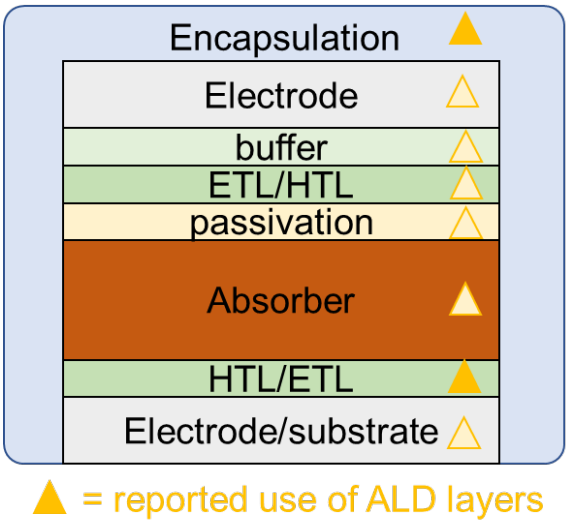

Figure 1.10. Illustration of application of ALD in PSCs.

In recent years, ALD-grown Al_2O_3 has attracted considerable attention for the encapsulation of PSCs. Seo et al. used a 50nm ALD-grown Al_2O_3 on top of PSCs.[125] The PSCs exhibited excellent thermal stability at 85°C for 500 h under the operational conditions. In another similar study, Ramos et al. used a thin 16 nm ALD Al_2O_3, which demonstrated high stability at 80% humidity for 94 days, retaining 75% of its initial efficiency.[126] Singh et al. demonstrated that the encapsulation of PSCs using ALD-Al_2O_3 provides protection not only from humidity but also from oxygen.[127] Aside from encapsulation, ALD-Al_2O_3 can also be used to passivate the surface of MHP. An example of this is the work done by Koushik et al., who deposited an ultrathin layer of ALD-Al_2O_3 on MHP, resulting in a 3% improvement in performance with a PCE of 18% and a decrease in hysteresis loss.[128] The Al_2O_3 incorporated device showed excellent stability in ambient humidity and retained 70% of its initial PCE after 70 days.

In addition, a few research works have demonstrated fabrication of inorganic MHP using ALD process. In a recent study, Weiß et al. reported synthesis of γ-$CsPbI_3$ MHP film at 100°C.[129] They prepared $CsPbI_3$ films utilizing a supercycle approach by depositing ALD- PbI_2 on top of ALD-CsI films in alternative cycle mode. Furthermore, ALD thin films are used for fabrication of transparent conductive oxides (TCO), for example, Hu et al. have demonstrated fabrication of AZO electrodes using ALD at a temperature of 150 °C.[130]

In this doctoral thesis, our primary focus lies in exploring the significance of ALD metal oxides as CTLs. Specifically, we delve into the roles of SnO_2 and NiO_X in this context, attributing their importance to their remarkable stability, well-documented charge transport characteristics as detailed in the previous section, and their inherent compactness achieved through the ALD process. In a ALD-SnO_2 based study, Lee et al. used 100°C-grown ALD-SnO_2 with various passivation strategies in n-i-p PSC, demonstrating a PCE of 20%.[131] They found that the surface passivation of SnO_2 is essential to reduce charge recombination at the perovskite and ETL interface and showed that the fabricated planar perovskite solar cells exhibit high reproducibility and stability. In a recent study, Ren et al. incorporated 50°C low-temperature ALD SnO_2 in PSC and perovskite tandem solar cells.[132] They achieved high-quality SnO_2 at such a low temperature using high-activity H_2O_2 as the oxygen source during the ALD steps. They achieved a PCE of 20.7% with an n-i-p single-junction PSC and a PCE of 26.67% in perovskite-silicon tandem solar cells with p-i-n architecture top PSCs. In several p-i-n PSCs in single junction and tandem, ALD-SnO_2 is used as a bilayer ETL configuration on an organic ETL, such as C60, to achieve record efficiency. Al-Ashouri et al. demonstrated an efficiency of 20.8% in p-i-n architecture PSCs using LiF/C60/SnO_2 top layer. In addition, they achieved a certified PCE of 29.15% in silicon–perovskite tandem solar cells. [133]

Similarly, in HTL, ALD-grown NiO_X has been extensively investigated for PSCs and several interface engineering strategies are used to achieve high efficiency and stability. The initial study on ALD-NiO_X in 2016 by Seo et al. used an ultra-thin 7.5 nm film of NiO_X, demonstrating high optical transmittance and interfacial properties.[134] The p-i-n PSC exhibited a champion-cell PCE of 16.4% without hysteresis. In another study by the same research group, the coupled impact of ALD-NiO_X HTL and ALD-AZO ETL in an p-i-n architecture achieved high stability at 85°C for 500 h, retaining 85% of the initial PCE.[135] Furthermore, in a recent study, a self-assembled phosphonic acid molecule, MeO-2PACz ([2-(3,6-dimethoxy-9H-carbazol-9-yl)ethyl]phosphonic acid), used as an interlayer between ALD-NiO_X and MHP, exhibited defect passivation, which improved the reproducibility of p-i-n PSCs and achieved a PCE of 20%.[136]

In summary, several research investigations have demonstrated enhanced efficiency and stability of PSCs by employing of ALD metal oxide CTLs. However, ALD metal oxide CTLs directly on MHP films have not been successfully incorporated without detrimental effects on the performance of the PSCs. In the next section, we review the scientific research on interface of ALD metal oxides on MHP films.

1.5.3 ALD Charge Transport Layer Growth on top of Metal Halide Perovskite

The direct ALD oxide growth on MHP film can damage the MHP underneath due to the reliance of ALD on chemical precursors, pressure, temperature and reactions. The reported PSCs, with ALD oxide deposited on top, have generally shown low PCEs in the range of 0.5%-8.2%.[137-140] In a study by Kim et al. exposed $MAPbI_{3-X}Cl_X$ film to various ALD precursors and investigated the degradation of the $MAPbI_{3-X}Cl_X$ as represent in Figure 1.11.[141] The study revealed complete decomposition of MHP film to PbI_2 upon exposure to ozone. When exposed to H_2O, they observed formation PbI_2; however, the damage was not as severe as exposure to ozone. In order to limit the damage due exposure to ozone or H_2O, they utilized an alternative non-hydrolytic precursor to deposit Al_2O_3 and TiO_X on $MAPbI_{3-X}Cl_X$ film. They did not observe any change in optical or structural properties of underneath MHP film with this new strategy.

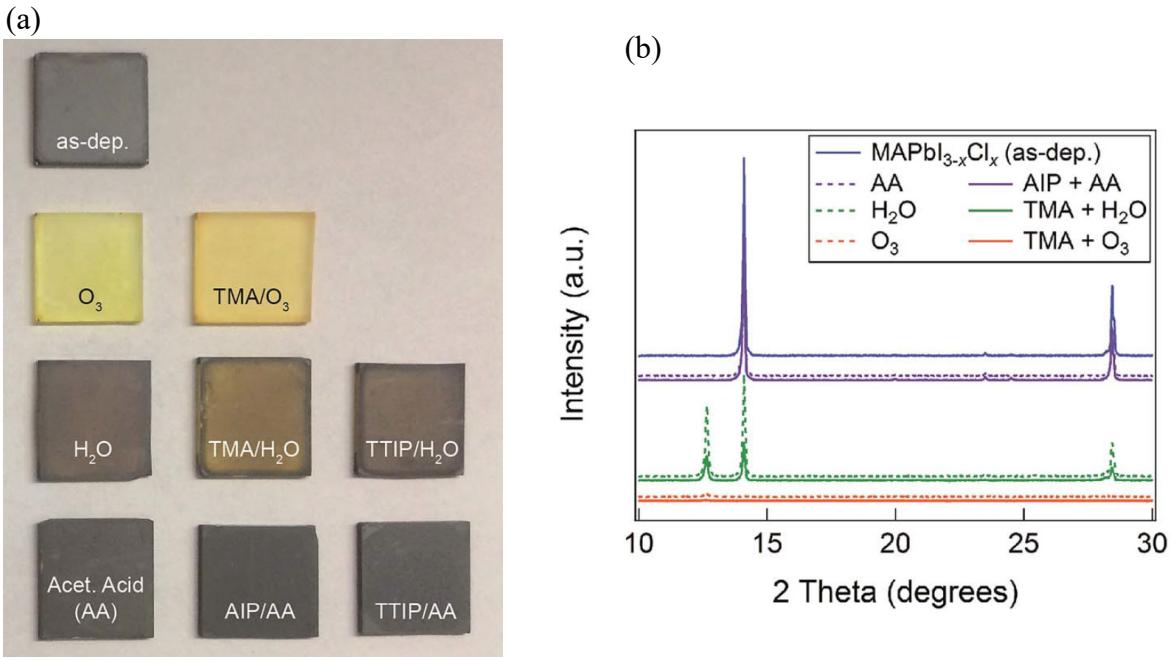

Figure 1.11. (a) Optical image of representative as-deposited $MAPbI_{3-X}Cl_X$ and exposed to O_3, H_2O, and acetic acid (b) XRD pattern of corresponding films.[141] TMA: trimethy aluminium, TTiP: titanium

In another research study, Hultqvist et al. compared the use of ZnO and SnO_X ALD processes on $FAPbI_3$:$MAPbBr_3$ based MHP.[142] They found that exposure to 100°C temperature, H_2O vapour pulsing and ALD vacuum condition did not cause any noticeable difference to MHP bulk crystallinity. However, they found that the organometallic precursors to be critical to the stability of the MHP film. Specifically, the Diethyl-Zn precursors rapidly decomposed the MHP bulk into lead halides and organic halides. In case of the tetrakisdimethylamino- Sn (TDMASn) precursors for SnO_2, their work did not find evidence of altercation in the MHP bulk. However, in the p-i-n

devices with ALD SnO_2 ETL, they achieved a poor PCE of 4%. Puzzled by the low performance, Hultqvist et al. reported another work in 2020 on interface investigation of MHP/ALD-SnO_2 using photoelectron spectroscopy. [143]

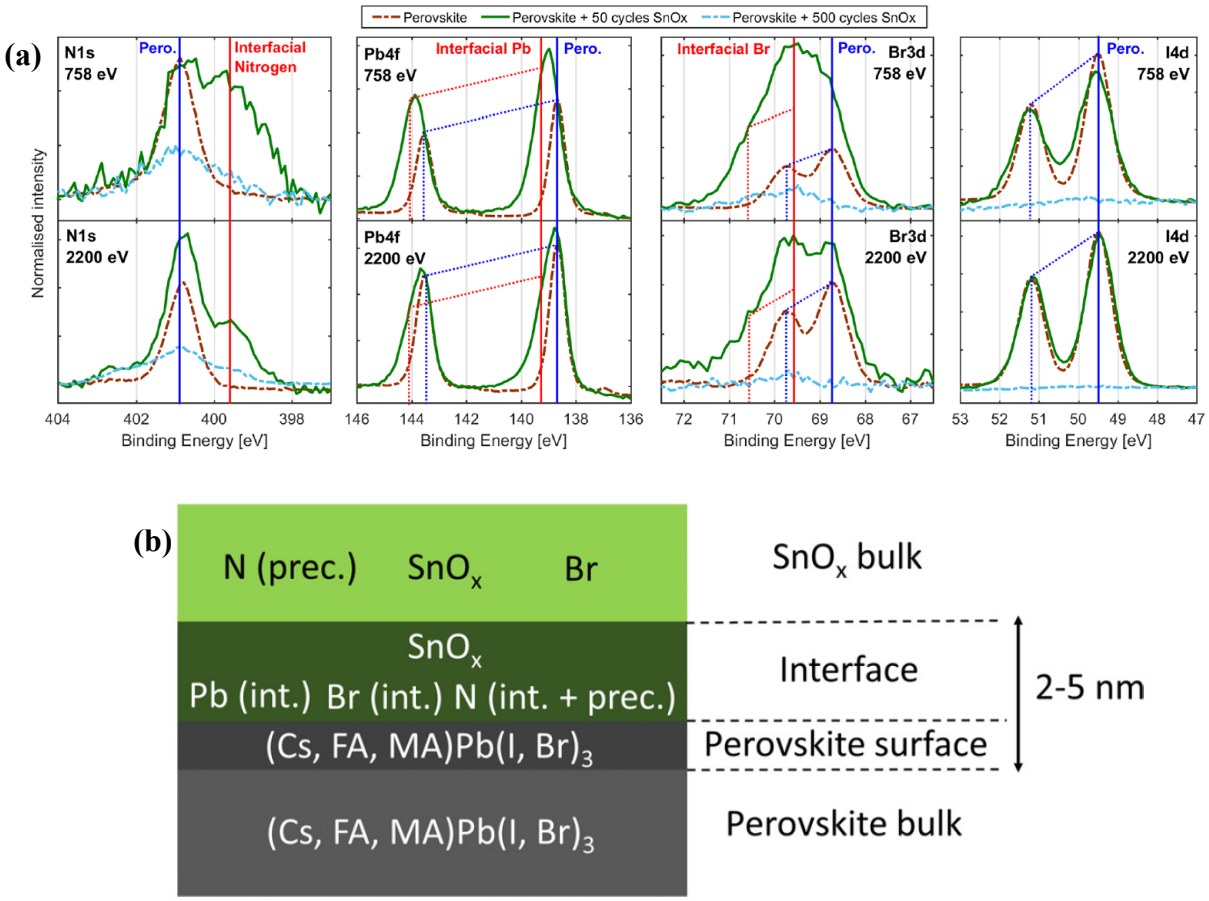

Figure 1.12. (a) SOXPES and HAXPES spectra N 1s, Pb 4f, Br 3d, I 4d, O 1s and Sn 3d core levels of perovskite with and without ALD-SnO_2 top layer (b) Schematic of the perovskite/SnO_2 interface chemistry based on SOXPES and HAXPES analyses. [143]

In this investigation, Hultqvist et al. incorporated a thin and thick layer of ALD-SnO_2 on top of triple cation $Cs_{0.05}FA_{0.79}MA_{0.16}PbBr_{0.51}I_{2.49}$ MHP. They used soft and hard X-ray photoelectron spectroscopy with excitation energies of 758 eV and 2200 eV to probe the MHP/ALD-SnO_2 interface and tracked the evolution N 1s, Pb 4f, Br 3d, I 4d core levels with reference to pristine MHP (see Figure 1.12 (a)). They observed the formation of additional chemical species involving Pb, Br, and N at the interface and suggest this causes the formation of an electron barrier layer. They conclude that the defective species originate from an interfacial layer of 2-5 nm on top of MHP film (see Figure 1.12(b)). Further, their work claimed a strong interaction between MHP surface and TDMASn precursor during initial exposure.

Another study conducted by Bracesco et al. investigated the interface between ALD-SnO_2 and $FA_{0.85}Cs_{0.15}Pb(I_{0.92}Br_{0.08})_3$ using X-ray photoelectron spectroscopy (XPS).[144] The ALD-SnO_2 was grown similarly on MHP film using TDMASn and H_2O ALD precursors at 100°C. The researchers found formation of defective new species at the MHP/ALD-SnO_2 interface namely, I_2, Br_2, $PbBr_2$ and a new nitrogen based species. Bracesco et al. performed another follow up study reported in 2023, which investigated on the formamidinium (FA) cation losses in exposure of ALD-SnO_2 precursors employing in-situ infrared spectroscopy (see schematic in Figure 1.13).[145] They investigated the effect of ALD temperature, pressure, TDMASn and H_2O precursors. Their work found that the exposure to vacuum condition, 100° C temperature or H_2O half cycle had negligible impact on the chemistry of MHP. In contrast, exposure of TDMASn caused prominent modification to MHP, for eg., 10 pulses of this precursor resulted in 4% loss in FA cation. Furthermore, using IR-spectroscopy, they identified the defective nitrogen species at MHP/ALD-SnO_2 as trapped *sym-triazin*e which is a degraded by-product of FA species.

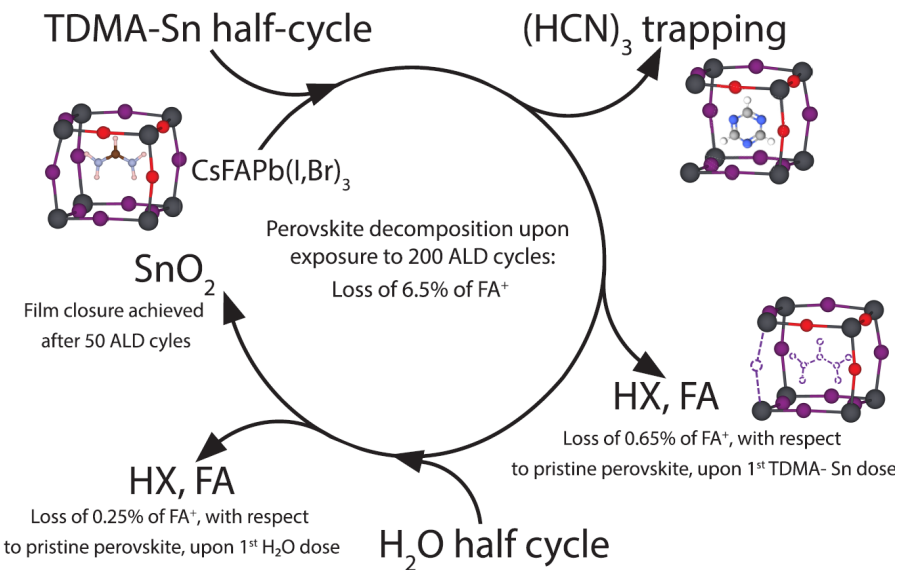

Figure 1.13. Schematic of effect of the exposure of H_2O and TDMASn precursors on formamidinium cation.[145]

In summary, the interaction of ALD precursors with MHP can be detrimental because of possible unwanted chemical reactions. An ALD process temperature of less than 100°C and vacuum conditions do not have any impact on the MHP film. Similarly, reactant precursors, such as H_2O and H_2O_2, do not lead to observable alterations in the MHP surface and bulk. However, the organometallic ALD precursors used in ALD growth are crucial and can have a severe impact on the MHP surface. Important questions still remain, such as the effects of these undesired interfacial reactions and chemical defects on the electronic band alignment. In addition, it is uncertain whether this interfacial damage is limited to the top interface or extends deeper into the subsurface region.

However, these insights are essential prerequisites for the development of damage-free ALD metal-oxide deposition processes for MHPs. Therefore, these factors constitute the foundational inspiration for my doctoral thesis. Moreover, in the course of my thesis research, I utilized XPS and hard X-ray photoelectron spectroscopy (HAXPES) to investigate the evolution of the electronic band alignment and chemistry of the buried interfaces of ALD-derived SnO_2 and NiO_X on MHP absorbers. The following section provides an overview of the fundamental principles of photoelectron spectroscopy.

1.6. Hard X-ray Photoelectron Spectroscopy

1.6.1 Fundamentals of Photoelectron Spectroscopy

Photoelectron spectroscopy (PES) is a technique that relies on the photoelectric effect, which involves the emission of electrons from a material upon bombardment with photons. PES is a non-invasive method used to investigate the chemical and electronic properties of the surface and interface regions of materials. It employs monochromatic X-rays or ultraviolet (UV) photons with known energy to release electrons from either the core level or valence band of a sample. The photoemission process typically involves three steps (Figure 1.14), which are as follows:

1. **Photoionization**: In this step, high-energy photons from sources such as X-ray tubes, gas discharge lamps, or synchrotron-based sources excite electrons in the bulk of the material.
2. **Travel of the Excited Electron**: After photoionization, the photoelectron travels through the bulk towards the surface of the material, possibly experiencing energy loss. Electrons that reach the surface without losing energy contribute to the elastic peak in the spectrum, while those that undergo inelastic collisions create an inelastic background.
3. **Photoelectron Emission and Analysis**: The photoelectron then crosses the surface of the material and experiences energy loss related to the surface potential. Finally, it travels through the vacuum to the analyzer.

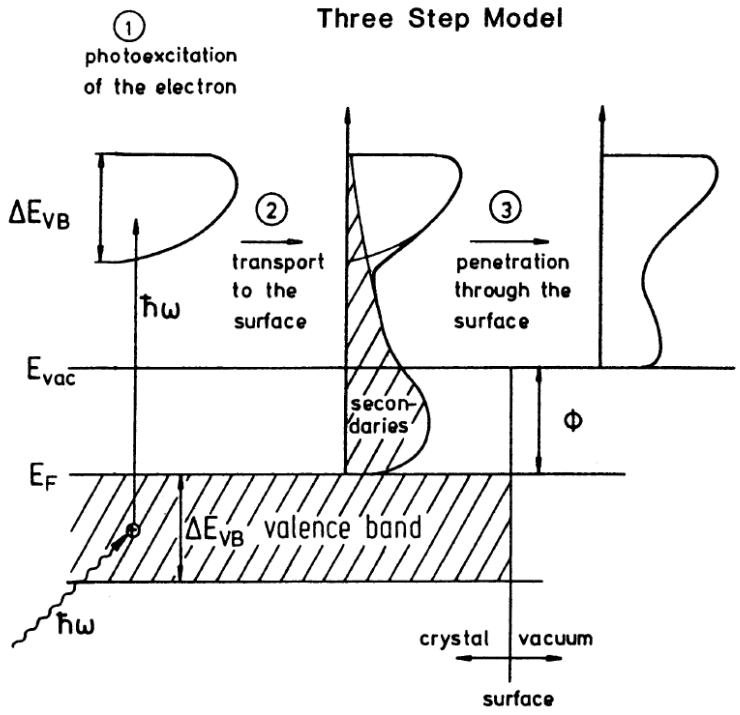

Figure 1.14. Schematics of the Three-step model of the valence band photoemission process.[146]

To ensure that both the sample and spectrophotometer share the same Fermi level, they are connected to a common ground in PES measurements. The binding energy (E_{BE}) is determined using following expression:

$$E_{BE} = h\upsilon - E_{KE} - \phi_{analyser} \qquad \text{Equation 1.1}$$

In this equation, hν represents the energy of the photon, E_{KE} is the kinetic energy of the emitted photoelectron, and $\varphi_{analyzer}$ signifies the work function of the spectrophotometer's analyser (see Figure 1.15). To determine the $\varphi_{analyzer}$, a reference sample, typically composed of metallic gold, is used where the Au4f core level signal positioned at 84 eV is used as reference. Alternatively, the adventitious carbon C1s signal, located at 285 eV, is sometimes employed as a reference. It is important to note that relying on the binding energy of adventitious carbon can be unreliable since it is influenced by the surface's work function rather than the Fermi level. [147,148]

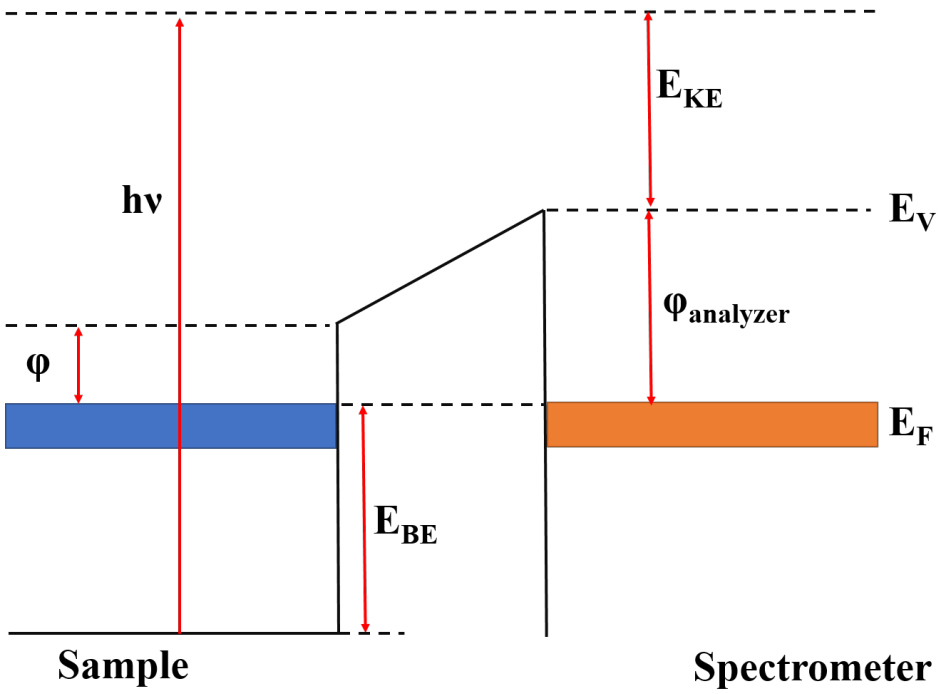

Figure 1.15. Energy-level diagram of the sample and the spectrometer in a core-level photoemission experiment of a conducting sample.

The PES experiments are carried out in an ultra-high vacuum, which increases the mean free path of the electrons and diminishes the likelihood of the emitted photoelectron being scattered en route to the detector. The PES technique can be employed to analyze the chemistry of materials or molecules in either a gas, liquid, or solid state. It is crucial when analyzing solids that the material be conductive to avoid any charging effects that may shift the binding energy of the core levels. Alternatively, non-conductive samples can be neutralized using an electron gun, thereby eliminating any charging effect.

1.6.2 Synchrotron Radiation for HAXPES

HAXPES has emerged as a powerful technique to study the bulk properties and buried interfaces using hard X-rays typically in the range of 2-10 keV.[149] The early development of XPS was limited to soft X-rays with Al K-alpha line (1486.7 eV) focusing on the surface properties of materials. With advancement of powerful X-ray sources, HAXPES become a standard tool for non-destructive study of the buried interface with vast applications in solar cell, energy storage, materials science, fundamental physics and etc. With the current technology, hard X-rays can be generated via synchrotron beamlines or in-lab technology,[150] such as utilizing the Ag Lα line (2984.2 eV), Ga Kα radiation (9252 eV) and etc. The synchrotron based HAXPES generates intense and focused beam of X-rays, which is useful to obtain high resolution spectra of the core level electrons.

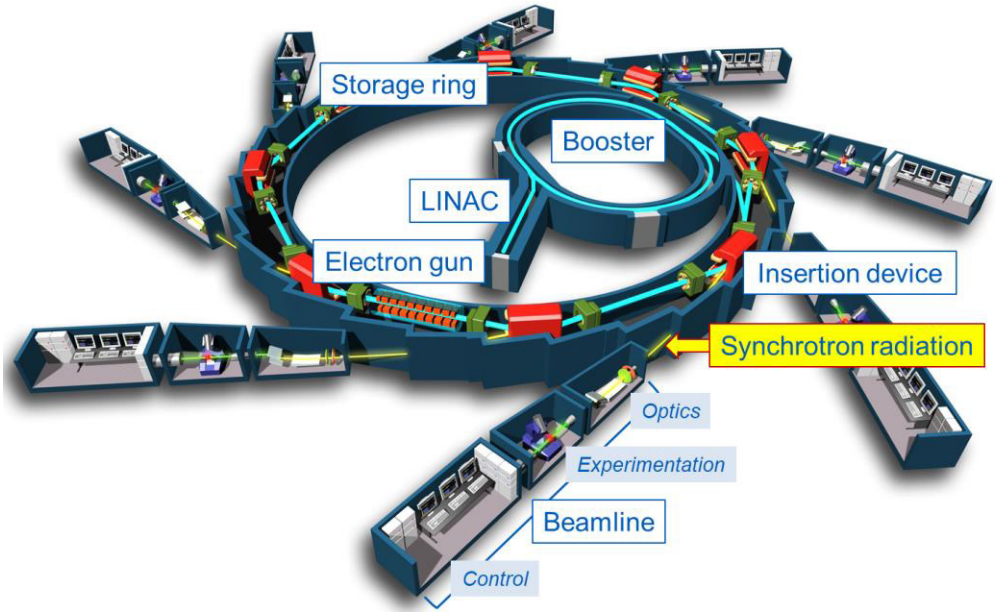

Figure 1.16. Illustration of synchrotron facility.[151]

Figure 1.16 represents an illustration of a synchrotron facility. A synchrotron is a type of circular particle accelerator, in which the charged particles (electrons) are accelerated through a sequence of magnets reaching the speed of light, which emits bright radiation. The electrons in the synchrotron are generated using an electron gun and then transported by applying an electric field to the linear accelerator (LINAC), which accelerates the electrons to a higher energy. Subsequently, the electron moves to the booster, gaining energy in the range of several MeV to a few GeV at a speed almost equal to the speed of light. In the next step, electrons are injected into the storage ring, where they move in a circular path by an array of magnets. These accelerated electrons produce very intense light, known as synchrotron light, which contains a wide spectrum of energies, from IR to hard X-rays. The bright and focused beam of X-rays is then directed into the beamline where the hard X-rays are monochromated either using a silicon crystal (photon energy of $\gtrsim$ 2000 eV) or a plane grating monochromator (photon energy of $\lesssim$2000 eV), and further focused using X-ray optics to an end station where measurements are performed.

1.6.3 Intensity and Probing Depth in HAXPES

The quantitative analysis of sample relies on the intensity of the photoelectron signal originated from various energy levels of the elements in the sample. The intensity of the photoelectron signal in PES is influenced by multiple parameters discussed below, and for a photoelectron to be detected as a signal, it must traverse from the atomic absorption site to the analyzer without undergoing any inelastic processes, in line with the energy conservation principle as described in Equation 1.1. As discussed earlier in the fundamentals of PES, the elastic collisions contribute to photoelectron spectra and inelastic electrons detected as background of the core level spectra (see Figure 1.15(a). The probability of inelastic scattering of a photoelectron is described by the inelastic mean free path (IMFP), which is the average distance (λ) between two consecutive inelastic collisions. The probability of a photoelectron emitted from the surface of the sample that does not undergo inelastic scattering is characterized by an exponential dependence on the depth at which it originated. This depth dependence is utilized to express the differential photoemission signal intensity, $dI_{z'}$, arising from a volume of 'dv' at a depth z′ from the surface. The expression for $dI_{z'}$ is given by:

$$dI_{z'} = I_0 \exp(-\frac{l}{\lambda})dv = I_0 \exp(-\frac{z'}{\lambda\cos\alpha})dv \qquad \text{Equation 1.2}$$

where 'l' is the path length of the photoelectron from the originating point to the surface in the direction of the electron analyzer, α is the angle between the electron detection and the surface normal, and I_0 is a proportionality constant that depends on the photon flux, transmission function of the spectrometer, and photoemission cross-section (σ).

The above equation 1.2 indicates that the dI of a core level decreases exponentially with increase in the depth z. When the angle of detection α is zero, 95% of the total signal originates from the surface region of a 3λ thickness and the remaining 5% originates form a deeper region of the sample (Figure 1.17).[152] This explains the surface sensitivity of LabXPS with Al kα source, where the λ in the range of 0.5-2nm. Furthermore, the surface sensitivity is significantly influenced by the detection angle relative to the surface normal; greater angles enhance surface sensitivity by requiring photoelectrons to traverse a longer path through the material to exit tangentially from the surface. The buried interface can be accessed by increasing the IMFP of the photoelectron, which can be accomplished by increasing the X-ray photon energy. The availability of advanced synchrotron facilities enables the tuning of the IMFP through the use of hard X-rays with different kinetic energy.

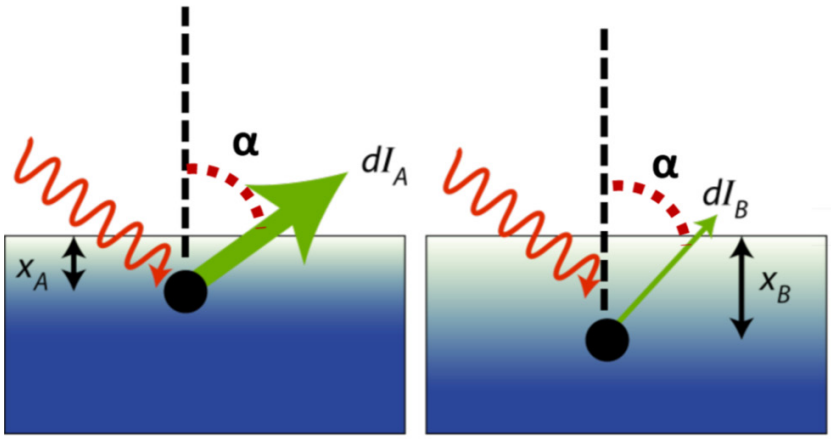

Figure 1.17. Photoelectrons generated at different distances, X_A and X_B, from the surface of the material show different intensities in the photoemission signal, with the intensity dropping off exponentially with X.[152]

The TPP-2M developed by Tanuma et al. can be used to calculate the IMFP,[153] as shown in Figure 1.18. This figure displays the IMFP values of 41 elemental solid with varying electron energy. It is observed that the majority of the intensity from techniques such as UPS, SOXPES, and XPS comes from below 2 nm, 5 nm, and 10 nm, respectively. This makes it challenging to probe buried interfaces, such as those found in perovskite solar cells, using these techniques. In contrast HAXPES with high kinetic energy, can detect signal from deeper than 10 nm, making it a more suitable technique for probing such interfaces.[154] From this, it is clear that HAXPES offers a significant increase in bulk sensitivity compared to standard lab based XPS. It should be noted that the buried interface can also be accessed via sputter depth-profiling XPS. However, sputter etching typically damages the material and ultimately modifies the chemistry of the buried interface.[155] In this case, HAXPES is useful for studying the buried interface without causing significant damage to the material. Sensitive materials, such as MHP, can still be affected by exposure to high-intensity X-rays. This type of damage can be restricted by tuning the intensity using beam-attenuating filters (Al- or Be-based filters). The specifications of the beam-attenuating filters are presented in the experimental parameters of the HAXPES section of the following chapter, where further details can be found.

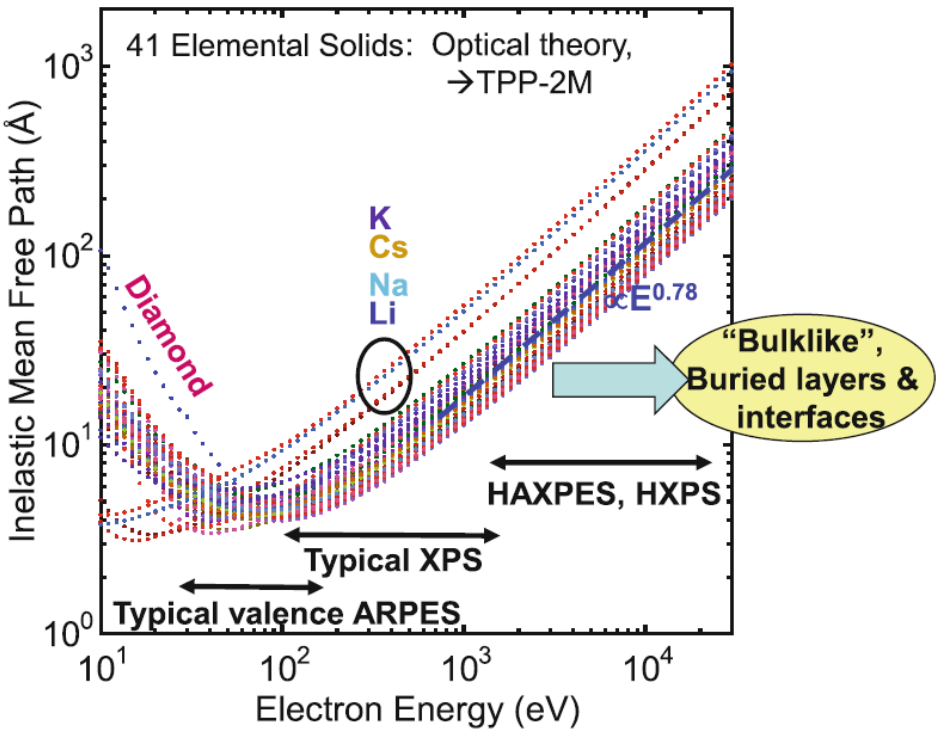

Figure 1.18. Energy dependence of electron inelastic mean free paths as calculated from optical properties for 41 elements, with values closely related to the TTP-2M formula .[156]

1.7. Summary

In this chapter, we discussed the fundamentals of MHP materials, stability and working principle of PSCs. Further, this chapter reviewed various organic and inorganic CTLs used in PSCs and discussed the advantages and shortcoming of these functional layers. In addition, this chapter described the fundamentals of ALD, its application in PSCs, and challenges. Several examples of interface studies ALD-oxides on top of MHP are also discussed in this chapter. In the last part, we described fundamentals of photoelectron spectroscopy and advantages of HAXPES for probing the buried interface.

■ REFERENCES

1. NREL efficiency chart, https://www.nrel.gov/pv/cell-efficiency.
2. Rose, G., 1840. Ueber einige neue Mineralien des Urals. *Journal für praktische Chemie*, *19*(1), pp.459-468.
3. Kojima, A., Teshima, K., Shirai, Y. and Miyasaka, T., 2009. Organometal halide perovskites as visible-light sensitizers for photovoltaic cells. *Journal of the american chemical society*, *131*(17), pp.6050-6051.

4. Weber, D., 1978. $CH_3NH_3PbX_3$, ein Pb (II)-system mit kubischer perowskitstruktur/$CH_3NH_3PbX_3$, a Pb (II)-system with cubic perovskite structure. *Zeitschrift für Naturforschung B*, *33*(12), pp.1443-1445.
5. Chilvery, A., Das, S., Guggilla, P., Brantley, C. and Sunda-Meya, A., 2016. A perspective on the recent progress in solution-processed methods for highly efficient perovskite solar cells. *Science and Technology of advanced MaTerialS*, *17*(1), pp.650-658.
6. Hasnain, S.M., 2023. Examining the advances, obstacles, and achievements of tin-based perovskite solar cells: a review. *Solar Energy*, *262*, p.111825.
7. Green, M.A., Ho-Baillie, A. and Snaith, H.J., 2014. The emergence of perovskite solar cells. *Nature photonics*, *8*(7), pp.506-514.
8. Goldschmidt, V.M., 1926. Die gesetze der krystallochemie. *Naturwissenschaften*, *14*(21), pp.477-485.
9. Saliba, M., Matsui, T., Seo, J.Y., Domanski, K., Correa-Baena, J.P., Nazeeruddin, M.K., Zakeeruddin, S.M., Tress, W., Abate, A., Hagfeldt, A. and Grätzel, M., 2016. Cesium-containing triple cation perovskite solar cells: improved stability, reproducibility and high efficiency. *Energy & environmental science*, *9*(6), pp.1989-1997.
10. McMeekin, D.P., Sadoughi, G., Rehman, W., Eperon, G.E., Saliba, M., Hörantner, M.T., Haghighirad, A., Sakai, N., Korte, L., Rech, B. and Johnston, M.B., 2016. A mixed-cation lead mixed-halide perovskite absorber for tandem solar cells. *Science*, *351*(6269), pp.151-155.
11. Li, Z., Yang, M., Park, J.S., Wei, S.H., Berry, J.J. and Zhu, K., 2016. Stabilizing perovskite structures by tuning tolerance factor: formation of formamidinium and cesium lead iodide solid-state alloys. *Chemistry of Materials*, *28*(1), pp.284-292.
12. Eperon, G.E., Habisreutinger, S.N., Leijtens, T., Bruijnaers, B.J., van Franeker, J.J., DeQuilettes, D.W., Pathak, S., Sutton, R.J., Grancini, G., Ginger, D.S. and Janssen, R.A., 2015. The importance of moisture in hybrid lead halide perovskite thin film fabrication. *ACS nano*, *9*(9), pp.9380-9393.
13. Zhang, Y., Osetsky, Y.N. and Weber, W.J., 2021. Tunable chemical disorder in concentrated alloys: defect physics and radiation performance. *Chemical Reviews*, *122*(1), pp.789-829.
14. Hao, F., Stoumpos, C.C., Chang, R.P. and Kanatzidis, M.G., 2014. Anomalous band gap behavior in mixed Sn and Pb perovskites enables broadening of absorption spectrum in solar cells. *Journal of the American Chemical Society*, *136*(22), pp.8094-8099.
15. Ou, Q., Bao, X., Zhang, Y., Shao, H., Xing, G., Li, X., Shao, L. and Bao, Q., 2019. Band structure engineering in metal halide perovskite nanostructures for optoelectronic applications. *Nano Materials Science*, *1*(4), pp.268-287.
16. Guo, P., Hossain, M.K., Shen, X., Sun, H., Yang, W., Liu, C., Ho, C.Y., Kwok, C.K., Tsang, S.W., Luo, Y. and Ho, J.C., 2018. Room-Temperature Red–Green–Blue Whispering-Gallery Mode Lasing and White-Light Emission from Cesium Lead Halide Perovskite ($CsPbX_3$, X= Cl, Br, I) Microstructures. *Advanced Optical Materials*, *6*(3), p.1700993.
17. Kim, J., Ho-Baillie, A. and Huang, S., 2019. Review of novel passivation techniques for efficient and stable perovskite solar cells. *Solar RRL*, *3*(4), p.1800302.

18. Leijtens, T., Bush, K., Cheacharoen, R., Beal, R., Bowring, A. and McGehee, M.D., 2017. Towards enabling stable lead halide perovskite solar cells; interplay between structural, environmental, and thermal stability. *Journal of Materials Chemistry A*, *5*(23), pp.11483-11500.
19. Huang, J., Tan, S., Lund, P.D. and Zhou, H., 2017. Impact of H_2O on organic–inorganic hybrid perovskite solar cells. *Energy & Environmental Science*, *10*(11), pp.2284-2311.
20. Christians, J.A., Miranda Herrera, P.A. and Kamat, P.V., 2015. Transformation of the excited state and photovoltaic efficiency of CH3NH3PbI3 perovskite upon controlled exposure to humidified air. *Journal of the American Chemical Society*, *137*(4), pp.1530-1538.
21. Leijtens, T., Hoke, E.T., Grancini, G., Slotcavage, D.J., Eperon, G.E., Ball, J.M., De Bastiani, M., Bowring, A.R., Martino, N., Wojciechowski, K. and McGehee, M.D., 2015. Mapping electric field-induced switchable poling and structural degradation in hybrid lead halide perovskite thin films. *Advanced Energy Materials*, *5*(20), p.1500962.
22. Habisreutinger, S.N., Leijtens, T., Eperon, G.E., Stranks, S.D., Nicholas, R.J. and Snaith, H.J., 2014. Carbon nanotube/polymer composites as a highly stable hole collection layer in perovskite solar cells. *Nano letters*, *14*(10), pp.5561-5568.
23. Sheikh, A.D., Bera, A., Haque, M.A., Rakhi, R.B., Del Gobbo, S., Alshareef, H.N. and Wu, T., 2015. Atmospheric effects on the photovoltaic performance of hybrid perovskite solar cells. *Solar Energy Materials and Solar Cells*, *137*, pp.6-14.
24. Bryant, D., Aristidou, N., Pont, S., Sanchez-Molina, I., Chotchunangatchaval, T., Wheeler, S., Durrant, J.R. and Haque, S.A., 2016. Light and oxygen induced degradation limits the operational stability of methylammonium lead triiodide perovskite solar cells. *Energy & Environmental Science*, *9*(5), pp.1655-1660.
25. Ball, J.M. and Petrozza, A., 2016. Defects in perovskite-halides and their effects in solar cells. *Nature Energy*, *1*(11), pp.1-13.
26. Conings, B., Drijkoningen, J., Gauquelin, N., Babayigit, A., D'Haen, J., D'Olieslaeger, L., Ethirajan, A., Verbeeck, J., Manca, J., Mosconi, E. and Angelis, F.D., 2015. Intrinsic thermal instability of methylammonium lead trihalide perovskite. *Advanced Energy Materials*, *5*(15), p.1500477.
27. Dualeh, A., Gao, P., Seok, S.I., Nazeeruddin, M.K. and Grätzel, M., 2014. Thermal behavior of methylammonium lead-trihalide perovskite photovoltaic light harvesters. *Chemistry of Materials*, *26*(21), pp.6160-6164.
28. Cheng, Y. and Ding, L., 2021. Pushing commercialization of perovskite solar cells by improving their intrinsic stability. *Energy & Environmental Science*, *14*(6), pp.3233-3255.
29. Snaith, H.J., Abate, A., Ball, J.M., Eperon, G.E., Leijtens, T., Noel, N.K., Stranks, S.D., Wang, J.T.W., Wojciechowski, K. and Zhang, W., 2014. Anomalous hysteresis in perovskite solar cells. *The journal of physical chemistry letters*, *5*(9), pp.1511-1515.
30. Zhao, L., Kerner, R.A., Xiao, Z., Lin, Y.L., Lee, K.M., Schwartz, J. and Rand, B.P., 2016. Redox chemistry dominates the degradation and decomposition of metal halide perovskite optoelectronic devices. *ACS Energy Letters*, *1*(3), pp.595-602.

31. Kim, G.Y., Senocrate, A., Yang, T.Y., Gregori, G., Grätzel, M. and Maier, J., 2018. Large tunable photoeffect on ion conduction in halide perovskites and implications for photodecomposition. *Nature materials*, *17*(5), pp.445-449.
32. Wang, Z., Shi, Z., Li, T., Chen, Y. and Huang, W., 2017. Stability of perovskite solar cells: a prospective on the substitution of the A cation and X anion. *Angewandte Chemie International Edition*, *56*(5), pp.1190-1212.
33. Xu, T., Chen, L., Guo, Z. and Ma, T., 2016. Strategic improvement of the long-term stability of perovskite materials and perovskite solar cells. *Physical Chemistry Chemical Physics*, *18*(39), pp.27026-27050.
34. Li, L., Wei, M., Carnevali, V., Zeng, H., Zeng, M., Liu, R., Lempesis, N., Eickemeyer, F.T., Luo, L., Agosta, L. and Dankl, M., 2023. Buried Interface Engineering Enables Efficient and 1,960-hour Isos-L-2i Stable Inverted Perovskite Solar Cells. *Advanced Materials*, p.2303869.
35. Hussain, I., Tran, H.P., Jaksik, J., Moore, J., Islam, N. and Uddin, M.J., 2018. Functional materials, device architecture, and flexibility of perovskite solar cell. *Emergent Materials*, *1*, pp.133-154.
36. Habibi, M., Zabihi, F., Ahmadian-Yazdi, M.R. and Eslamian, M., 2016. Progress in emerging solution-processed thin film solar cells–Part II: Perovskite solar cells. *Renewable and Sustainable Energy Reviews*, *62*, pp.1012-1031.
37. Huang, Y., Liu, T., Liang, C., Xia, J., Li, D., Zhang, H., Amini, A., Xing, G. and Cheng, C., 2020. Towards simplifying the device structure of high-performance perovskite solar cells. *Advanced Functional Materials*, *30*(28), p.2000863.
38. Wang, S., Sakurai, T., Wen, W. and Qi, Y., 2018. Energy level alignment at interfaces in metal halide perovskite solar cells. *Advanced Materials Interfaces*, *5*(22), p.1800260.
39. Ou, Q.D., Li, C., Wang, Q.K., Li, Y.Q. and Tang, J.X., 2017. Recent advances in energetics of metal halide perovskite interfaces. *Advanced Materials Interfaces*, *4*(2), p.1600694.
40. Schulz, P., Cahen, D. and Kahn, A., 2019. Halide perovskites: is it all about the interfaces?. *Chemical reviews*, *119*(5), pp.3349-3417.
41. Hamed, M.S. and Mola, G.T., 2020. Mixed halide perovskite solar cells: progress and challenges. *Critical Reviews in Solid State and Materials Sciences*, *45*(2), pp.85-112.
42. Wang, Y., Yue, Y., Yang, X. and Han, L., 2018. Toward long-term stable and highly efficient perovskite solar cells via effective charge transporting materials. *Advanced Energy Materials*, *8*(22), p.1800249.
43. Shin, S.S., Lee, S.J. and Seok, S.I., 2019. Metal oxide charge transport layers for efficient and stable perovskite solar cells. *Advanced Functional Materials*, *29*(47), p.1900455.
44. Singh, T., Singh, J. and Miyasaka, T., 2016. Role of metal oxide electron-transport layer modification on the stability of high performing perovskite solar cells. *ChemSusChem*, *9*(18), pp.2559-2566.
45. Zhang, T., He, Q., Yu, J., Chen, A., Zhang, Z. and Pan, J., 2022. Recent progress in improving strategies of inorganic electron transport layers for perovskite solar cells. *Nano Energy*, p.107918.

46. Jia, L., Chen, M. and Yang, S., 2020. Functionalization of fullerene materials toward applications in perovskite solar cells. *Materials Chemistry Frontiers*, *4*(8), pp.2256-2282.
47. Schulz, P., Whittaker-Brooks, L.L., MacLeod, B.A., Olson, D.C., Loo, Y.L. and Kahn, A., 2015. Electronic level alignment in inverted organometal perovskite solar cells. *Advanced Materials Interfaces*, *2*(7), p.1400532.
48. Fan, Y., Wu, F., Liu, F., Han, M., Chang, K., Zhu, L., Li, Q. and Li, Z., 2022. A perylene diimide dimer-based electron transporting material with an A–D–A structure for efficient inverted perovskite solar cells. *Journal of Materials Chemistry C*, *10*(7), pp.2544-2550.
49. Liu, D., Wang, Q., Traverse, C.J., Yang, C., Young, M., Kuttipillai, P.S., Lunt, S.Y., Hamann, T.W. and Lunt, R.R., 2018. Impact of ultrathin C60 on perovskite photovoltaic devices. *ACS nano*, *12*(1), pp.876-883.
50. Li, B., Zhen, J., Wan, Y., Lei, X., Liu, Q., Liu, Y., Jia, L., Wu, X., Zeng, H., Zhang, W. and Wang, G.W., 2018. Anchoring fullerene onto perovskite film via grafting pyridine toward enhanced electron transport in high-efficiency solar cells. *ACS applied materials & interfaces*, *10*(38), pp.32471-32482.
51. Tian, C., Sun, C., Chen, J., Song, P., Hou, E., Xu, P., Liang, Y., Yang, P., Luo, J., Xie, L. and Wei, Z., 2022. Fullerene derivative with flexible alkyl chain for efficient tin-based perovskite solar cells. *Nanomaterials*, *12*(3), p.532.
52. Hu, L., Li, S., Zhang, L., Liu, Y., Zhang, C., Wu, Y., Sun, Q., Cui, Y., Zhu, F., Hao, Y. and Wu, Y., 2020. Unravelling the role of C60 derivatives as additives into active layers for achieving high-efficiency planar perovskite solar cells. *Carbon*, *167*, pp.160-168.
53. Deng, L.L., Xie, S.Y. and Gao, F., 2018. Fullerene-Based Materials for Photovoltaic Applications: Toward Efficient, Hysteresis-Free, and Stable Perovskite Solar Cells. *Advanced Electronic Materials*, *4*(10), p.1700435.
54. Jeng, J.Y., Chiang, Y.F., Lee, M.H., Peng, S.R., Guo, T.F., Chen, P. and Wen, T.C., 2013. CH3NH3PbI3 perovskite/fullerene planar-heterojunction hybrid solar cells. *Advanced materials*, *25*(27), pp.3727-3732.
55. Luo, D., Yang, W., Wang, Z., Sadhanala, A., Hu, Q., Su, R., Shivanna, R., Trindade, G.F., Watts, J.F., Xu, Z. and Liu, T., 2018. Enhanced photovoltage for inverted planar heterojunction perovskite solar cells. *Science*, *360*(6396), pp.1442-1446.
56. Wehrenfennig, C., Eperon, G.E., Johnston, M.B., Snaith, H.J. and Herz, L.M., 2014. High charge carrier mobilities and lifetimes in organolead trihalide perovskites. *Advanced materials*, *26*(10), pp.1584-1589.
57. Sun, S., Salim, T., Mathews, N., Duchamp, M., Boothroyd, C., Xing, G., Sum, T.C. and Lam, Y.M., 2014. The origin of high efficiency in low-temperature solution-processable bilayer organometal halide hybrid solar cells. *Energy & Environmental Science*, *7*(1), pp.399-407.
58. Chen, L., Li, C., Xian, Y., Fu, S., Abudulimu, A., Li, D.B., Friedl, J.D., Li, Y., Neupane, S., Tumusange, M.S. and Sun, N., 2023. Incorporating Potassium Citrate to Improve the Performance of Tin-Lead Perovskite Solar Cells. *Advanced Energy Materials*, p.2301218.

59. Warby, J., Zu, F., Zeiske, S., Gutierrez-Partida, E., Frohloff, L., Kahmann, S., Frohna, K., Mosconi, E., Radicchi, E., Lang, F. and Shah, S., 2022. Understanding performance limiting interfacial recombination in pin perovskite solar cells. *Advanced Energy Materials*, *12*(12), p.2103567.
60. Mariotti, S., Köhnen, E., Scheler, F., Sveinbjörnsson, K., Zimmermann, L., Piot, M., Yang, F., Li, B., Warby, J., Musiienko, A. and Menzel, D., 2023. Interface engineering for high-performance, triple-halide perovskite–silicon tandem solar cells. *Science*, *381*(6653), pp.63-69.
61. De Bastiani, M., Armaroli, G., Jalmood, R., Ferlauto, L., Li, X., Tao, R., Harrison, G.T., Eswaran, M.K., Azmi, R., Babics, M. and Subbiah, A.S., 2022. Mechanical reliability of fullerene/tin oxide interfaces in monolithic perovskite/silicon tandem cells. *ACS Energy Letters*, *7*(2), pp.827-833.
62. Aydin, E., Altinkaya, C., Smirnov, Y., Yaqin, M.A., Zanoni, K.P., Paliwal, A., Firdaus, Y., Allen, T.G., Anthopoulos, T.D., Bolink, H.J. and Morales-Masis, M., 2021. Sputtered transparent electrodes for optoelectronic devices: Induced damage and mitigation strategies. *Matter*, *4*(11), pp.3549-3584.
63. Ponseca Jr, C.S., Savenije, T.J., Abdellah, M., Zheng, K., Yartsev, A., Pascher, T., Harlang, T., Chabera, P., Pullerits, T., Stepanov, A. and Wolf, J.P., 2014. Organometal halide perovskite solar cell materials rationalized: ultrafast charge generation, high and microsecond-long balanced mobilities, and slow recombination. *Journal of the American Chemical Society*, *136*(14), pp.5189-5192.
64. Bi, D., Tress, W., Dar, M.I., Gao, P., Luo, J., Renevier, C., Schenk, K., Abate, A., Giordano, F., Correa Baena, J.P. and Decoppet, J.D., 2016. Efficient luminescent solar cells based on tailored mixed-cation perovskites. *Science advances*, *2*(1), p.e1501170.
65. Hu, H., Dong, B., Hu, H., Chen, F., Kong, M., Zhang, Q., Luo, T., Zhao, L., Guo, Z., Li, J. and Xu, Z., 2016. Atomic layer deposition of TiO2 for a high-efficiency hole-blocking layer in hole-conductor-free perovskite solar cells processed in ambient air. *ACS applied materials & interfaces*, *8*(28), pp.17999-18007.
66. Shahiduzzaman, M., Hossain, M.I., Otani, S., Wang, L., Umezu, S., Kaneko, T., Iwamori, S., Tomita, K., Tsang, Y.H., Akhtaruzzaman, M. and Knipp, D., 2021. Low-temperature treated anatase TiO2 nanophotonic-structured contact design for efficient triple-cation perovskite solar cells. *Chemical Engineering Journal*, *426*, p.131831.
67. Xia, G., Liu, H., Zhao, X., Dong, X., Wang, S. and Li, X., 2019. Seeding-method-processed anatase TiO2 film at low temperature for efficient planar perovskite solar cell. *Chemical Engineering Journal*, *370*, pp.1111-1118.
68. Wang, Y., Wan, J., Ding, J., Hu, J.S. and Wang, D., 2019. A rutile TiO_2 electron transport layer for the enhancement of charge collection for efficient perovskite solar cells. *Angewandte Chemie International Edition*, *58*(28), pp.9414-9418.
69. Shahiduzzaman, M., Visal, S., Kuniyoshi, M., Kaneko, T., Umezu, S., Katsumata, T., Iwamori, S., Kakihana, M., Taima, T., Isomura, M. and Tomita, K., 2018. Low-temperature-processed brookite-based TiO_2 heterophase junction enhances performance of planar perovskite solar cells. *Nano Letters*, *19*(1), pp.598-604.

70. Heo, J.H., Song, D.H. and Im, S.H., 2014. Planar $CH_3NH_3PbBr_3$ hybrid solar cells with 10.4% power conversion efficiency, fabricated by controlled crystallization in the spin-coating process. *Advanced Materials*, *26*(48), pp.8179-8183.
71. Lu, H., Zhong, J., Ji, C., Zhao, J., Li, D., Zhao, R., Jiang, Y., Fang, S., Liang, T., Li, H. and Li, C.M., 2020. Fabricating an optimal rutile TiO2 electron transport layer by delicately tuning TiCl4 precursor solution for high performance perovskite solar cells. *Nano Energy*, *68*, p.104336.
72. Wu, W.Q. and Wang, L., 2019. A 3d hybrid nanowire/microcuboid optoelectronic electrode for maximised light harvesting in perovskite solar cells. *Journal of Materials Chemistry A*, *7*(3), pp.932-939.
73. Shahiduzzaman, M., Hossain, M.I., Visal, S., Kaneko, T., Qarony, W., Umezu, S., Tomita, K., Iwamori, S., Knipp, D., Tsang, Y.H. and Akhtaruzzaman, M., 2021. Spray pyrolyzed TiO 2 embedded multi-layer front contact design for high-efficiency perovskite solar cells. *Nano-micro letters*, *13*, pp.1-17.
74. Yang, D., Yang, R., Zhang, J., Yang, Z., Liu, S.F. and Li, C., 2015. High efficiency flexible perovskite solar cells using superior low temperature TiO 2. *Energy & Environmental Science*, *8*(11), pp.3208-3214.
75. Giordano, F., Abate, A., Correa Baena, J.P., Saliba, M., Matsui, T., Im, S.H., Zakeeruddin, S.M., Nazeeruddin, M.K., Hagfeldt, A. and Graetzel, M., 2016. Enhanced electronic properties in mesoporous TiO_2 via lithium doping for high-efficiency perovskite solar cells. *Nature communications*, *7*(1), p.10379.
76. Goto, K., Kawashima, T. and Tanabe, N., 2006. Heat-resisting TCO films for PV cells. *Solar energy materials and solar cells*, *90*(18-19), pp.3251-3260.
77. Yang, W., Zhong, D., Shi, M., Qu, S. and Chen, H., 2019. Toward highly thermal stable perovskite solar cells by rational design of interfacial layer. *Iscience*, *22*, pp.534-543.
78. Jung, H.S. and Park, N.G., 2015. Perovskite solar cells: from materials to devices. *small*, *11*(1), pp.10-25.
79. Zhang, Q., Dandeneau, C.S., Zhou, X. and Cao, G., 2009. ZnO nanostructures for dye-sensitized solar cells. *Advanced materials*, *21*(41), pp.4087-4108.
80. Rajbhandari, P.P. and Dhakal, T.P., 2020. Low temperature ALD growth optimization of ZnO, TiO_2, and Al_2O_3 to be used as a buffer layer in perovskite solar cells. *Journal of Vacuum Science & Technology A*, *38*(3).
81. Liu, D. and Kelly, T.L., 2014. Perovskite solar cells with a planar heterojunction structure prepared using room-temperature solution processing techniques. *Nature photonics*, *8*(2), pp.133-138.
82. Yang, J., Siempelkamp, B.D., Mosconi, E., De Angelis, F. and Kelly, T.L., 2015. Origin of the thermal instability in $CH_3NH_3PbI_3$ thin films deposited on ZnO. *Chemistry of Materials*, *27*(12), pp.4229-4236.
83. Zhang, P., Wu, J., Zhang, T., Wang, Y., Liu, D., Chen, H., Ji, L., Liu, C., Ahmad, W., Chen, Z.D. and Li, S., 2018. Perovskite solar cells with ZnO electron-transporting materials. *Advanced Materials*, *30*(3), p.1703737.

84. Bush, K.A., Bailie, C.D., Chen, Y., Bowring, A.R., Wang, W., Ma, W., Leijtens, T., Moghadam, F. and McGehee, M.D., 2016. Thermal and environmental stability of semi-transparent perovskite solar cells for tandems enabled by a solution-processed nanoparticle buffer layer and sputtered ITO electrode. *Advanced Materials*, *28*(20), pp.3937-3943.
85. Mao, G.P., Wang, W., Shao, S., Sun, X.J., Chen, S.A., Li, M.H. and Li, H.M., 2018. Research progress in electron transport layer in perovskite solar cells. *Rare Metals*, *37*, pp.95-106.
86. Ke, W., Fang, G., Liu, Q., Xiong, L., Qin, P., Tao, H., Wang, J., Lei, H., Li, B., Wan, J. and Yang, G., 2015. Low-temperature solution-processed tin oxide as an alternative electron transporting layer for efficient perovskite solar cells. *Journal of the American Chemical Society*, *137*(21), pp.6730-6733.
87. Min, H., Lee, D.Y., Kim, J., Kim, G., Lee, K.S., Kim, J., Paik, M.J., Kim, Y.K., Kim, K.S., Kim, M.G. and Shin, T.J., 2021. Perovskite solar cells with atomically coherent interlayers on SnO2 electrodes. *Nature*, *598*(7881), pp.444-450.
88. Uddin, A. and Yi, H., 2022. Progress and challenges of SnO_2 electron transport layer for perovskite solar cells: A critical review. *Solar RRL*, *6*(6), p.2100983.
89. Zhang, C., Wei, K., Hu, J., Cai, X., Du, G., Deng, J., Luo, Z., Zhang, X., Wang, Y., Yang, L. and Zhang, J., 2023. A review on organic hole transport materials for perovskite solar cells: Structure, composition and reliability. *Materials Today*.
90. Sharma, D., Mehra, R. and Raj, B., 2022. Comparative study of hole transporting layers commonly used in high-efficiency perovskite solar cells. *Journal of Materials Science*, *57*(45), pp.21172-21191.
91. Yoo, J.J., Wieghold, S., Sponseller, M.C., Chua, M.R., Bertram, S.N., Hartono, N.T.P., Tresback, J.S., Hansen, E.C., Correa-Baena, J.P., Bulović, V. and Buonassisi, T., 2019. An interface stabilized perovskite solar cell with high stabilized efficiency and low voltage loss. *Energy & Environmental Science*, *12*(7), pp.2192-2199.
92. Jiang, Q., Zhao, Y., Zhang, X., Yang, X., Chen, Y., Chu, Z., Ye, Q., Li, X., Yin, Z. and You, J., 2019. Surface passivation of perovskite film for efficient solar cells. *Nature Photonics*, *13*(7), pp.460-466.
93. Yang, W.S., Park, B.W., Jung, E.H., Jeon, N.J., Kim, Y.C., Lee, D.U., Shin, S.S., Seo, J., Kim, E.K., Noh, J.H. and Seok, S.I., 2017. Iodide management in formamidinium-lead-halide–based perovskite layers for efficient solar cells. *Science*, *356*(6345), pp.1376-1379.
94. Ono, L.K., Raga, S.R., Remeika, M., Winchester, A.J., Gabe, A. and Qi, Y., 2015. Pinhole-free hole transport layers significantly improve the stability of $MAPbI_3$-based perovskite solar cells under operating conditions. *Journal of Materials Chemistry A*, *3*(30), pp.15451-15456.
95. Juarez-Perez, E.J., Leyden, M.R., Wang, S., Ono, L.K., Hawash, Z. and Qi, Y., 2016. Role of the dopants on the morphological and transport properties of spiro-MeOTAD hole transport layer. *Chemistry of Materials*, *28*(16), pp.5702-5709.
96. Schulz, P., Edri, E., Kirmayer, S., Hodes, G., Cahen, D. and Kahn, A., 2014. Interface energetics in organo-metal halide perovskite-based photovoltaic cells. *Energy & Environmental Science*, *7*(4), pp.1377-1381.

97. Schloemer, T.H., Christians, J.A., Luther, J.M. and Sellinger, A., 2019. Doping strategies for small molecule organic hole-transport materials: impacts on perovskite solar cell performance and stability. *Chemical Science*, *10*(7), pp.1904-1935.

98. Noh, J.H., Jeon, N.J., Choi, Y.C., Nazeeruddin, M.K., Grätzel, M. and Seok, S.I., 2013. Nanostructured TiO 2/CH 3 NH 3 PbI 3 heterojunction solar cells employing spiro-OMeTAD/Co-complex as hole-transporting material. *Journal of Materials Chemistry A*, *1*(38), pp.11842-11847.

99. Kasparavicius, E., Magomedov, A., Malinauskas, T. and Getautis, V., 2018. Long-term stability of the oxidized hole-transporting materials used in perovskite solar cells. *Chemistry–A European Journal*, *24*(39), pp.9910-9918.

100. Yang, J., Siempelkamp, B.D., Liu, D. and Kelly, T.L., 2015. Investigation of CH3NH3PbI3 degradation rates and mechanisms in controlled humidity environments using in situ techniques. *ACS nano*, *9*(2), pp.1955-1963.

101. Li, Z., Xiao, C., Yang, Y., Harvey, S.P., Kim, D.H., Christians, J.A., Yang, M., Schulz, P., Nanayakkara, S.U., Jiang, C.S. and Luther, J.M., 2017. Extrinsic ion migration in perovskite solar cells. *Energy & Environmental Science*, *10*(5), pp.1234-1242.

102. Ko, Y., Kim, Y., Lee, C., Kim, Y. and Jun, Y., 2018. Investigation of hole-transporting poly (triarylamine) on aggregation and charge transport for hysteresisless scalable planar perovskite solar cells. *ACS applied materials & interfaces*, *10*(14), pp.11633-11641.

103. Endres, J., Kulbak, M., Zhao, L., Rand, B.P., Cahen, D., Hodes, G. and Kahn, A., 2017. Electronic structure of the CsPbBr3/polytriarylamine (PTAA) system. *Journal of Applied Physics*, *121*(3).

104. Rombach, F.M., Haque, S.A. and Macdonald, T.J., 2021. Lessons learned from spiro-OMeTAD and PTAA in perovskite solar cells. *Energy & Environmental Science*, *14*(10), pp.5161-5190.

105. Luo, J., Xia, J., Yang, H., Chen, L., Wan, Z., Han, F., Malik, H.A., Zhu, X. and Jia, C., 2018. Toward high-efficiency, hysteresis-less, stable perovskite solar cells: unusual doping of a hole-transporting material using a fluorine-containing hydrophobic Lewis acid. *Energy & Environmental Science*, *11*(8), pp.2035-2045.

106. Wang S, Huang Z, Wang X, Li Y, Günther M, Valenzuela S, Parikh P, Cabreros A, Xiong W, Meng YS. Unveiling the role of tBP–LiTFSI complexes in perovskite solar cells. Journal of the American Chemical Society. 2018 Nov 6;140(48):16720-30.

107. Jing, X., Zhang, Z., Chen, T. and Luo, J., 2023. Review of Inorganic Hole Transport Materials for Perovskite Solar Cells. *Energy Technology*, *11*(2), p.2201005.

108. Ma, Y., Zhang, Y., Zhang, H., Lv, H., Hu, R., Liu, W., Wang, S., Jiang, M., Chu, L., Zhang, J. and Li, X.A., 2021. Effective carrier transport tuning of CuOx quantum dots hole interfacial layer for high-performance inverted perovskite solar cell. *Applied Surface Science*, *547*, p.149117.

109. Park, H., Jeong, S., Kim, E., Shin, S. and Shin, H., 2022. Hole-Transporting Vanadium-Containing Oxide (V2O5–x) Interlayers Enhance Stability of α-$FAPbI_3$-Based Perovskite Solar Cells (~ 23%). *ACS Applied Materials & Interfaces*, *14*(37), pp.42007-42017.

110. Li, M., Li, H., Zhuang, Q., He, D., Liu, B., Chen, C., Zhang, B., Pauporté, T., Zang, Z. and Chen, J., 2022. Stabilizing Perovskite Precursor by Synergy of Functional Groups for NiOx-Based Inverted Solar Cells with 23.5% Efficiency. *Angewandte Chemie International Edition*, *61*(35), p.e202206914.

111. Wang, K.C., Jeng, J.Y., Shen, P.S., Chang, Y.C., Diau, E.W.G., Tsai, C.H., Chao, T.Y., Hsu, H.C., Lin, P.Y., Chen, P. and Guo, T.F., 2014. P-type mesoscopic nickel oxide/organometallic perovskite heterojunction solar cells. *Scientific reports*, *4*(1), p.4756.

112. Cai, X., Hu, T., Hou, H., Zhu, P., Liu, R., Peng, J., Luo, W. and Yu, H., 2023. A review for nickel oxide hole transport layer and its application in halide perovskite solar cells. *Materials Today Sustainability*, p.100438.

113. Kim, J.H., Liang, P.W., Williams, S.T., Cho, N., Chueh, C.C., Glaz, M.S., Ginger, D.S. and Jen, A.K.Y., 2015. High-performance and environmentally stable planar heterojunction perovskite solar cells based on a solution-processed copper-doped nickel oxide hole-transporting layer. *Advanced materials*, *27*(4), pp.695-701.

114. Chen, X., Zhao, L. and Niu, Q., 2012. Electrical and optical properties of p-type Li, Cu-codoped NiO thin films. *Journal of electronic materials*, *41*, pp.3382-3386.

115. Xu, L., Chen, X., Jin, J., Liu, W., Dong, B., Bai, X., Song, H. and Reiss, P., 2019. Inverted perovskite solar cells employing doped NiO hole transport layers: A review. *Nano Energy*, *63*, p.103860.

116. Wang, Q., Chueh, C.C., Zhao, T., Cheng, J., Eslamian, M., Choy, W.C. and Jen, A.K.Y., 2017. Effects of self-assembled monolayer modification of nickel oxide nanoparticles layer on the performance and application of inverted perovskite solar cells. *ChemSusChem*, *10*(19), pp.3794-3803.

117. Boyd, C.C., Shallcross, R.C., Moot, T., Kerner, R., Bertoluzzi, L., Onno, A., Kavadiya, S., Chosy, C., Wolf, E.J., Werner, J. and Raiford, J.A., 2020. Overcoming redox reactions at perovskite-nickel oxide interfaces to boost voltages in perovskite solar cells. *Joule*, *4*(8), pp.1759-1775.

118. Xing, Z., Xiao, J., Hu, T., Meng, X., Li, D., Hu, X. and Chen, Y., 2020. Atomic Layer Deposition of Metal Oxides in Perovskite Solar Cells: Present and Future. *Small Methods*, *4*(12), p.2000588.

119. Zardetto, V., Williams, B.L., Perrotta, A., Di Giacomo, F., Verheijen, M.A., Andriessen, R., Kessels, W.M.M. and Creatore, M., 2017. Atomic layer deposition for perovskite solar cells: research status, opportunities and challenges. *Sustainable Energy & Fuels*, *1*(1), pp.30-55.

120. Ritala, M. and Leskelä, M., 2002. Atomic layer deposition. In *Handbook of Thin Films* (pp. 103-159). Academic Press.

121. Fournier, O. 2021, Synth`ese par ALD et caract´erisation de couches extractrices d'electrons pour application dans les cellules solaires `a base de perovskite, Doctoral thesis.

122. George, S.M., 2010. Atomic layer deposition: an overview. *Chemical reviews*, *110*(1), pp.111-131.

123. Potts, S.E., Profijt, H.B., Roelofs, R. and Kessels, W.M., 2013. Room-Temperature ALD of Metal Oxide Thin Films by Energy-Enhanced ALD. *Chemical Vapor Deposition*, *19*(4-6), pp.125-133.

124. Zhao, W. and Duan, Y., 2021. Advanced Applications of Atomic Layer Deposition in Perovskite-Based Solar Cells. *Advanced Photonics Research*, *2*(7), p.2100011.

125. Seo, S., Jeong, S., Bae, C., Park, N.G. and Shin, H., 2018. Perovskite solar cells with inorganic electron-and hole-transport layers exhibiting long-term (≈ 500 h) stability at 85° C under continuous 1 sun illumination in ambient air. *Advanced Materials*, *30*(29), p.1801010.

126. Ramos, F.J., Maindron, T., Béchu, S., Rebai, A., Frégnaux, M., Bouttemy, M., Rousset, J., Schulz, P. and Schneider, N., 2018. Versatile perovskite solar cell encapsulation by low-temperature ALD-Al_2O_3 with long-term stability improvement. *Sustainable Energy & Fuels*, *2*(11), pp.2468-2479.

127. Singh, R., Ghosh, S., Subbiah, A.S., Mahuli, N. and Sarkar, S.K., 2020. ALD Al_2O_3 on hybrid perovskite solar cells: Unveiling the growth mechanism and long-term stability. *Solar Energy Materials and Solar Cells*, *205*, p.110289.

128. Koushik, D., Verhees, W.J., Kuang, Y., Veenstra, S., Zhang, D., Verheijen, M.A., Creatore, M. and Schropp, R.E., 2017. High-efficiency humidity-stable planar perovskite solar cells based on atomic layer architecture. *Energy & Environmental Science*, *10*(1), pp.91-100.

129. Weiß, A., Popov, G., Atosuo, E., Vihervaara, A., Jalkanen, P., Vehkamaki, M., Leskela, M., Ritala, M. and Kemell, M., 2022. Atomic layer deposition of CsI and $CsPbI_3$. *Chemistry of Materials*, *34*(13), pp.6087-6097.

130. Liu, H., Liu, Y.F., Xiong, P.P., Chen, P., Li, H.Y., Hou, J.W., Kang, B.N. and Duan, Y., 2017. Aluminum-doped zinc oxide transparent electrode prepared by atomic layer deposition for organic light emitting devices. *IEEE Transactions on Nanotechnology*, *16*(4), pp.634-638.

131. Lee, Y., Lee, S., Seo, G., Paek, S., Cho, K.T., Huckaba, A.J., Calizzi, M., Choi, D.W., Park, J.S., Lee, D. and Lee, H.J., 2018. Efficient planar perovskite solar cells using passivated tin oxide as an electron transport layer. *Advanced Science*, *5*(6), p.1800130.

132. Ren, N., Zhu, C., Li, R., Mazumdar, S., Sun, C., Chen, B., Xu, Q., Wang, P., Shi, B., Huang, Q. and Xu, S., 2022. 50° C low-temperature ALD SnO2 driven by H_2O_2 for efficient perovskite and perovskite/silicon tandem solar cells. *Applied Physics Letters*, *121*(3).

133. Al-Ashouri, A., Köhnen, E., Li, B., Magomedov, A., Hempel, H., Caprioglio, P., Márquez, J.A., Morales Vilches, A.B., Kasparavicius, E., Smith, J.A. and Phung, N., 2020. Monolithic perovskite/silicon tandem solar cell with> 29% efficiency by enhanced hole extraction. *Science*, *370*(6522), pp.1300-1309.

134. Seo, S., Park, I.J., Kim, M., Lee, S., Bae, C., Jung, H.S., Park, N.G., Kim, J.Y. and Shin, H., 2016. An ultra-thin, un-doped NiO hole transporting layer of highly efficient (16.4%) organic–inorganic hybrid perovskite solar cells. *Nanoscale*, *8*(22), pp.11403-11412.

135. Seo, S., Jeong, S., Bae, C., Park, N.G. and Shin, H., 2018. Perovskite solar cells with inorganic electron-and hole-transport layers exhibiting long-term (≈ 500 h) stability at 85° C under continuous 1 sun illumination in ambient air. *Advanced Materials*, *30*(29), p.1801010.

136. Zhu, X., Lau, C.F.J., Mo, K., Cheng, S., Xu, Y., Li, R., Wang, C., Zheng, Q., Liu, Y., Wang, T. and Lin, Q., 2022. Inverted planar heterojunction perovskite solar cells with high ultraviolet stability. *Nano Energy*, *103*, p.107849.

137. Bracesco, A.E., Burgess, C.H., Todinova, A., Zardetto, V., Koushik, D., Kessels, W.M.E., Dogan, I., Weijtens, C.H., Veenstra, S., Andriessen, R. and Creatore, M., 2020. The chemistry and energetics of the interface between metal halide perovskite and atomic layer deposited metal oxides. *Journal of Vacuum Science & Technology A*, *38*(6).

138. Yang, Y., Zhang, Y., Bai, L., Malouangou, D.M., Matondo, J.T., Pan, J., Dai, S., Cai, M., Liu, X. and Guli, M., 2022. Research progress of atomic layer deposition technology to improve the long-term stability of perovskite solar cells. *Journal of Materials Chemistry C*, *10*(3), pp.819-839.

139. Raiford, J.A., Oyakhire, S.T. and Bent, S.F., 2020. Applications of atomic layer deposition and chemical vapor deposition for perovskite solar cells. *Energy & Environmental Science*, *13*(7), pp.1997-2023.

140. Raiford, J.A., Chosy, C., Reeves, B.A. and Bent, S.F., 2021. Tailoring the Surface of Metal Halide Perovskites to Enable the Atomic Layer Deposition of Metal Oxide Contacts. *ACS Applied Energy Materials*, *4*(9), pp.9871-9880.

141. Kim, I.S. and Martinson, A.B., 2015. Stabilizing hybrid perovskites against moisture and temperature via non-hydrolytic atomic layer deposited overlayers. *Journal of Materials Chemistry A*, *3*(40), pp.20092-20096.

142. Hultqvist, A., Aitola, K., Sveinbjornsson, K., Saki, Z., Larsson, F., Torndahl, T., Johansson, E., Boschloo, G. and Edoff, M., 2017. Atomic layer deposition of electron selective SnOx and ZnO films on mixed halide perovskite: compatibility and performance. *ACS applied materials & interfaces*, *9*(35), pp.29707-29716.

143. Hultqvist, A., Jacobsson, T.J., Svanström, S., Edoff, M., Cappel, U.B., Rensmo, H., Johansson, E.M., Boschloo, G. and Törndahl, T., 2021. SnOx Atomic Layer Deposition on Bare Perovskite—An Investigation of Initial Growth Dynamics, Interface Chemistry, and Solar Cell Performance. *ACS applied energy materials*, *4*(1), pp.510-522.

144. Bracesco, A.E., Burgess, C.H., Todinova, A., Zardetto, V., Koushik, D., Kessels, W.M.E., Dogan, I., Weijtens, C.H., Veenstra, S., Andriessen, R. and Creatore, M., 2020. The chemistry and energetics of the interface between metal halide perovskite and atomic layer deposited metal oxides. *Journal of Vacuum Science & Technology A*, *38*(6).

145. Bracesco, A.E., Jansen, J.W.P., Xue, H., Zardetto, V., Brocks, G., Kessels, W.M., Tao, S. and Creatore, M., 2023. In Situ IR Spectroscopy Studies of Atomic Layer-Deposited SnO_2 on Formamidinium-Based Lead Halide Perovskite. *ACS Applied Materials & Interfaces*, *15*(31), pp.38018-38028.

146. Hüfner, S., 2013. *Photoelectron spectroscopy: principles and applications*. Springer Science & Business Media.

147. Greczynski, G. and Hultman, L., 2020. Compromising science by ignorant instrument calibration—need to revisit half a century of published XPS data. *Angewandte Chemie*, *132*(13), pp.5034-5038.

148. Greczynski, G. and Hultman, L., 2020. X-ray photoelectron spectroscopy: towards reliable binding energy referencing. *Progress in Materials Science*, *107*, p.100591.

149. Woicik, J. ed., 2015. *Hard X-ray Photoelectron Spectroscopy (HAXPES)* (Vol. 59). Springer.

150. Regoutz, A., Mascheck, M., Wiell, T., Eriksson, S.K., Liljenberg, C., Tetzner, K., Williamson, B.A., Scanlon, D.O. and Palmgren, P., 2018. A novel laboratory-based hard X-ray photoelectron spectroscopy system. *Review of Scientific Instruments*, *89*(7).

151. Dindault, C., 2019. *Development of coevaporated hybrid perovskite thin films for solar cells applications* (Doctoral dissertation, Université Paris-Saclay (ComUE)).

152. Sarma, D.D., Santra, P.K., Mukherjee, S. and Nag, A., 2013. X-ray photoelectron spectroscopy: a unique tool to determine the internal heterostructure of nanoparticles. *Chemistry of Materials*, *25*(8), pp.1222-1232.

153. Tanuma, S., Powell, C.J. and Penn, D.R., 2011. Calculations of electron inelastic mean free paths. IX. Data for 41 elemental solids over the 50 eV to 30 keV range. *Surface and interface analysis*, *43*(3), pp.689-713.

154. Borgatti, F., Offi, F., Torelli, P., Monaco, G. and Panaccione, G., 2013. Interfacial and bulk electronic properties of complex oxides and buried interfaces probed by HAXPES. *Journal of Electron Spectroscopy and Related Phenomena*, *190*, pp.228-234.

155. Béchu, S., Ralaiarisoa, M., Etcheberry, A. and Schulz, P., 2020. Photoemission spectroscopy characterization of halide perovskites. *Advanced Energy Materials*, *10*(26), p.1904007.

156. Fadley, C.S., 2010. X-ray photoelectron spectroscopy: Progress and perspectives. *Journal of Electron Spectroscopy and Related Phenomena*, *178*, pp.2-32.

Chapter 2
Experimental Methodology, Material Properties and Characterizations

Preface: *This chapter contains the information on device architectures, materials and deposition methods used in this Ph.D. work. In addition, this chapter also introduces all the characterization techniques and key parameters employed.*

Contents

2.1. Device Architecture

This section provides a brief overview of all the device architectures used in this study. In Chapter 3, a p-i-n architecture is employed to investigate the interface between the $FA_{0.7}Cs_{0.3}Pb(I_{0.9}Br_{0.1})_3$ MHP and ALD-SnO_2 (see Figure 2.1 (a)). In addition, a PCBM organic buffer layer was used between MHP and ALD-SnO_2 for a comparative study, as shown in figure 2.1 (b). Chapter 4 focuses on the interface study between MHP and ALD-NiO_X in n-i-p architecture devices, as shown in Figure 2.1 (c). Furthermore, for comparison, buffer layers were incorporated between MHP and ALD-NiO_X including PTAA (in Chapter 4) and (2-(3,6-Dimethoxy-9H-carbazol-9-yl)ethyl) phosphonic acid MeO-2PACz (in chapter 5) as shown in figure 2.1 (d). In the following sections, we describe all the materials used, and the key deposition process and parameters.

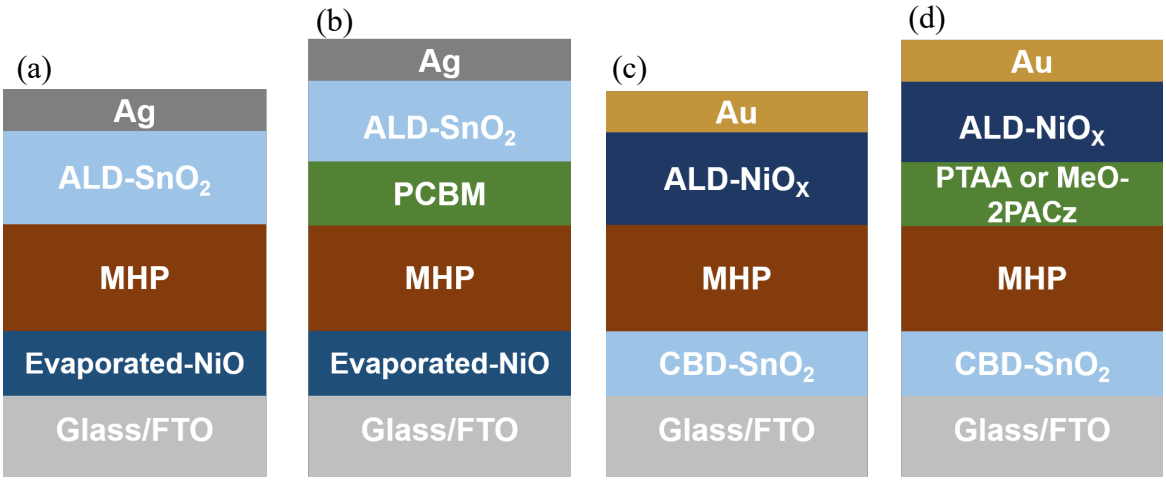

Figure 2.1. Schematic of different perovskite solar cell architecture used in this thesis a) p-i-n architecture with FTO/Evaporated-NiO/MHP/ALD-SnO_2/Ag used in chapter 3 b) p-i-n architecture with FTO/Evaporated-NiO/MHP/ALD-SnO_2/PCBM/Ag used in chapter 3 c) n-i-p architecture with FTO/CBD-SnO_2/MHP/ALD-NiO_X/Au used in chapter 4 d) n-i-p architecture with FTO/CBD-SnO_2/MHP/ PTAA or MeO-2PACz/ ALD-NiO_X Au used in chapter4 and chapter 5. MHP: $FA_{0.7}Cs_{0.3}Pb(I_{0.9}Br_{0.1})_3$

2.2. Materials and Methods

2.2.1. Metal Halide Perovskite

In this section, we describe the deposition procedure and thermal stability of double-cation mixed-halide perovskite $FA_{0.7}Cs_{0.3}Pb(I_{0.9}Br_{0.1})_3$ used in this work. For MHP deposition, formamidinium iodide (FAI, >99.99%) was procured from Greatcell Solar Materials, whereas lead bromide ($PbBr_2$, ultra-dry 99.999%), lead iodide (PbI_2, ultra-dry 99.999%), cesium iodide (CsI, 99.999%), N, N-dimethylformamide (DMF, anhydrous 99.8%), dimethyl sulfoxide (DMSO, ≥99.7%), and ethyl acetate (anhydrous, 99.8%) were purchased from Sigma-Aldrich. The devices are fabricated on a fluorine-doped tin oxide (FTO) coated glass, which was procured from Solems.

The MHP thin films are prepared by the spin coating technique inside Jacomex glovebox maintaining an inert atmosphere. Typically, the MHP is deposited onto a FTO-coated glass/ charge transport layer (CTL) stack measuring 2*2 cm^2, with multiple samples prepared in a single batch, usually ranging from 16 to 24. A 1.2M solution of double-cation mix-halide perovskite, $FA_{0.7}Cs_{0.3}Pb(I_{0.9}Br_{0.1})_3$ is prepared by dissolving PbI_2, $PbBr_2$, FAI, and CsI in DMF/DMSO(4:1) corresponding to the stoichiometric ratio mentioned here. To fabricate the films, 40 µL of perovskite precursor solution is spun at 1000 rpm for 10 seconds and 6000 rpm for 30 seconds, and 250 µL of ethyl acetate is dripped in a continuous stream within 15 seconds remaining in the second spin cycle, followed by film annealing at 100 °C for 30 min on Präziterm open hot plate inside the glovebox (Figure 2.2). Note that these process parameters are developed in IPVF.

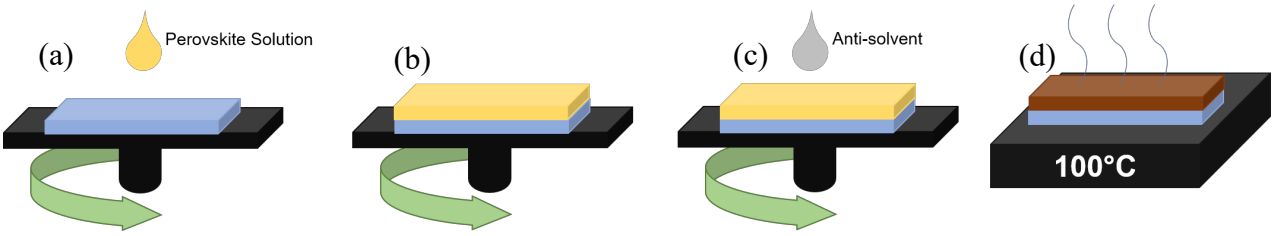

Figure 2.2. Schematic $FA_{0.7}Cs_{0.3}Pb(I_{0.9}Br_{0.1})_3$ MHP absorber deposition. a) MHP precursor solution is dynamically dropped onto the substrate. b) Thin film formation c) 15 seconds before the end of the spin coating procedure, an anti-solvent is dispensed on the rotating substrate to supersaturate the liquid thin film and initialize perovskite crystallization. d) A final thermal annealing step at 100°C for 30 minutes completes the perovskite crystallization process and evaporates residual solvents.

2.2.2. Electron Transport Layers (ETLs)

In this section, we elaborate on the deposition technique and the parameters of the ETLs used, including SnO_2 and PCBM.

- **Chemical bath deposition of SnO_2 for n-i-p PSCs**

The Chemical bath deposition (CBD) of SnO_2 is utilized as the ETL in n-i-p architecture PSCs in the Chapter 4 and 5. CBD is a low-temperature method (60-75°C) for depositing thin films by immersing substrates in a precursor solution. It enables large-area deposition, yielding dense and uniform films with good reproducibility. It has proven to be highly effective in preparing high-efficiency PSCs using SnO_2.[1] CBD typically involves two steps: nucleation and particle growth, where a solid phase forms from the solution.

The chemicals used for CBD which are hydrochloric acid (HCl) with a concentration of 36%, tin chloride dihydrate ($SnCl_2.2H_2O$, purity ≥99.99% trace metals basis), urea (ACS reagent, 99.0-100.5%), thioglycolic acid ($HSCH_2COOH$, 98%), potassium chloride (KCl, purity≥99.0%) were procured from Sigma Aldrich. To begin the CBD process for SnO_2, the bath solution is prepared two days prior to the deposition and stored in the refrigerator at approximately 5°C. The CBD solution consists of 400 ml of deionized (DI) water, 5 ml of 36% conc. HCl, 5 g of urea, 1.083 g $SnCl_2.2H_2O$ and 100 µL of thiogycolic acid. For the deposition of SnO_2, the CBD solution is further diluted with DI water in a volumetric ratio of 1:5. The 5*10 cm^2 FTO substrates are then immersed in the bath for 1 hour at a temperature of 70°C. After the hour elapses, the substrates are rinsed with water and subsequently immersed once again in a freshly prepared diluted bath solution for an additional hour. This double dipping ensures full coverage of the substrates. In the next step, the substrates undergo annealing at a temperature of 180°C for a duration of 1 hour using a ROBAX open hotplate in an ambient atmosphere. This annealing process helps enhance the film's properties. The CBD-SnO_2 are further treated with a 1 mM KCl solution, prepared by dilution using DI water, through the spin coating method. This treatment aims to improve the interface between the SnO_2 film and the MHP layer. Subsequently, the substrates undergo another heat treatment at 180°C for 1 hour.

- **Atomic layer deposition of SnO_2 for p-i-n PSCs**

The ALD-SnO_2 is incorporated on MHP film in p-i-n architecture for interface investigation which is discussed in Chapter 3. The SnO_2 layer is deposited by thermal ALD in a Beneq TFS-200 reactor using TDMASn (Tetrakis(dimethylamido)tin(IV)) and H_2O_2 precursors. All chemicals are used as received. TDAMSn is heated in a hot solid source system Beneq HS300 at T_{TDMASn} = 60°C. The deposition temperature is set to 100°C at a pressure of 1-3mbar. The samples are kept in the ALD chamber for 15 minutes before starting the deposition process to stabilize the chamber temperature. The ALD SnO_2 deposition is done using the following sequence TDMASn (Pulse)/N_2 (purge)/H_2O_2 (Pulse)/ N_2 (purge) with the corresponding pulse and times of 0.5/3/0.3/3s and with a growth per cycle (GPC) of 1.85 Å/cycle.

- **PCBM Organic Electron Transport Layer for p-i-n PSCs**

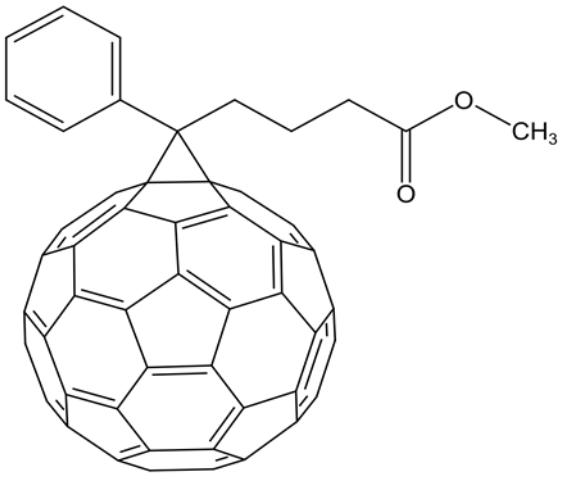

Figure 2.3. Chemical structure of phenyl-C61-butyric acid methylester (PCBM).

The Phenyl-C61-butyric acid methyl ester (PCBM) powder (purity>99.9%) and anhydrous chlorobenzene solvent (purity>99.8%) were procured from Sigma Aldrich. The PCBM is deposited using spin coating technique in the Jacomex glovebox. To deposit the PCBM layer, 20 mg of PCBM is dissolved in 1 mL of anhydrous chlorobenzene. The solution is stirred for 3-4 hours. Next, 40 µL of the PCBM solution is spin-coated onto the perovskite film at 2000 rpm for 40 seconds. Finally, the samples are annealed at 60 °C for 10 minutes on a Präziterm open hot plate inside the glovebox. This recipe was used for the HAXPES interface study described in Chapter 3. However, we found pinholes with this recipe and modified it to obtain a smooth film, which demonstrates the improved device performance described in Chapter 3. In the modified recipe, 30 min before PCBM deposition, the solution was heated to 60 °C and maintained at this temperature during the deposition process.

2.2.3. Hole Transport Layers (HTLs)

- **Evaporated NiO for p-i-n PSCs**

NiO is deposited on the clean FTO substrate by thermal evaporation of Ni and subsequent annealing in ambient atmosphere. The 20nm thick Ni film is deposited at a base pressure of 7×10^{-6} mbar and deposition rate of $1\ \dot{A}\ s^{-1}$, followed by a 10 min UV-ozone treatment. The samples are then moved to a nabertherm oven and annealed at 300 °C for 3 hours to oxidize nickel thin film in an ambient atmosphere. This deposition technique is used in the p-i-n architecture in the chapter 3.

- **Atomic layer deposition of NiO_X for n-i-p PSCs**

The ALD-NiO_X is incorporated on MHP film in n-i-p architecture for interface investigation which is discussed in Chapter 4. The NiO_x layer is deposited by thermal ALD in a Beneq TFS-200 reactor using Bis(N,N'-di-t-butylacetamidinato)nickel(II)) (Ni $(amd)_2$) and H_2O precursors. The deposition temperature is set at 100°C and pressure at 1mbar. The samples are kept in the ALD chamber for 30 minutes before starting the deposition process to stabilize the chamber temperature. The ALD NiO_x deposition is done using the following sequence Ni $(amd)_2$ (Pulse)/N_2 (purge)/H_2O (Pulse)/ N_2 (purge) with the corresponding pulse and purge time 0.3/5/0.8/5s.

- **PTAA Organic Hole Transport Layer for n-i-p PSCs**

The chemical used including bis(trifluoromethane)sulfonimide lithium salt (Li-TFSI, 99.95%), and 4-tert-butylpyridine (t- BP, 98%), acetonitrile (anhydrous, 99.8%), toluene (anhydrous, 99.8%) and poly(triaryl amine) (PTAA) are procured from Sigma Aldrich. In order to deposit the PTAA layer, a solution was prepared by dissolving 10 mg of PTAA, in 1 ml of toluene. To enhance the properties of the PTAA layer, 2.3 µL of a LiTFSI stock solution (110 mg/mL in acetonitrile) and 2.0 µL of 4-tert-butylpyridine were added to the PTAA solution. The deposition process involved spin-coating the PTAA solution onto the desired substrate at a speed of 4000 rpm for 30 seconds in the Jacomex globebox. This controlled deposition method ensured the formation of a uniform PTAA layer with desirable properties for subsequent device fabrication or characterization.

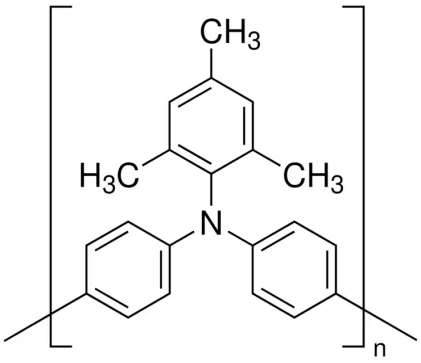

Figure 2.4. Chemical structure of poly[bis(4- phenyl)(2,4,6-trimethylphenyl)amine] (PTAA).

2.2.4. Phosphonic acid based Self-assembled MeO-2PACz Molecule

In our study, (2-(3,6-Dimethoxy-9H-carbazol-9-yl) ethyl) phosphonic acid (MeO-2PACz) is used chapter 3 as HTL for fabrication of complete PSCs. Furthermore, we have explored the potential of utilizing MeO-2PACz as promising top interlayers between MHP layers and ALD-NiO_X films in N-I-P configuration in the chapter 5. The MeO-2PACz molecules were purchased from TCI chemical.

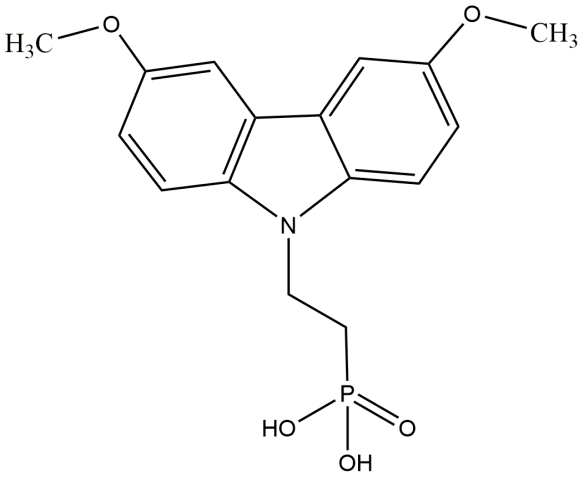

Figure 2.5. Chemical structure of MeO-2PACz molecule.

To prepare the MeO-2PACz layer for deposition, a solution with a concentration of 2 mmol/l was prepared using the appropriate solvent (as indicated below). The solution was then ultrasonicated at 35 °C for 15 min to ensure complete dissolution. Anhydrous ethanol served as the solvent when depositing this layer on FTO, whereas anhydrous isopropyl alcohol (IPA) was utilized for MHP. The choice of IPA as the solvent for MHP deposition is necessary because of compatibility issues with ethanol. The deposition process involves static mode spin coating of 100µl solutions onto MHP film at 1500 rpm for 35 seconds, with an acceleration rate of 500 rpm/sec in the glovebox. After the spin coating, the samples are heated at 100 °C for 10 minutes to evaporate the solvent.

2.2.5. Metal Electrode

The metal electrodes such as Ag, Au are used as the top contact for p-i-n and n-i-p architectures respectively for PSCs fabrication. The deposition of these metal contacts is achieved through thermal evaporation conducted under ultra-high vacuum conditions of $6*10^{-7}$ mbar. The deposition process involves initially depositing a 10 nm thick layer of the electrode material at a rate of 0.01 nm/s, followed by the subsequent deposition of the remaining 90 nm at a rate of 0.1 nm/s.

2.3. Characterization Techniques

2.3.1. X-ray Diffraction (XRD)

X-ray diffraction (XRD) is a widely employed technique in the field of materials science and crystallography, primarily utilized to investigate the atomic arrangement within crystalline materials. The underlying principle of XRD is based on the phenomenon of constructive interference, which occurs when a scattered X-ray beam, after impinging upon a periodic material, combines coherently and is subsequently captured by a detector.[2]

The X-ray beam utilized in this technique is composed of collimated monochromatic X-rays emitted from a cathode tube. During the XRD measurement, the angle θ, formed between the incident X-rays and the surface of the material, is systematically varied over a predetermined range of values. This variation in angle enables the generation of a diffractogram, which plots the recorded photon counts against the 2θ angle. The occurrence of constructive interference is governed by Bragg's law, a fundamental principle in XRD analysis:

$$n\lambda = 2dsin(\theta) \qquad \text{Equation 2.1.}$$

In this equation, n represents an integer, λ denotes the wavelength of the incident X-ray photon, and d represents the interplanar spacing within the periodic material. When the conditions outlined by Bragg's law are satisfied, constructive interference between the incident X-ray beam and the lattice planes occurs. By analyzing the diffractogram obtained from XRD experiments, a wealth of valuable information can be extracted. This includes details about the crystal structure of the material under investigation, providing insights into the arrangement of atoms within the crystal lattice. Additionally, XRD can reveal information about the material's orientation, grain size, phase, etc.[3]

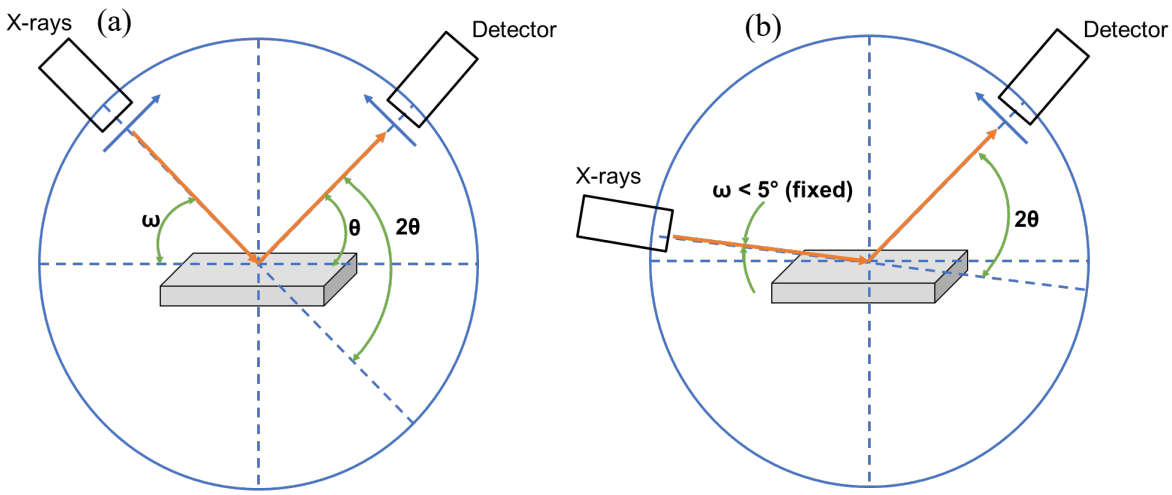

Figure 2.6. Schematics of a) bragg X-ray diffraction (XRD), b) grazing incidence X-ray diffraction (GiXRD).

We utilized the panalytical system with the highscore software package for XRD characterizations. Bragg-benton configuration was used for studying the crystal structure and phases of MHP film. Adiitionaly, we employed the grazing incidence mode to study the structural properties of the ultra-thin ALD-oxide film (see Figure 2.3). Grazing incidence XRD (GIXRD) is a surface-sensitive technique that uses a small incident angle to enhance the diffraction signal of ultra-thin films.[4]

2.3.2. Scanning Electron Microscopy (SEM)

Scanning Electron Microscopy (SEM) is an incredibly versatile and frequently utilized advanced characterization technique that facilitates an in-depth exploration of the morphological attributes and compositional nuances of specimens by procuring high-resolution, magnified imagery. In essence, this methodological approach offers a window into the microscopic world, yielding detailed visual data that contribute significantly to the scientific understanding of the studied samples. [5]

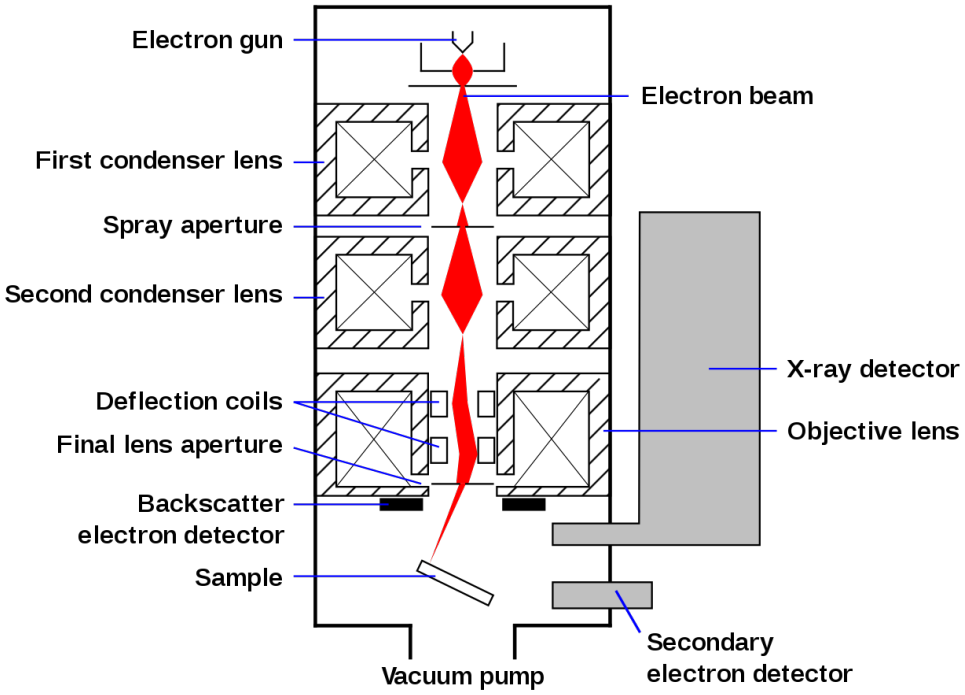

Figure 2.7. Working principle of scanning electron microscope (SEM).[6]

SEM functions by deploying a low-energy electron beam, which originates from an electron gun and is meticulously guided toward the target sample (see Figure 2.4). In its trajectory, the electron beam is refined by passing through an intricate array of lenses and apertures under vacuum conditions, resulting in a sharp focus on the sample's atomic surface. Irradiation of the sample triggers numerous atomic interactions, giving rise to distinct signals in the form of secondary, backscattered, and diffracted backscattered electrons. Each category of these electrons contributes uniquely to our understanding of the sample. Secondary electrons, due to their sensitivity to the sample's topography and texture, offer invaluable insights into its morphological properties. Conversely, backscattered electrons, attuned to atomic number variations, illuminate the compositional diversity of the sample, allowing us to identify its compositional heterogeneities an essential aspect for investigating intricate materials. These signals are collected by a detector, and a high-resolution image is produced. This study used a Zeiss Merlin VP Compact Field Emission Gun (FEG) Scanning Electron Microscope for obtaining the SEM images.

2.3.3. Ultraviolet-Visible Spectroscopy (UV-Vis)

Ultraviolet-Visible (UV-Vis) spectroscopy is a powerful analytical technique used to quantify the absorption, transmission, and reflection properties of a substance based on the variation of these parameters with wavelength, specifically within the range of 200-1100 nm.[7] This technique operates on the principle of light attenuation as it traverses a material that absorbs electromagnetic radiation. When light impinges upon a sample, it can be absorbed, reflected, or transmitted. The detector within the spectrophotometer captures the intensity of light that has been reflected or transmitted from the substance. It then compares this captured intensity to that of the incident light. The output of the spectrophotometer is a value representative of this intensity ratio, expressed across different wavelengths. Thus, UV-Vis spectroscopy provides a detailed understanding of a material's interaction with light of various wavelengths, underpinning its application in numerous fields. In this work, we employed the Agilent Cary 5000 spectrophotometer to measure the absorbance in the range of 350 m -800 nm.

2.3.4. X-ray Photoelectron Spectroscopy (XPS)

In the previous chapter, we extensively discussed the fundamental principle of X-ray Photoelectron Spectroscopy (XPS). In this section, we will now focus on the experimental setup employed for XPS analysis in our research.

For the characterization of the samples, XPS measurements were carried out using a Thermofisher ScientificTM Nexsa spectrometer, which had a spot size of 400 μm. During the XPS analysis, specific acquisition parameters were set for both survey spectra and high-energy resolution spectral windows. For the survey spectra, the Constant Analyzer Energy (CAE) was set at 100 eV, with a step size of 1 eV and a dwell time of 100 ms. On the other hand, for the high-energy resolution spectral windows, the CAE was set at 20 eV, with a smaller step size of 0.1 eV and the same dwell time of 100 ms. These parameters ensured accurate and precise measurements during the XPS analysis of the experimented samples in our research work.

2.3.5. Hard X-ray Photoelectron Spectroscopy (HAXPES)

HAXPES measurements were conducted at the HiKE endstation located at the BESSY II KMC-1 beamline at Helmholtz-Zentrum Berlin.[8,9] The endstation is equipped with a Scienta R4000 electron analyzer, allowing it to use of the excitation energy range (i.e., 2 – 10 keV) provided by the KMC-1 bending magnet beamline (see Figure 2.5). The electron analyzer is positioned at an angle of 90° to the beamline; x-rays are linearly polarized with the polarization vector aligned with the analyzer entrance.

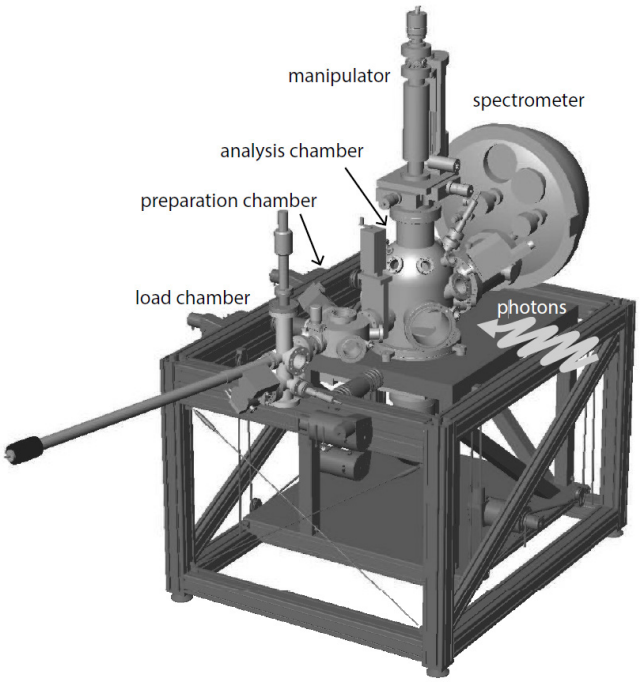

Figure 2.8. Schematic the HIKE end station at KMC-1 at BESSY II, Berlin.[8]

Two different excitation energies are employed in this work, making use of different diffraction orders of the Si (111) crystal pair of the KMC-1 double crystal monochromator (i.e., 2 keV in 1st order and 6 keV in 3rd order); with these excitations, it is possible to probe the topmost and buried layers of approximately 11 and 25 nm, respectively. [10] The actual probing depth of the measurements is governed by the exponential attenuation of the photoemission signal, with $(1^{-e-1}) \times 100\% \approx 63\%$ of the measured signal arising from within one inelastic mean free path (IMFP) of the sample surface. While there can be considerable variation related to the strength of specific photoemission lines and the statistical quality of the measurement, it is reasonable to assume that the measurement can contain some information from up to 4×IMFP: $(1^{-e-4}) \times 100\% \approx 98\%$ of the signal will originate from within this distance from the surface, although only approximately 3% of the signal will originate from the region between 3×IMFP and 4×IMFP.

Measurement protocols involving the use of beam attenuating filters were implemented in this experiment, aiming at preventing/minimizing beam-induced damage to the sample. This includes the use of an Al filter that effectively reduces the 2 keV photon flux by 93% and the 6 keV flux by 50% of their unfiltered values. When probing the band bending by tracking the I 3d core level, as well as the use of a Be filter that effectively reduces the 2 keV photon flux by 75% and the 6 keV photon flux by 10% of their unfiltered values for measurements related to compositional analysis. In addition, we applied a segmented data acquisition approach to compare the evolution of core levels under X-ray radiation and move sample spots. The fitted peak intensity of the obtained HAXPES spectra of different core levels is normalized to the maximum intensity.

Core level	Excitation energy (eV)	IMFP (Å)	Cross section (σ)
C 1s	2003	43.6	15.31
	6009	116.64	0.56
N 1s	2003	41.33	27.75
	6009	114.75	1.1
Pb $4f_{7/2}$	2003	46.62	127.78
	6009	119.18	2.26
I $3d_{5/2}$	2003	36.8	228.16
	6009	111.01	5.7
Br $3d_{5/2}$	2003	48	14.83
	6009	120.5	0.2
Cs $3d_{5/2}$	2003	34.6	279.86
	6009	109.22	7.18
Sn $3d_{5/2}$	2003	39.54	165.25
	6009	113.27	3.79
O 1s	2003	38.59	46.04
	6009	112.48	1.92

Table 2.1. IMFP and σ values of C 1s, N 1s, Pb $4f_{7/2}$, I $3d_{5/2}$, Br $3d_{5/2}$, Cs $3d_{5/2}$, Sn $3d_{5/2}$, O 1s core levels at 2 keV and 6 keV excitation. [11-14]

Data treatment of HAXPES measurement is done using two software packages, i.e. IGOR Pro and CasaXPS. We used IGOR Pro software to correct the scale energy and intensity of collected photopeaks. The analyzer records the kinetic energy of the photoelectrons; therefore, it is converted to binding energy (BE) by subtracting their value from excitation energy. In the next step, the energy scale is calibrated using the Au $4f_{7/2}$ BE position. Au 4f spectra are collected from a gold film during samples characterization. Assuming the peak position of Au $4f_{7/2}$ at 84 eV and finding the deviation from this value, all the recorded spectra are shifted accordingly. Next, we corrected the intensity; each spectrum is divided by number of sweeps and beam current. The corrected data are then transferred to CasaXPS for peak fitting. For peak fitting of the elements orbital levels of p, d, and f doublet peaks, three constraints (namely, the area ratio, full-width-half-maximum (FWHM) equality, and orbital splitting value of their states) are applied.

For the quantification assessment, the raw area of each component extracted from CasaXPS is divided by IMFP[11] (Table 2.1), photoionization cross-section (σ) and electron analyzer's transmission factor.[12-14] As σ values are dependent on measurement geometry due to the polarization of the exciting X-rays, the employed σ values for the core levels of interest (shown in Table S1) were interpolated from values computed for photoionizations resulting in photoelectron kinetic energies ranging between 1 – 10 keV via Eqn. (3) of ref. [12]. For this, tabulated theoretical angular distribution parameters found in refs. [12-14] were used, setting θ: 0° [i.e., the direction of the (measured) photoelectrons being the same as the direction of the exciting photon polarization] and ϕ:90° [i.e., the direction of the (measured) photoelectrons being perpendicular with respect to the exciting photon direction].

2.3.6. Kelvin Probe (KP)

The Kelvin probe method quantifies the work function of a material's surface by evaluating the contact potential difference between a reference electrode and the material. This involves employing a conductive probe tip to establish a capacitor with the sample. By applying a small AC voltage to generate a current flow termed the Kelvin signal, the probe tip measures the potential difference. The obtained Kelvin signal is subsequently compared to a reference potential acquired from a known work function reference electrode. This comparative analysis enables the determination of the contact potential difference and, consequently, the work function of the sample surface.[15]

We utilized a macroscopic Kelvin probe (KP) system, specifically the Besocke Delta Phi: Kelvin Control 07 and Kelvin Probe S instruments, to obtain the work function (WF) data of the ALD metal-oxides. A gold tip (Kelvin Probe S) was employed, and its work function was determined by measuring the contact potential difference (CPD) relative to a reference sample, an evaporated gold sample, which is assumed to have a work function of 4.8 eV (missing citation). To monitor the temporal variation of CPD, we recorded the CPD value using a multimeter (Keithley 2635Bé) connected to the CPD output of the KP system. The samples under investigation were electrically grounded to the KP Faraday cage. In order to establish proper grounding of the bilayers, a lateral area with the transparent conductive oxide (TCO) (ITO or FTO) was left exposed. This allowed us to ground the samples laterally, ensuring a maximum lateral distance of 2 cm between the tip and the contact. The low sheet resistance of the TCOs guaranteed good electrical contact.

2.3.7. Current Density-Voltage Measurements (J-V)

The efficiency of a solar cell is obtained through current density (J) and voltage (V) measurement while the device is exposed to light that replicates the spectrum of 1 Sun under 1.5 air mass (AM). The JV curve is obtained by increasing the voltage applied to the solar cell electrodes and simultaneously measuring the current density (Figure 2.6). The J-V curve represents two key parameters of a solar cell i.e. the open circuit voltage and short circuit current. The open circuit voltage (V_{OC}) is the maximum voltage in the solar cell when no current flows through the electrodes and the short circuit current density (J_{SC}) is the maximum current density in the solar cell when the voltage is zero.

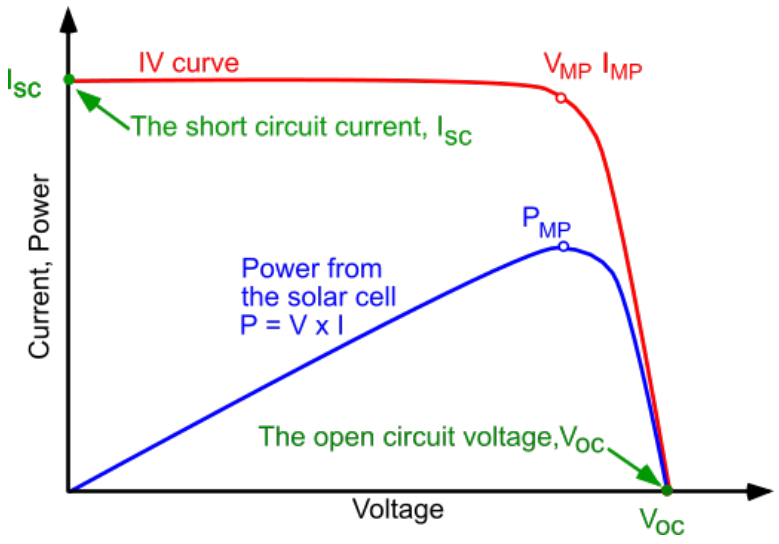

Figure 2.9. I-V curve of Solar cells indicating I_{SC}, V_{OC} and P_{max}.[16]

To determine the maximum power density of a solar cell, the relationship between current density and voltage can be utilized through the following formula:

$$\frac{d(J_{max} \times V_{max})}{dV} = 0 \qquad \text{Equation 2.2}$$

Comparing and benchmarking solar cells typically does not involve using the maximum power. Instead, the fill factor (FF) parameter is employed. The fill factor is the ratio of the maximum power point to the product of the short circuit current density (J_{SC}) and open circuit voltage (V_{OC}). In ideal cases, the fill factor of efficient solar cells can approach unity. The fill factor (FF) is calculated as follows:

$$FF = \frac{P_{max}}{V_{OC} \times J_{SC}} \qquad \text{Equation 2.3}$$

The power conversion efficiency (PCE) of a solar cell is determined by dividing the output power of the solar cell by the incident power. However, it is well-documented that perovskite solar cells experience degradation, resulting in a noticeable reduction in PCE. Therefore, static PCE measurements alone do not provide sufficient information. To gain a better understanding of perovskite solar cell performance, tracking the maximum power point (MPP) over a given period of time is necessary.

Moreover, the shape of the J-V curve in a solar cell is influenced by its internal electrical resistance. The series resistance (Rs) is associated with the inherent resistivity of the charge transport layers, photoactive layer, and electrodes. The shunt resistance (Rsh) is determined by the uniformity of each layer within the solar cell stack. When low-quality films exhibit pinholes, the shunt resistivity decreases. Taking into account both of these resistances, the diode equation for solar cells can be expressed as follows:

$$I = I_L - I_0\left(e^{\frac{q(V+IR_S)}{K_BT}} - 1\right) - \frac{(V+IR_S)}{R_{sh}} \quad \text{Equation 2.4}$$

Here, I_L represents the photocurrent, I_0 is the saturation current, k_B is Boltzmann's constant, and T is the absolute temperature. For solar cells to be highly efficient, it is crucial to minimize the series resistance (Rs) and maximize the shunt resistance (Rsh). The JV measurements of the Perovskite Solar Cells (PSCs) were performed by illuminating the cells from the glass side. This illumination was accomplished using an Oriel Sol3A AAA sun simulator with an aperture area of 0.09 cm^2. A voltage bias was forwardly and reversely applied to the devices using a digital source meter (Keithley 2400).

2.3.8. External Quantum Efficiency (EQE)

External Quantum Efficiency (EQE) measurement is a fundamental technique used to evaluate the performance of solar cells in converting incident photons into collected charge carriers, with consideration of the wavelength of the incident radiation. It provides insights into the efficiency of a solar cell across different wavelengths of light. EQE is expressed as a ratio of the number of collected charge carriers to the number of incident photons, and it is plotted against the corresponding wavelength of the photons. By analyzing the EQE spectrum, researchers can understand how effectively a solar cell utilizes photons of different energies.

The short-circuit current value (Jsc) can be determined from the EQE (External Quantum Efficiency) spectrum using following equation:

$$J_{sc} = -q\int_0^{\infty} EQE(\lambda)\phi(\lambda)d\lambda \qquad \text{Equation 2.4}$$

In this equation, q represents the elementary charge, $\phi(\lambda)$ corresponds to the density of the incident photon spectra. To carry out this measurement, an Oriel IQE200 system was employed, which was coupled with a source meter (Keithley 2400) and a 300W xenon lamp. The measurement specifically focused on perovskite solar cells and covered the wavelength range from 300 nm to 850 nm.

2.4. Collaborations

This section provides information on the external and internal collaboration done during this doctoral research work. The fabrication of devices and the majority of material characterization procedures were carried out at IPVF (Institut Photovoltaïque d'Ile-de-France). The XPS analysis, on the other hand, was conducted at ILV (Institut Lavoisier de Versailles), Versailles. Additionally, the HAXPES studies were performed at the HIKE beamline station located in BESSY (Berlin Electron Storage Ring Society), Berlin.

The ALD materials (SnO_2 and NiO_X) used in this thesis were developed by Damien Coutancier, a CNRS research engineer at IPVF. Kelvin Probe measurements were performed in collaboration with Davide Regaldo, a Ph.D. candidate at IPVF. Furthermore, the operational stability of the n-i-p PSCs mentioned in Chapter 5 was evaluated by Karim Medjoubi, a researcher at IPVF. In addition, the HAXPES data analysis of MHP/ALD-SnO_2 elaborated in Chapter 3 was performed collaboratively with Javid Hajhemati, a Postdoctoral researcher in our group.

2.5. Summary

This chapter describes the device architecture, materials, methods, and characterization techniques employed in this thesis work. By providing a comprehensive background, it establishes a solid foundation for the subsequent chapters focused on the investigation of the interface between Perovskite and ALD-Oxides.

■ References

1. Anaraki, E.H., Kermanpur, A., Steier, L., Domanski, K., Matsui, T., Tress, W., Saliba, M., Abate, A., Grätzel, M., Hagfeldt, A. and Correa-Baena, J.P., 2016. Highly efficient and stable planar perovskite solar cells by solution-processed tin oxide. *Energy & Environmental Science*, *9*(10), pp.3128-3134.
2. Ermrich, M. and Opper, D., 2013. XRD for the analyst. *Getting acquainted with the principles. Second. Panalytical*.
3. Bunaciu, A.A., UdriŞTioiu, E.G. and Aboul-Enein, H.Y., 2015. X-ray diffraction: instrumentation and applications. *Critical reviews in analytical chemistry*, *45*(4), pp.289-299.
4. Levine, J.R., Cohen, J.B., Chung, Y.W. and Georgopoulos, P., 1989. Grazing-incidence small-angle X-ray scattering: new tool for studying thin film growth. *Journal of Applied Crystallography*, *22*(6), pp.528-532.
5. Reimer, L. and Microscopy, S.E., 2010. Scanning Electron Microscopy. *Springer Series in Optical Sciences*, *45*, p.135.
6. https://en.wikipedia.org/wiki/Scanning_electron_microscope (creative commons license).

7. Passos, M.L. and Saraiva, M.L.M., 2019. Detection in UV-visible spectrophotometry: Detectors, detection systems, and detection strategies. *Measurement*, *135*, pp.896-904.
8. Gorgoi, M., Svensson, S., Schäfers, F., Öhrwall, G., Mertin, M., Bressler, P., Karis, O., Siegbahn, H., Sandell, A., Rensmo, H. and Doherty, W., 2009. The high kinetic energy photoelectron spectroscopy facility at BESSY progress and first results. *Nuclear Instruments and Methods in Physics Research Section A: Accelerators, Spectrometers, Detectors and Associated Equipment*, *601*(1-2), pp.48-53.
9. Schaefers, F., Mertin, M. and Gorgoi, M.K.M.C., 2007. KMC-1: A high resolution and high flux soft x-ray beamline at BESSY. *Review of Scientific Instruments*, *78*(12).
10. Schulz, P., Cahen, D. and Kahn, A., 2019. Halide perovskites: is it all about the interfaces?. *Chemical reviews*, *119*(5), pp.3349-3417.
11. Shinotsuka, H., Tanuma, S., Powell, C.J. and Penn, D.R., 2015. Calculations of electron inelastic mean free paths. X. Data for 41 elemental solids over the 50 eV to 200 keV range with the relativistic full Penn algorithm. *Surface and Interface Analysis*, *47*(9), pp.871-888.
12. Trzhaskovskaya, M.B., Nefedov, V.I. and Yarzhemsky, V.G., 2001. Photoelectron angular distribution parameters for elements Z= 1 to Z= 54 in the photoelectron energy range 100–5000 eV. *Atomic Data and Nuclear Data Tables*, *77*(1), pp.97-159.
13. Trzhaskovskaya, M.B., Nefedov, V.I. and Yarzhemsky, V.G., 2002. Photoelectron angular distribution parameters for elements Z= 55 to Z= 100 in the photoelectron energy range 100–5000 eV. *Atomic Data and Nuclear Data Tables*, *82*(2), pp.257-311.
14. Trzhaskovskaya, M.B., Nikulin, V.K., Nefedov, V.I. and Yarzhemsky, V.G., 2006. Non-dipole second order parameters of the photoelectron angular distribution for elements Z= 1–100 in the photoelectron energy range 1–10 keV. *Atomic Data and Nuclear Data Tables*, *92*(2), pp.245-304.
15. Melitz, W., Shen, J., Kummel, A.C. and Lee, S., 2011. Kelvin probe force microscopy and its application. *Surface science reports*, *66*(1), pp.1-27.
16. www.pveducation.org.

Chapter 3
Interface Study of Perovskite and ALD SnO_2

Preface: *Despite the advantages of ALD, the deposition of metal oxides directly on bare perovskite can so far not been achieved without damaging the perovskite layer underneath. In addition, the changes to the physicochemical and electronic properties at the perovskite interface upon exposure to the ALD precursors can alter the material and hence device functionality. Herein, we report on a synchrotron-based hard X-ray photoelectron spectroscopy (HAXPES) investigation of the interface between metal halide perovskite (MHP) and ALD-SnO_2. In addition, we assess the effectiveness of introducing a thin interlayer of the organic electron transport material Phenyl-C61-butyric acid methyl ester (PCBM) between MHP and ALD-SnO2 to mitigate the effect of ALD deposition.*

Contents

3.1. Introduction

Chapter 1 introduced a select set of examples focusing on the interface study of ALD-SnO_2 on MHP. We emphasized the lack of clarity regarding how ALD precursors impact the chemistry of the buried interface and the alteration of the interfacial electronic band configuration of MHP. In this chapter, we present a synchrotron-based HAXPES interface study of $FA_{0.7}Cs_{0.3}Pb(I_{0.9}Br_{0.1})_3$ MHP with a thin ALD SnO_2 overlayers using two different photon energies (2 and 6 keV) for excitation that provide different information depths (see Chapter 2, Section 2.3.5) and hence assess the surface and buried interface properties, respectively (see Figure 3.1). Additionally, we conducted a comparative analysis, examining the impact of the ALD process with and without PCBM as an organic buffer layer between MHP and ALD-SnO_2. The primary objective of this study is twofold: firstly, to determine the influence of the ALD-SnO_2 precursor on the deeper layers of the MHP interface, and secondly, to track the evolution of band alignment while considering the potential occurrence of unwanted chemical reactions resulting from the interaction between ALD-SnO_2 precursors and the MHP surface.

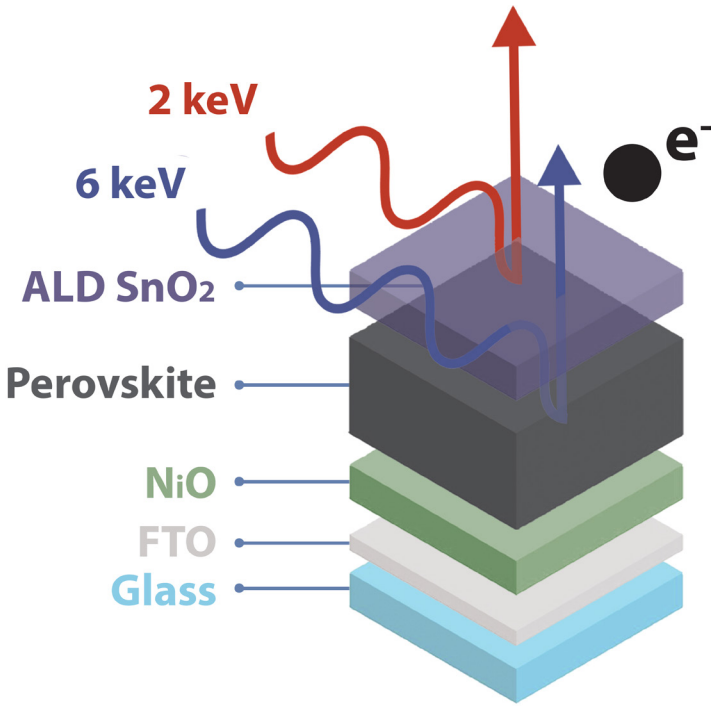

Figure 3.1. Schematics of different probing depth of our HAXPES measurement using 2 keV (probes MHP/SnO_2 interface) and 6 keV (probes deeper in MHP) photon energies.

3.2. Preliminary Thermal Stability assessment of MHP

In this section, we discuss the preliminary thermal stability test of $FA_{0.7}Cs_{0.3}Pb(I_{0.9}Br_{0.1})_3$MHP film, which is conducted under conditions similar to the Atomic Layer Deposition (ALD) process, specifically at a pressure of 1-3 millibars. The purpose of this preliminary analysis was to determine the temperature at which ALD Oxides could be safely deposited on the MHP film without causing thermal degradation. The samples underwent post-annealing treatments at temperatures of 100°C, 150°C, and 200°C for a duration of 1 hour at 1 mbar pressure. The experiment is performed inside MBraun glovebox using a closed hotplate with a low vacuum of 1mbar.

Upon subjecting the MHP film to post-annealing at 100°C, it was observed that the X-ray diffraction (XRD) signature remained unchanged compared to the reference sample, as depicted in Figure 3.2(b). This indicates that the MHP bulk remained stable at the temperature of 100°C. However, after annealing at 150°C for 1 hour, a peak associated with PbI_2 emerged at an angle of 12.5°. Subsequently, when the MHP film was annealed at 200°C for 1 hour, the perovskite peaks completely disappeared, while a prominent PbI_2 peak with high intensity became apparent. This signifies the complete degradation of the MHP film at a temperature of 200°C.

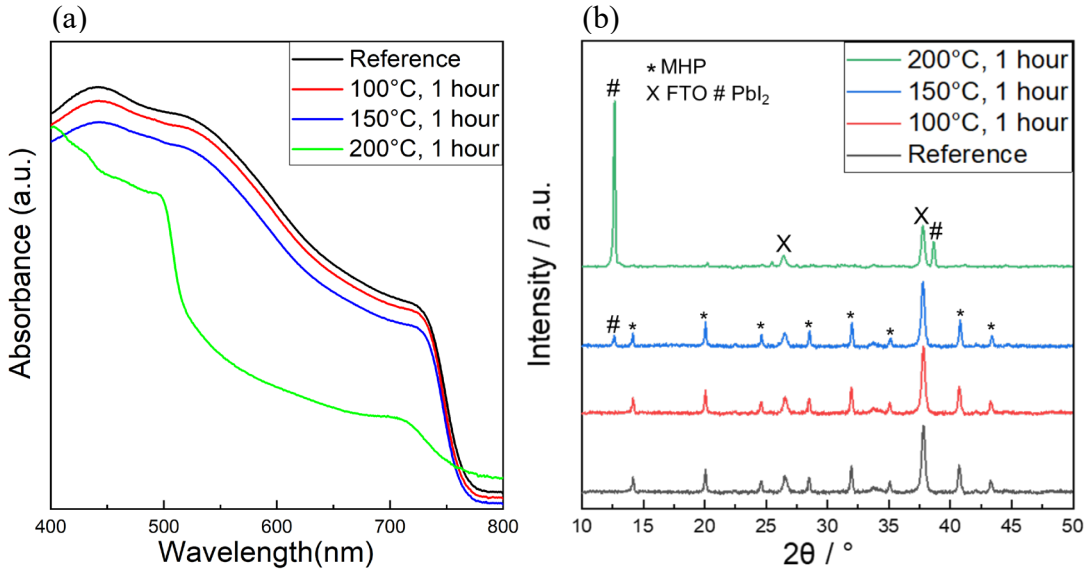

Figure 3.2. MHP films with different post-annealing temperatures for 1 hour at 1 mbar in nitrogen environment (a) UV-Vis absorption spectra (b) XRD pattern.

An assessment of the MHP film's absorbance is also conducted following the 1-hour heat treatments. A slight decrease in absorbance is observed after subjecting the film to 100°C heat treatment, as shown in Figure 3.2. (a). As the annealing temperature increased, the absorbance of the MHP film further declined, with a significant effect observed in the sample subjected to 200°C heat treatment. This trend indicates that at 200°C, the MHP film had completely converted into PbI_2. In summary,

based on the above findings, it can be concluded that a temperature of 100°C at 1 mbar pressure is thermally safe for the deposition of ALD oxides on bulk MHP films.

3.3. Chemical Properties of ALD-SnO_2 using XPS

XPS was employed to investigate the chemical nature of 5nm ALD-SnO_2 grown on silicon wafer, as illustrated in Figure 3.3. In Figure 3.3(a), the Sn $3d_{5/2}$ contribution in the spectra is centered around 486.7 eV, indicating the presence of Sn in the IV oxidation state.[1] In the O 1s core level, one of the contributions, centered around 530.3 eV, is attributed to SnO_2, while the contribution at 531.6 eV is associated with the presence of -OH groups (see Figure 3.3(b)).

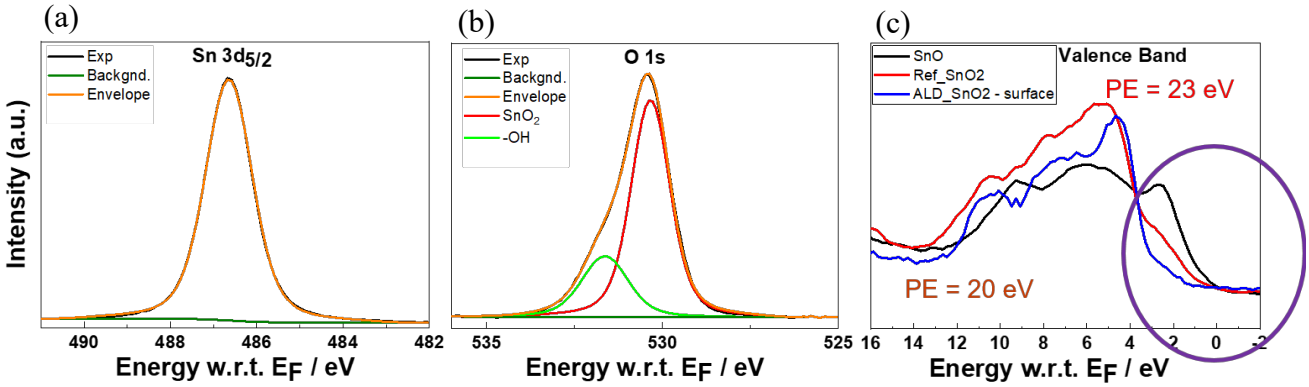

Figure 3.3. XPS spectra (Al-kα 1486.7 eV) of ALD-SnO_2 grown on Si wafer at 100°C (a) Sn $3d_{5/2}$ (b) O 1s (c) Valence band.

However, the binding energy of the Sn $3d_{5/2}$ core level for Sn^{4+} and Sn^{2+} states show a small difference of only 0.5 eV, which is insufficient to clearly distinguish between the two Sn states. To overcome this challenge, the valence band spectra become crucial. In the valence spectra, a distinct peak at a lower binding energy is observed specifically for the Sn^{2+} state.[2] Analyzing the VB spectra obtained from the ALD-SnO_2 film, represented in blue color, no peak is observed at the lower binding energy of the VB spectra. Instead, it closely matches the VB spectra of the SnO_2 reference, represented in red color, which is obtained from the thermo avantage database (Figure 3.3 (c)). This comparison suggests that the ALD-SnO_2 film aligns with the SnO_2 reference material and does not exhibit the characteristic peak associated with the Sn^{2+} state. Therefore, VB spectra supports the conclusion that the ALD-SnO_2 film on silicon wafer predominantly consists of Sn in the IV oxidation state (Sn^{4+}), consistent with the XPS analysis.

3.4. Interface and surface study of MHP, PCBM and ALD-SnO_2

The device architectures used in this interface study are comprised of F-doped tin oxide(FTO)-coated glass substrate, evaporated NiO, $FA_{0.7}Cs_{0.3}Pb(I_{0.9}Br_{0.1})_3$ MHP with and without a 40nm PCBM buffer layer, and ALD SnO_2 (see Figure 3.4). For this interface HAXPES study, 30 cycles of ALD SnO_2 are deposited on top of MHP and PCBM layers. This corresponds to a 5 nm thick ALD SnO_2 film grown on a reference Si substrate in the same deposition run. However, note that the growth rates can differ for various substrates.

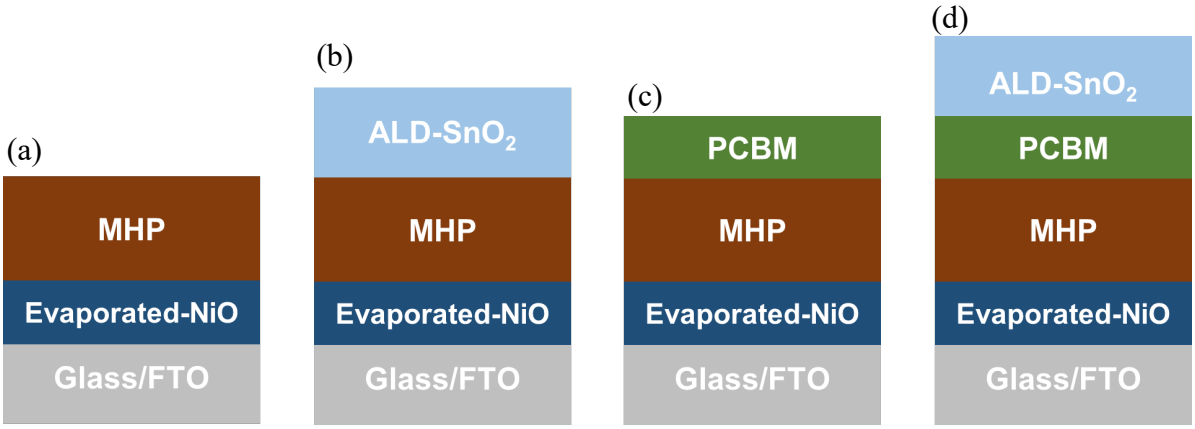

Figure 3.4. Schematic of different device architecture used in this section for interface study a) FTO/ Evaporated-NiO/ MHP, b) FTO/ Evaporated-NiO/ MHP/ ALD-SnO_2, c) FTO/ Evaporated-NiO/ MHP/ PCBM d) FTO/ Evaporated-NiO/ MHP/ PCBM/ ALD-SnO_2.

3.4.1 Structural and optical properties

Figure 3.5(a) illustrates the X-ray diffraction (XRD) patterns of the bare MHP film, with ALD-SnO_2, PCBM, and PCBM/ALD-SnO_2 overlayers. Comparing the pattern of all samples, we observe a low-intensity PbI_2 peak at 12.5° for the samples with the ALD-SnO_2 layer on top. As this MHP bulk is found to be thermally stable at 100 °C, we attribute the formation of the PbI_2 peak to the chemical reaction between the MHP layer and the ALD precursors. Even the use of a protective PCBM interlayer does not fully inhibit this reaction (as indicated by the smaller but visible PbI_2 related peak in the corresponding X-ray diffraction pattern). The presence of PbI_2 is also observable in the absorbance spectra of the samples with ALD-SnO_2 as shown in Figure 3.5(b) as a slight increase starting at a wavelength of around 515 nm (i.e., the band gap of PbI_2) and rising toward the UV-region.[3] We see that while the samples with ALD-SnO_2 present higher absorption in the wavelength range between 400 nm and 550 nm, the absorption becomes slightly lower for wavelengths longer than 550 nm. The samples containing a PCBM interlayer demonstrate increased absorption in the wavelength range between 400 to 650 nm, as indicated by the orange/red spectra, in contrast to the sample without a PCBM interlayer, represented by the green/blue spectra. We

attribute this observation to the parasitic absorption in the PCBM film itself. The long-wavelength absorption onset at 750 nm is attributed to the fundamental absorption onset of the used double cation MHP.

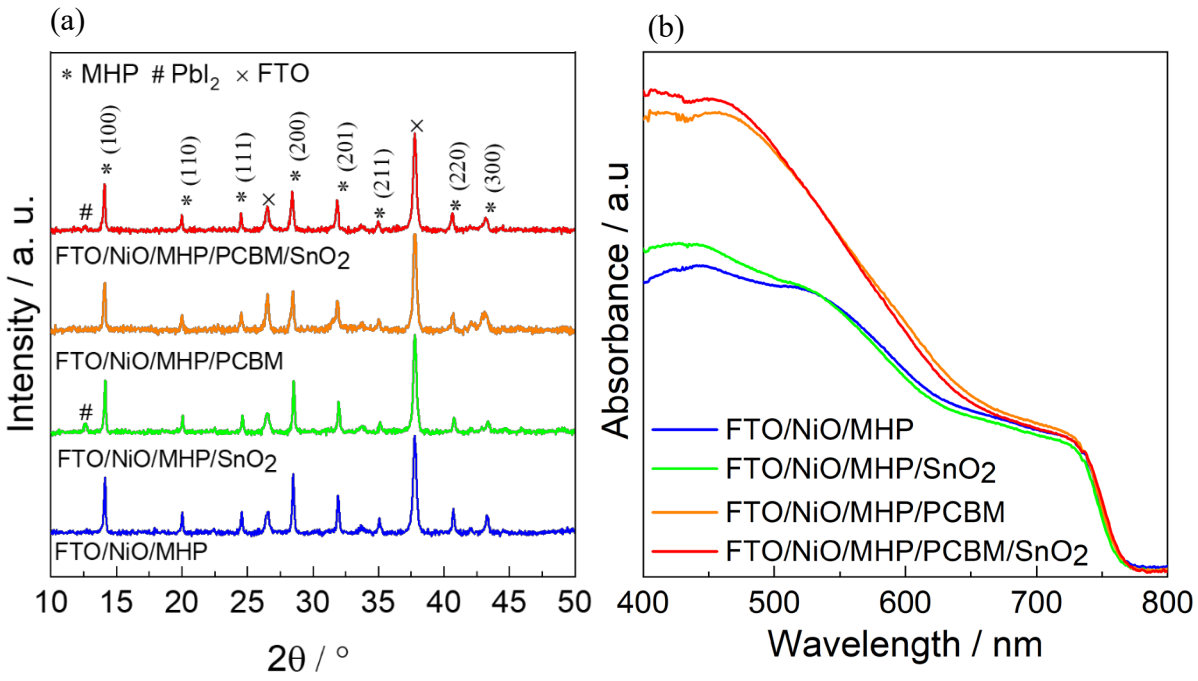

Figure 3.5. (a) XRD pattern of double cation MHP films with and without (PCBM)/ALD-SnO_2 top layers (b) UV-Vis absorption spectra of samples with and without (PCBM)/ALD-SnO_2 top layers.

3.4.2 Surface Morphology

We examined the morphologies of MHP, MHP/ALD-SnO_2, MHP/PCBM, and MHP/PCBM/ALD-SnO_2 using SEM, as shown in Figure 3.6. The morphology of the MHP sample with the SnO_2 overlayer remained unchanged when compared to the bare MHP film, as shown in Figure 3.6 (a) and (b). However, in the MHP/PCBM samples, multiple pinholes were detected, marked with red circles, which exposed the MHP surface, as depicted in Figure 3.6(c). The presence of a pinhole in the PCBM film may result from the aggregation of PCBM molecules in the solution before the spin-coating process.[4] Consequently, this allows the ALD precursors to permeate through the pinholes, can cause undesired chemical reactions. Thus, it becomes apparent that the PCBM buffer layer cannot completely limit possible undesirable interactions between the MHP and ALD precursors (evident from the XRD study). Furthermore, as depicted in Figure 3.6(d), several white dots were observed in the MHP/PCBM/ALD-SnO_2 sample, indicating partial coverage of the pinholes by the SnO_2 deposition.

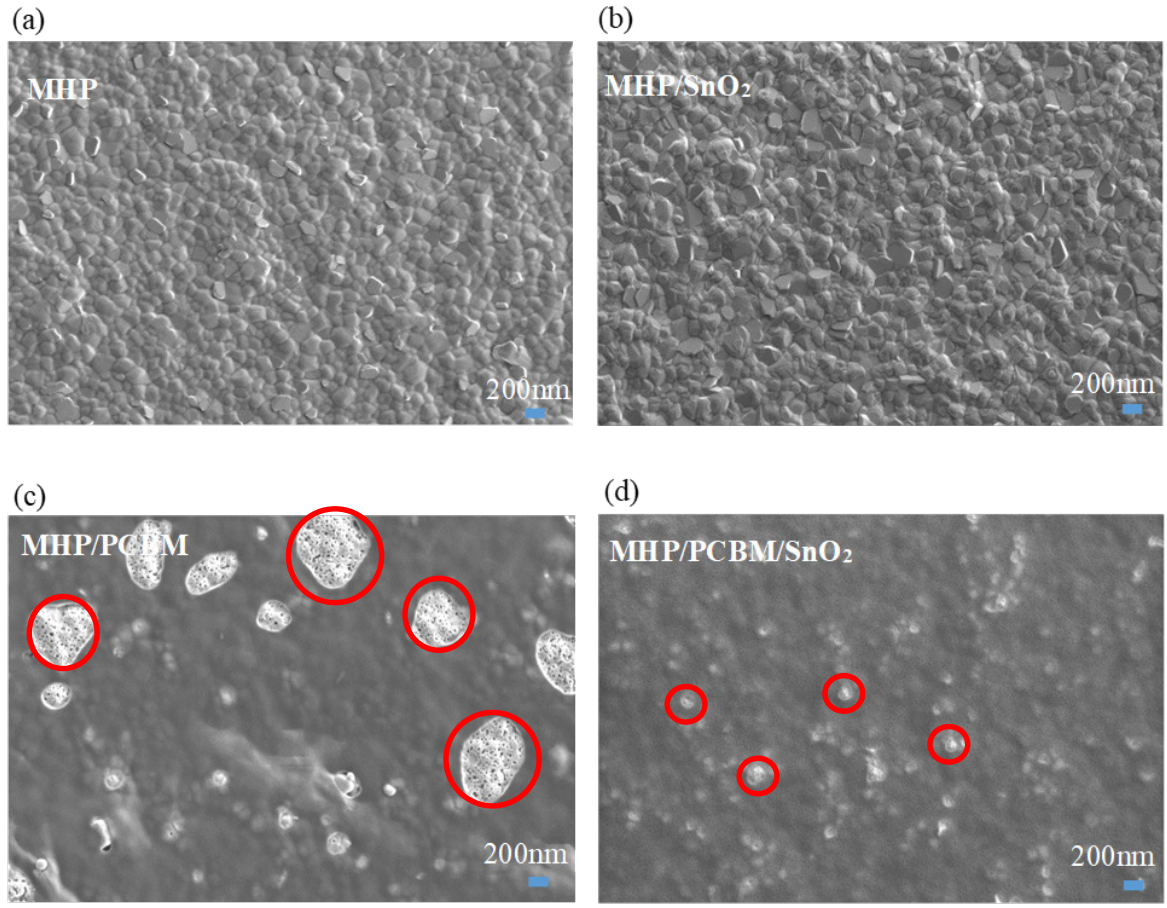

Figure 3.6. SEM images of a) FTO/NiO/MHP, b) FTO/NiO/MHP /SnO_2, c) FTO/NiO/MHP /PCBM, d) FTO/NiO/MHP/PCBM/SnO_2. The white spots correspond to pinholes in the PCBM layer for the perovskite/PCBM sample.

3.4.3 HAXPES analysis of MHP and MHP: ALD-SnO_2

The HAXPES spectra of the Cs $3d_{5/2}$, N 1s, Pb 4f, I 3d, Sn $3d_{5/2}$, and O 1s core level regions of the bare MHP samples and after ALD SnO_2 deposition are depicted in Figure 3.7. The intensities of the various MHP core levels are normalized to maximum intensity for better data visualization. The I 3d and Pb 4f core level signals of pristine MHP show a minor shift in peak position (10-100 meV) between the data acquired for photon energies of 2 keV and 6 keV, respectively (see Table 3.2). Considering the spectral resolution of our HAXPES experiment, we do not consider a shift of this order of magnitude to be significant.

The deposition of SnO_2 results in a larger shift of the lead and iodine core levels by approximately 200 and 300 meV to lower binding energies, respectively. These peak shifts are presumably indicating a change in electronic structure (i.e., band-bending), which can be caused by defect formation at the interface; notably this coincides with the formation of PbI_2 that we observed by

XRD. We also monitored and compared the ratio of iodine to lead at the surface and subsurface of the perovskite layer before and after the ALD-SnO_2 deposition. The quantification shows that before SnO_2 deposition, the I/Pb ratio near the MHP surface is 2.7 i.e., almost equal to the expected stoichiometry value, decreasing to 2.4 with increasing probing depth. After SnO_2 deposition, we observed a more severe iodine deficiency and a contrary I/Pb profile, i.e., the deficiency is more apparent in the 2 keV measurements, in which the calculated I/Pb ratio is 0.7, i.e., almost one fourth of the initial stoichiometry ratio. In comparison, we find the ratio to be higher (1.7) in the more bulk-sensitive 6 keV measurements, indicating that this I depletion is driven by the interface formation with the SnO_2 or its synthesis process. Halide deficiency forms deep-level defects in the metal halide perovskite solar cells, which likely increases interfacial charge recombination and impede carrier extraction, negatively affecting PSCs performance.[5] Upon SnO_2 deposition, a new peak appears at 138.9 and 139.2 eV (for 2 and 6 keV photon energy, respectively) in the Pb 4f core-level spectra for the MHP/SnO_2 sample, which corresponds to the Sn 4s core level. The shift in binding energy of Sn 4s core level could be related to band bending in the SnO_2 film; however, the precision of the fit is significantly affected by the adjacent Pb 4f core level fitting. Therefore, testing this hypothesis required further analysis of the Sn 3d and O 1s core levels, as presented below.

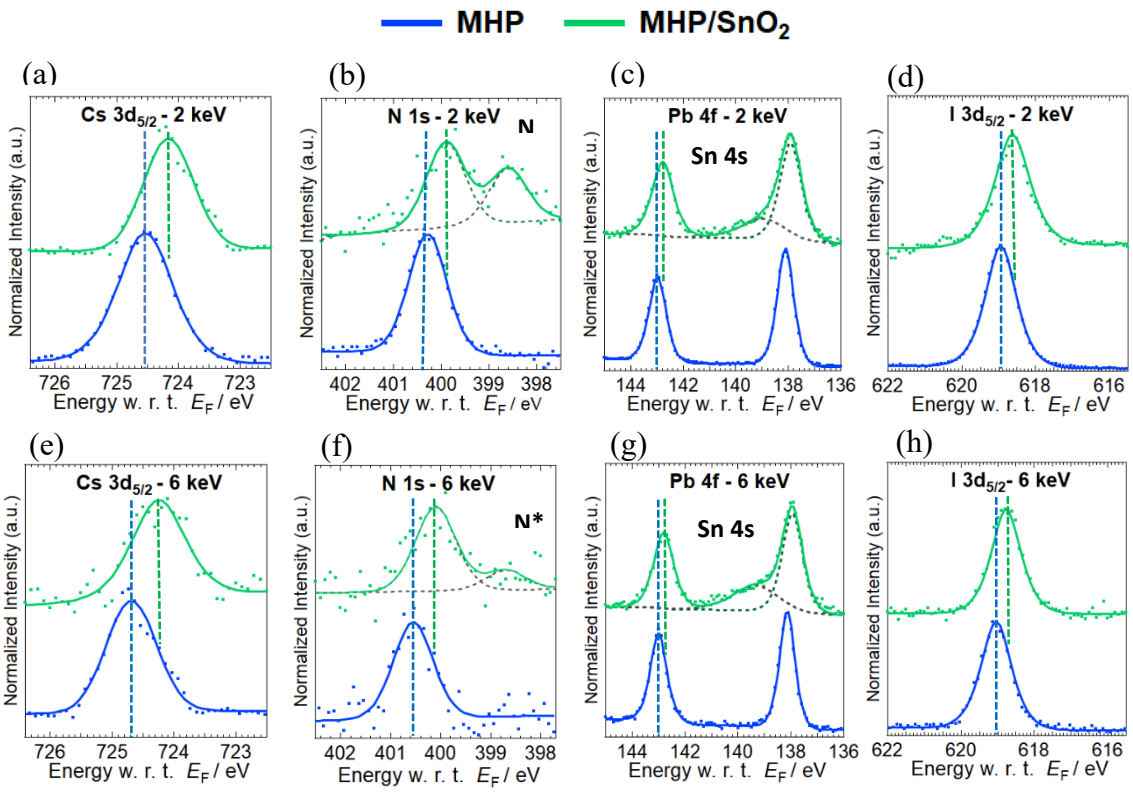

Figure 3.7. (a-h) HAXPES high-resolution spectra (including fit analysis of some core levels) of Cs $3d_{5/2}$, N 1s, Pb 4f, and I $3d_{5/2}$of double cation MHP without (blue spectra) and with (green spectra) ALD SnO_2 top layers recorded using 2 and 6 keV excitation energy with Beryllium (Be) filter. N indicates the peak component of a new nitrogen species as a reaction product of the ALD-SnO_2 deposition.*

However, first we closely inspect the N 1s spectra, for which a new nitrogen peak is observed at 398.7 eV in case of the MHP sample with ALD-SnO_2 (see Figure 3.7 (b) and (f)). The relative intensity of this peak is higher at 2 keV excitation, indicating that the nitrogen species causing this N 1s contribution is predominantly present within the ALD-SnO_2 layer or at the MHP/ALD-SnO_2 interface. Note that the corresponding peak intensity using 6 keV photon energy is close to the detection limit. The formation of a new chemical state of the nitrogen species (N^*) at the MHP interface would be consistent with an interfacial chemical reaction between MHP and ALD precusors, as has been suggested before.[6]

The emergence of the detected nitrogen species can be attributed to two potential origins: firstly, as a reaction/degradation product of the TDMASn ALD precursor such as dimethylamine derivative, and secondly, as a degradation product arising from the formamidinium (FA) species present within the MHP structure due to unwanted reaction with the ALD precursor. A plausible candidate for this degradation product is the *sym*-triazine, a nitrogen-containing heterocycle recognized as 1,2,5-triazine.[7,8] We note that the presence of *sym*-triazine at a FA-based halide perovskite/ALD-SnO_2 interfaces was further corroborated by FTIR measurements.[9] Furthermore, the N 1s peak around 400 eV related to the FA species in MHP shifts by approximately 400-500 meV to lower binding energy after SnO_2 deposition, mostly in accordance with the I 3d and Pb 4f core level shifts. The Cs $3d_{5/2}$ core level spectra exhibit a similar shift to lower binding energies. Hence, all MHP related core levels (e.g., Pb 4f, I 3d, N 1s, Cs $3d_{5/2}$) shift to lower binding energies upon ALD-SnO_2 deposition (see Figure 3.8 and Table 3.1), providing evidence for an upward band bending in the MHP films towards the interface with the metal oxide overlayer.

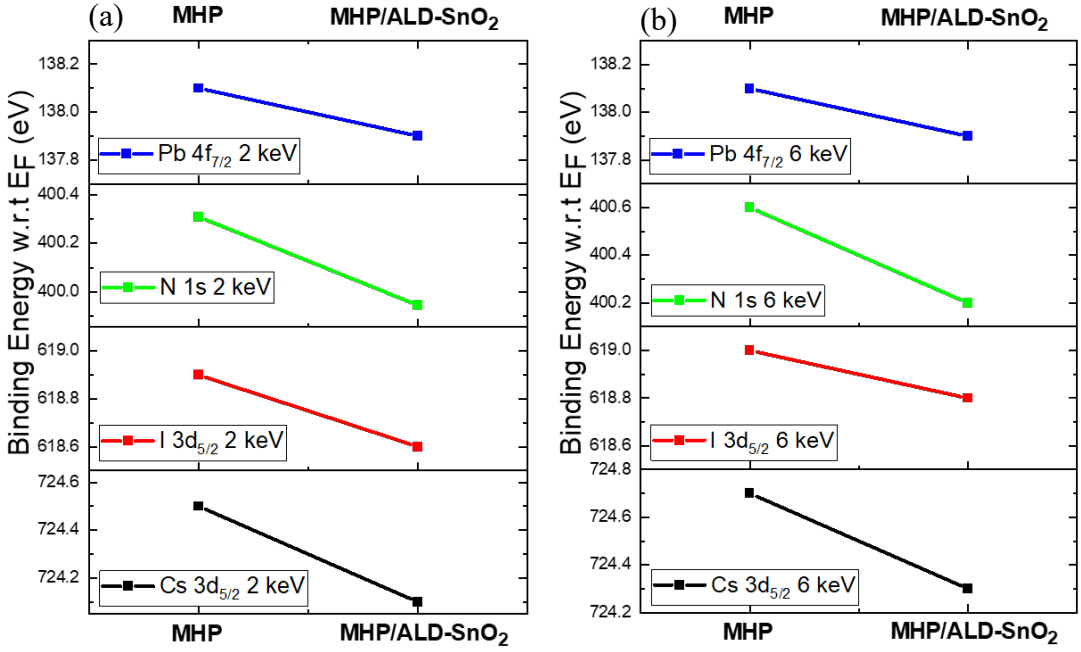

Figure 3.8. Illustration of binding energy of MHP core levels for MHP, MHP/ALD-SnO_2 (30 ALD Cycles) recorded at (a) 2 keV excitation energy (b) 6 keV excitation energy using Be filter.

We note that exposure to high-energy X-rays can induce damage to MHP samples, leading to inaccurate measurements of band bending.[10] To mitigate this issue, an aluminum (Al) filter was utilized to attenuate the 2 keV X-ray beam by a factor of 15 before it reached the sample in order to minimize the creation of defects that would shift the Fermi level and thereby impact band bending determination. We analyzed the binding energy shift of the I $3d_{5/2}$ core level (measured on a fresh sample spot with the attenuated X-ray beam) as an indicator of the magnitude of band bending, which amounts to approximately 400 meV for both 2 keV and 6 keV photon energy (see Figure 3.9 and Table 3.1). Assuming nearly flat band conditions at the MHP surfae prior to interface formation, this upward band bending corresponds to an interfacial electron extraction barrier, which is detrimental to PSCs performance.

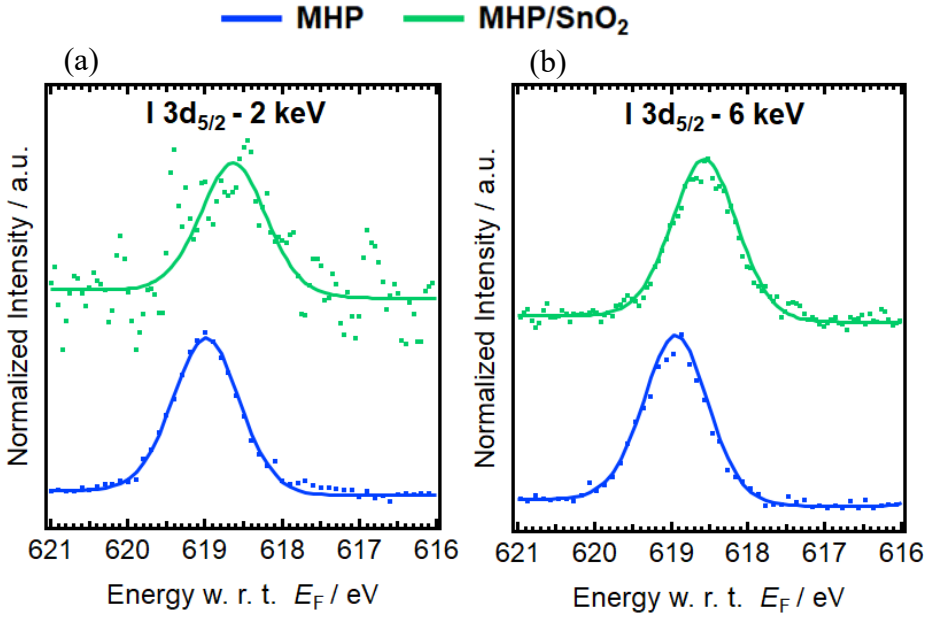

Figure 3.9. HAXPES detail spectra of the I $3d_{5/2}$ core level for the samples with double cation MHP with and without SnO_2 top layers measured using 2 and 6 keV excitations with Al filter. Curve fit results are included.

Sn $3d_{5/2}$ peak is located at 486.7 and 486.9 eV for 2 keV and 6 keV photon energy, respectively, corresponding to the Sn^{4+} state.[11] The shift in the binding energy of Sn $3d_{5/2}$ core level by 200 meV is similar to that observed for the Sn 4s levels discussed above and indicates a slight downward band bending in the SnO_2 film towards the MHP/SnO_2 interface, which would favor the transport of electrons towards the presumably defect-rich interface and thus again negatively affected PSC performance.

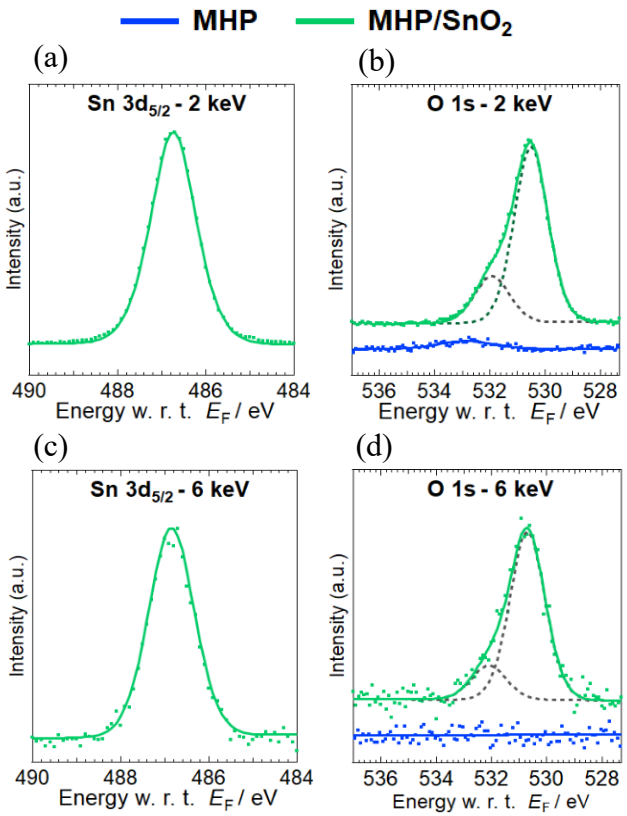

Figure 3.10. (a-d) HAXPES high-resolution spectra (including fit analysis of some core levels) of Sn $3d_{5/2}$, and O 1s of double cation MHP without (blue spectra) and with (green spectra) ALD SnO_2 top layers recorded using 2 and 6 keV excitation energy with Beryllium (Be) filter.

For the MHP/SnO_2 samples, we see the presence of two O 1s components using 2 keV and 6 keV photon energy. The O 1s peak located at 530.7 eV when using 6 keV corresponds to the SnO_2 contribution, while the same peak is shifted to a lower binding energy of 530.5 eV when using 2 keV, corroborating band bending in the SnO_2 film. The signals at 531.9 eV and 532.1 eV seen in the spectra acquired at 2 keV and 6 keV photon energy, respectively, are attributed to the presence of hydroxides.[12] These residual by-products, such as hydroxides, are commonly observed in low-temperature ALD processes and can typically be eliminated by post-annealing treatment at temperatures around 150-200°C.[13] However, in this case, the low thermal stability of the MHP limits such post-heat treatment, as illustrated in Section 3.2. However, also the presence of "hydroxide" like species ascribed to surface adsorbates (particularly for the bare MHP sample) cannot be ruled out. This would be in line with the observation of one minor peak in the 2 keV data (blue line in Figure 3.10(b)), while this peak is below the noise floor of the HAXPES measurements in the 6 keV data (Figure 3.10(d)).

Sample	MHP vs MHP/SnO_2	
Excitation energy	2003 eV	6009 eV
	Shift (meV)	Shift (meV)
I $3d_{5/2}$ (Al filter)	400	400
Cs $3d_{5/2}$ (Be filter)	400	400
N 1s (Be filter)	500	400
Pb $4f_{7/2}$ (Be filter)	200	200
I $3d_{5/2}$ (Be filter)	300	300

Table 3.1. Binding energy shift of Cs $3d_{5/2}$, Pb 4f, I 3d, Sn $3d_{5/2}$ measured using 2 keV and 6 keV excitation energy.

3.4.4 HAXPES analysis of MHP: PCBM and MHP: PCBM: ALD-SnO_2

For comparison the HAXPES results of the samples with PCBM buffer layer deposited on MHP film with and without ALD-SnO_2 overlayer are shown in Figure 3. We use a 40 nm thick PCBM interlayer in this experiment to protect the MHP from the potentially detrimental effect of the interface formation with ALD-SnO_2. Detecting signal from the buried MHP layer, as shown in Figure 3.11, beneath the PCBM layer of nominal thickness of 40 nm is unexpected for the 2 keV-excited measurements [the IMFP of the photoelectrons of PCBM (assuming density of 1.63 g/cm^3) is approximately 4 nm at 2 keV and 11 nm for 6 keV excitation] and hence suggests for the presence of pinholes in the PCBM layer, which is confirmed by corresponding scanning electron microscopy image (see Figure 3.6 (c)). We use this opportunity to compare the MHP core level data of these samples before and after ALD deposition. Because MHP-related signal for these samples can be collected only through the area of the pinholes of the PCBM films, i.e., sample regions with overlayers insufficiently thick to completely attenuate photoelectron signals originating from the buried MHP absorber, the obtained spectra of MHP core levels exhibit markedly low signal-to-noise ratios. As the Pb 4f and I 3d are the most prominent MHP-related lines, further data analysis is limited to spectra of these core levels. In addition, the absence of any discernible signal of the N 1s core level is of particular interest (see Figure 3.11 (c) and (f)). This observation holds significant implications, as it suggests that the observed additional nitrogen contribution in the MHP/ALD-SnO_2 sample is not a mere by-product of the ALD process but instead arises from interfacial chemical reactions specific to the deposition directly on top of the MHP without buffer layer.

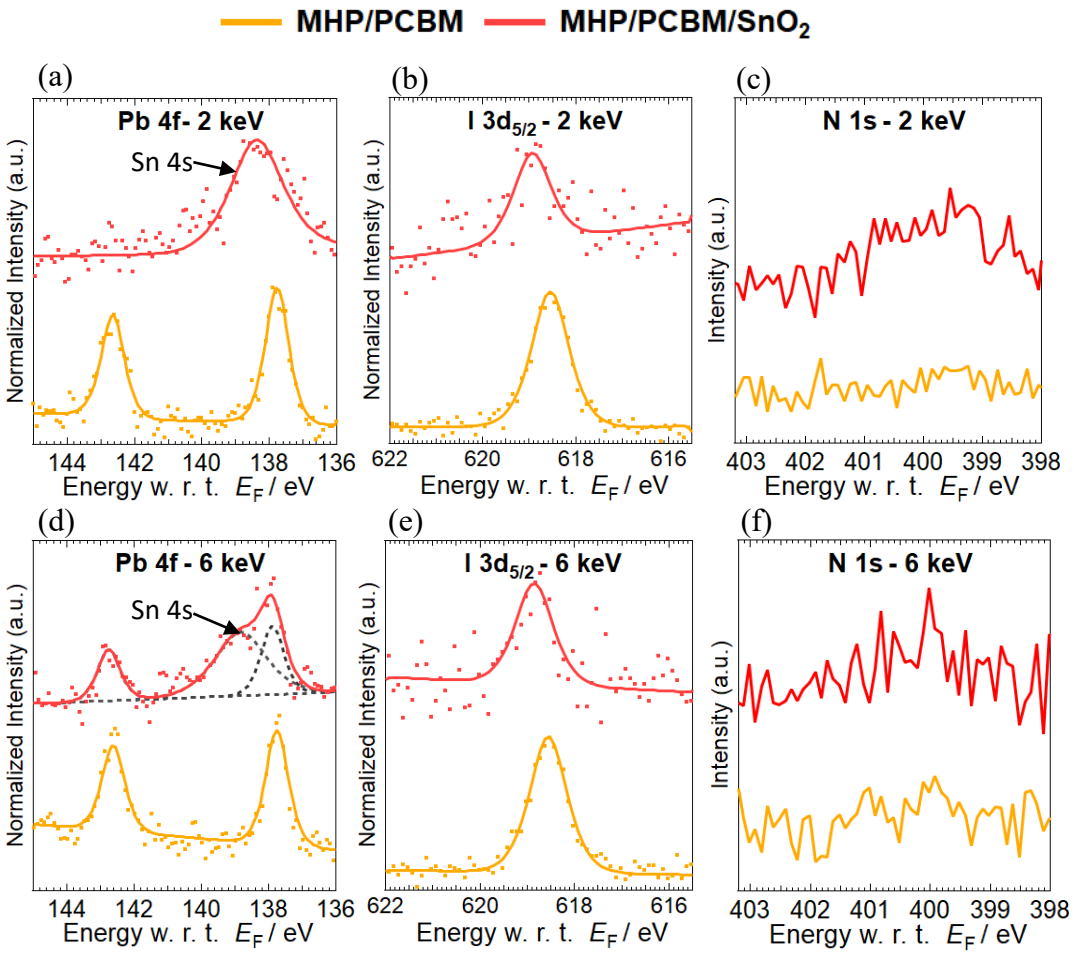

Figure 3.11. HAXPES detail spectra of the i.e Pb 4f, I 3d, and N 1s core levels for the samples with double cation MHP/PCBM hetero-interfaces with and without SnO_2 top layers measured using 2 and 6 keV excitations with Be filter. Curve fit results are included.

After ALD SnO_2 deposition, the Pb 4f core-level spectra do not exhibit any signature of Pb at 2 keV photon energy, indicating that the MHP layer is buried under a closed PCBM and ALD SnO_2 layers, or that pinholes are sufficiently small/few that the Pb 4f signal, unlike the stronger I 3d, is not distinguishable from the background. Furthermore, this behavior indicates that iodine from the MHP might be migrating through the organic buffer layer towards the top interface. Here, as in Figure 3.11(a), we observe the Sn 4s peak at a binding energy of 138.2 eV. Whereas at 6 keV photon energy, we observe peaks corresponding to Pb 4f core-level spectra. After the ALD process, the I 3d core levels shift by almost 400 meV and 300 meV to higher binding energy, compared to the MHP/PCBM reference, for the 2 keV- and 6 keV-excited spectra, respectively (see Figure 3.11(b) and (e)). The peak shift observed can be linked to the creation of even small amounts of donor states in the perovskite layer during the deposition process.[14]

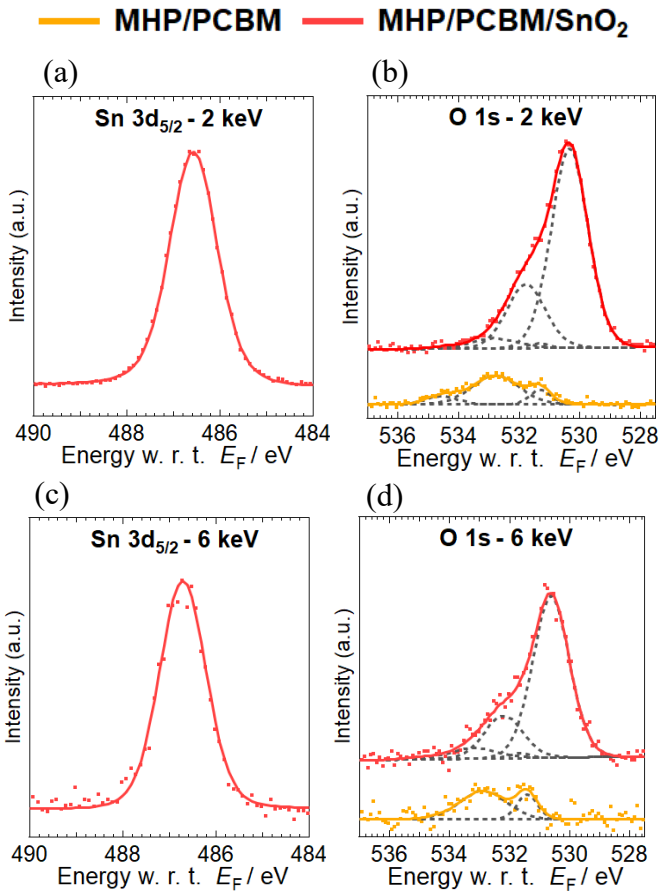

Figure 3.12. HAXPES detail spectra of the i.e Sn $3d_{5/2}$, and O 1s core levels for the samples with double cation MHP/PCBM hetero-interfaces with and without SnO_2 top layers measured using 2 and 6 keV excitations with Be filter. Curve fit results are included.

The Sn $3d_{5/2}$ peak is located at 486.6 and 486.7 eV for 2 keV and 6 keV photon energy, respectively, corresponding to the Sn^{4+} state as shown in the Figure 3.12. The core level shift is indicating a slight downward band bending in the SnO_2 film towards the PCBM/SnO_2 interface, which is observed similarly for the MHP/SnO_2 sample. Fitting the O 1s spectra of samples with a PCBM top layer and without ALD layer leads to the observation of three peaks that belongs to the carbon contamination, single and double oxygen-carbon bond in the carboxyl group of the PCBM molecule. After the ALD process, we see the appearance of two new peaks corresponding to Sn^{4+} oxide and hydroxide (see Table 3.2). The O 1s core level peak corresponding to Sn^{4+} oxide is located at 530.3 eV and 530.7 eV for the 2 keV- and 6 keV-excited spectra, respectively. These shifts in the binding energy of the O 1s core level are presumably due to band bending in the SnO_2 film.

Sample		MHP		MHP/SnO_2		MHP/PCBM		MHP/PCBM/SnO_2	
		Position (eV)		Position (eV)		Position (eV)		Position (eV)	
Excitation Energy		2003 eV	6009 eV	2003 eV	6009 eV	2003 eV	6009 eV	2003 eV	6009 eV
Cs $3d_{5/2}$		724.5	724.7	724.1	724.3	724.2	724.1	724.2	724.5
N 1s	MHP	400.3	400.6	399.9	400.2	-	-	-	-
	2^{nd}	-	-	398.7	398.7	-	-	-	-
Pb $4f_{7/2}$		138.1	138.1	137.9	137.9	137.8	137.8	-	137.8
I $3d_{5/2}$		618.9	619.0	618.6	618.8	618.5	618.6	618.9	618.9
Sn $3d_{5/2}$		-	-	486.7	486.9	-	-	486.6	486.7
O 1s	Sn^{4+} Oxide	-	-	530.5	530.7	-	-	530.3	530.6
	-OH	-	-	531.9	532	-	-	531.8	532.2
	C=O	-	-	-	-	531.3	531.4	531.4	531.6
	C-O	-	-	-	-	532.8	532.9	532.9	533.2

Table 3.2. Binding energy data of Cs $3d_{5/2}$, Pb 4f, I 3d, Sn $3d_{5/2}$, and O 1s measured using 2 keV and 6 keV excitation energy with Be filter.

The present research demonstrates that the PCBM buffer layer inadequately protects the MHP layer from exposure to ALD precursors, as evidenced by the existence of pinholes. This inadequacy exerts a detrimental impact on the overall performance of the device. Therefore, we modified the recipe for deposition of the PCBM film to improve the coverage for PSCs fabrication as shown in Figure A3 in the Annex. In the modified recipe, the PCBM solution in chlorobenzene is heated to 60°C prior to spin coating. The modified PCBM recipe is then incorporated to fabricate p-i-n PSCs discussed later in this chapter. However, first we closely inspect the impact of individual precursors (TDMASn and H_2O_2) on MHP and MHP/PCBM samples in the next section.

3.4.5 Effect of exposure of ALD SnO_2 precursors on MHP and PCBM

In this section, we analyzed the impact of exposure to individual precursors, H_2O_2 and TDMASn, on the MHP and MHP/PCBM samples using LabXPS. Our objective was to determine which of the precursors caused interfacial reactions and defect formation. We focused on the N 1s core level, as we had previously observed clear evidence of the formation of new species in the MHP/ALD-SnO_2 samples.

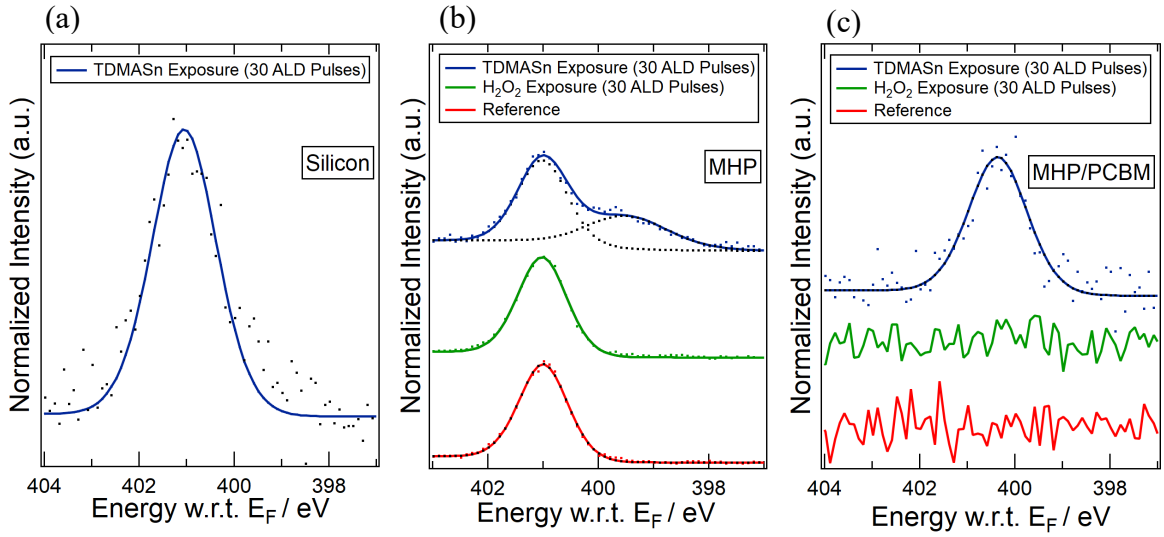

Figure 3.13. XPS spectra (Al-kα 1486.7 eV) of N 1s core level of (a) Silicon wafer exposed to TDMASn precursor (b) MHP (c) MHP/PCBM showing comparison of reference, H_2O_2 exposed and TDMASn exposed.

We exposed a silicon wafer to the TDMASn precursor to record the N 1s position of the precursor, which served as a reference for comparison with the MHP and MHP/PCBM samples. The N 1s peak originating from the TDMASn component was located at 401 eV on the silicon sample, as shown in Figure 3.13 (a). For the MHP sample, we did not observe any changes to the N 1s core level even after exposure to 30 pulses of H_2O_2 precursor compared to the reference sample. However, when exposed to 30 pulses of TDMASn precursor, we observed the formation of an additional peak attributed to the chemical reaction between MHP and TDMASn (see Figure 3.13(b)) Although we did not observe any changes to MHP on exposure to H_2O_2, we cannot completely rule out the possibility of both these precursors reacting together with MHP during SnO_2 formation. For the PCBM reference and H_2O_2 exposed sample, we did not detect any signal from MHP-FA species due to the thick PCBM film itself. Upon exposure to the TDMASn precursor, we observed the formation of a new peak corresponding to the nitrogen contribution from the TDMASn precursor itself (see Figure 3.13(c)). In summary, the exposure of TDMASn precursors on MHP caused interfacial reaction resulting in the formation of defective species. However, no evidence of such unwanted

reaction was found upon exposure of H_2O_2 precursor. In the next section, we proceeded to integrate complete p-i-n solar cells and evaluate their performance.

3.5. Perovskite Solar Cells: JV Characteristics

The performance evaluation of p-i-n perovskite solar cells was carried out under standard one-sun conditions using J-V measurements, as presented in Figure 3.14 (a). These cells were made in five different configurations:

a) Glass/FTO/MeO-2PACz/MHP/PCBM/Ag
b) Glass/FTO/MeO-2PACz/MHP/ ALD-SnO_2 (60 ALD cycles)/Ag
c) Glass/FTO/MeO-2PACz/MHP/PCBM/ALD-SnO_2 (60 ALD cycles)/Ag
d) Glass/FTO/MeO-2PACz/MHP/PCBM-modified/Ag
e) Glass/FTO/MeO-2PACz/MHP/PCBM-modified/ALD-SnO_2 (60 ALD cycles)/Ag

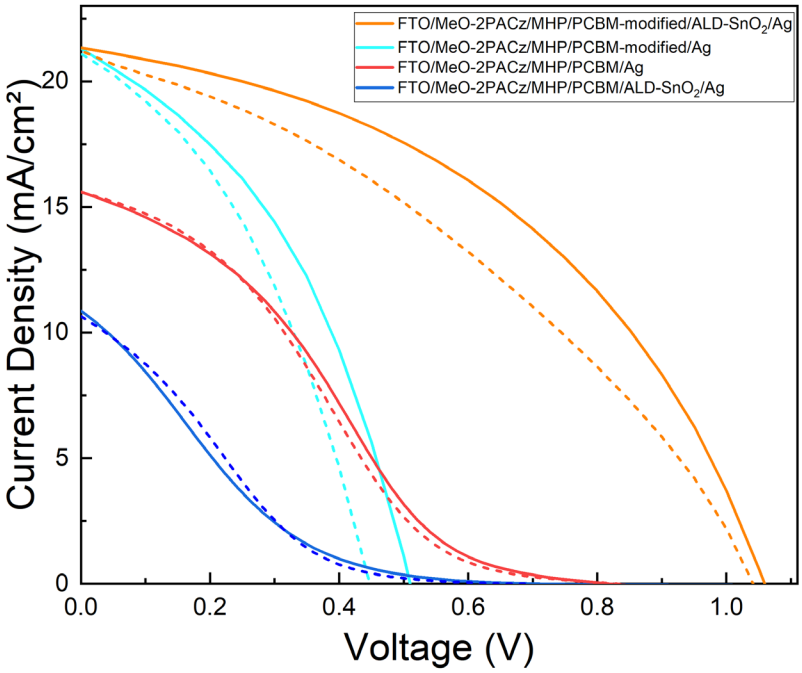

Figure 3.14. J-V characteristics data of p-i-n configuration solar cells. The dotted curves indicate the forward scan, and the solid lines indicate the reverse scan.

The reference devices using PCBM as the ETL exhibited low performance, with a maximum PCE of 3.3%, V_{OC} of 0.83V, J_{SC} of 15.6 mA/cm_2, and fill factor of 27% (see Table 3.3). The devices with an ALD-SnO_2 ETL proved to be non-functional, confirming the negative impact of interfacial defects. The devices that integrated PCBM and SnO_2 double ETL layers showed a very low efficiency of almost 1%. This was due to the presence of pinholes in the PCBM film, which allowed ALD precursors to reach the MHP layer and degrade its performance.

To address this issue, we modified the PCBM deposition recipe to create a pin-hole-free film (see Figure A3 in the Annex) and improved the PCE to 4.3% (PCBM only ETL). Additionally, when we combined the modified PCBM and ALD SnO_2, we observed enhanced performance with a PCE of 10%, V_{OC} of 1.03V, and J_{SC} of 21.3 mA/cm^2. However, the device had a low fill factor of 44% and requires further process optimizations.

	FTO/ MeO-2PACz /MHP/PCBM /Ag		**FTO/ MeO-2PACz /MHP/PCBM-modified/ Ag**		**FTO/ MeO-2PACz /MHP/PCBM /ALD-SnO_2 /Ag**		**FTO/ MeO-2PACz /MHP/PCBM-modified/ALD-SnO_2 /Ag**	
	Reverse Scan	Forward Scan	Reverse Scan	Forward Scan	Reverse Scan	Forward Scan	Reverse Scan	Forward Scan
J_{SC} (mA/cm^2)	**15.6**	**15.6**	**21.1**	**21.3**	**10.85**	**10.64**	**21.3**	**21.1**
V_{OC} (volts)	**0.83**	**0.81**	**0.45**	**0.5**	**0.69**	**0.67**	**1.06**	**1.03**
FF (%)	**24**	**27**	**38**	**40**	**13.70**	**16.27**	**44**	**36**
PCE (%)	**3.2**	**3.3**	**3.6**	**4.3**	**1.04**	**1.17**	**9.9**	**7.9**

Table 3.3. J-V characteristics data of PIN configuration solar cells.

3.6. Summary

In summary, we report a synchrotron-based HAXPES interface investigation between MHP and ALD-SnO_2. This advanced characterization provided important information on the formation of new chemical species (nitrogen compound, lead dihalides) at the interface. More in-depth analysis was performed to track the modification of band alignment induced by newly created interfacial defects. The Pb 4f, I 3d, N 1s, and Cs 3d core level peaks shifted to lower binding energy for the samples with ALD-SnO_2 overlayer; corresponding to upward band bending at the interface (see Figure 3.15). This upward bending at the interface acts as a strong electron barrier and is therefore not ideal for working solar cells. The work is also extended to a system with a 40 nm PCBM interlayer between MHP and SnO_2. Further, the PCBM layer does not fully protect the MHP from exposure to ALD precursors, as evidenced by the observed (low-intensity) PbI_2 signature revealed by X-ray diffraction measurements. Hence, we observe undesirable chemical reactions at the interface in both cases that may negatively affect the electronic interface properties. Furthermore, to address this issue, a modified PCBM deposition recipe was employed that exhibited a pinhole-free morphology, consequently improving the PCE of PCBM/ALD-SnO_2 ETL device stack devices from 1% to 10%.

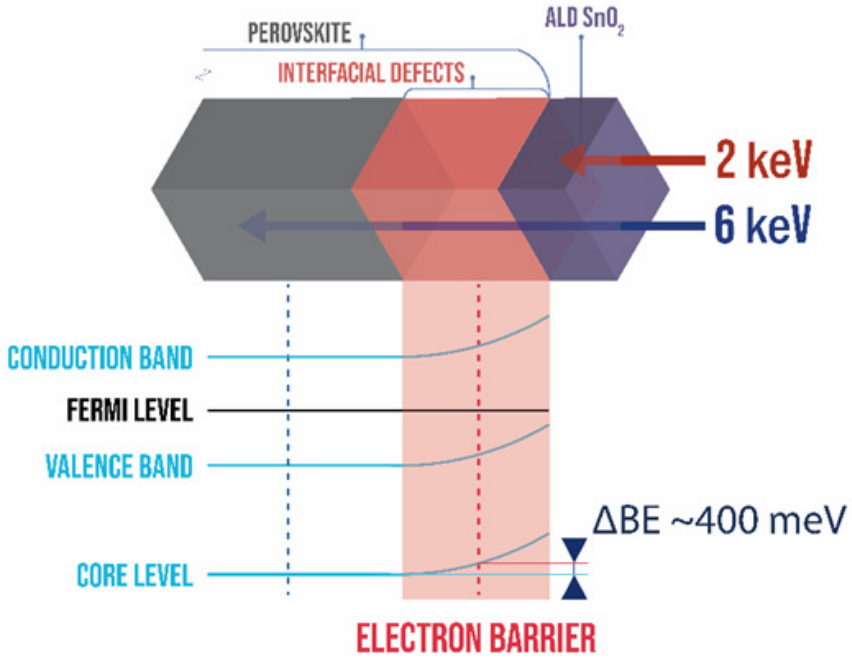

Figure 3.15. Illustration demonstrating electron barrier at perovskite/ALD-SnO_2 interface as result of defects which originated from the interaction between perovskite and ALD precursors.

■ REFERENCES

1. Kwoka, M., Ottaviano, L., Passacantando, M., Santucci, S., Czempik, G. and Szuber, J., 2005. XPS study of the surface chemistry of L-CVD SnO2 thin films after oxidation. *Thin Solid Films*, *490*(1), pp.36-42.
2. Themlin, J.M., Chtaïb, M., Henrard, L., Lambin, P., Darville, J. and Gilles, J.M., 1992. Characterization of tin oxides by x-ray-photoemission spectroscopy. *Physical Review B*, *46*(4), p.2460.
3. Jain, S.M., Philippe, B., Johansson, E.M., Park, B.W., Rensmo, H., Edvinsson, T. and Boschloo, G., 2016. Vapor phase conversion of PbI2 to CH3NH3PbI3: Spectroscopic evidence for formation of an intermediate phase. *Journal of Materials Chemistry A*, 4(7), pp.2630-2642.
4. Sutthana, S., Hongsith, K., Ruankham, P., Wongratanaphisan, D., Gardchareon, A., Phadungdhitidhada, S., Boonyawan, D., Kumnorkaew, P., Tuantranont, A. and Choopun, S., 2017. Interface modification of CH3NH3PbI3/PCBM by pre-heat treatment for efficiency enhancement of perovskite solar cells. Current Applied Physics, 17(4), pp.488-494.
5. Wu, W.Q., Rudd, P.N., Ni, Z., Van Brackle, C.H., Wei, H., Wang, Q., Ecker, B.R., Gao, Y. and Huang, J., 2020. Reducing surface halide deficiency for efficient and stable iodide-based perovskite solar cells. *Journal of the American Chemical Society*, 142(8), pp.3989-3996.
6. Deng, K. and Li, L., 2016. Advances in the application of atomic layer deposition for organometal halide perovskite solar cells. *Advanced Materials Interfaces*, 3(21), p.1600505.

7. Thampy, S., Zhang, B., Park, J.G., Hong, K.H. and Hsu, J.W., 2020. Bulk and interfacial decomposition of formamidinium iodide (HC(NH2)2I) in contact with metal oxide. *Materials Advances*, 1(9), pp.3349-3357.
8. Gunasekar, G.H., Park, K., Ganesan, V., Lee, K., Kim, N.K., Jung, K.D. and Yoon, S., 2017. A covalent triazine framework, functionalized with Ir/N-heterocyclic carbene sites, for the efficient hydrogenation of CO2 to formate. *Chemistry of Materials*, 29(16), pp.6740-6748.
9. Bracesco, A.E., Jansen, J.W.P., Xue, H., Zardetto, V., Brocks, G., Kessels, W.M., Tao, S. and Creatore, M., 2023. In Situ IR Spectroscopy Studies of Atomic Layer-Deposited SnO2 on Formamidinium-Based Lead Halide Perovskite. ACS Applied Materials & Interfaces.
10. Milotti, V., Cacovich, S., Ceratti, D.R., Ory, D., Barichello, J., Matteocci, F., Di Carlo, A., Sheverdyaeva, P.M., Schulz, P. and Moras, P., 2023. Degradation and Self-Healing of FAPbBr3 Perovskite under Soft-X-Ray Irradiation. *Small Methods*, p.2300222.
11. Moulder, J.F., 1992. Handbook of X-ray Photoelectron Spectroscopy: A Reference Book of Standard Spectra for Identification and Interpretation of XPS Data, Physical Electronics Division, *Perkin-Elmer Corporation*, 978-0-9627026-2-4.
12. Bracesco, A.E., Burgess, C.H., Todinova, A., Zardetto, V., Koushik, D., Kessels, W.M.E., Dogan, I., Weijtens, C.H., Veenstra, S., Andriessen, R. and Creatore, M., 2020. The chemistry and energetics of the interface between metal halide perovskite and atomic layer deposited metal oxides. *Journal of Vacuum Science & Technology A*, 38(6).
13. Elam, J.W., Baker, D.A., Hryn, A.J., Martinson, A.B., Pellin, M.J. and Hupp, J.T., 2008. Atomic layer deposition of tin oxide films using tetrakis (dimethylamino) tin. *Journal of Vacuum Science & Technology A*, 26(2), pp.244-252.
14. Dunfield, S.P., Bojar, A., Cacovich, S., Frégnaux, M., Klein, T., Bramante, R., Zhang, F., Regaldo, D., Dufoulon, V., Puel, J.B. and Teeter, G., 2021. Carrier gradients and the role of charge selective contacts in lateral heterojunction all back contact perovskite solar cells. *Cell Reports Physical Science*, 2(8).

Chapter 4
Interface Study of Perovskite and ALD NiO_X

Preface: *This chapter reports the interface, solar cell characteristics, and operational stability of n-i-p configuration perovskite solar cells using an ALD-NiO_X hole-transport interlayer. The objective of this chapter is to investigate and understand the impact of the ALD-NiO_X process on the surface of MHP using a set of advanced characterization techniques and to study its effects on n-i-p solar cell performance. Furthermore, a PTAA organic buffer layer was incorporated to mitigate unwanted chemical reactions between MHP and ALD-NiO_X for the fabrication of stable perovskite solar cells. We found that the PTAA/NiO_X double HTL exhibited improved solar cell performance and operational stability.*

Contents

4.1. Introduction

In Chapter 1, we discussed the prospective advantages of ALD materials for the fabrication of stable PSCs, while also addressing the challenges associated with depositing ALD-Oxides onto MHP film. Our previous chapter highlighted the negative impact of ALD-SnO_2 on MHP film, leading to a detrimental effect on PSC performance. In this chapter, we examine the viability of ALD-NiO_X HTL as a replacement for organic HTLs such as spiro-OMETAD and PTAA in n-i-p architecture solar cells. The use of organic HTLs in n-i-p architecture solar cells has resulted in low device longevity,[1-5] prompting us to consider ALD-NiO_X as a potential candidate for hole selective top contact in PSCs. Our investigations in this chapter focus on the interface between MHP and ALD-NiO_X, and we use LabXPS and synchrotron-based HAXPES techniques to study this interface. Additionally, we introduce a PTAA organic buffer layer between MHP and ALD-NiO_X to enable a comparative analysis and to mitigate potential interfacial reactions between MHP and ALD-NiO_X.
The next section is dedicated to analyzing the structure and chemistry of ALD-NiO_X deposited on silicon wafers at a temperature of 100°C. This analysis of a reference layer is crucial for comparing the characteristics of ALD-NiO_X grown on MHP and PTAA, as the properties of ALD oxides can vary on the underlying chemical surface termination of the layer on which they are grown (as discussed previously in chapter 1). Such a comparison is necessary to understand the differences in the chemical composition of ALD-NiO_X on MHP and PTAA.

4.2. Chemical properties of ALD-NiO_X using XPS

To determine the chemical composition of ALD-NiO_X on a Si wafer, XPS was used to analyze the N 1s, C 1s, Si 2p, Ni 2p, and O 1s core levels, as shown in Figure 4.1. Two samples with different thicknesses of NiO_X were used for this study: one with 5 nm NiO_X 62 ALD cycles (thin overlayer) and the other with 10 nm NiO_X- 125 ALD cycles (thick overlayer). First, we analyzed the N 1s, C 1s, and Si 2p core levels to check for any contamination or ALD by-products in the sample.
We observed a low-intensity noisy peak at the N 1s core level, which makes it challenging to identify a clear peak (Figure 4.1(a)). Although there may be a minimal contribution from the amidinate component of the $Ni(amd)_2$ precursors, it is hard to confirm its presence due to its low signal-to-noise ratio. In the C 1s core level, we detected four peaks originating from carbon contamination due to exposure to the atmosphere. Even brief exposure to atmosphere can cause the formation of a thin layer of carbonaceous material, which are commonly known as adventitious carbon.[8] Adventitious carbon is generally consisting of a variety of hydrocarbon species with small amount of single and double bonded oxygen atoms.[9-10] In Figure 4.1 (b), the C 1s core level analysis for both thin and thick NiO_X samples shows that the major contribution originates from the C-C and C-

H components at 285.2 eV. The C-OH, C=O, and O-C-O components are located at 286.7, 288.2, and 289.2 eV respectively.[11] Moreover, this finding indicates that carbon-bonded oxygen molecules affect the assessment of NiO_X when analyzing the O 1s core level. Therefore, in this chapter, we used O 1s for the qualitative compositional analysis of the NiO_X film, and for quantification, we relied on the Ni 2p core level. No signal was detected in the Si 2p core level for the 10 nm NiO_X sample, as it has reached the limit of the the probing depth of our laboratory-based XPS experiment which is approximately 10 nm (chapter 1). In the case of the thin NiO_X sample, the results presented in Figure 4.1 (C) reveal two distinct contributions: one originating from silicon and another from the silicon dioxide (SiO_2) species.[12]

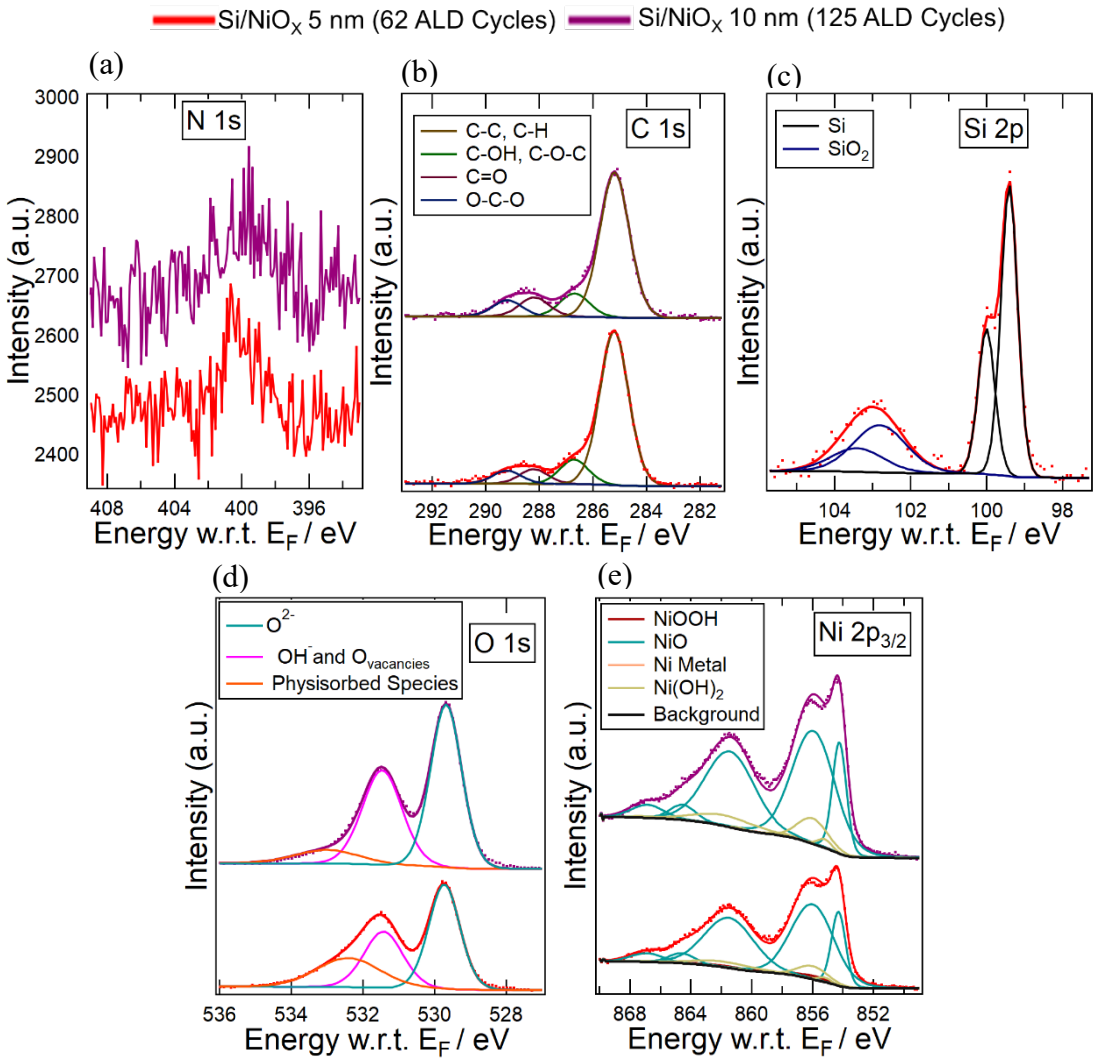

Figure 4.1. XPS spectra (Al-Kα 1486.7 eV) of 5 and 10nm ALD-NiO_X grown on Si wafer at 100°C (a) N 1s, (b) C 1s, (c) Si 2p, (d) O 1s and (e)Ni $2p_{3/2}$.

Furthermore, we study the Ni 2p and O 1s core levels to assess the surface chemical properties of ALD-NiO_X film. NiO_X films commonly exhibit multiple subspecies of the NiO_XH_Y formula, including NiO, $Ni(OH)_2$, NiOOH, and metallic nickel.[13,14] These subspecies, specifically $Ni(OH)_2$ and NiOOH, can exist in different phases, including, β-$Ni(OH)_2$, α-$Ni(OH)_2$, β-NiOOH, and γ-NiOOH.[15-20] The Ni 2p3/2 signal envelope in Figure 4.1(e) was analyzed using the method developed by Biesinger et al.[13], from which the Ni $2p_{3/2}$ signal from various NiO_XH_Y subspecies was decomposed into their theoretical shake-up structure from Gupta and Sen analysis.[19,20] This particular procedure is based on the identification of 34 distinct peaks including the shake-up structures, each corresponding to one of the four primary chemical states of $NiO_X(OH)_Y$ as described above. We decomposed the Ni $2p_{3/2}$ signal obtained from our samples based on the assumption that it would be a linear combination of individual signals from NiO, $Ni(OH)_2$, β-NiOOH and γ-NiOOH and metallic nickel. However, it's important to note that this assumption does not guarantee that the shake-up and plasmon loss structures for each phase in our samples mirror those of pure individual samples. Inelastic processes could potentially occur between photoelectrons and other atoms or molecules within the NiO_X structure[21], impacting the XPS signal, and these factors were not considered in our analysis.

By employing quantitative analysis on the Ni 2p3/2 peak represented in Table 4.1, we determined that the most significant contribution is the NiO phase, accounting for 83% and 85% of the total composition for the thin and thick NiO_X film, respectively. On the other hand, the $Ni(OH)_2$ and NiOOH phases were found to be present in relatively lower concentrations, constituting approximately 10-13% and 2-7% respectively. Notably, no traces of metallic nickel were detected within the ALD-NiO_X film. Few studies have provided evidence of the existence of $Ni(OH)_2$ and NiOOH species in NiO_X, which play a significant role in p-type doping and the improvement of hole transport properties in the material.[22,23] Nevertheless, it is important to note that high concentrations of these species can exhibit high reactivity and cause damage upon interaction with MHP films. For example, the Ni^{3+} species (i.e., NiOOH) in NiO_X can readily react with the halides present in the MHP, leading to the deterioration of the MHP film and the formation of numerous trap defects at the MHP/NiO_X interface.[22]

In the O 1s core level analysis, our investigation revealed three distinct contributions with binding energies measured at 529.6 eV, 531.5 eV, and 533 eV, respectively. These contributions were identified as O^{2-}, OH^-, $O_{vacancies}$ ($O_{vacancies}$ refer to the oxygen adjecent to Ni vacancy) and physisorbed species,[24,25] as visually depicted in Figure 4.2 (d). The O^{2-} peak primarily originates from the NiO phase, SiO_2 and minor contribution from the NiOOH phase. On the other hand, the OH^- peak corresponds to the $Ni(OH)_2$, NiOOH phases of ALD-NiO_X and adventitious carbon.

Composition	ALD NiO_X (5nm) Area(%)	ALD NiO_X (10nm) Area(%)
NiO	83	85
Ni metal	0	0
$Ni(OH)_2$	10	13
NiOOH	7	2

Table 4.1. Quantification of Ni $2p_{3/2}$ core level of 5 and 10nm ALD NiO_X grown on a silicon wafer.

4.3. Interface and surface study of MHP, PTAA and ALD-NiOx

In the previous section, we evaluated the surface chemical nature of the ALD grown NiO_X. In this section, we investigate the interface, surface study of the ALD-NiO_X grown on MHP and MHP/PTAA in a n-i-p architecture. The device architectures used in this study are comprised of glass-FTO-CBD-SnO_2-$FA_{0.7}Cs_{0.3}Pb(I_{0.9}Br_{0.1})_3$ MHP with and without a 20nm PTAA buffer layer, and ALD-NiO_X (see Figure 4.2).

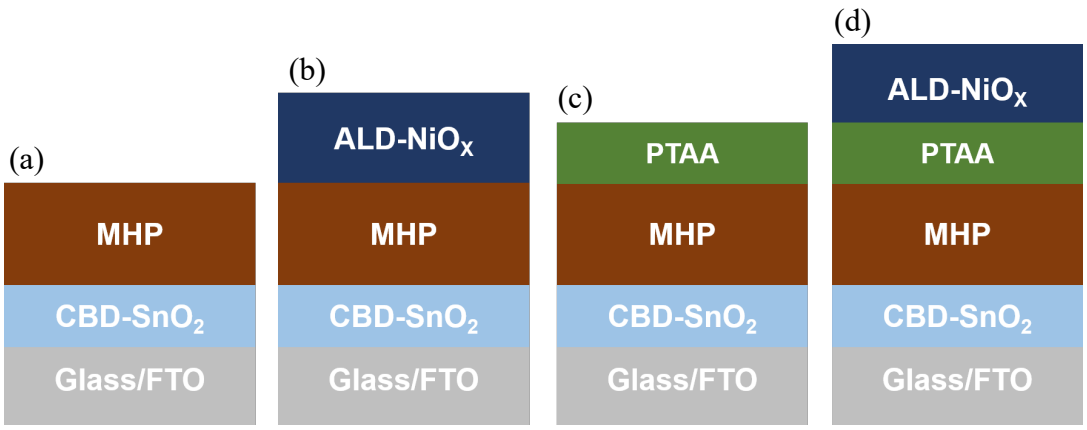

Figure 4.2. Schematic of different device architecture used in this section for interface study a) FTO/CBD-SnO_2/MHP, b) FTO/CBD-SnO_2/MHP/ALD-NiO_X, c) FTO/CBD-SnO_2/MHP/PTAA d) FTO/CBD-SnO2/MHP/PTAA/ALD-NiO_X.

4.3.1. Structural and Optical Properties

Figure 4.3(a) illustrates the XRD patterns of bare MHP film, with ALD-NiO_X, with PTAA, and with PTAA/ALD-NiO_X overlayers. The XRD signature with 2θ in the range of 10°–50° displays signals corresponding to different planes of the MHP bulk. The XRD signature of the MHP materials did not exhibit any change for the samples with the ALD-NiO_X overlayer in comparison with the reference MHP and MHP/PTAA samples. In the previous chapter with the ALD-SnO_2 overlayer, we observed the formation of PbI_2; however, we did not observe the formation of any such compounds in this case with the ALD-NiO_X overlayer (see the zoomed XRD pattern with 2θ in the range of 12-15° in Figure A6 in the Annex). This implies that the bulk structure of the MHP material remained unchanged after exposure to the ALD-NiO_X precursors at a temperature of 100°C.

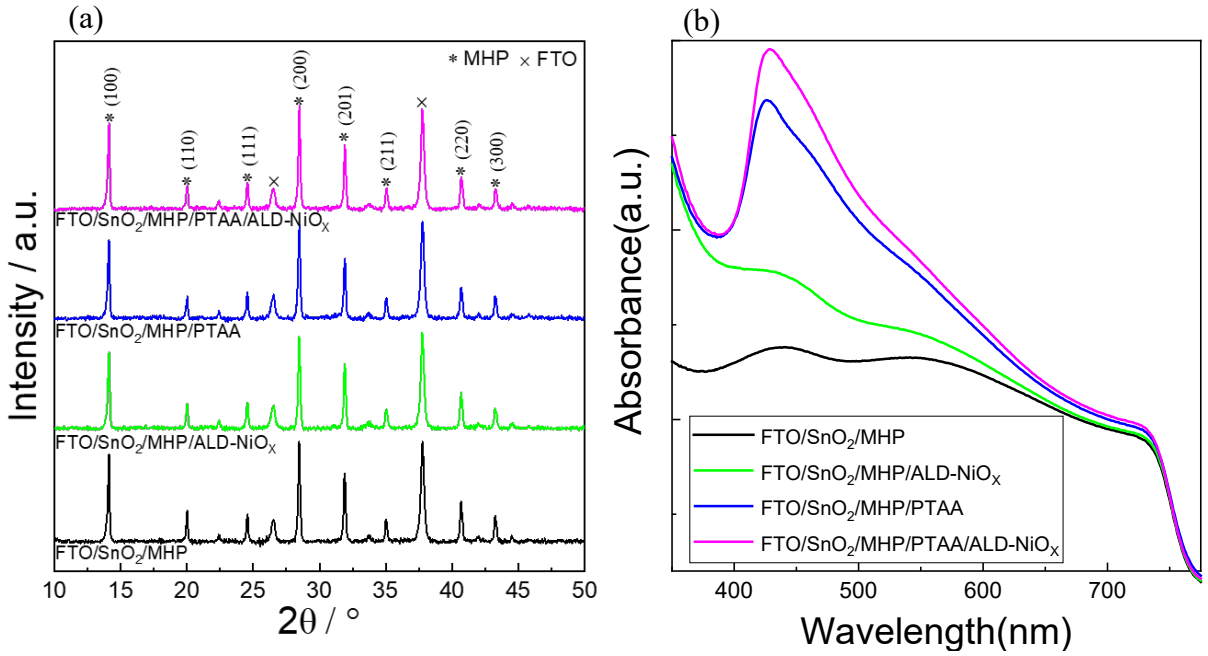

Figure 4.3. (a) XRD pattern of double cation MHP film with and without ALD-NiO_X, PTAA, PTAA/ALD-NiO_X top layers (b) UV-Vis absorption spectra of samples with and without ALD-NiO_X, PTAA, PTAA/ALD-NiO_X top layers.

The UV-Vis absorption spectra in Figure 4.3(b) show an increase in absorbance within the 400-700 nm wavelength range upon the addition of ultrathin PTAA (blue spectra) in reference to the MHP sample (black spectra). The increase in absorbance is likely due to the inherent absorption properties of the PTAA overlayer. Additionally, the MHP/NiO_X sample (green spectra) resulted in an increased absorbance ranging from 350-600 nm in comparison to absorbance of the bare MHP film. Given that the optical bandgap of ALD-NiO_X is approximately 3.9 eV (corresponding to 320 nm) (see Figure A7 in the Annex), we would not anticipate an absorbance increase for wavelengths beyond 320 nm with incorporation of ALD-NiO_X. The increase in absorbance suggests the emergence of new chemical defects that exhibit parasitic absorption in this range. Interestingly, we observed a

slight rise in absorbance in the range of 450-600 when comparing the MHP/PTAA (blue spectra) and MHP/PTAA/ALD-NiO_X (pink spectra) samples. This indicates that the PTAA layer acts as protective buffer layer, mitigating the interfacial defect formation. Alternatively, the ALD-NiO_X layer on PTAA might be thinner due to a lower growth rate on the PTAA surface compared to the MHP surface. Both hypotheses are further examined in the next sections of this chapter using XPS analysis.

4.3.2. Surface Morphology

We examined the morphologies of the MHP, MHP/ALD-NiO_X, MHP/PTAA, and MHP/PTAA/ALD-NiO_X samples using SEM, as shown in Figure 4.4. No noticeable changes were observed in the morphology of the MHP sample with the NiO_X overlayer when compared to the bare MHP film (Figure 4.4 (a) and (b)). In the MHP/PTAA samples, we observed several pinholes marked with red circles, exposing the MHP surface as the perovskite grains were clearly visible through the pinholes (Figure 4.4(c)).

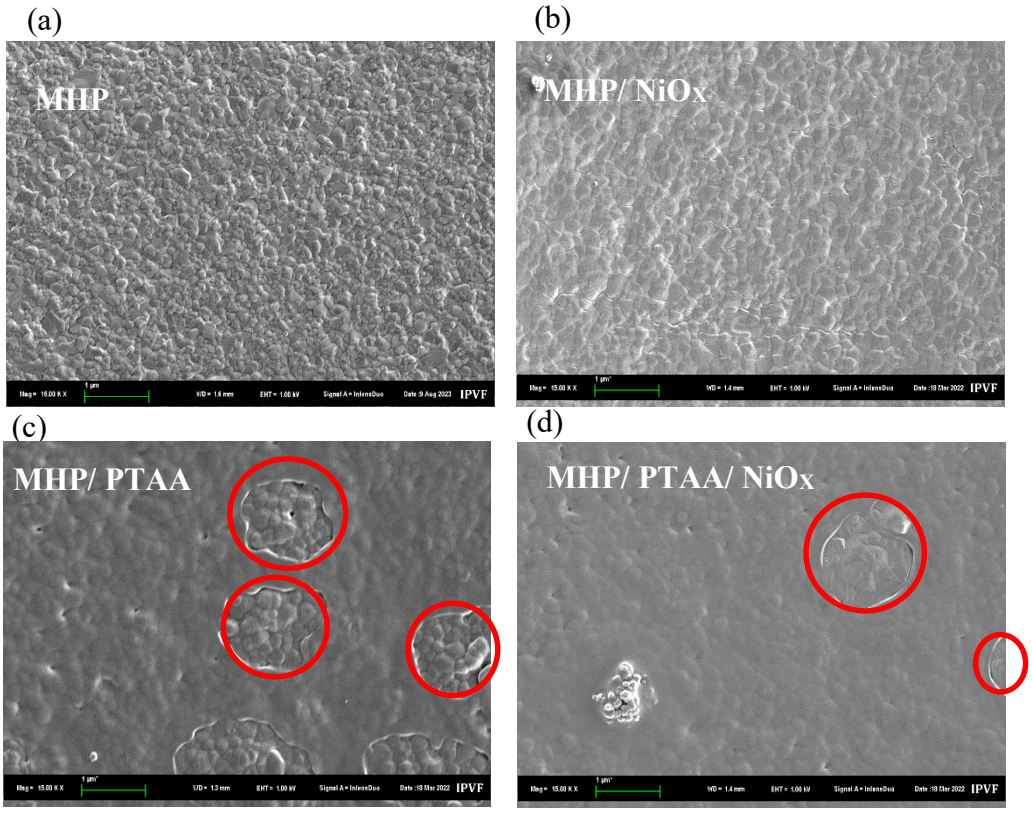

Figure 4.4. SEM images of (a) glass/FTO/CBD-SnO_2/MHP, (b) glass/FTO/CBD-SnO_2/MHP/ALD-NiO_X, (c) glass/FTO/CBD-SnO_2/MHP/PTAA and (d) glass/FTO/CBD-SnO_2/MHP/PTAA/ALD-NiO_X.

Pinholes are detrimental to device stability as they allow the diffusion of degrading ions, water, and oxygen into the perovskite.[26] The presence of pinholes in PTAA films has been reported in several studies and is explained in a review paper by Rombach et al.[27] Therefore, the PTAA buffer layer cannot completely mitigate unwanted interactions between the MHP and ALD precursors due to the presence of submicron-sized pinholes. Similarly, in the Figure 4.4(d) representation of the MHP/PTAA/ALD-NiO_X sample, we observed the presence of some pinholes originating from the PTAA film.

4.3.3. Surface and Interface Chemical Properties

This section dives into the in-depth surface and interface studies of MHP, MHP/ALD-NiO_X, MHP/PTAA, and MHP/PTAA/ALD-NiO_X by employing lab-based XPS and synchrotron-based HAXPES.

4.3.3.1 Lab based XPS analysis of MHP and MHP: ALD-NiO_X

Here, we analyze the various core levels of MHP and ALD-NiO_X using lab-based XPS with an excitation energy of 1486.7 eV to understand the chemical interaction of MHP and ALD precursors, the nature of ALD-oxide, and the interface between the MHP and ALD-NiO_X. The XPS spectra of the Cs $3d_{5/2}$, I $3d_{5/2}$, N 1s, Pb 4f, O 1s, and Ni $2p_{3/2}$ core level regions from the samples with bare MHP and after ALD NiO_X deposition of two different thicknesses which are produced by 62 ALD cycles (corresponding to a thin NiO_X film of 5 nm on Si) and 125 ALD cycles (corresponding to a thicker ALD NiO_X film of 10 nm on Si), respectively, are depicted in Figure 4.5.

The intensities of the various MHP core levels are normalized to maximum intensity for better data visualization. We do not observe any measurable change in the binding energies of Cs 3d and I 3d core levels after the deposition of ALD-NiO_X samples in comparison to the bare MHP as depicted in Table 4.3. The binding energy of the Pb 4f core level shifts to 200 meV to higher binding energy after ALD-NiO_X deposition (see Figure 4.6). Furthermore, we observed peak broadening of Pb 4f core level with an increase in FWHM value from 0.8 eV for pristine MHP film to 1 eV for both thicknesses of MHP/ALD-NiO_X samples. The alterations in binding energy and peak broadening of Pb 4f core level in comparison to pristine MHP indicates the formation of Pb species in a different chemical environment. A plausible candidate for this degradation product is the $PbBr_2$ which is also reported in literature as a degradation product of MHPs due to the interaction of the ALD precursors with the perovskite.[28] However, due to the minimal contribution of this new species, it is challenging to distinguish it from the primary MHP peak, and therefore, we did not assign a separate peak for this new contribution.

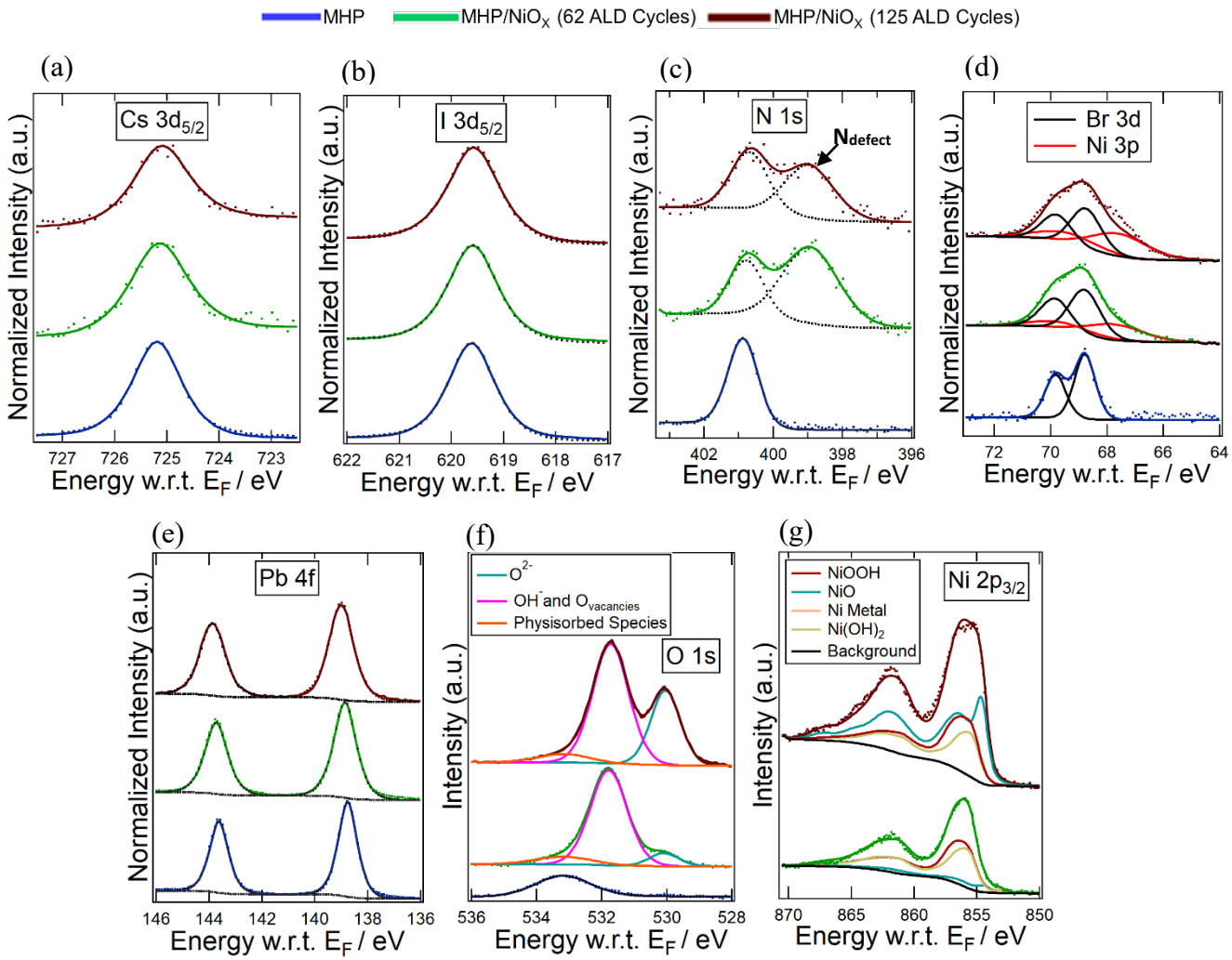

Figure 4.5. XPS spectra (Al-kα 1486.7 eV) of FTO/CBD-SnO_2/MHP (in blue colour), FTO/CBD-SnO_2/MHP/ALD-NiO_X 62 ALD cycles (in green colour) and FTO/CBD-SnO_2/MHP/ALD-NiO_X 125 ALD cycles (in brown colour) (a) Cs $3d_{5/2}$ (b) I $3d_{5/2}$ (c) N 1s (d) Br 3d, Ni 3p (e) Pb 4f (f) O 1s (g) Ni $2p_{3/2}$.

Furthermore, the Br 3d core level of the pristine MHP sample is positioned at 68.8 eV (Br $3d_{5/2}$) and 69.8 eV (Br $3d_{3/2}$) as shown in Figure 4.5 (d). For the NiO_X overlayer samples, we found that the Br 3d core-level data as the binding energy overlapped with the Ni 3p core-level data from ALD-NiO_X. To fit the Br 3d core levels for MHP MHP/ALD-NiO_X samples, we adopted an indirect approach. In this new approach, we first fitted the Ni 3p core level in this binding energy range (64-75 eV) for MHP/PTAA/ALD-NiO_X, where we did not detect any signal from the Br core levels as it was attenuated completely, which is, evident from the MHP/PTAA reference sample (see Figure A8 in the Annex). In the next step, we obtained the area ratio of Ni $3p_{3/2}$ and Ni $2p_{1/2}$ (ratio 0.025) from the MHP/PTAA/NiO_X sample and then applied this ratio to the MHP/NiO_X sample to obtain the intensity of the Ni $3p_{3/2}$ core level. Furthermore, we used the Ni 3p peak position of MHP/PTAA/NiO_X as a reference, applied it to the MHP/NiO_X sample, and shifted the peak by the

same distance difference in the Ni 2p core level of both samples. The Ni 3p core level for the MHP/NiO_X sample is positioned at 67.8 eV (Ni $3p_{3/2}$) and 69.6 eV (Ni $3p_{1/2}$) (see Figure 4.5 (d) red color peaks). For both thicknesses of the NiO_X sample set, we observed an increase in the peak width (FWHM:1.2) and intensity of the bromine contribution compared to that of the pristine MHP film (FWHM:0.9), which corroborates the previous hypothesis of the formation of $PbBr_2$. However, it is important to note that the nature of the NiO_X films is different for MHP and PTAA, as confirmed in the following sections. This, combined with the fact that the Ni 3p core levels are highly dependent on the exact chemical nature of the NiO_XH_Y layer, severely impeded the accurate identification and quantification of the Br 3d core level in the MHP film after ALD-NiO_X deposition. Consequently, we suspect that there is still a contribution from the Ni contribution in the Br 3d peaks, as we observed a two-fold increase in the peak intensity of the thick ALD-NiO_X compared to the thin ALD-NiO_X. Hence, we did not consider the Br core level in the quantification study.

Next, a closer look at the N 1s core level will reveal whether the organic cation in the perovskite, i.e. the FA+, sustained any changes upon the ALD-NiO_X overlayer deposition. Here, we find the emergence of a new nitrogen component (N_{defect}) with a peak centroid position at 398.9 eV and 399 eV for the 62 and 125 ALD cycles of MHP/ALD-NiO_X samples, respectively (Figure 4.5 (c)). The formation of a new chemical state of the nitrogen species at the MHP interface corroborates the occurrence of an interfacial chemical reaction between the ALD-NiO_X precursors and the MHP surface. Indeed, we found that the intensity of the N_{defect} contribution is lower for the thicker ALD NiO_X sample. This observation has important implications, as it indicates that the additional nitrogen contribution in the MHP/ALD-NiO_X sample is not just a by-product of the low-temperature ALD process; otherwise, the intensity of the N_{defect} contribution would have increased with increasing thickness, but instead it resulted from specific interfacial chemical reactions in this system. We suspect the chemical reaction could be between the nitrogen-containing $Ni(amd)_2$ precursor and the MHP film, resulting in the formation of new nitrogen-based chemically defective species at the interface. The N 1s peak positioned at 400.9 eV related to the FA species in MHP shifts by 100-200 meV to lower binding energy after NiO_X deposition due to changes in the local chemical environment with formation of defective interface such as new N_{defect} species.

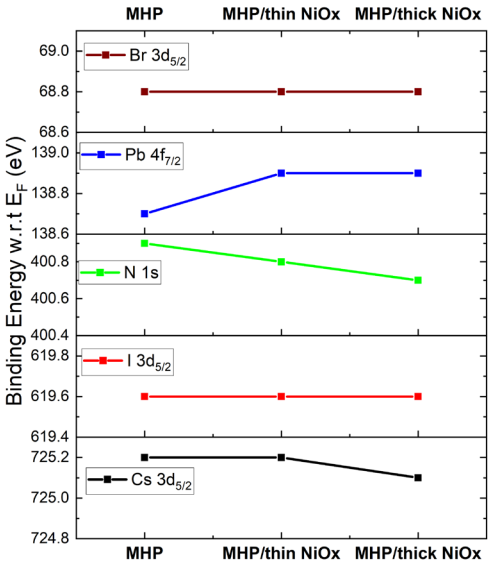

Figure 4.6. Illustration of binding energy of MHP core levels for MHP, MHP/thin-NiO_X, MHP/thick-NiO_X sample.

In order to evaluate the interfacial chemical reaction between MHP and ALD-NiO_X precursors in-depth, we tracked the stoichiometry ratio of I 3d, Pb 4f, N 1s, Cs 3d core levels before and after deposition of ALD NiO_X and compared these values with the theoretical stoichiometry as shown in Table 4.2 and Figure 4.7. The stoichiometric ratio indicated here is the ratio of the corrected intensity of each core level w.r.t transmission factor, inelastic mean free path (IMFP), relative sensitivity factors (R.S.F.) divided by the sum of the intensities of I 3d, Pb 4f, N 1s, Cs 3d core levels (refer to chapter 2 for detailed methodology). The stoichiometric ratio of the Pb 4f core level increased from 0.21 for the MHP sample to 0.37 for the sample with ALD-NiO_X overlayer. In N 1s core level, the peak related to FA species in MHP at 400.9 eV, we find severe nitrogen deficiency with a decrease in the composition ratio from 0.17 to 0.1 after ALD-NiO_X deposition. In part, the FA species deficiency is also related to the interfacial reaction causing degradation of FA and formation of N* species.

Furthermore, we observe severe Cs deficiency, where we found the concentration decreased to 0.02 for the MHP/ALD-NiO_X from the initial concentration of 0.05 for the pristine MHP sample. We also observe an 8% decrease in iodine concentration with NiO_X overlayer, i.e, 0.56 and 0.51 for MHP and MHP/ALD-NiO_X samples respectively. Collectively, we observed FA, Cs, I deficiency, and Pb surplus for MHP/ALD-NiO_X sample, which infers to interfacial chemical reactions and the formation of chemical defects. In addition, this decreased concentration the above-mentioned species and along with the increase in Pb concentration after ALD deposition supports the presence of a $PbBr_2$ species that has been hypothesized with binding energy shift and peak broadening. In consequence, this likely leads to increased interfacial charge recombination, which would impede carrier extraction and PSCs performance which we will probe later in this chapter.

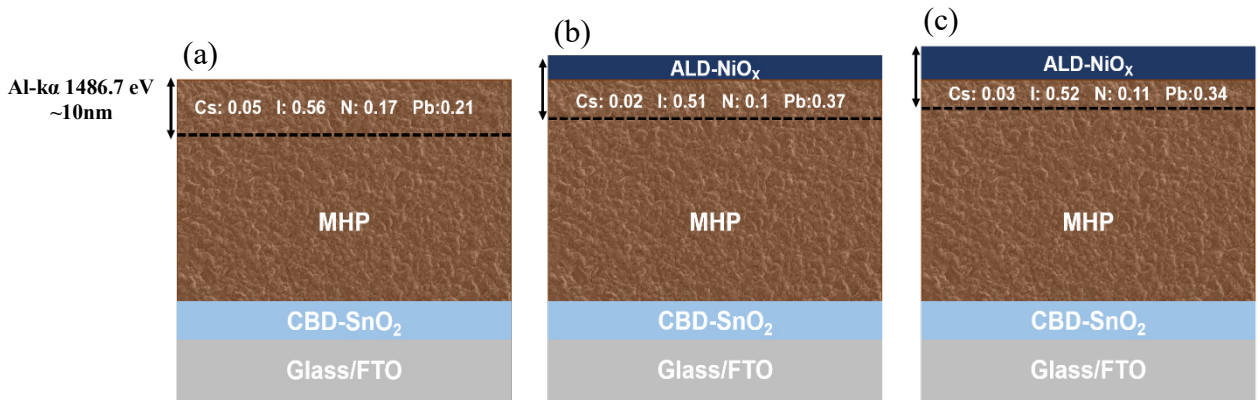

Figure 4.7. Schematic illustration summarizing the compositional gradient evolution of MHP composition using lab based XPS with excitation energy Al-kα 1486.7 eV (a) MHP (b) MHP/ALD-NiO_X (62 ALD cycles) (c) MHP/ALD-NiO_X (125 ALD.cycles).

	Theoretical	MHP	MHP:NiO_X (62 ALD Cycles)	MHP:NiO_X (125 ALD Cycles)
I $3d_{5/2}$	0.57	0.56	0.51	0.52
Pb $4f_{7/2}$	0.21	0.21	0.37	0.34
N 1s (FA species)	0.15	0.17	0.1	0.11
Cs $3d_{5/2}$	0.06	0.05	0.02	0.03
N_{defect} / N_{FA}	-	-	2.2	1.13

Table 4.2. Stochiometric ratios of I $3d_{5/2}$, Pb $4f_{7/2}$, N 1s, Cs $3d_{5/2}$ core levels of MHP, MHP/NiO_X (62 ALD Cycles), MHP/NiO_X (125 ALD Cycles).

The O 1s core level region, contains three distinct contributions as discussed earlier corresponding to O^{2-}, OH^-, and physisorbed species positioned at 530.1 eV, 531.8 eV, and 533.2 eV, respectively. We observed a high concentration of OH^- species corresponding to $Ni(OH)_2$ and NiOOH species and a small amount of NiO species linked to O^{2-} contribution. We observed an increase in the O^{2-} intensity peak with an increase in the thickness of ALD-NiO_X as shown in Figure 4.5 (f). We suspect that owing to the interfacial reaction and the surface properties of MHP, the initial NiO_X layer formed is predominately composed of $Ni(OH)_2$ and NiOOH species. Furthermore, after a certain thickness of NiO_X, film growth occurs on the already deposited NiO_X film, leading to the complete chemical conversion of ALD precursors, resulting in an increased concentration of NiO species. Additional confirmation of the observed trend for the O 1s core level was obtained using the Ni $2p_{3/2}$ core level, which aided in ruling out the possibility of any errors resulting from potential sample contamination that give rise to additional contributions in the O1s core level measurement. The fitting of Ni 2p3/2 was accomplished using the methodology outlined in Section 4.1.2, and

Figure 4.5(g) displays the envelope for each subspecies of NiO_X, encompassing NiO, $Ni(OH)_2$, Ni metal and NiOOH. Upon quantifying the Ni $2p_{3/2}$ core level contribution, we found the concentration of NiO is only 8% for the thin ALD NiO_X film which is almost 10 times lower than the concentration of NiO present in NiO_X film grown in the same ALD deposition run on a silicon wafer (see Table 4.5).

Sample		**MHP**		**MHP/NiO_X**			
Excitation energy				62 ALD Cycles		125 ALD Cycles	
		Position (eV)	FWHM (eV)	Position (eV)	FWHM (eV)	Position (eV)	FWHM (eV)
Cs $3d_{5/2}$		725.2	1.1	725.2	1.2	725.1	1.2
N 1s	MHP	400.9	1	400.8	1.1	400.7	1.1
	2nd	-	-	398.9	1.8	399	1.8
Pb $4f_{7/2}$		138.7	0.8	138.9	1	138.9	1
I $3d_{5/2}$		619.6	1	619.6	1.1	619.6	1.1
Br $3d_{5/2}$		68.8	0.9	68.8	1.2	68.8	1.2
NiO_X	NiO	-	-	854.4	1	854.7	1
	α-$Ni(OH)_2$	-	-	855.4	1.1	855.2	1.1
	γ-NiOOH	-	-	855.5	1.5	855.6	1.5
	β-NiOOH(3+)	-	-	855.3	1.5	855.6	1.5
	β-NiOOH(2+)	-	-	855.5	1.1	855.4	1.1
O 1s	O^{2-}	-	-	530.1	1.1	530	1.1
	$-OH^-$ and $O_{vaccancies}$	-	-	531.8	1.3	531.7	1.3
	Physisorbed Species	533.2	2	533.2	2	533.2	2

Table 4.3. XPS Peak position and FWHM of Cs $3d_{5/2}$, N 1s, Pb 4f, I $3d_{5/2}$, Br $3d_{5/2}$ O 1s and Ni 2p3/2 core levels for FTO/CBD-SnO2/MHP, FTO/CBD-SnO2/MHP/ALD-NiO_X 62 ALD cycles and FTO/CBD-SnO2/MHP/ALD-NiO_X 125 ALD cycles samples. Ni $2p_{3/2}$ core level representing peaks originating from NiO_X films which exhibited multiple subspecies of the NiO_XH_Y formula, including NiO, $Ni(OH)_2$, NiOOH.

The thin NiO_X film, mainly consisted of $Ni(OH)_2$ and NiOOH species, as observed from the Ni 2p core level. Additionally, we found that the NiO concentration in the MHP/NiO_X sample increased from 8% to 50% with an increase in the thickness of the ALD NiO_X film (in Table 4.5.) corroborating the trend observed for the evolution of the O 1s core level. The increase in NiO concentration and decrease of the other NiO_xH_y components with thicker NiO_X films suggest highly defective NiO_X film formation during the initial growth of the MHP. To limit the interfacial reactions, we investigated the use of an organic PTAA buffer layer to protect the MHP from reaction with the ALD precursors, which is discussed next.

4.3.3.2 Lab based XPS analysis of MHP: PTAA and MHP: PTAA: ALD-NiO_X

The XPS spectra of the N 1s, Pb 4f, O 1s, and Ni $2p_{3/2}$ core level regions from the samples MHP/PTAA and PTAA/NiO_X deposition of two different thickness which corresponds to 62 ALD cycles (thin NiO_X film) and 125 ALD cycles (thick ALD NiO_X film) are depicted in Figure 4.8. Given that the probing depth of the LabXPS is approximately 10 nm, it is unlikely to detect any signal from MHP Core levels due to the presence of a 20 nm thick PTAA buffer layer. Nonetheless, we are able to detect a weak and noisy signal originating from the I 3d and Pb 4f core level through the pin-holes in PTAA film (discussed earlier in this chapter in section 4.3.2). Note that the evaluation of MHP core levels is restricted to qualitative assessments only, due to the extremely low signal-to-noise ratio. No quantitative analysis is performed in this context. However, in the following section dedicated to HAPXES analysis, we will present quantitative data, as it provides us with better data quality for our study.

The N 1s core level in the MHP/PTAA sample is located at 400.3 eV, corresponding to the triaryl amine compound present in PTAA. It's important to note that we do not detect any nitrogen signal from the FA species of MHP film because the PTAA layer attenuates these signals. Even if we potentially detect signals through pinholes in the PTAA film, distinguishing it is challenging due to the low signal-to-noise ratio. After ALD NiO_X deposition the N 1s peak shifts to the higher binding energy of 400.6 eV, while the peak width remains unchanged with an FWHM value of 1.1 eV as shown in Figure 4.8(b). The I 3d core level shifted by 500 and 600 meV to a higher binding energy for the thin and thick NiO_X samples, respectively, compared to the MHP/PTAA sample (see Figure 4.8(a)). Furthermore, the Pb 4f core level is shifted 1 eV to a higher binding energy and broadening of the peak from 1.2 to 1.6 eV upon incorporation of the ALD overlayer. This could be related to the interaction between MHP and ALD precursors though the pinholes.

Figure 4.8 (d) shows the O 1s core level of the MHP/PTAA sample with and without NiO_X overlayer. In the acquired O 1s spectra of bare MHP/PTAA, we observe a peak at 533.2 eV corresponding to oxygen species in the LiTFSi dopant of PTAA and physisorbed species. Furthermore, with the addition of the NiO_X, we observe two new peaks at 530.5 and 532.2 eV corresponding to O^{2-} (NiO) and OH^- (hydroxide, oxy-hydroxide) species, respectively. We found that the intensity of O^{2-} species is higher than the concentration of OH^- species which implies the presence of a higher concentration of NiO in comparison to the $Ni(OH)_2$ and NiOOH in the ALD-NiO_X film. The contributions of different NiO_X species are further evaluated using the Ni $2p_{3/2}$ core level.

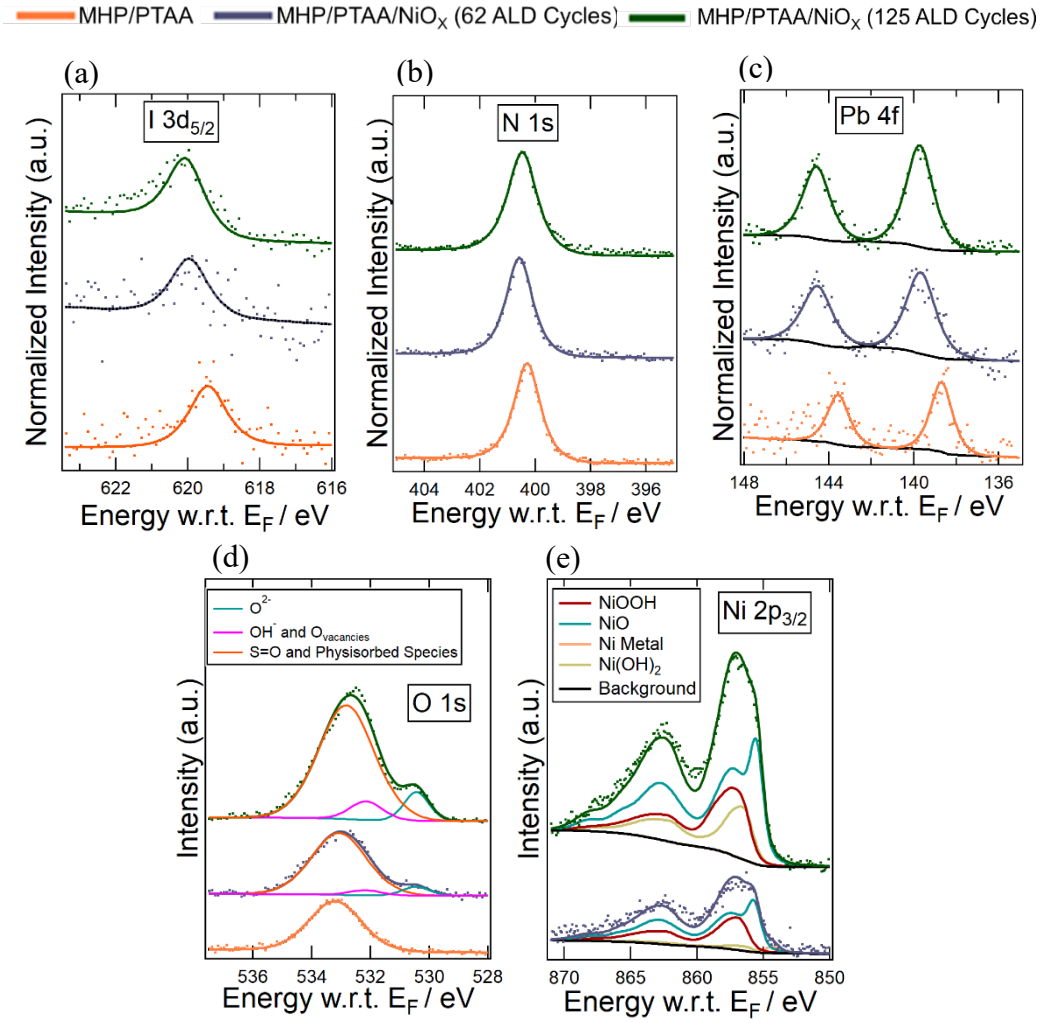

Figure 4.8. XPS spectra (Al-Kα 1486.7 eV) of FTO/CBD-SnO_2/MHP/PTAA (in orange color), FTO/CBD-SnO_2/MHP/PTAA/ALD-NiO_X 62 ALD cycles (in light-blue color) and FTO/CBD-SnO_2/MHP/PTAA/ALD-NiO_X 125 ALD cycles (in dark-green color) (a) I $3d_{5/2}$ (b) N 1s (c) Pb 4f (d) O 1s (d) Ni $2p_{3/2}$.

Sample		MHP/PTAA		MHP/PTAA/NiO_X			
Excitation energy				62 ALD Cycles		125 ALD Cycles	
		Position (eV)	FWHM (eV)	Position (eV)	FWHM (eV)	Position (eV)	FWHM (eV)
N 1s		400.3	1.1	400.6	1.1	400.5	1.1
Pb $4f_{7/2}$		138.7	1.2	139.7	1.6	139.7	1.5
I $3d_{5/2}$		619.4	1.2	619.9	1.2	620	1.2
NiO_X	NiO	-	-	855.7	1.1	855.5	1.1
	α-$Ni(OH)_2$	-	-	856.2	1.1	856.2	1.1
	γ-NiOOH	-	-	856.4	1.4	856.9	1.5
	β-NiOOH(3+)	-	-	856.9	1.5	856.9	1.5
	β-NiOOH(2+)	-	-	856.6	1.1	856.4	1.1
O 1s	O^{2-}	-	-	530.5	1.1	530.4	1.1
	$-OH^-$ and $O_{vaccancies}$	-	-	532.2	1.3	532.1	1.3
	Physisorbed Species	533.2	2.1	533.1	2.2	532.8	2.2

Table 4.4. XPS peak position and FWHM of N 1s, Pb 4f, O 1s and Ni 2p3/2 core levels for FTO/CBD-SnO_2/MHP/PTAA, FTO/CBD-SnO_2/MHP/PTAA/ALD-NiO_X (62 ALD cycles), and FTO/CBD-SnO_2/MHP/PTAA/ALD-NiO_X (125 ALD cycles) samples.

The Ni $2p_{3/2}$ core level contains four major contributions i.e.; NiO, $Ni(OH)_2$, NiOOH, and Ni metal as shown in Figure 4.8 (e) as discussed earlier in the section 4.2. Upon quantifying the Ni $2p_{3/2}$ core level, we found a high concentration of NiO i.e.; 61% and 53% for the sample with a thin and thick NiO_X overlayer, respectively as shown in Table 4.5. The PTAA buffer layer limits the interaction between the sensitive MHP film and ALD precursors; however, it does not completely mitigate the interaction owing to the pinhole in the PTAA film. In addition, the ALD-NiO_X grown on PTAA comprised a high percentage of NiO, closely matched the chemistry of the NiO_X film grown on Si, and could function as a suitable HTL for PSCs. In the following section, we will investigate the MHP surface and subsurface region using synchrotron-based HAXPES with different photon energies, similar to the study presented in Chapter 3. The objective of this study is to explore a buried interface and obtain information about a deeper surface region of the interface. Furthermore, we aim to track any potential band-bending due to the interfacial chemical defects originating from ALD process.

Composition	MHP:NiO_X 62 ALD Cycles	MHP:NiO_X 125 ALD Cycles	MHP:PTAA:NiO_X 62 ALD Cycles	MHP:PTAA:NiO_X 125 ALD Cycles
NiO	8	56	61	53
Ni metal	1	0	2	0
$Ni(OH)_2$	42	30	4	19
NiOOH	49	14	33	28

Table 4.5. Quantification of ALD-NiO_X film utilizing Ni $2p_{3/2}$ fitting that includes NiO, $Ni(OH)_2$, NiOOH, and metallic nickel contribution on MHP and MHP/PTAA sample.

4.3.4. Synchrotron-based HAXPES Study

HAXPES measurements were conducted at the HiKE endstation located at the BESSY II KMC-1 beamline at Helmholtz-Zentrum Berlin (HZB), using photon energies of 2 keV and 6 keV. These photon energies correspond to probing depths of 11 and 25 nm, respectively (described in Chapters 2 and 3). In this section, we elaborate on the interface study of ALD-NiO_X on MHP with and without a PTAA buffer layer at photon energies of 2 keV and 6 keV.

4.3.4.1. Hard X-ray Stability of MHP

To mitigate beam damage, a beryllium filter is used during sample measurements, which effectively reduces the 2 keV photon flux by 75% and the 6 keV photon flux by 10% of their unfiltered values to reduce beam damage (refer to Chapter 2, Subsection 2.3.5). However, even with this precaution, prolonged exposure to hard X-rays can damage the MHP sample. Consequently, we conducted a comprehensive study of beam damage using a Be filter. The approach involved exposing the pristine MHP film to hard X-rays at the same spot for three sweeps while tracking the various MHP core levels.

Our primary objective in this study was to investigate the evolution of the Cs $3d_{5/2}$, I $3d_{5/2}$, N 1s, and Pb 4f core levels in pristine MHP samples. To achieve this, we conducted measurement sweeps using photon energies of 2 keV and 6 keV for each of these core levels, with each measurement sweep lasting approximately 2–3 hours. We performed three consecutive sweeps, exposing the same spot to intense hard X-rays (passing through the Be filter) for a cumulative duration of approximately 8 hours.

Our investigations found that intense hard X-rays did not cause any changes in the peak position or peak width at either 2 keV or 6 keV photon energies as demonstrated in Figure 4.9 (a-h). Additionally, it is important to note that during our measurement sweeps, we encountered no instances of binding energy shifts or peak broadening. This consistent behaviour across successive sweeps further reinforces the remarkable stability within these core levels, even under prolonged hard X-ray exposure. In summary, this study confirms the inherent stability and resilience of pristine MHP films subjected to extended hard X-ray conditions.

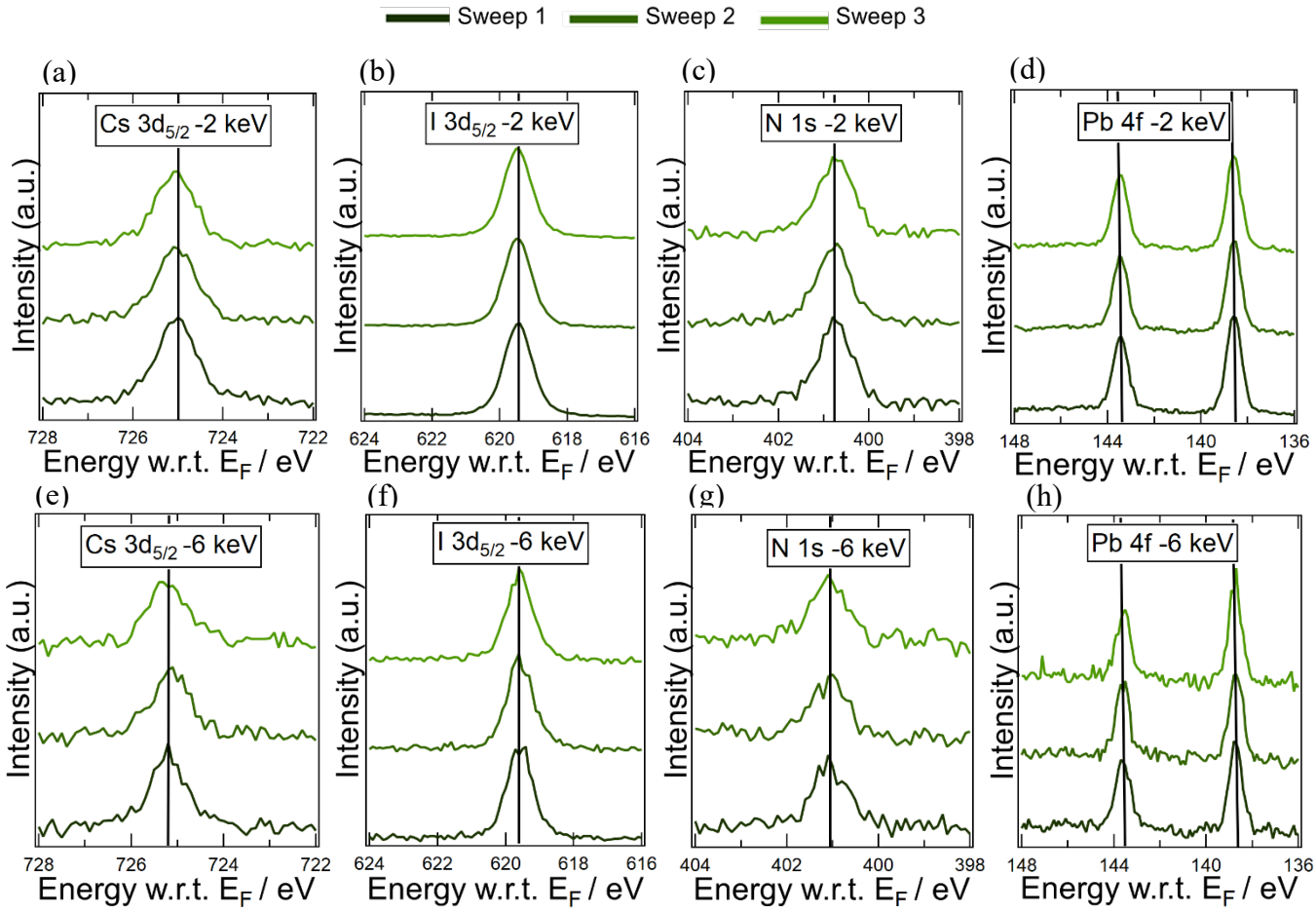

Figure 4.9. HAXPES Spectra of different core levels (a) Cs $3d_{5/2}$ 2 keV (b) I $3d_{5/2}$ 2 keV (c) N 1s 2 keV (d) Pb 4f 2 keV (e) Cs $3d_{5/2}$ 6 keV (f) I $3d_{5/2}$ 6 keV (g) N 1s 6 keV (h) Pb 4f 6 keV with 3 sweeps on the same spot of FTO/CBD-SnO_2/MHP. Each core level graph represents three sweeps color coded from dark to light green.

4.3.4.2 HAXPES analysis of MHP and MHP: ALD-NiOx

The HAXPES spectra of the Cs $3d_{5/2}$, N 1s, Pb 4f, and I 3d core level regions from the samples with bare MHP and after ALD NiO_X (62 ALD cycles) deposition are depicted in Figure 4.10. The intensities of the MHP core levels are normalized to maximum intensity for better data visualizations. The I 3d, Pb 4f and Cs 3d core level signals of pristine MHP show a minor shift in peak position of 100 meV between the data acquired for photon energies of 2 keV and 6 keV respectively (see Table 4.7). Considering the spectral resolution of our HAXPES experiment is approximately 100 meV, we do not consider a shift of this order of magnitude significant.

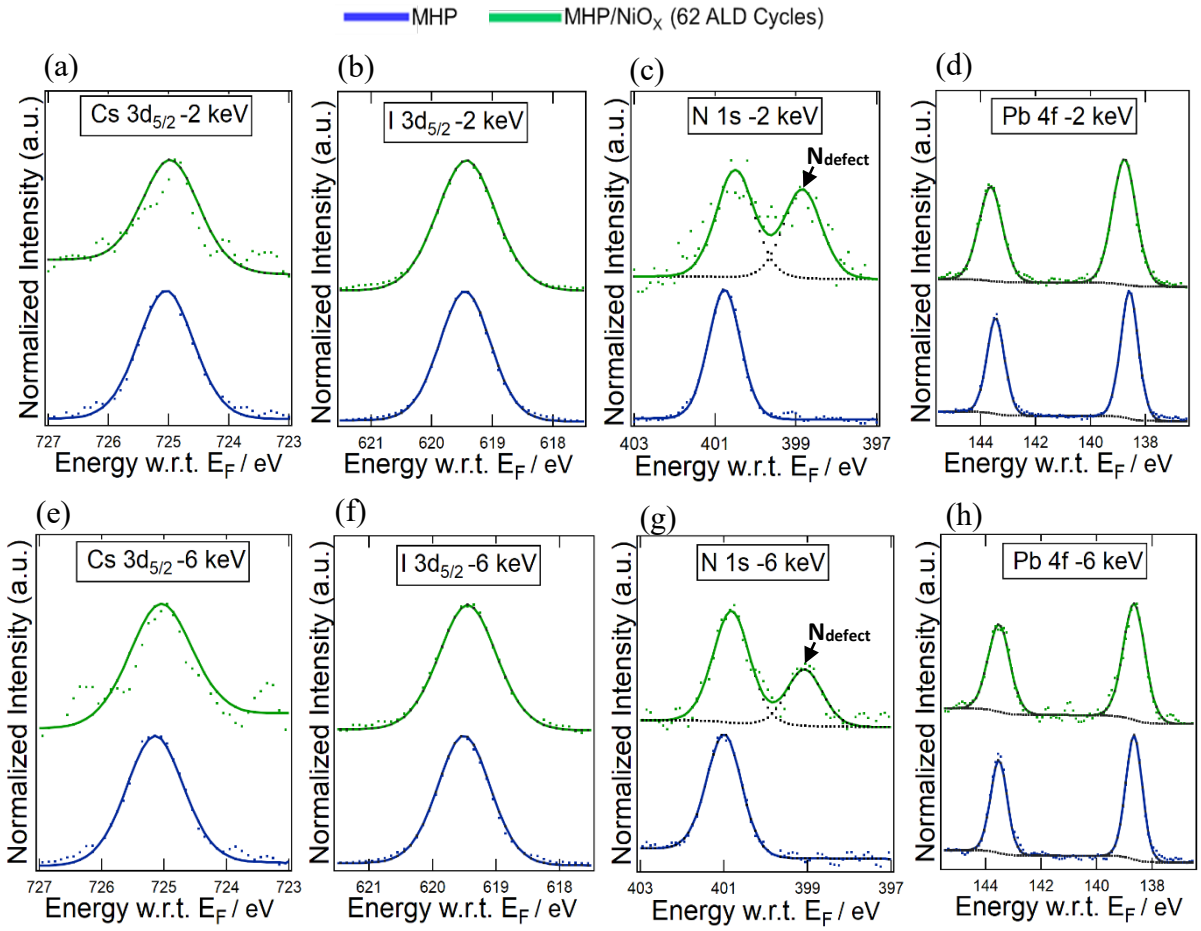

Figure 4.10. (a-h) HAXPES detail spectra (include fit analysis of some core levels) of Cs $3d_{5/2}$, I $3d_{5/2}$, N 1s, and Pb 4f of double cation MHP without (blue spectra) and with (green spectra) ALD NiO_X top layers recorded with 2 and 6 keV excitation energy using Be filter.

After NiO_X deposition, we do not observe any change in peak position and width for I $3d_{5/2}$ and Cs $3d_{5/2}$ core levels at both 2 and 6 keV photon energies with respect to bare MHP film (Figure 4.10 and Table 4.7). The Pb 4f core level shifts to higher binding energy of 200 meV after NiO_X deposition from 138.6 eV to 138.8 eV at 2 keV photon energy, whereas, the core level is still located at 138.6 eV for 6 keV photon energy (see Figure 4.11). Additionally, we observed the Pb 4f peak broadening to a FWHM of 1 and 0.9 eV under 2 and 6 keV excitation energies for the sample NiO_X overlayer with reference to bare MHP film (FWHM value of 0.7). The core level shift and peak broadening at 2 keV indicates formation of $PbBr_2$ at the interface and this observation is coherent with our previous lab based XPS analysis. Additionally, the absence of changes in the Pb 4f core-level peak position at 6 keV in comparison to pristine MHP implies that the chemical defect is localized primarily to the interfacial region, likely in low concentration. Furthermore, the Br 3d core-level spectra exhibited a low signal-to-noise ratio; therefore, it is not included in the analysis here (see Figure A11 in the Annex).

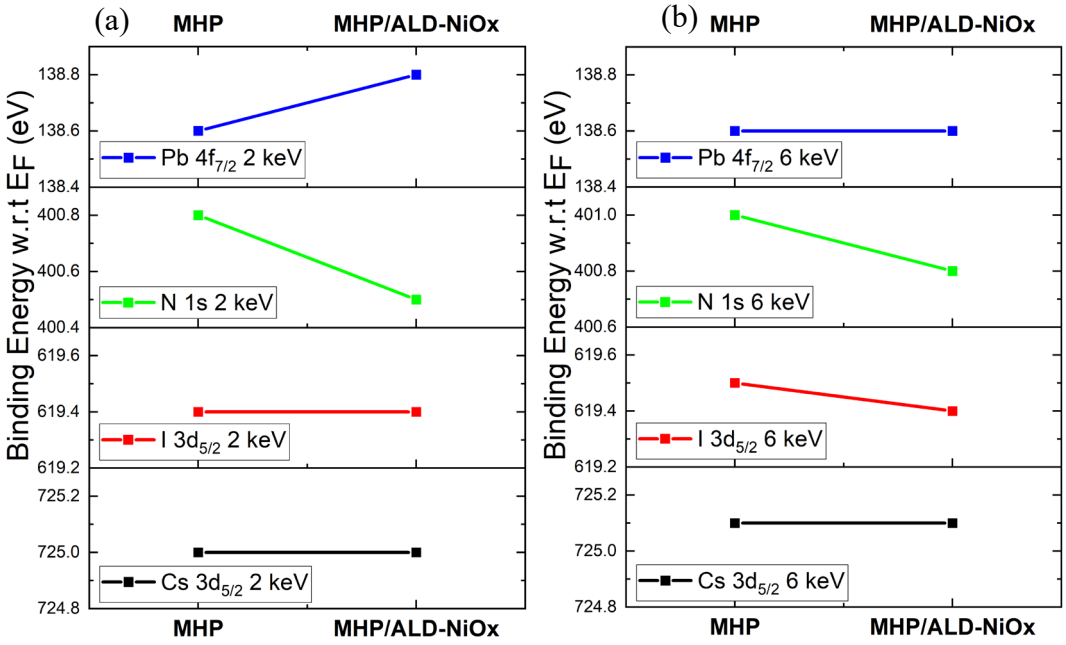

Figure 4.11. Illustration of binding energy of MHP core levels for MHP, MHP/ALD-NiO_X (62 ALD Cycles) recorded at (a) 2 keV excitation energy (b) 6 keV excitation energy using Be filter.

In the N 1s core level, we observed a new nitrogen peak (N_{defect}) at 398.8 and 399 eV at photon energies of 2 and 6 keV, respectively. The intensity of the N_{defect} peak decreased when we moved the photon energy from 2 keV to 6 keV (N_{defect}/N_{FA} ratio of 0.82 and 0.5 at 2 and 6 keV respectively), which indicates that these defective species are confined to the interface region. The N 1s peak, located at 400.8 and 401 eV energy levels at 2 and 6 keV photon energies, respectively, corresponds to the FA species within MHP. Following the deposition of NiO_X, this peak shifts by 300 meV

towards lower binding energy due to alterations in the surrounding chemical environment at the interface. Furthermore, a quantitative approach is implemented to study the interfacial reactions and its effect on the stoichiometry of MHP film after incorporation ALD-NiO_X overlayer. Previously, in section 4.3.3.1, we have already discussed similar approach to quantify the lab XPS data. Herein, we have the added advantage of high energy photon energies to estimate the extent of damage in the buried subsurface region of the MHP film.

The quantitative ratios of I $3d_{5/2}$, Pb $4f_{7/2}$, N 1s, Cs $3d_{5/2}$ core levels with and without NiO_X overlayer are shown in Table 4.6 and Figure 4.12. The stoichiometric ratio of iodine of the MHP samples is 0.58 and 0.55 at 2 and 6 keV, respectively. The disparity in the ratio indicates that the surface is iodine rich whereas the sub-surface region is slightly iodine deficient. After deposition of the NiO_X overlayer, we found a slight iodine deficiency in both the surface and subsurface regions with the ratio dropping down to 0.53 at 2 and 6 keV. Similarly, slight deficiency is also found in the nitrogen component corresponding FA species at 401 eV, where the ratio decreased from 0.17 (for MHP sample) to 0.15 (MHP/NiO_X sample) under both photon energies. This trend is also observed for cesium, where the stoichiometry ratio decreased by 60% (from 0.05 to 0.02) and 33% (from 0.06 to 0.04) at 2 and 6 keV excitation respectively with addition of the ALD overlayer. Following the ALD NiO_X deposition at 2 keV, there was a significant increase in the compositional ratio of Pb, rising from 0.2 to 0.31; furthermore, at 6 keV photon energy, an increase from 0.22 to 0.27 was also observed in this core level, indicating a Pb surplus.

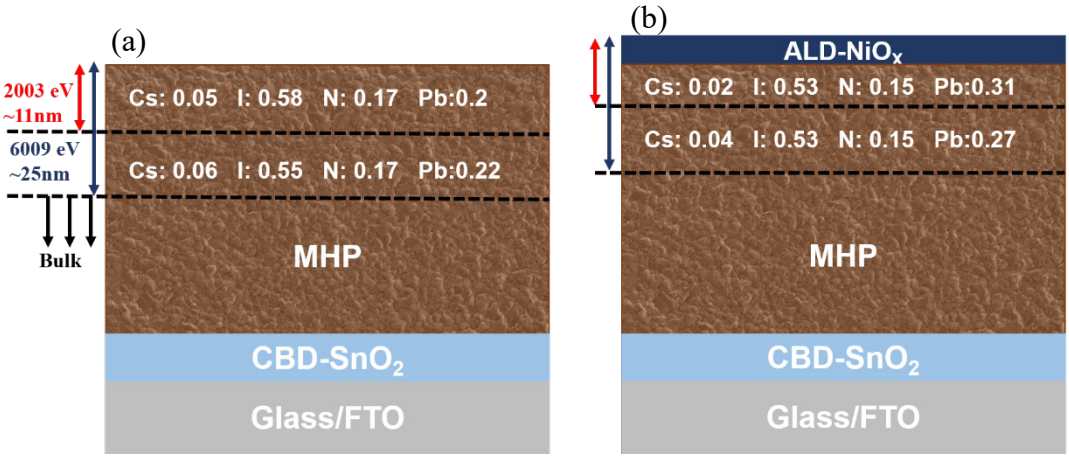

Figure 4.12. Schematic illustration summarizing the compositional gradient evolution of MHP composition using synchrotron-based HAXPES with excitation energy 2 and 6 keV (a) MHP (b) MHP/ALD-NiO_X (62 ALD cycles).

In summary, we observed deficiencies in iodine, cesium, and nitrogen, along with an excess of lead in the MHP/ALD-NiO_X system. These observations confirm the presence of interfacial reactions between the ALD precursors and MHP, resulting in the formation of defective interfaces. It is probable that the initial few nanometers of the ALD-NiO_X film contained a mixture of various species originating from undesired chemical reactions. Moreover, in our quantification study, we found that changes in composition were also evident at an excitation energy of 6 keV for the MHP/NiO_X sample, indicating that the damage to the MHP film might have propagated to the deeper interfacial region.

Core levels		Theoretical	MHP	MHP:NiO_X (62 ALD Cycles)
I $3d_{5/2}$	2 keV	0.57	0.58	0.53
	6 keV	0.57	0.55	0.53
Pb $4f_{7/2}$	2 keV	0.21	0.20	0.31
	6 keV	0.21	0.22	0.27
N 1s	2 keV	0.15	0.17	0.15
	6 keV	0.15	0.17	0.15
Cs $3d_{5/2}$	2 keV	0.06	0.05	0.02
	6 keV	0.06	0.06	0.04
N_{defect}/N_{FA}	2 keV	-	-	0.82
	6 keV	-	-	0.5

Table 4.6. Stoichiometric ratios of I $3d_{5/2}$, Pb $4f_{7/2}$, N 1s, Cs $3d_{5/2}$ core levels of MHP and MHP/NiO_X (62 ALD Cycles) under 2 and 6 keV excitation energies.

The nature of ALD-NiO_X film is investigated by tracking the Ni 2p and O 1s core levels as shown in Figure 4.13**.** In the O 1s core level with three distinct contributions as discussed earlier corresponding to O^{2-}, OH^-, and physisorbed species. Herein, we found high concentration OH peak contribution both at 2 and 6 keV excitations that confirm our previous XPS study finding. We focus on the quantitative analysis of Ni 2p peak for accurate estimation of the various contributions in NiO_X film. The Ni $2p_{3/2}$ core level with the contributions corresponding to NiO, $Ni(OH)_2$, NiOOH, and Ni metal at 2 and 6 keV represented in Figure 4.13 (b), (d) and Table 4.8. Upon quantification, we found that the NiO contributions were 56% and 38% at 2 and 6 keV, respectively. The low concentration of NiO at 6 keV excitation energy, which provides an enhanced signal from the buried parts of the layer, confirms our previous hypothesis put forward in the labXPS study that the initial NiO_X growth on MHP mainly contains hydroxide (17%) and oxy-hydroxide (43%) species due to partial conversion of ALD precursors and interfacial reaction.

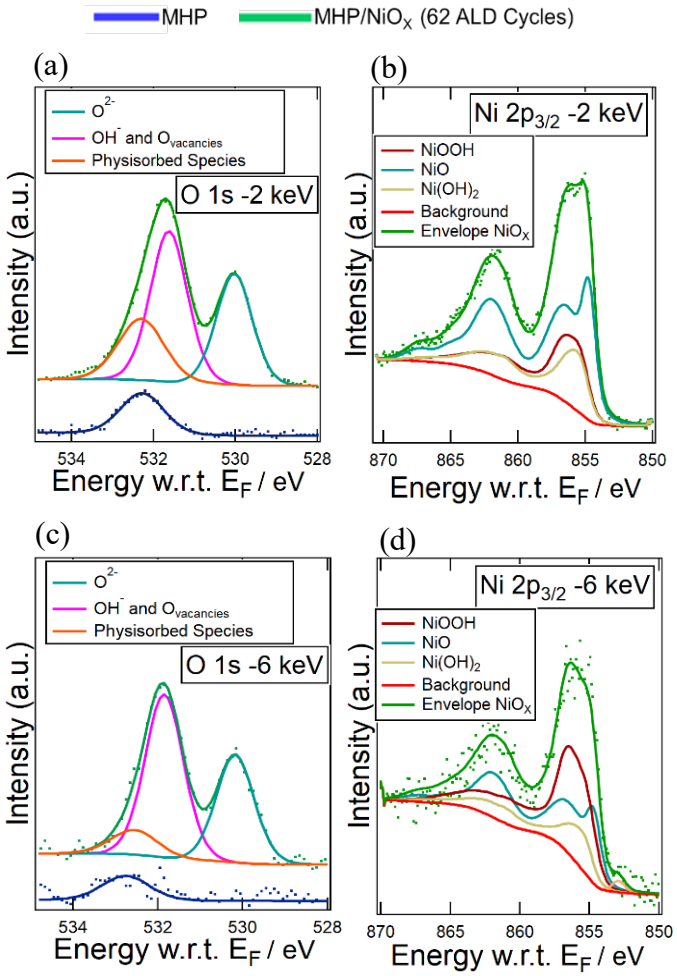

Figure 4.13. (a-d) HAXPES detail spectra (include fit analysis of some core levels) of O 1s, and Ni $2p_{3/2}$ of double cation MHP without (blue spectra) and with (green spectra) ALD NiO_X top layers recorded with 2 and 6 keV excitation energy using Be filter.

A discrepancy emerged between the LabXPS and HAXPES data regarding the quantification of the Ni 2p3/2 core level in the NiO_X film. It is important to note that for the LabXPS and HAXPES experiments, samples were produced in separate batches at different times. In the LabXPS analysis, we found that only 8% NiO was present in the MHP/NiO_X film (62 ALD cycles), whereas the concentration was 56% in HAXPES for the same number of ALD cycles. We suspected that the thickness of the NiO_X overlayer was different in both the experiments. As discussed earlier, the thickness of 62 ALD cycles of the NiO_X recipe corresponded to 5 nm when grown on a silicon wafer. Furthermore, we previously established that the thickness can differ depending on the surface chemistry of the substrates. To determine whether there is a thickness reproducibility issue of ALD-NiO_X when grown on MHP, we estimated the overlayer thickness using the following expression:

$$d = -\lambda \ln\left(\frac{I}{I_0}\right) \qquad \text{Equation 4.1}$$

In Equation 4.1, d represents the thickness of the overlayer, λ denotes the IMFP at a given kinetic energy in the overlayer, I signifies the intensity of the core level with the overlayer (core level of an element of the substrate), and I_0 is the intensity of the core level without the overlayer. To estimate the thickness, we relied on the I $3d_{5/2}$ core level of the MHP for both the datasets. We found that the MHP/NiO_X (62 ALD cycles) samples used in LabXPS experiment measured 1.3 nm, whereas the samples used in HAXPES experiment measured 4 nm. This discrepancy suggests inconsistent ALD growth on the MHP film across different ALD runs, despite our ability to consistently reproduce the growth on a silicon wafer. However, it is important to note that the calculations for overlayer thickness are based on the assumption that the underlying layer remains constant. In our case, the MHP interface underwent changes owing to the formation of interfacial chemical defects. Therefore, there is a potential for error in the ALD-NiO_X thickness estimation. However, the ratio of thickness between the two sample sets (XPS and HAXPES experiments) will remain unaffected, assuming a comparable margin of error in the thickness estimation.

Sample		**MHP**				**MHP/NiO_X**			
Excitation energy		2003 eV		6009 eV		2003 eV		6009 eV	
		Position (eV)	FWHM (eV)	Position (eV)	FWHM (eV)	Position (eV)	FWHM (eV)	Position (eV)	FWHM (eV)
Cs $3d_{5/2}$		725	1.1	725.1	1.1	725	1.1	725.1	1.1
N 1s	MHP	400.8	0.9	401	1	400.5	1.1	400.8	1
	2^{nd}	-	-	-	-	398.8	1.1	399	1
Pb $4f_{7/2}$		138.6	0.7	138.6	0.7	138.8	1	138.6	0.9
I $3d_{5/2}$		619.4	1	619.5	1	619.4	1.1	619.4	1.1
NiO_X	NiO	-	-	-	-	854.7	1.1	854.7	1.1
	α-$Ni(OH)_2$	-	-	-	-	855.2	1.1	855.2	1.1
	γ-NiOOH	-	-	-	-	855.3	1.4	854.9	1.4
	β-NiOOH(3+)	-	-	-	-	855.1	1.4	854.9	1.4
	β-NiOOH(2+)	-	-	-	-	855.2	1.1	855.2	1.1
O 1s	O^{2-}	-	-	-	-	530	1	530.2	1.1
	$-OH^-$ and $O_{vaccancies}$	-	-	-	-	531.7	1.2	531.8	1.1
	Physisorbed Species	532.3	1.3	532.8	1.3	532.8	1.3	532.6	1.3

Table 4.7. HAXPES peak position and FWHM of Cs $3d_{5/2}$, N 1s, Pb 4f, I $3d_{5/2}$, O 1s and Ni 2p3/2 core levels for FTO/CBD-SnO_2/MHP, FTO/CBD-SnO_2/MHP/ALD-NiO_X 62 ALD cycles under 2 and 6 keV excitation energy.

In summary, the resultant MHP: ALD-NiO_X sample contains several defective species at the interface and the NiO_X film has excessive hydroxide and oxy-hydroxide species specifically in the first few nanometers of the growth. In addition, the growth of NiO_X MHP film are not reproducible. Hence, the combination defective interface, NiO_X film and in-consistent growth is not suitable for incorporating the ALD film directly on top of the MHP without severely damaging the MHP and compromising the PSCs performance. With the HAXPES analysis, we were able to probe the different depths of the interface in a non-destructive approach and found the damage to the interface is extended to a deeper subsurface region. In the next section, we extend our HAXPES of the interface with inclusion of PTAA buffer layer between MHP and ALD-NiO_X.

4.3.4.3 HAXPES analysis of MHP: PTAA and MHP: PTAA: ALD-NiO_X

The HAXPES spectra of the N 1s, Pb $4f_{7/2}$, O 1s, and Ni 2p3/2 core level regions of the MHP/PTAA and MHP/PTAA/NiO_X samples (62 ALD cycles) at photon energies of 2 and 6 keV are shown in Figure 4.14. In the previous LabXPS study, we detected extremely noisy signals at the I 3d core level, which limited the quantitative analysis of the core level. Utilizing HAXPES, we obtained better signal quality (probably aided by the presence of pinholes), which allowed us to analyze the iodine core levels, as shown in Figure 4.14 (a) and (d). The I 3d core level shifted by 200 meV to higher binding energy from 619.3 to 619.5 eV after NiO_X deposition. The binding energy shift could be due to the interaction between the exposed MHP through pinholes and ALD precursors. However, we did not observe any shift in the core level at 6 keV excitations. The Pb 4f core level also shifted to a higher binding energy of 100 meV at photon energies of both 2 and 6 keV (see Figure 4.14 (c) and (f)). In the previously discussed LabXPS analysis, we observed that the Pb 4f core level shifted to a higher binding energy of 1 eV after NiO_X deposition. We were unable to confirm this significant difference in binding energy shift. Furthermore, the N 1s core level peak corresponding to the triaryl amine compound in PTAA shifted to a higher binding energy by 300 meV at 2 and 6 keV excitation (see Figure 4.14 (b) and (e)).

In addition, we monitored and compared the ratio of iodine to lead at the surface (2 keV excitation energy) and subsurface (6 keV excitation energy) of the MHP layer in the MHP/PTAA sample before and after ALD-NiO_X deposition. The quantification shows that before NiO_X deposition, the I/Pb ratios near the MHP surface and subsurface are 2.8 and 2.7, respectively, that is, almost equal to the expected stoichiometry value. After NiO_X deposition, we observed a slight iodine deficiency with the I/Pb ratio dropping to 2.2 and 2.4 under 2 and 6 keV excitation energies respectively. This could be related to the interaction of the ALD precursors with MHP through the pinholes, as hypothesized earlier in accordance with the binding energy shifts.

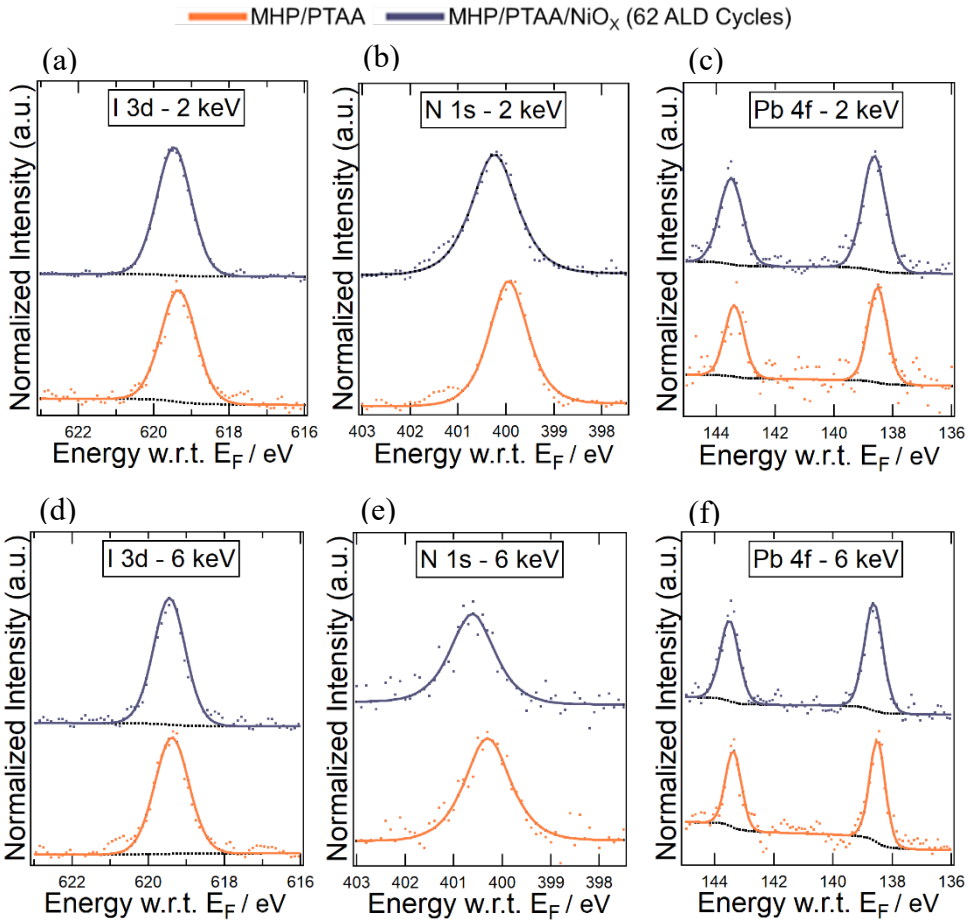

Figure 4.14. (a-f) HAXPES detail spectra (include fit analysis of some core levels) of I $3d_{5/2}$, N 1s and Pb $4f_{7/2}$ of double cation MHP: PTAA without (orange spectra) and with (light-blue spectra) ALD NiO_X top layers recorded with 2 and 6 keV excitation energy using Be filter.

The signal acquired at 6 keV for the Ni 2p and O 1s core levels exhibited low signal-to-noise ratio, preventing us from incorporating this dataset into our analysis (see raw data Figure 4.15 (c) and (d)). The low signal-to-noise ratio stems from the exceptionally thin sample thickness in comparison to MHP/ALD-NiO_X (see Figure A10 in the Annex) and the relatively low photoionization cross-section associated with a photon energy of 6 keV. Hence, the examination of NiO_X overlayer core levels is confined to a photon energy of 2 keV.

In the O 1s spectra obtained from the MHP/PTAA sample, a clear peak at 533 eV was visible, corresponding to oxygen species within the LiTFSi dopant of PTAA, as well as physisorbed species present. Furthermore, when NiO_X was introduced, the spectra showed the emergence of two new peaks at 530.4 and 532.1 eV, attributed to O^{2-} (NiO) and OH^- (hydroxide, oxy-hydroxide) species, respectively. This noticeable difference in intensity between the O^{2-} species and the OH^- species (as seen in Figure 4.15(a)) strongly suggests a significant contribution of NiO within the ALD film, which is consistent with our previous observations made through LabXPS analysis. As shown in Figure 4.15(b), the Ni $2p_{3/2}$ core level components were found to be predominantly composed of

NiO, $Ni(OH)_2$, and NiOOH, with no indications of metallic nickel species. Through quantitative analysis, the composition was determined to be 74% NiO, 8% $Ni(OH)_2$, and 18% NiOOH (as presented in Table 4.8). As mentioned earlier, in the LabXPS analysis, we found that 61% of NiO was present in the MHP/PTAA/NiO_X (62 ALD cycles) samples. The variance in NiO concentration may be attributed to slight differences in thickness between sample batches, similar to what was discussed earlier in the context of MHP/NiO_X sample sets. However, it's worth noting that for the MHP/PTAA/NiO_X sample sets, the variability in NiO concentration is not as pronounced as in the MHP/NiO_X sample sets. In summary, both the HAXPES and LabXPS investigations corroborated the presence of a substantial concentration of NiO species within the ALD-NiO_X film in the PTAA based samples.

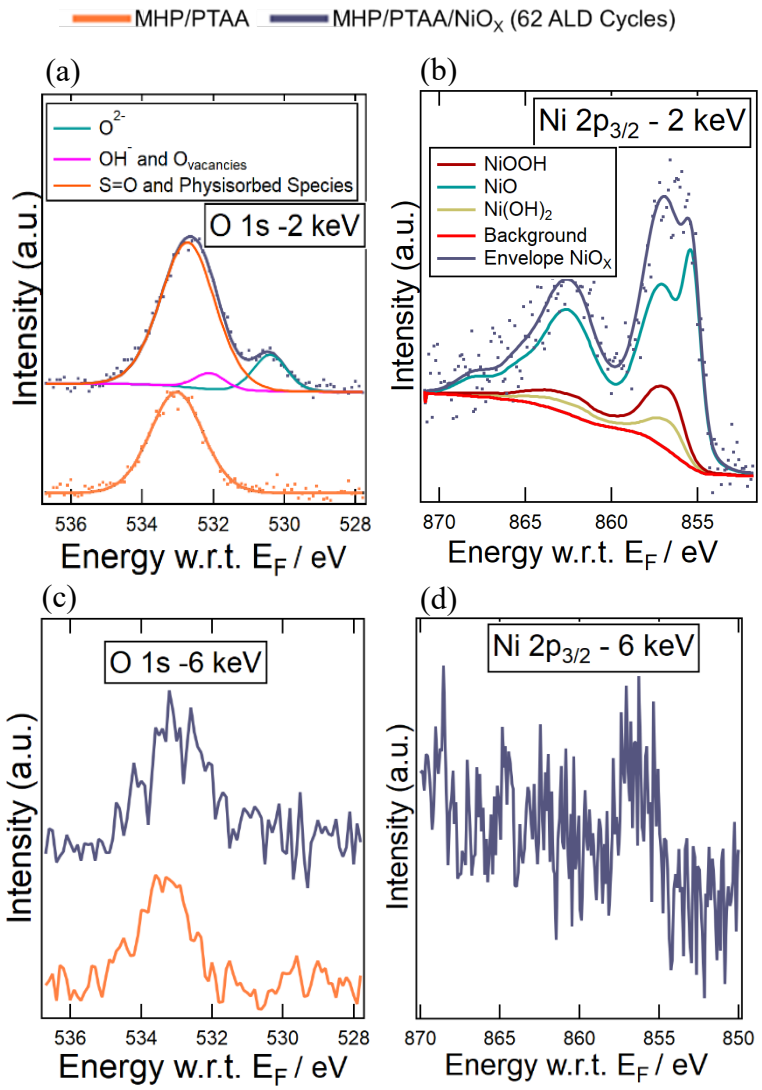

Figure 4.15. (a-d) HAXPES detail spectra (include fit analysis of some core levels) of Ni $2p_{3/2}$, and O 1s of double cation MHP: PTAA without (orange spectra) and with (light-blue spectra) ALD NiO_X top layers recorded with 2 and 6 keV excitation energy using Be filter.

Composition	MHP:NiO_X 62 ALD Cycles (%)		MHP:PTAA:NiO_X 62 ALD Cycles (%)	
	2 keV	6 keV	2 keV	6 keV
NiO	56	38	74	-
Ni metal	0	2	0	-
$Ni(OH)_2$	20	17	8	-
NiOOH	34	43	18	-

Table 4.8. Quantification of ALD-NiO_X film utilizing Ni $2p_{3/2}$ fitting that includes NiO, $Ni(OH)_2$, NiOOH, and metallic nickel contribution under 2 and 6 keV excitations.

Sample		**MHP/PTAA**				**MHP/PTAA/NiO_X**			
Excitation energy		2003 eV		6009 eV		2003 eV		6009 eV	
		Position (eV)	FWHM (eV)	Position (eV)	FWHM (eV)	Position (eV)	FWHM (eV)	Position (eV)	FWHM (eV)
N 1s		399.9	0.9	400.3	1.1	400.2	1.1	400.6	1.1
Pb $4f_{7/2}$		138.5	0.8	138.5	0.7	138.6	0.9	138.6	0.7
I $3d_{5/2}$		619.3	1.1	619.4	1	619.5	1.1	619.4	1
NiO_X	NiO	-	-	-	-	855.3	1.1	-	-
	α-$Ni(OH)_2$	-	-	-	-	856.2	1.1	-	-
	γ-NiOOH	-	-	-	-	855.9	1.4	-	-
	β-NiOOH(3+)	-	-	-	-	856.9	1.4	-	-
	β-NiOOH(2+)	-	-	-	-	856.2	1.1	-	-
O 1s	O^{2-}	-	-	-	-	530.4	1.1	-	-
	$-OH^-$ and $O_{vaccancies}$	-	-	-	-	532.1	1	-	-
	Physisorbed Species	533	1.7	-	-	532.7	1.8	-	-

Table 4.9. HAXPES peak position and FWHM of N 1s, Pb 4f, I $3d_{5/2}$, O 1s and Ni 2p3/2 core levels for FTO/CBD-SnO_2/MHP/PTAA, FTO/CBD-SnO_2/MHP/PTAA/ALD-NiO_X 62 ALD cycles under 2 and 6 keV excitation energy.

4.3.5. Effect of Exposure of ALD-NiOx Precursors on MHP and PTAA

In this section, we study the effect of exposure to individual precursors, H_2O and $Ni(amd)_2$, on MHP and MHP/PTAA samples. The goal of this experiment was to determine which of the precursors was responsible for the interfacial reactions and defect formation. For this investigation, we focus on the N 1s core level, as we found previously clear evidence of the formation of new species with the MHP/ALD-NiO_X samples.

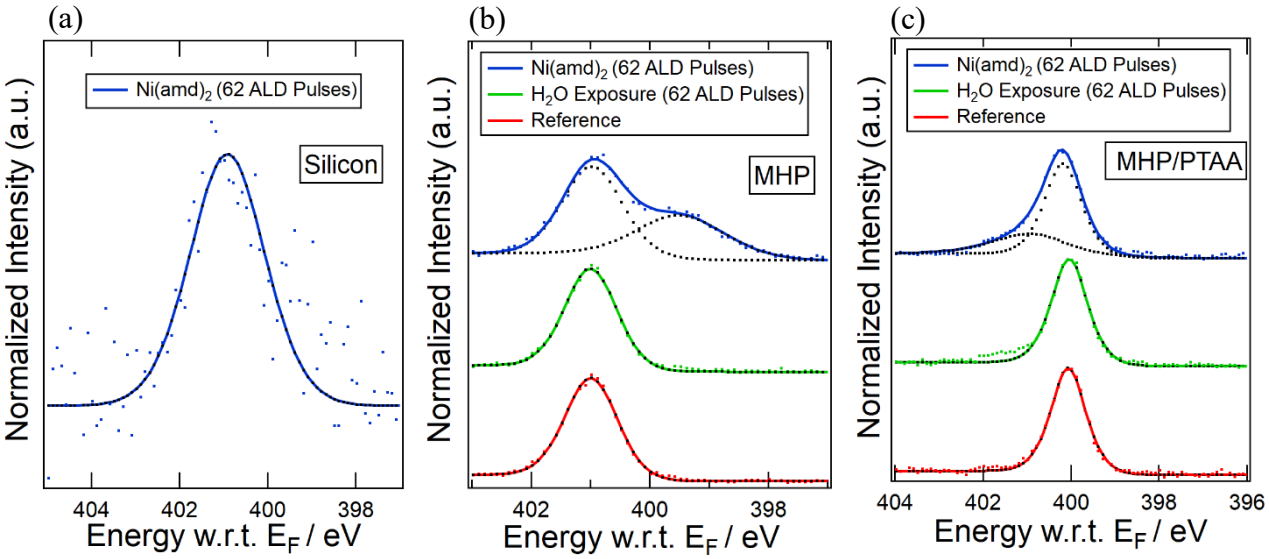

Figure 4.16. XPS spectra (Al-kα 1486.7 eV) of N 1s core level of (a) Silicon wafer exposed to $Ni(amd)_2$ precursor (b) MHP (c) MHP/PTAA showing comparison of reference, H_2O exposed and $Ni(amd)_2$ exposed.

A silicon wafer is exposed to $Ni(amd)_2$ to record the N 1s position of the precursor, which served as a reference for comparison with the MHP and MHP/PTAA samples. The N 1s peak originating from the $Ni(amd)_2$ component is located at 400.9 eV on the silicon sample, as shown in Figure 4.16 (a). For the MHP sample, we did not observe any changes to the N 1s core level even after exposure to 62 pulses of H_2O precursor with the peak positioned at 400.9 eV superimposing with the previously described reference peak of $Ni(amd)_2$, as shown in Figure 4.16 (b). However, when exposed to 62 pulses of $Ni(amd)_2$ precursor, we observed the formation of an additional peak at 399.5 eV binding energy. This new peak is attributed to the chemical reaction between MHP and $Ni(amd)_2$.

For the MHP/PTAA sample, we did not observe any change in the N 1s core level due to exposure to H_2O, as compared to the reference sample, with the peak positioned at 400 eV corresponding to the amine group in PTAA, as shown in Figure 4.16 (c). Upon exposure to the $Ni(amd)_2$ precursor, we observed the formation of a new peak at 400.9 eV, which is at the same peak position as the nitrogen contribution from the $Ni(amd)_2$ precursor itself. This indicates successful chemical grafting of the precursor onto the PTAA surface. We did not find any observable evidence of the formation

of defect species in the MHP/PTAA sample compared to the MHP sample, which suggests that PTAA restricts the interaction between MHP and ALD precursors. To note, the pinholes in the PTAA film remain of great concern and can have detrimental impact of performance or reproducibility of PSCs.

4.3.6. Work-function of ALD-NiO_X

In the previous sections, we provided an account of the growth of ALD-NiO_X on surfaces consisting of MHP and PTAA, outlining their respective characteristics. We noted that the chemical nature of the ALD oxide differs significantly between these surfaces, such as low concentration of NiO and high concertation of NiOOH and $Ni(OH)_2$ when grown on the MHP. The oxidation state of the cation also affects the work function of an oxide, which can impact the energy level alignment. Transition metals such as Ni, with many stable oxides are more susceptible to oxidation or reduction, which could alter the conductivity or energy level alignment within a device, potentially leading to changes in its functionality. [30]

Hence, this section shifts the focus toward examining how these chemical distinctions affect the work function of ALD-NiO_X. To investigate this, we used a Kelvin probe in a nitrogen atmosphere to measure the work function of ALD-NiO_X with varying thicknesses (62, 125 ALD cycles) for both the FTO/SnO_2/MHP and FTO/SnO_2/MHP/PTAA configurations. Our findings revealed that the work function of ALD NiO_X on MHP was lower than that of the bare MHP surface (Table 4.10). Furthermore, we observed a notable difference in the work functions of the thicker and thinner NiO_X layers, measuring at 3.8 and 4.1 eV, respectively. The alteration in work function can be linked to the evolving chemical properties of the ALD oxide as its thickness increases. The hydroxide-terminated NiO_X film is known to have a lower work function compared to pure NiO film (work function in the range of 6.2-6.7 eV).[30] It is important to note that the pure NiO film is an insulator, and a small amount of hydroxide and oxy-hydroxide species (10-20%) is essential for the p-type doping of the material. [31] However, in our case, the NiO_X film grown on MHP majorly consists of hydroxide and oxy-hydroxide species in the first few nanometers, in combination with various defective species that exhibit extremely low work functions and are unsuitable for use as a HTL.

FTO/SnO_2/	MHP	MHP/NiO_X		MHP/PTAA	MHP/PTAA/NiO_X	
		62 ALD Cycles	125 ALD Cycles		62 ALD Cycles	125 ALD Cycles
Work Function (eV)	4.3	4.1	3.8	4.5	4.5	4.6

Table 4.10. Work-function of ALD NiO_x grown on different surfaces.

The NiO_X film on PTAA exhibited a much higher work function, approximately 4.5-4.6 eV, compared to the MHP/NiO_X samples, which had a work function of around 3.8-4.1 eV. The significant difference in work function can be attributed to two key factors: an increased concentration of NiO within the NiO_X film and a reduced presence of hydroxide and oxy-hydroxide species. To evaluate the suitability of the NiO_X film as an HTL, we proceeded to integrate it into a complete device structure. We then conducted an in-depth analysis of the device performance, which is thoroughly discussed in the following section of this study.

4.4. Perovskite Solar Cells: J-V, EQE and Photostability

The performance evaluation of N-I-P perovskite solar cells was carried out under standard one-sun conditions using J-V measurements, as presented in Figure 4.17 (a). These cells were made in three different configurations:

(a) glass/FTO/CBD-SnO_2/MHP/PTAA/Au

(b) glass/FTO/CBD-SnO_2/MHP/ALD-NiO_X (125 and 185 ALD Cycles) /Au

(c) glass/FTO/CBD-SnO_2/MHP/PTAA/ALD-NiO_X (125 and 185 ALD Cycles) /Au

Among these configurations, the reference devices utilizing PTAA as the HTL displayed optimal performance, reaching a maximum power conversion efficiency (PCE) of 8.83%, open-circuit voltage (V_{OC}) of 0.83V, short-circuit current density (J_{SC}) of 19.27 mA/cm2, and fill factor of 54% (refer to Table 4.11). On the other hand, the devices employing an ALD-NiO_X HTL only were not functional, confirming the detrimental influence of interfacial defects and a high concentration of the hydroxyl-terminated NiO_X film. Intriguingly, the devices that synergistically integrated PTAA and NiO_X layers achieved significantly improved performance, with PCE values reaching as high as 15.99%, a V_{OC} of 1.12V, J_{SC} of 20.12 mA/cm^2, and a fill factor of 70%. Furthermore, the EQE spectra of the PTAA/NiO_X HTL devices in Figure 4.17 (b) (green and blue) demonstrated higher EQE in the range of 350-750 nm compared to the PTAA device (in red).

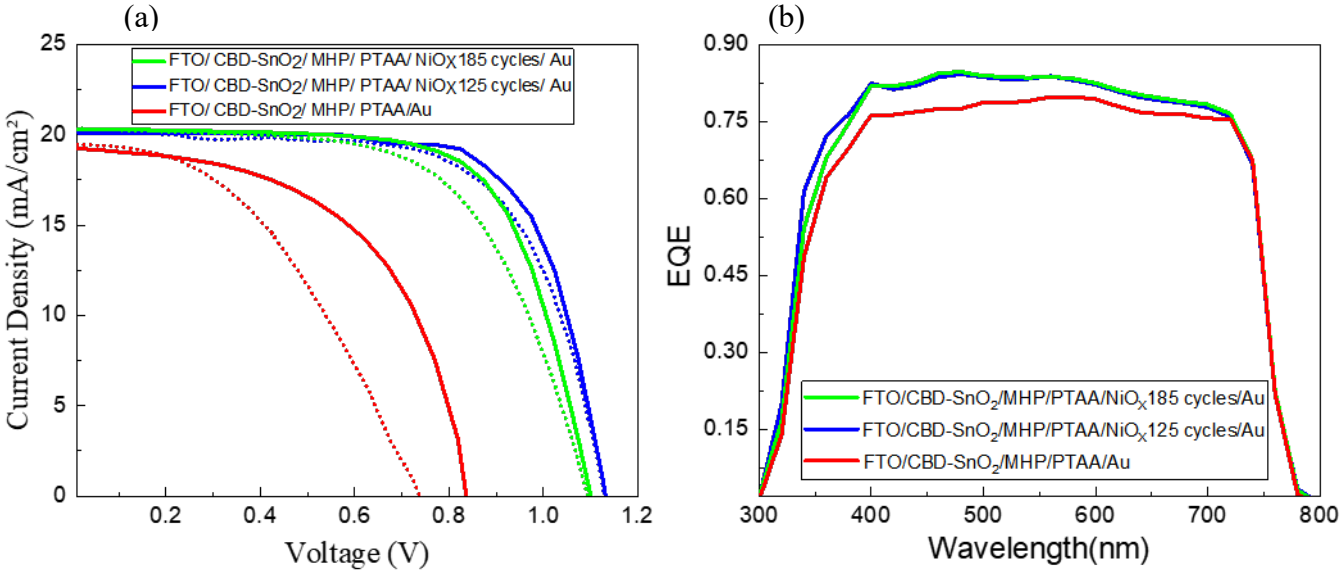

Figure 4.17. J-V characteristics of NIP perovskite solar cells with and without ALD NiO_x overlayer. a) J-V curve b) EQE spectra.

The introduction of both PTAA and ALD NiO_X layers led to a two-fold enhancement in device performance. The protective role of the PTAA buffer layer during ALD process, coupled with the efficient electron-blocking attributes of the NiO_X layer on top of PTAA, contributed to this improvement. This marked improvement aligns with our prior findings, which were substantiated and elucidated through the XPS and Kelvin probe studies Furthermore, it's plausible that the ALD NiO_X layer played a role in mitigating defects on the PTAA surface, thereby contributing to the observed enhancements in V_{OC} and fill factor for the device.

	FTO/CBD-SnO_2/ PSK/PTAA/Au		**FTO/CBD-SnO2/ PSK/PTAA/NiO_X 125 ALD Cycles /Au**		**FTO/CBD-SnO2/ PSK/PTAA/NiO_X 185 ALD Cycles/Au**	
	FW	RV	FW	RV	FW	RV
J_{SC} (mA/cm^2)	19.3	19.5	20.2	20.1	20.4	20.3
V_{OC} (volts)	0.84	0.74	1.13	1.12	1.09	1.07
FF (%)	55	43	66	70	62	68
PCE (%)	8.8	6.2	15.1	16	13.7	15.3

Table 4.11. J-V characteristics data of champion NIP perovskite solar cells with and without ALD NiO_x overlayer.

The performance of the photovoltaic parameters, including V_{OC}, J_{SC}, FF, and PCE, is presented in Figure 4.18. In the instance of the reference device utilizing PTAA, a discernible pattern emerges where V_{OC} remains within the range of 0.7-0.9V and FF varies between 42-48% across all devices. This collective behavior leads to lower PCE values. On the other hand, the addition of NiO_X to the PTAA results in a noticeable enhancement, demonstrated by increased V_{OC} (1-1.1V), J_{SC} (20-22 mA/cm^2), and FF (41-71%), which ultimately results in a significantly higher PCE compared to the reference devices. However, it is important to note that there is a greater variation in the fill factor, ranging from 41% to 71% (as seen in Figure 4.18 (C)) among the devices within the batch and this variation contributes to a higher standard deviation in the PCE, ranging from 10-16%.

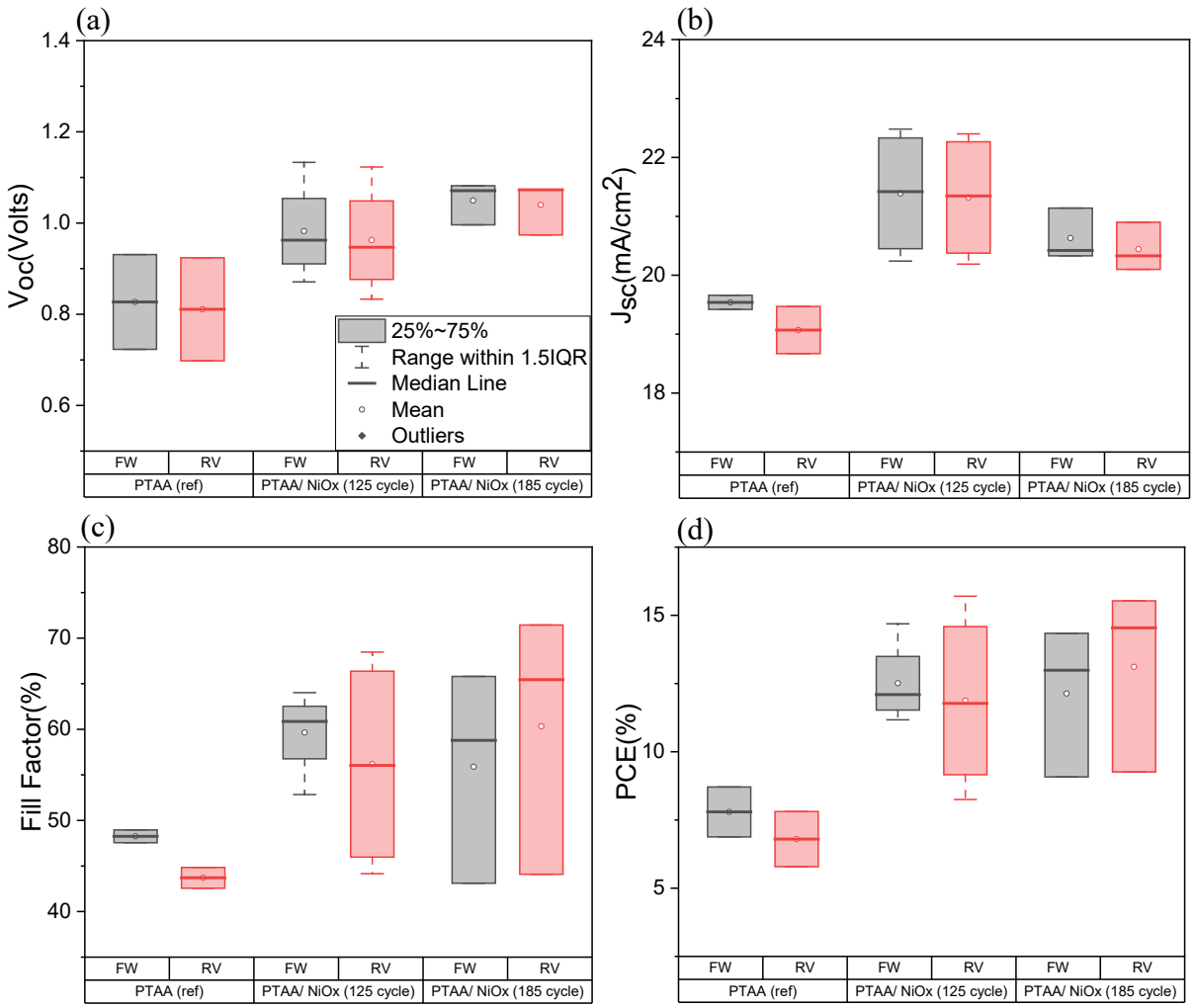

Figure 4.18. Statistical J-V characteristics of NIP perovskite solar cells a) V_{OC} b) J_{SC} (c) FF (d) PCE.

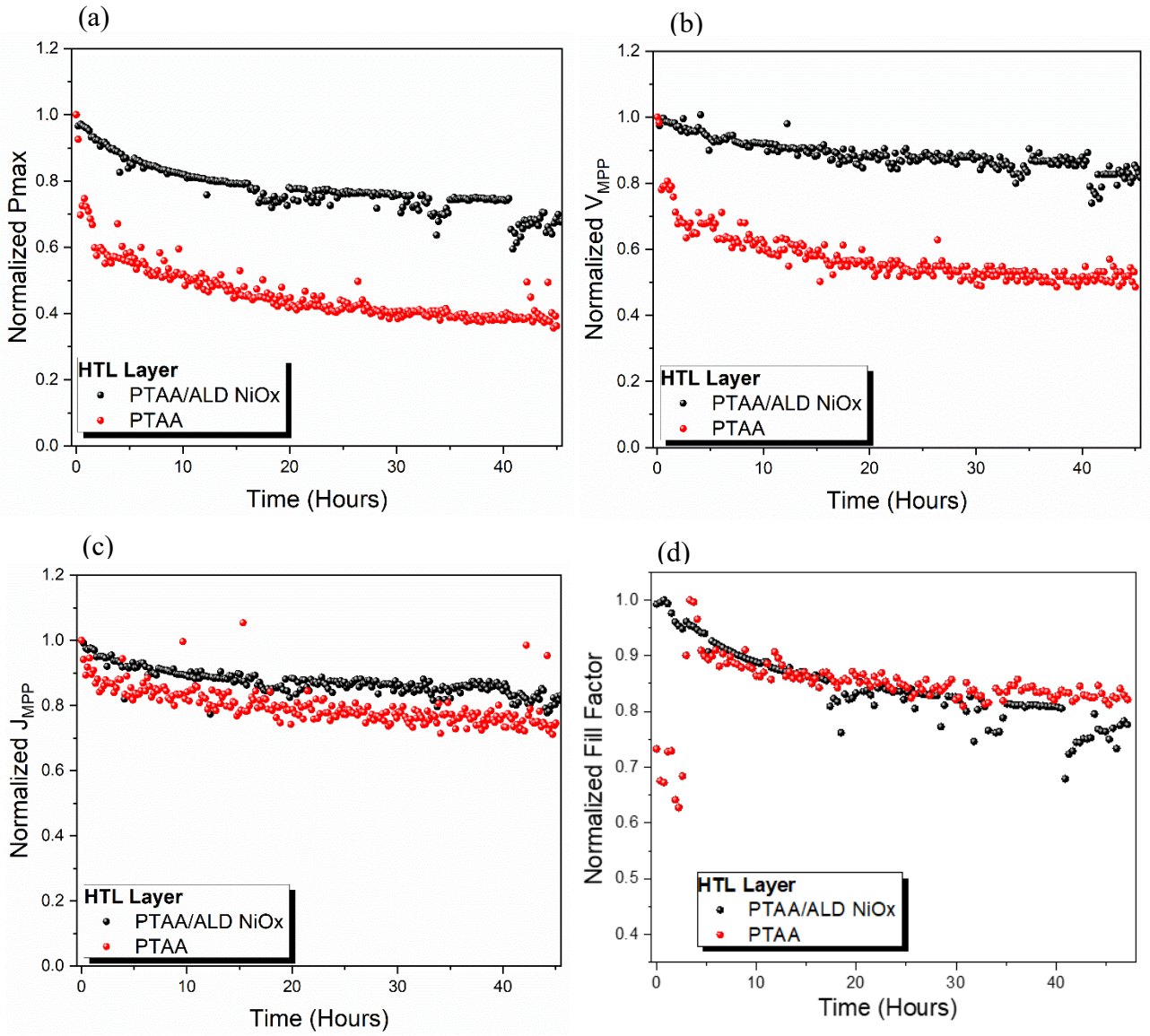

Figure 4.19. Photo-stability of J-V parameters of NIP perovskite solar cells with and without ALD NiO_x (185 ALD cycles) interlayer a) P_{max} b) J_{MPP} c) J_{MPP} d) Fill Factor.

PSCs are prone to stability issues when they are exposed to constant photon exposure. Previously, we discussed that compact ALD layers act as ion blockers and can enhance the photostability of PSCs. In this study, the PTAA/NiO_X device was compared with a reference PTAA device in indoor accelerated aging for 50 hours under an LED solar simulator with a spectrum that matched AM1.5G in a climate chamber kept under an N_2 atmosphere. The maximum power point tracking (MPPT) was conducted throughout the aging process, and J-V characterizations were recorded every 20 minutes.

The reference PTAA device exhibited a steep decline in P_{MAX} during the first 5 h, with a nearly 50% reduction in PCE (see Figure 4.19 (a)). This reduction in efficiency can be attributed to a substantial decrease in the V_{OC} of the device, as shown in Figure 4.19(b), which is caused by an increase in trap states resulting from ion migration through the pinholes.[32]The increase in trap states leads to increased non-radiative recombination, causing a significant decline in photovoltage and ultimately affecting the PCE.[33,34]

The PTAA/NiO_X-coupled HTL device retained 80-90% of its PCE for 50 hours with stable J_{MPP} and V_{MPP}. The improved operational stability of this device is due to the compact nature of the ALD oxide, which acts as an ion blocker, limiting the formation of trap states. In summary, the inclusion of ALD-NiO_X in the n-i-p architecture significantly improved device performance and operational stability due to the superior thin-film properties of ALD-Oxide. Additionally, this architecture can be used for the fabrication of semi-transparent solar cells because of the tough nature of ALD NiO_X films compared to soft organic CTLs, which can facilitate damage-free sputtering of the top transparent conductive oxide (TCO) layer. It also opens opportunities for the fabrication of all-perovskite tandem devices.

4.5. Summary

In summary, our study focused on n-i-p configuration perovskite solar cells using an ALD-NiO_X hole-transport interlayer. We conducted an extensive analysis of the interface, solar cell characteristics, and operational stability. We employed LabXPS and synchrotron-based HAXPES techniques to investigate the chemical details of both the perovskite and ALD-NiO_X interfaces. The HAXPES study used photon energies of 2 keV and 6 keV to probe different depths of the interface. The characterization revealed crucial insights into the emergence of new chemical defects, particularly nitrogen compounds, at the interface. We found that the MHP/NiO_X sample had a stoichiometric evolution with deficiencies in iodine, cesium, nitrogen, and excess Pb. The new interfacial species and severe modification of the stoichiometry of MHP imply the formation of several defects at the interface, originating from the chemical interaction between the MHP and ALD-NiO_X precursors (see Figure 4.20). We also found that the ALD-NiO_X-grown MHP exhibited a low concentration of NiO during the initial growth (8-39%) and a high concentration of hydroxide and oxy-hydroxide species. The high concentrations of hydroxide and oxy-hydroxide species are detrimental to the stability of MHP, as they can react rapidly with MHP, causing rapid degradation. The NiO_X film grown on MHP had extremely low work functions (in the range of 3.8-4.1) due to high hydroxyl contribution, making it unsuitable for use as an HTL.

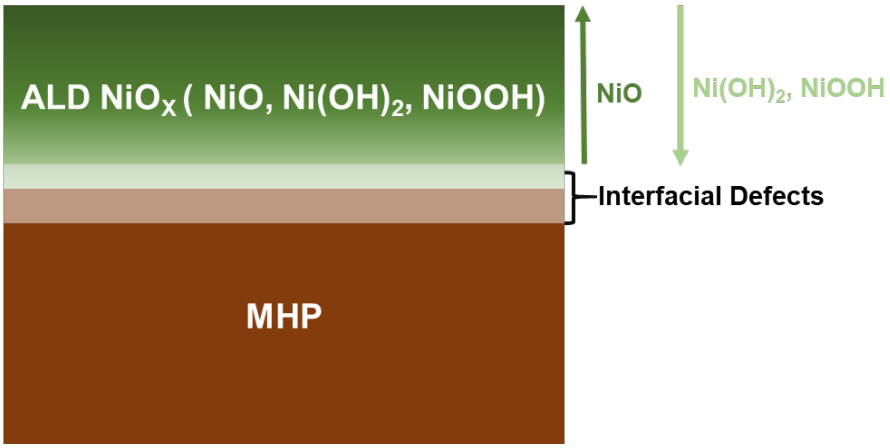

Figure 4.20. Illustration of MHP/ALD-NiO_X and interfacial defects. The NiO_X layer exhibits an increase in the NiO concentration with an increase in the ALD-NiO_X film thickness.

The work was also extended to a system with a 20 nm PTAA interlayer between the MHP and ALD-NiO_X. The PTAA interlayer was found to limit the MHP from interacting with the ALD-NiO_X precursors. However, the presence of pin-holes in the PTAA films doesn't fully inhibit the interaction between MHP and ALD precursors. The ALD-NiO_X films on PTAA had a higher concentration of NiO in the range of 61-74%, resulting in a higher work function of 4.5-4.6 measured using a kelvin probe. Upon incorporation of the PTAA/NiO_X in the PSCs, a champion cell PCE of 16% was recorded, and a significant enhancement of operational stability under ambient conditions with respect to the PTAA HTL-based device was observed due to the compact and ion-blocking properties of the ALD oxides.

■ REFERENCES

1. Kim, J., Park, N., Yun, J.S., Huang, S., Green, M.A. and Ho-Baillie, A.W., 2017. An effective method of predicting perovskite solar cell lifetime–Case study on planar CH3NH3PbI3 and HC (NH2) 2PbI3 perovskite solar cells and hole transfer materials of spiro-OMeTAD and PTAA. *Solar Energy Materials and Solar Cells*, *162*, pp.41-46.
2. Yang, J., Siempelkamp, B.D., Liu, D. and Kelly, T.L., 2015. Investigation of CH3NH3PbI3 degradation rates and mechanisms in controlled humidity environments using in situ techniques. *ACS nano*, *9*(2), pp.1955-1963.
3. Li, Z., Xiao, C., Yang, Y., Harvey, S.P., Kim, D.H., Christians, J.A., Yang, M., Schulz, P., Nanayakkara, S.U., Jiang, C.S. and Luther, J.M., 2017. Extrinsic ion migration in perovskite solar cells. *Energy & Environmental Science*, *10*(5), pp.1234-1242.
4. Mesquita, I., Andrade, L. and Mendes, A., 2019. Temperature impact on perovskite solar cells under operation. *ChemSusChem*, *12*(10), pp.2186-2194.

5. Domanski, K., Correa-Baena, J.P., Mine, N., Nazeeruddin, M.K., Abate, A., Saliba, M., Tress, W., Hagfeldt, A. and Grätzel, M., 2016. Not all that glitters is gold: metal-migration-induced degradation in perovskite solar cells. *ACS nano*, *10*(6), pp.6306-6314.
6. Hsu, C.C., Su, H.W., Hou, C.H., Shyue, J.J. and Tsai, F.Y., 2015. Atomic layer deposition of NiO hole-transporting layers for polymer solar cells. *Nanotechnology*, *26*(38), p.385201.
7. Mali, S.S., Kim, H., Kim, H.H., Shim, S.E. and Hong, C.K., 2018. Nanoporous p-type NiOx electrode for pin inverted perovskite solar cell toward air stability. *Materials Today*, *21*(5), pp.483-500.
8. Swift, P., 1982. Adventitious carbon—the panacea for energy referencing?. *Surface and Interface Analysis*, *4*(2), pp.47-51.
9. Barr, T.L. and Seal, S., 1995. Nature of the use of adventitious carbon as a binding energy standard. *Journal of Vacuum Science & Technology A: Vacuum, Surfaces, and Films*, *13*(3), pp.1239-1246.
10. Piao, H. and Mcintyre, N.S., 2002. Adventitious carbon growth on aluminium and gold–aluminium alloy surfaces. *Surface and Interface Analysis: An International Journal devoted to the development and application of techniques for the analysis of surfaces, interfaces and thin films*, *33*(7), pp.591-594.
11. Biesinger, M.C., 2022. Accessing the robustness of adventitious carbon for charge referencing (correction) purposes in XPS analysis: Insights from a multi-user facility data review. Applied Surface Science, 597, p.153681.
12. Wagner, C.D., Naumkin, A.V., Kraut-Vass, A., Allison, J.W., Powell, C.J. and Rumble Jr, J.R., 2003. NIST standard reference database 20, Version 3.4 (Web version). *National Institute of Standards and Technology: Gaithersburg, MD*, *20899*.
13. Biesinger, M.C., Payne, B.P., Lau, L.W., Gerson, A. and Smart, R.S.C., 2009. X-ray photoelectron spectroscopic chemical state quantification of mixed nickel metal, oxide and hydroxide systems. *Surface and Interface*, *41*(4), pp.324-332.
14. Grosvenor, A.P., Biesinger, M.C., Smart, R.S.C. and McIntyre, N.S., 2006. New interpretations of XPS spectra of nickel metal and oxides. *Surface Science*, *600*(9), pp.1771-1779.
15. Mansour, A.N., 1994. Characterization of NiO by XPS. *Surface Science Spectra*, *3*(3), pp.231-238.
16. Mansour, A.N. and Melendres, C.A., 1994. Characterization of electrochemically prepared γ-NiOOH by XPS. *Surface Science Spectra*, *3*(3), pp.271-278.
17. Mansour, A.N., 1994. Characterization of β-$Ni(OH)_2$ by XPS. *Surface Science Spectra*, *3*(3), pp.239-246.
18. Mansour, A.N. and Melendres, C.A., 1994. Characterization of α-$Ni(OH)_2$ by XPS. *Surface Science Spectra*, *3*(3), pp.255-262.
19. Gupta, R.P. and Sen, S.K., 1974. Calculation of multiplet structure of core p-vacancy levels. *Physical Review B*, *10*(1), p.71.
20. Gupta, R.P. and Sen, S.K., 1975. Calculation of multiplet structure of core p-vacancy levels. II. *Physical Review B*, *12*(1), p.15.

21. Major, G.H., Fairley, N., Sherwood, P., Linford, M.R., Terry, J., Fernandez, V. and Artyushkova, K., 2020. Practical guide for curve fitting in x-ray photoelectron spectroscopy. *Journal of Vacuum Science & Technology A*, *38*(6).
22. Peng, Z., Zuo, Z., Qi, Q., Hou, S., Fu, Y. and Zou, D., 2023. Managing the Double-Edged Sword of Ni3+ in Sputter-Deposited NiO x by Interfacial Redox Reactions for Efficient Perovskite Solar Cells. *ACS Applied Energy Materials*, *6*(3), pp.1396-1403.
23. Yan, M., Xiang, T., Yu, X., Xiao, J., Li, W., Ku, Z., Huang, F., Zhong, J., Peng, Y. and Cheng, Y.B., 2020. Room-temperature Sputtered NiOx for hysteresis-free and stable inverted Cs-FA mixed-cation perovskite solar cells. *Materials Science in Semiconductor Processing*, *115*, p.105129.
24. Roberts, M.W. and Smart, R.S.C., 1984. The defect structure of nickel oxide surfaces as revealed by photoelectron spectroscopy. *Journal of the Chemical Society, Faraday Transactions 1: Physical Chemistry in Condensed Phases*, *80*(11), pp.2957-2968.
25. Carley, A.F., Chalker, P.R. and Roberts, M.W., 1985. Defects in oxide overlayers at nickel single-crystal surfaces. *Proceedings of the Royal Society of London. A. Mathematical and Physical Sciences*, *399*(1816), pp.167-179.
26. Hawash, Z., Ono, L.K., Raga, S.R., Lee, M.V. and Qi, Y., 2015. Air-exposure induced dopant redistribution and energy level shifts in spin-coated spiro-MeOTAD films. *Chemistry of Materials*, *27*(2), pp.562-569.
27. Rombach, F.M., Haque, S.A. and Macdonald, T.J., 2021. Lessons learned from spiro-OMeTAD and PTAA in perovskite solar cells. *Energy & Environmental Science*, *14*(10), pp.5161-5190.
28. Powell, C.J., 1978. The physical basis for quantitative surface analysis by Auger electron spectroscopy and X-ray photoelectron spectroscopy. *Quantitative surface analysis of materials*, pp.5-30.
29. Bracesco, A.E., Burgess, C.H., Todinova, A., Zardetto, V., Koushik, D., Kessels, W.M.E., Dogan, I., Weijtens, C.H., Veenstra, S., Andriessen, R. and Creatore, M., 2020. The chemistry and energetics of the interface between metal halide perovskite and atomic layer deposited metal oxides. *Journal of Vacuum Science & Technology A*, *38*(6).
30. Greiner, M.T., Helander, M.G., Wang, Z.B., Tang, W.M. and Lu, Z.H., 2010. Effects of processing conditions on the work function and energy-level alignment of NiO thin films. *The Journal of Physical Chemistry C*, *114*(46), pp.19777-19781.
31. Duan, H., Chen, Z., Xu, N., Qiao, S., Chen, G., Li, D., Deng, W. and Jiang, F., 2021. Non-stoichiometric NiOx nanocrystals for highly efficient electrocatalytic oxygen evolution reaction. *Journal of Electroanalytical Chemistry*, *885*, p.114966.
32. Wolff, C.M., Caprioglio, P., Stolterfoht, M. and Neher, D., 2019. Nonradiative recombination in perovskite solar cells: the role of interfaces. *Advanced Materials*, *31*(52), p.1902762.
33. Stolterfoht, M., Caprioglio, P., Wolff, C.M., Márquez, J.A., Nordmann, J., Zhang, S., Rothhardt, D., Hörmann, U., Amir, Y., Redinger, A. and Kegelmann, L., 2019. The impact of energy alignment and interfacial recombination on the internal and external open-circuit voltage of perovskite solar cells. *Energy & environmental science*, *12*(9), pp.2778-2788.

34. Gelmetti, I., Montcada, N.F., Pérez-Rodríguez, A., Barrena, E., Ocal, C., García-Benito, I., Molina-Ontoria, A., Martín, N., Vidal-Ferran, A. and Palomares, E., 2019. Energy alignment and recombination in perovskite solar cells: weighted influence on the open circuit voltage. *Energy & Environmental Science*, *12*(4), pp.1309-1316.

Chapter 5
Molecular Interface Engineering of Perovskite and ALD-NiO_X

Preface: *This chapter reports an extension of the interface study in the previous chapter by introducing a phosphonic acid-based molecule (2-(3,6-Dimethoxy-9H-carbazol-9-yl)ethyl) phosphonic acid (MeO-2PACz) between MHP and ALD-NiO_X in an n-i-p architecture. In this chapter, the effectiveness of MeO-2PACz molecules in limiting unwanted interfacial reactions between the MHP surface and ALD-NiO_X precursors is discussed. This chapter also includes a HAXPES investigation to probe the buried interface to obtain the above-mentioned information.*

Contents

5.1. Introduction

In this chapter, we evaluate the effectiveness of (2-(3,6-Dimethoxy-9H-carbazol-9-yl)ethyl) phosphonic acid (MeO-2PACz) molecule (Figure 5.1) as an alternative buffer layer between MHP and ALD-NiO_X. In the previous chapter, the PTAA buffer layer partly limited the interfacial reaction between MHP and ALD-NiO_X. However, we observed that pinholes in the PTAA film did not completely protect the MHP during the ALD process. Additionally, we found parasitic absorption in the visible region after the incorporation of the PTAA film. Although parasitic absorption does not affect the performance of opaque solar cells, it can be a huge concern for semi-transparent and tandem devices. Hence, there is a need for an ultrathin buffer layer that does not exhibit absorption in the visible range and simultaneously shields the MHP from the ALD process.

In recent years, phosphonic acid-based molecules have shown great potential for role interface passivation, buffer layers, and CTLs in perovskite solar cells.[1-5] Among the various phosphonic acid-based molecules, MeO-2PACz molecules have been extensively studied and proven to be effective as HTL, buffer layer, and passivation layer in PSCs.[6-9] The utilization of these devices has demonstrated remarkable outcomes, including a high PCE exceeding 20%.[10,11] Moreover, this phosphonic acid molecule has been employed for passivating MHP surfaces,[12] effectively reducing non-radiative recombination at the interface between the MHP layer and selective contact. This passivation strategy contributed to the achievement of enhanced device performance.

In this study, we evaluate the effectiveness of MeO-2PACz as a buffer layer within the MHP/ALD-NiO_X n-i-p architecture, utilizing synchrotron-based HAXPES. Our investigation is centered on determining whether MeO-2PACz has the potential to reduce the interaction between ALD precursors and MHP, while also serving as a substrate to facilitate high-quality NiO_X growth and enhance interface passivation.

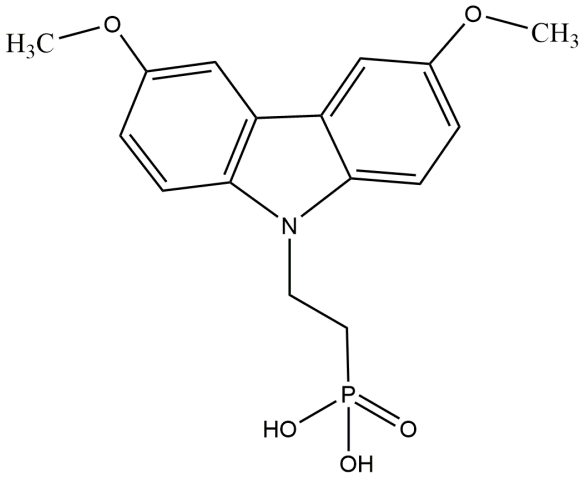

Figure 5.1. Chemical structure of MeO-2PACz molecule.

5.2. Interface and surface study of MHP, MeO-2PACz and ALD-NiO_X

The device architectures used in this study are comprised of glass/FTO, CBD-SnO_2, $FA_{0.7}Cs_{0.3}Pb(I_{0.9}Br_{0.1})_3$ MHP with and without a MeO-2PACz buffer layer, and ALD-NiO_X 62 ALD cycles (see Figure 5.2).

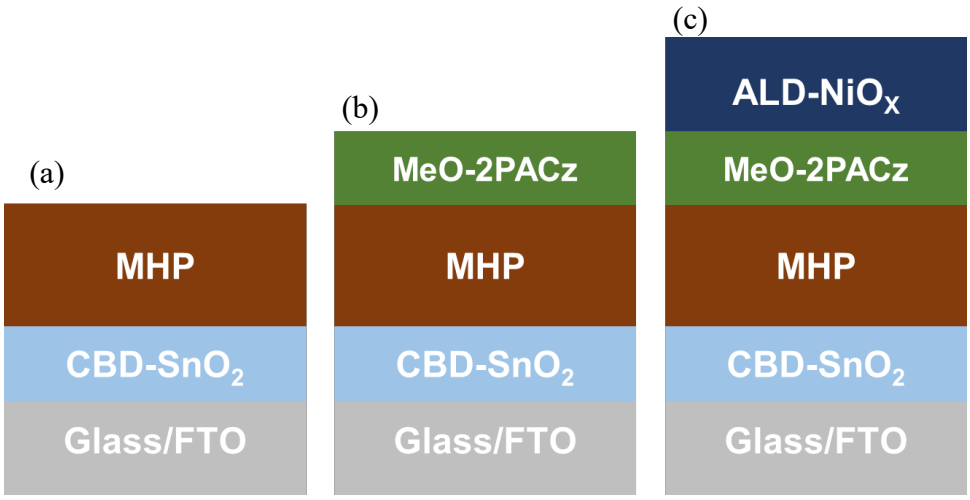

Figure 5.2. Schematic of different device architecture used in this section for interface study a) FTO/CBD-SnO_2/MHP, b) FTO/CBD-SnO_2/MHP/MeO-2PACz c) FTO/CBD-SnO2/MHP/ MeO-2PACz /ALD-NiO_X.

5.2.1. Structural and Optical Properties

Figure 5.3(a) illustrates the XRD patterns of a bare MHP film, with MeO-2PACz, and with MeO-2PACz /ALD-NiO_X overlayers. The XRD signature with 2θ in the range of 10°–50° displays signals corresponding to different planes of the MHP bulk. The XRD signature of the MHP materials did not exhibit any change for the samples ALD-NiO_X overlayer in comparison with the reference MHP and MHP/MeO-2PACz samples. This implies that the bulk structure of MHP material remains unchanged after being exposed to the ALD-NiO_X precursors at a temperature of 100°C.

The UV-Vis absorption spectra in Figure 5.3(b) show a slight increase in absorbance within the 30-600 nm wavelength range upon the addition of an ultrathin MeO-2PACz (green spectra) in reference to the MHP sample (blue spectra). This increase in absorbance is likely due to the inherent absorption properties of the MeO-2PACz overlayer. Additionally, the MHP/MeO-2PACz/NiO_X sample (brown spectra) resulted in an increased absorbance ranging from 350-600 nm in comparison to bare MHP and MHP/MeO-2PACz film. Given that the optical bandgap of ALD-NiO_X is approximately 3.9 eV (corresponding to 320 nm) (see Figure A7 in the Annex), we would not anticipate an absorbance increase for wavelengths beyond 320 nm with the incorporation of ALD-

NiO_X. The increase in absorbance suggests the emergence of new chemical defects that exhibit parasitic absorption in this range. In the next section, we investigated the MHP interface using HAXPES to determine if any possible formation of interfacial defects due to the interaction between the ALD precursors and MHP occurred.

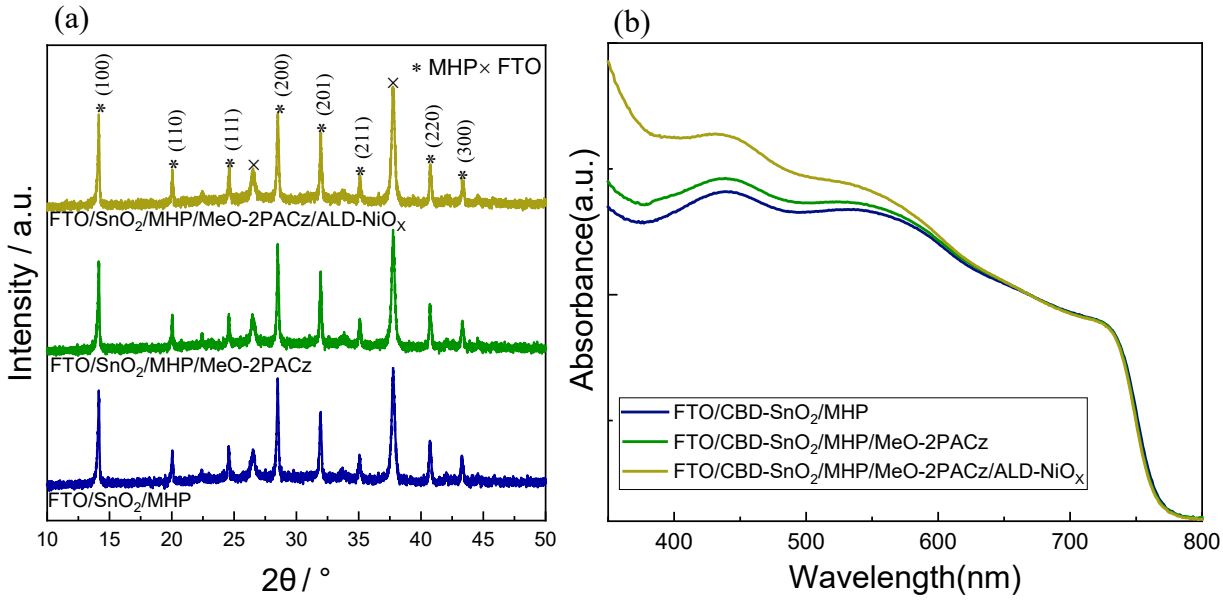

Figure 5.3. (a) XRD pattern of double cation MHP film with and without MeO-2PACz, MeO-2PACz /ALD-NiO_X top layers (b) UV-Vis absorption spectra of samples with and without MeO-2PACz, MeO-2PACz /ALD-NiO_X top layers.

5.2.2. HAXPES analysis of MHP, MHP: MeO-2PACz and MHP: MeO-2PACz: ALD-NiO_X

The HAXPES spectra of the Cs 3d5/2, N 1s, Pb 4f, I 3d, Ni 2p3/2, and P 2p core level regions from the samples with bare MHP, MHP/MeO-2PACz and MHP/MeO-2PACz/ALD NiO_X (62 ALD cycles) deposition are presented in Figure 5.4. The intensities of the various MHP core levels have been normalized to maximum intensity for improved data visualization. Notably, the I 3d, Pb 4f, Cs 3d, and N1s core level signals of the pristine MHP exhibit a minor shift in peak position of 100 meV between the data acquired for photon energies of 2 keV and 6 keV, as shown in Table 5.1.

After MeO-2PACz deposition on MHP, we detected a peak corresponding to the P 2p core level binding energy of 134 eV at 2 keV excitation energy (see Figure 5.4 (i)), confirming the grafting of MeO-2PACz molecules on MHP. However, the signal acquired at 6 keV for the P 2p core level had a low signal-to-noise ratio, preventing us from incorporating this dataset into our analysis. Additionally, in the N 1s core level, we observed a new peak at 400 eV at 2 and 6 keV corresponding to the nitrogen entity of the SAM layer, reconfirming the successful grafting. Furthermore, the MHP-related N 1s core level peak shifted to a higher binding energy of 200 meV at both 2 and 6

keV photon energies after grafting of the MeO-2PACz molecules. Similarly, the Cs 3d, I 3d, and Pb 4f core levels were also shifted to higher binding energy for the MHP/MeO-2PACz sample with respect to bare MHP. This shift to higher binding energy could be due to the chemical binding of the -OMe electronegative group of the SAM with the MHP surface. In summary, we observed successful grafting of MeO-2PACz on MHP surface, resulting in the shift of MHP core levels to higher binding energy and consequently a downward band bending at the MHP/MeO-2PACz interface.

For the MHP/MeO-2PACz/ALD-NiO_X sample, we observed that the Cs 3d core level shifted to a lower binding energy of 200 meV with the peak positioned at 725 eV under both 2 and 6 keV photon energies with respect to the MHP/MeO-2PACz film (see Figure 5.4 (a), (e) and Table 5.1). Similarly, the I 3d and N 1s core levels of MHP also shifted to lower binding energy of 100 and 200 meV at 2 and 6 keV photon energies, respectively, after the deposition of NiO_X (see Figure 5.5). However, for the Pb 4f core level, the detected peak shifted to a higher binding energy of 100 meV and broadened by 400 meV with respect to the MHP/MeO-2PACz reference sample at an excitation energy of 2 keV. As discussed in the previous chapter, this could be an indication of the formation of new defective species, presumably $PbBr_2$, owing to chemical interactions between the MHP and ALD precursors. At 6 keV, we observed that the Pb 4f peak shifted to a lower binding energy of 200 meV, which is in line with the trend observed for the MHP core levels. These peak shifts presumably indicate upward band bending, which can be caused by the defect formation at the interface.

Furthermore, the N1s core level, we observed a new nitrogen peak (N_{defect}) at 399.1 eV originating from the unwanted chemical reactions. The intensity of the N_{defect} peak decreased when we moved the photon energy from 2 keV to 6 keV (N_{defect}/N_{FA} ratio of 1.54 and 0.63 at 2 and 6 keV respectively), which indicates the interfacial presence of this new defective species. At a photon energy of 6 keV, we detect a signal from a deeper surface, which provides concrete confirmation that the damage to the MHP is confined to the top interface.

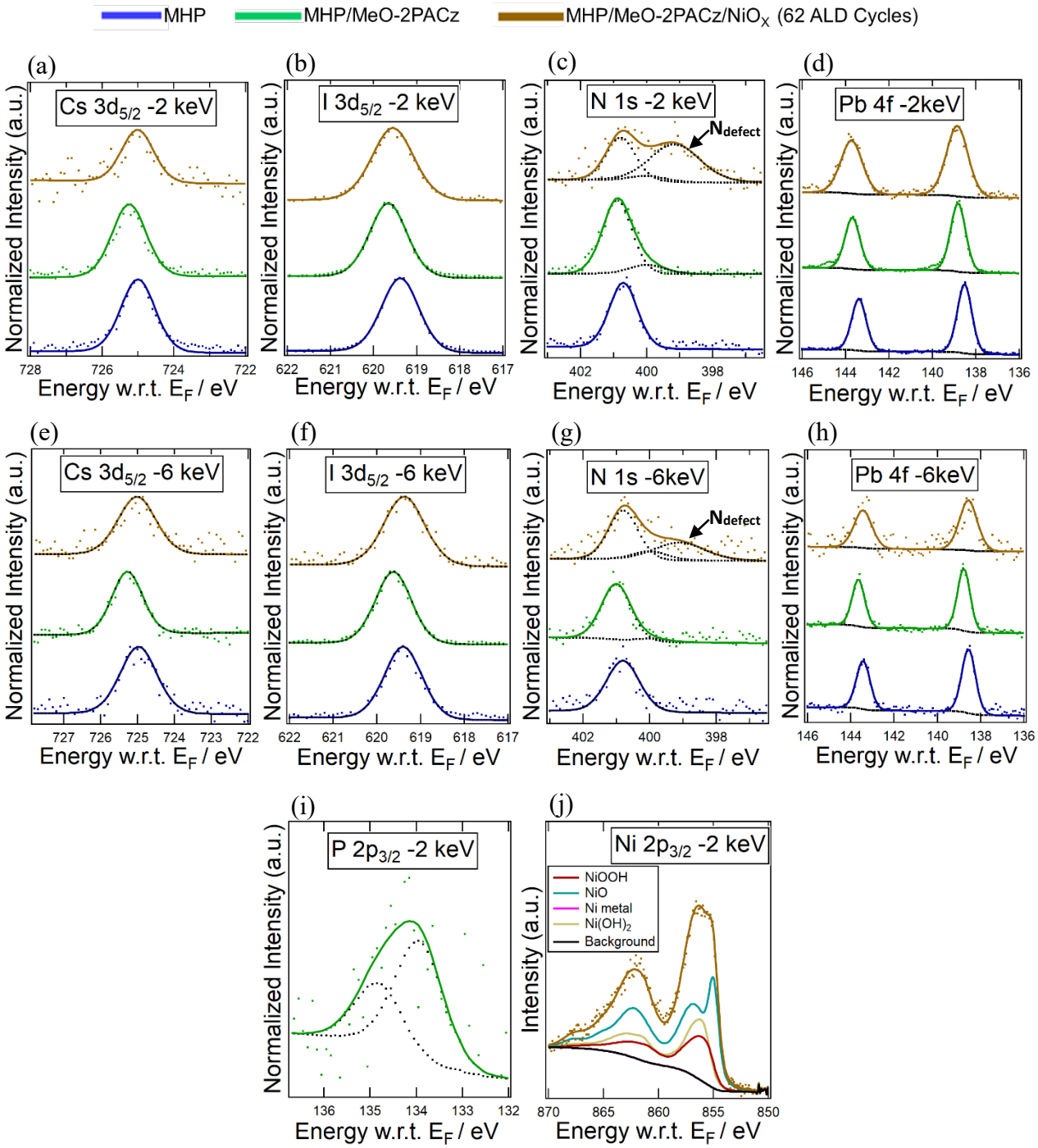

Figure 5.4. (a-j) HAXPES detail spectra (include fit analysis) of Cs $3d_{5/2}$, N 1s, Pb 4f, I 3d, P 2p, and Ni $2p_{3/2}$ of double cation MHP (blue spectra), MHP/MeO-2PACz (green spectra) and MHP/MeO-2PACz/ALD-NiO_X (yellow spectra) layers recorded with 2 and 6 keV excitation energy using Be filter.

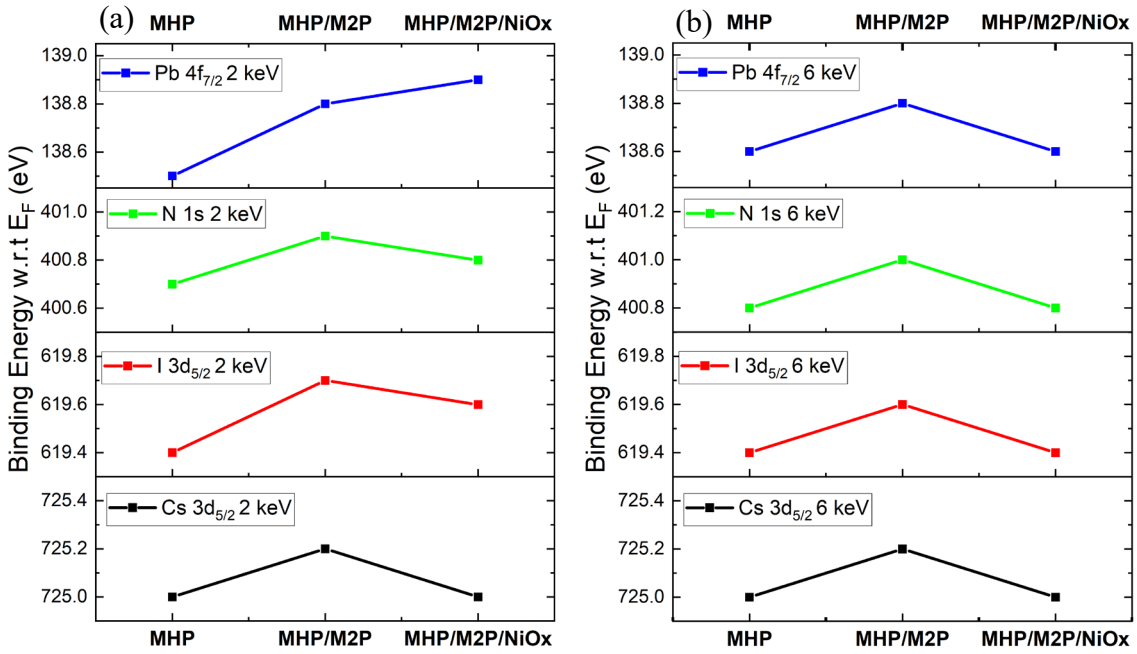

Figure 5.5. Illustration of binding energy of MHP core levels for MHP, MHP/MeO-2PACz, MHP/ MeO-2PACz / ALD-NiO_X (62 ALD Cycles) samples recorded at (a) 2 keV excitation energy (b) 6 keV excitation energy using Be filter. M2P: MeO-2PACz

In the previous chapter, we observed that the chemical nature of ALD-NiO_X varies on different surfaces. In this section, we examine the nature of ALD-NiO_X film grown on MeO-2PACz film by analyzing the Ni 2p core levels. The Ni 2p core level is only present at 2 keV, and the data obtained at 6 keV had a low signal-to-noise ratio. The Ni 2p3/2 core level, which includes contributions from NiO, $Ni(OH)_2$, NiOOH, and Ni metal at 2 keV, is presented in Figure 5.4 (j) and Table 5.1. We found that the NiO, $Ni(OH)_2$, and NiOOH contributions were 53%, 27%, and 20%, respectively. The concentration of hydroxide and oxy-hydroxide species in NiO_X is three times higher than in the ALD-NiO_X film grown on a silicon wafer (refer to Chapter 4). The high concentration of hydroxide and oxy-hydroxide species in NiO_X can readily react with the halides present in the MHP, leading to deterioration of the MHP film and the formation of numerous trap defects at the interface.[14]

Sample		MHP				MHP/MeO-2PACz				MHP/MeO-2PACz/NiO_X (62 ALD Cycles)			
Excitation energy		2003 eV		6009 eV		2003 eV		6009 eV		2003 eV		6009 eV	
		Position (eV)	FWHM (eV)	Position (eV)	FWHM (eV)	Position (eV)	FWHM (eV)	Position (eV)	FWHM (eV)	Position (eV)	FWHM (eV)	Position (eV)	FWHM (eV)
Cs $3d_{5/2}$		725	1.1	725	1.1	725.2	1.1	725.2	1	725	1	725	1.1
N 1s	MHP	400.7	1	400.8	1.1	400.9	1	401	1	400.8	1	400.8	1
	MeO2PACz	-	-	-	-	400	1.25	400	1.25	400	1.25	400	1.25
	N_{defect}	-	-	-	-	-	-	-	-	399.1	1.8	399.1	1.8
Pb $4f_{7/2}$		138.5	0.8	138.6	0.7	138.8	0.8	138.8	0.7	138.9	1.2	138.6	1
I $3d_{5/2}$		619.4	1	619.4	1	619.7	1	619.6	1	619.6	1.1	619.4	1.1
NiO_X	NiO	-	-	-	-	-	-	-	-	854.97	1.0	-	-
	α-$Ni(OH)_2$	-	-	-	-	-	-	-	-	855.75	1.1	-	-
	γ-NiOOH	-	-	-	-	-	-	-	-	855.8	1.5	-	-
	β-NiOOH(3+)	-	-	-	-	-	-	-	-	855.8	1.5	-	-
	β-NiOOH(2+)	-	-	-	-	-	-	-	-	855.3	1.1	-	-

Table 5.1. HAXPES peak position and FWHM of Cs $3d_{5/2}$, N 1s, Pb 4f, I $3d_{5/2}$ and Ni 2p3/2 core levels for FTO/CBD-SnO_2/MHP, FTO/CBD-SnO_2/MHP/MeO-2PACz, FTO/CBD-SnO_2/MHP/MeO-2PACz/ALD-NiO_X 62 ALD cycles under 2 and 6 keV excitation energy using Be filter.

In summary, the resulting MHP/MeO-2PACz/ALD-NiO_X sample exhibited multiple defects at the MHP interface, including nitrogen compounds and $PbBr_2$. Furthermore, upward band bending is observed at the interface, which is attributed to these defective chemical entities that could potentially affect hole transport. The presence of these defective species and band bending strongly suggest that the MeO-2PACz molecules were unable to effectively shield the MHP layer from interacting with the ALD precursors. This might be due to the extremely thin and non-compact nature of the MeO-2PACz molecule layer, which hinders its effectiveness as a protective barrier. Additionally, the NiO_X film deposited on MeO-2PACz contained an excessive amount of hydroxide and oxy-hydroxide species, which could readily react with the MHP interface. In the following section, we assess the photovoltaic (PV) characteristics of the n-i-p architecture by utilizing the FTO/SnO_2/MHP/MeO-2PACz/ALD-NiO_X/Au stack. This analysis will help us gain insights into how these interfacial defects affect the performance of photovoltaic solar cells (PSCs).

5.3. Perovskite Solar Cells: JV Characteristics

The performance evaluation of n-i-p perovskite solar cells was carried out under standard one-sun conditions using J-V measurements, as presented in Figure 5.6. These cells were made in two different configurations:

a) Glass/FTO/CBD-SnO_2/MHP/MeO-2PACz/Au
b) Glass/FTO/CBD-SnO_2/MHP/MeO-2PACz/ ALD-NiO_X (185 ALD Cycles)/Au

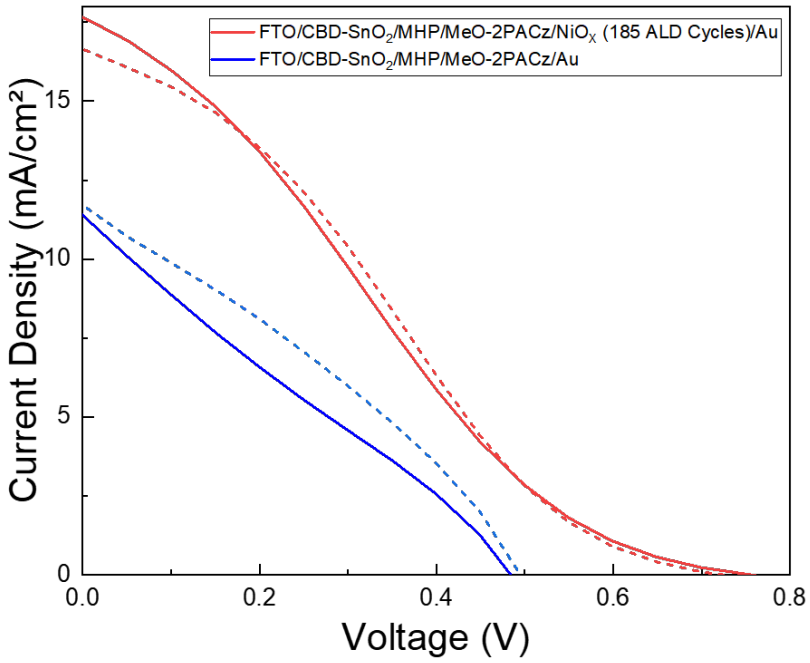

Figure 5.6. J-V characteristics data of n-i-p configuration solar cells. The dotted curves indicate the reverse scan, and the solid lines indicate the forward scan.

The devices that utilized MeO-2PACz as the HTL showed poor performance, with a maximum power conversion efficiency (PCE) of 1.8%, a voltage output (V_{OC}) of 0.5V, a short-circuit current density (J_{SC}) of 11.7 mA/cm^2, and a fill factor (FF) of 31% (as shown in Table 5.2). The devices that integrated MeO-2PACz and NiO_X double HTL layers displayed a low efficiency of almost 3%, due to the presence of defective species at the interface, which severely affected the hole transport and, consequently, the PCE. This conclusion is supported by the findings of the interface HAXPES study and the device performance, suggesting that MeO-2PACz is not suitable for use as a buffer layer between MHP and ALD-NiO_X.

FTO/CBD-SnO_2/ MHP/	**MeO-2PACz/Au**		**MeO-2PACz/NiO_X (185 ALD Cycles) /Au**	
	FW	RV	FW	RV
J_{SC} (mA/cm^2)	11.4	11.7	17.7	16.6
V_{OC} (volts)	0.48	0.5	0.76	0.72
FF (%)	25	31	22	26
PCE (%)	1.4	1.8	3	3.1

Table 5.2. J-V characteristics data of n-i-p perovskite solar cells with and without ALD NiO_x overlayer.

5.4. Summary

Our investigation focused on the effectiveness of the MeO-2PACz buffer layer between MHP and ALD-NiO_X in n-i-p configuration PSCs. We studied the interface between MHP, MeO-2PACz, and ALD-NiO_X using synchrotron-based HAXPES under 2 and 6 keV excitation energy. This advanced characterization provided important information on the formation of new chemical species (nitrogen compound, lead bromide) at the interface, as well as the modification of band alignment induced by newly created interfacial defects. Further analysis was conducted to track these changes. The Pb 4f, I 3d, N 1s, and Cs 3d core level peaks shifted to lower binding energy for the samples with ALD-NiO_X overlayer. The presence of these defective species and band bending strongly suggest that the MeO-2PACz molecules were unable to effectively shield the MHP layer from interacting with the ALD precursors, presumably due to the extremely thin and non-compact nature of the MeO-2PACz molecule layer. Additionally, we found that the ALD-NiO_X-grown on MeO-2PACz exhibited a high concentration of hydroxide and oxy-hydroxide species. These high concentrations of hydroxide and oxy-hydroxide species are detrimental to the stability of MHP, as they can react rapidly with MHP, causing rapid degradation. The devices that integrated MeO-2PACz and NiO_X double HTL layers displayed a low efficiency of almost 3%, due to the presence of defective species at the interface, which severely affected the hole transport and, consequently, the PCE.

■ REFERENCES

1. Wang, S., Guo, H. and Wu, Y., 2023. Advantages and challenges of self-assembled monolayer as hole-selective contact for perovskite solar cells. *Materials Futures*.
2. Ali, F., Roldán-Carmona, C., Sohail, M. and Nazeeruddin, M.K., 2020. Applications of self-assembled monolayers for perovskite solar cells interface engineering to address efficiency and stability. *Advanced Energy Materials*, *10*(48), p.2002989.
3. Isikgor, F.H., Zhumagali, S., T. Merino, L.V., De Bastiani, M., McCulloch, I. and De Wolf, S., 2023. Molecular engineering of contact interfaces for high-performance perovskite solar cells. *Nature Reviews Materials*, *8*(2), pp.89-108.
4. Wang, W., Wei, K., Yang, L., Deng, J., Zhang, J. and Tang, W., 2023. Dynamic self-assembly of small molecules enables the spontaneous fabrication of hole conductors at perovskite/electrode interfaces for over 22% stable inverted perovskite solar cells. *Materials Horizons*.
5. Cheng, H., Li, Y. and Zhong, Y., 2023. Towards cost efficient and stable perovskite solar cells and modules: the utilization of self-assembled monolayers. *Materials Chemistry Frontiers*.
6. Sun, X., Zhu, Z. and Li, Z.A., 2022. Recent advances in developing high-performance organic hole transporting materials for inverted perovskite solar cells. *Frontiers of Optoelectronics*, *15*(1), p.46.

7. Sun, J., Shou, C., Sun, J., Wang, X., Yang, Z., Chen, Y., Wu, J., Yang, W., Long, H., Ying, Z. and Yang, X., 2021. NiOx-seeded self-assembled monolayers as highly hole-selective passivating contacts for efficient inverted perovskite solar cells. *Solar RRL*, *5*(11), p.2100663.
8. Zhang, D., Zhang, H., Guo, H., Ye, F., Liu, S. and Wu, Y., 2022. Stable α-FAPbI3 in inverted perovskite solar cells with efficiency exceeding 22% via a self-passivation strategy. *Advanced Functional Materials*, *32*(27), p.2200174.
9. Roß, M., Gil-Escrig, L., Al-Ashouri, A., Tockhorn, P., Jost, M., Rech, B. and Albrecht, S., 2020. Co-evaporated pin perovskite solar cells beyond 20% efficiency: impact of substrate temperature and hole-transport layer. *ACS applied materials & interfaces*, *12*(35), pp.39261-39272.
10. Deng, X., Qi, F., Li, F., Wu, S., Lin, F.R., Zhang, Z., Guan, Z., Yang, Z., Lee, C.S. and Jen, A.K.Y., 2022. Co-assembled monolayers as hole-selective contact for high-performance inverted perovskite solar cells with optimized recombination loss and long-term stability. *Angewandte Chemie*, *134*(30), p.e202203088.
11. Magomedov, A., Al-Ashouri, A., Kasparavičius, E., Strazdaite, S., Niaura, G., Jošt, M., Malinauskas, T., Albrecht, S. and Getautis, V., 2018. Self-assembled hole transporting monolayer for highly efficient perovskite solar cells. *Advanced energy materials*, *8*(32), p.1801892.
12. Alghamdi, A.R., Yanagida, M., Shirai, Y., Andersson, G.G. and Miyano, K., 2022. Surface passivation of sputtered NiO x using a SAM interface layer to enhance the performance of perovskite solar cells. *ACS omega*, *7*(14), pp.12147-12157.
13. Guo, Y., Ma, J., Wang, H., Ye, F., Xiong, L., Lei, H. and Tan, Z., 2021. Overcoming Ni3+-Induced Non-Radiative Recombination at Perovskite-Nickel Oxide Interfaces to Boost Voltages in Perovskite Solar Cells. *Advanced Materials Interfaces*, *8*(16), p.2100920.
14. Boyd, C.C., Shallcross, R.C., Moot, T., Kerner, R., Bertoluzzi, L., Onno, A., Kavadiya, S., Chosy, C., Wolf, E.J., Werner, J. and Raiford, J.A., 2020. Overcoming redox reactions at perovskite-nickel oxide interfaces to boost voltages in perovskite solar cells. *Joule*, *4*(8), pp.1759-1775.

Conclusion and Perspectives

This doctoral dissertation is focused on the implementation of ALD-based metal oxide CTLs on MHP films to tailor the interfaces of perovskite solar cells. The primary objectives of this research were to gain fundamental understanding of the interactions between MHP and ALD precursors during the deposition process and to evaluate their influence on the performance of PSCs. Furthermore, this work involved the implementation of interlayer design strategies to ensure a controlled ALD process on the MHP films, for mitigating undesirable interfacial reactions between ALD precursors and MHP ions. Advanced characterization techniques, including XPS, synchrotron-based HAXPES, and Kelvin probe measurements, were employed to investigate the surface and interface properties of MHP/ALD-oxide structures. Chapter 3 focused on the investigation of the MHP/ALD-SnO_2 interface, while Chapters 4 and 5 delve into the examination of the MHP/ALD-NiO_X interface. The key findings of these studies are presented below, followed by a discussion of the future prospects for achieving stable perovskite solar cells.

In **Milestone I** the effects of the ALD process pressure and temperature on the double cation $FA_{0.7}Cs_{0.3}Pb(I_{0.9}Br_{0.1})_3$ MHP bulk were evaluated. This experiment was conducted under conditions similar to those of the ALD process, specifically at pressure of 1-3 millibars. The samples were post-annealed at temperatures of 100, 150, and 200°C for 1 h at a pressure of 1 millibar in a nitrogen environment. The bulk MHP remained stable at 100°C after heat treatment for 1 h. However, after annealing at 150°C for 1 h, we observed the degradation of MHP with the formation of PbI_2. At 200°C, the MHP material completely decomposed into PbI_2. This investigation found that ALD oxides could be safely deposited on double-cation MHP at 100°C without causing thermal degradation. Hence, subsequent studies of metal oxide depositions on MHP were performed by maintaining the ALD chamber at 100°C.

In **Milestone II**, we deposited metal oxides including SnO_2 (Chapter 3) and NiO_X (Chapter 4) on MHP using ALD and investigated the MHP interface using lab-based XPS and synchrotron-based HAXPES. The goal of this study was to determine and confirm the formation of chemical defects at the MHP/ALD-oxide interface and their impact on the electronic band configuration. Our HAXPES study on the MHP/ALD-SnO_2 interface revealed the formation of new chemical species such as *sym-triazine* and lead dihalides. To gain a deeper understanding of the modifications to the band alignment, we conducted further analysis using HAXPES to track the effects of these newly created interfacial defects. The results showed that the Pb 4f, I 3d, N 1s, and Cs 3d core level peaks shifted to lower binding energy for the samples with ALD-SnO_2 overlayer.

Milestone I

Bulk stability of MHP in ALD process pressure and temperature

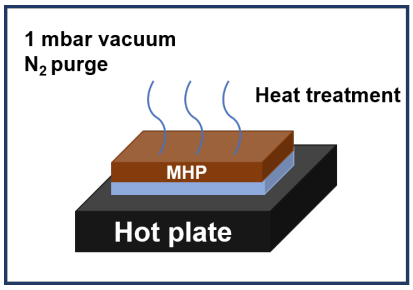

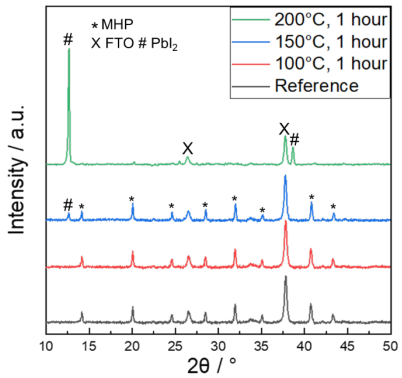

- Stable MHP bulk at 100°C heat treatment in 1 mbar pressure.
- Degrdation of MHP temprature above 150°C (PbI_2 formation).

Milestone II

ALD metal oxides (SnO_2 and NiO_X) process of MHP and its impact on the MHP interface

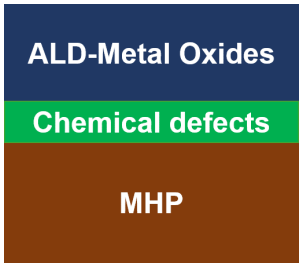

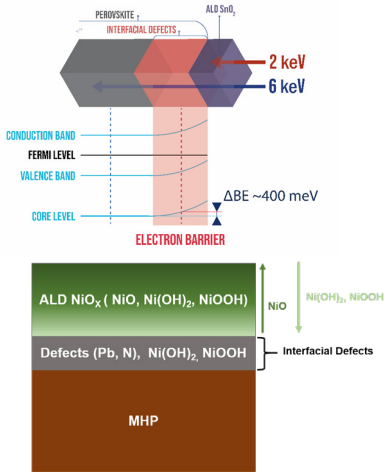

- Unwanted chemical reaction between ALD precursors and MHP.
- Formation of new chemical defect species at the MHP interface.
- Impact on electronic band configuraion at the MHP interface

---

Milestone III

Study of impact of individual ALD precursors on MHP

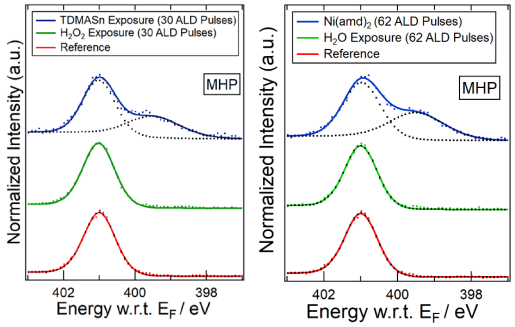

- Organometallic ALD precursors (TDMASn, $Ni(amd)_2$) used in ALD growth have a severe impact on the MHP surface.

Milestone IV

Introduction of organic buffer layer (PCBM, PTAA, MeO-2PACz) between MHP and ALD Oxide

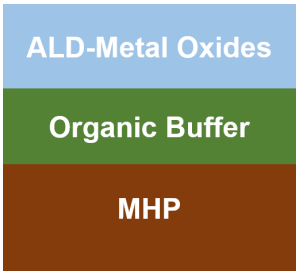

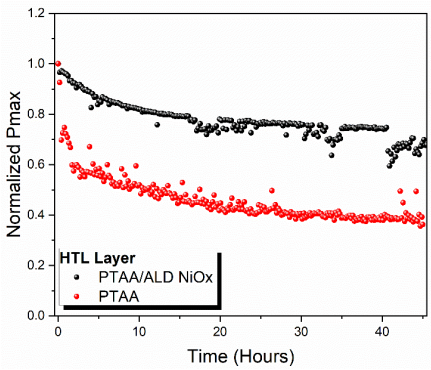

- Organic buffer layer partly mitigate interaction between ALD precursors and MHP.
- Enhanced operational stability of PSCs with incorporation of ALD-NiO_X on MHP/PTAA-buffer layer.

Figure 6.1. Final synopsis of the goal achievied within the study.

This indicates upward band bending at the interface, which poses a significant electron barrier and is therefore detrimental to PSCs performance.

In **Milestone II**, we also investigated the interface between MHP and ALD-NiO_X (Chapter 4). We observed the emergence of new chemical defects, particularly nitrogen compounds and lead bromide, at the MHP interface. Additionally, we found that the MHP/NiO_X sample showed a stoichiometric evolution with deficiencies in iodine, cesium, nitrogen, and excess lead. This suggests the formation of several defects at the interface as a result of the chemical interaction between the MHP and ALD-NiO_X precursors. We also discovered that the ALD-NiO_X grown on MHP had a low concentration of NiO during the initial growth (8-39%) and a high concentration of hydroxide and oxy-hydroxide species. The high concentrations of hydroxide and oxy-hydroxide species are detrimental to the stability of MHP, as they can react rapidly with MHP, leading to rapid degradation. The NiO_X film grown on MHP had extremely low work functions (in the range of 3.8-4.1) due to its high hydroxyl contribution, making it unsuitable for use as an HTL. Our findings provide evidence of interfacial chemical defect formation at the MHP interface due to the interaction between MHP and ALD precursors.

In **Milestone III**, we investigated the effect of individual ALD precursors on MHP. The goal of this experiment was to determine which of the precursors was responsible for interfacial reactions and defect formation. We observed no effect on the exposure of the reactant precursors (H_2O and H_2O_2) on the MHP surface. However, the exposure of the organometallic precursor (TDMASn, $Ni(amd)_2$) to MHP resulted in the formation of chemical defects, which is evident from the evolution of the new nitrogen contribution observed in the N 1s spectra (XPS study).

In Milestone IV, we introduced an organic buffer layer between the MHP and ALD-oxide to mitigate unwanted interfacial reactions. In the ALD-SnO2 study, we used a 40 nm PCBM interlayer between MHP and SnO_2 (Chapter 3). The X-ray diffraction measurements revealed that the PCBM layer did not fully protect the MHP from exposure to the ALD precursors due to the presence of pinholes. This led to undesirable chemical reactions at the interface and negatively affected the electronic interface properties. To address this issue, a modified PCBM deposition recipe was employed that resulted in a pinhole-free morphology, which improved the performance of PCBM/ALD-SnO_2 ETL device stack devices from 1% to 10%.

In ALD-NiO_X study, a 20 nm PTAA buffer layer was incorporated between the MHP and ALD-NiO_X (Chapter 4). The PTAA interlayer was found to limit the MHP from interacting with the ALD-NiOX precursors. However, due to pin-holes in the PTAA films, it does not fully prevent the interaction between MHP and ALD precursors. The ALD-NiO_X films on PTAA contained a higher concentration of NiO (61-74%) and had a higher work function (4.5-4.6) measured using a kelvin probe. Incorporating the PTAA/NiO_X into PSCs resulted in a champion cell PCE of 16% and

improved operational stability under ambient conditions due to the compact and ion-blocking properties of the ALD oxides.

In addition, we investigated the MeO-2PACz buffer layer between MHP and ALD-NiO_X in n-i-p configuration PSCs (Chapter 5). We found the formation of new chemical species, such as nitrogen compounds and lead bromide, at the interface, as well as the modification of band alignment due to newly created interfacial defects. The core level peaks of Pb 4f, I 3d, N 1s, and Cs 3d shifted to lower binding energy for the MHP/MeO-2PACz/ALD-NiO_X sample compared to the MHP/MeO-2PACz sample. The presence of these defective species and band bending strongly suggests that the MeO-2PACz molecules were unable to effectively shield the MHP layer from interacting with the ALD precursors presumably due to the extremely thin and non-compact nature of the MeO-2PACz molecule layer. We also found that the ALD-NiO_X grown on MeO-2PACz exhibited a high concentration of hydroxide and oxy-hydroxide species, which are detrimental to the stability of MHP as they can rapidly react with MHP, causing rapid degradation. As a result, the devices that integrated MeO-2PACz and NiO_X double HTL layers displayed a low efficiency of almost 3%, due to the presence of defective species at the interface that severely affected the hole transport and, consequently, the PCE.

Perspectives

In summary, this dissertation demonstrated that ALD precursors chemically interact with MHP, modifying the interface and electronic band alignment and severely impacting the performance of PSCs. Although the damage-free deposition of ALD materials on MHP seems daunting, there is still a broad avenue to be explored. In particular, we found that the organometallic precursors used in the ALD growth are crucial and can have a significant impact on the MHP surface. Organometallic ALD precursors tend to react with the organic cations of MHP. To address this issue, a promising approach is to develop organometallic precursors with reduced reactivity or to use stable inorganic MHP for incorporating ALD oxides in perovskite solar cells. Another intriguing possibility is the application of a suitable interlayer, such as two-dimensional (2D) perovskite, between the MHP and ALD metal oxide films. The implementation of such interlayers presents a viable solution for shielding the perovskite material from direct interaction with ALD precursors. These approaches hold significant potential for preserving the structural integrity and performance of MHPs and can ultimately contribute to the advancement and optimization of ALD processes for PSCs.

Annex

Chapter 3

Thermal Stability assessment of MHP

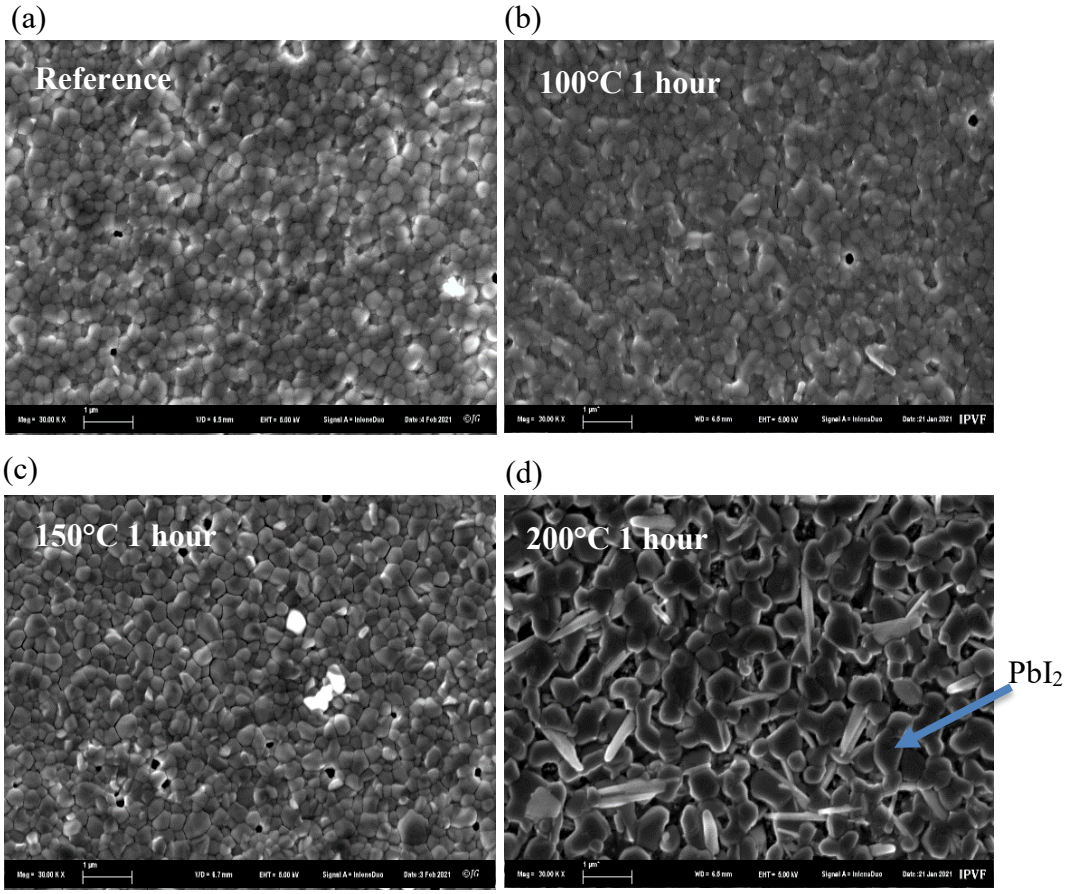

Figure A1. Scanning electron microscopy (SEM) images of MHP films with different post-annealing temperatures of (a) reference (b) 100°C (c) 150°C (d) 200°C for 1 hour at 1mbar in a nitrogen environment.

Structural Properties of ALD-SnO_2

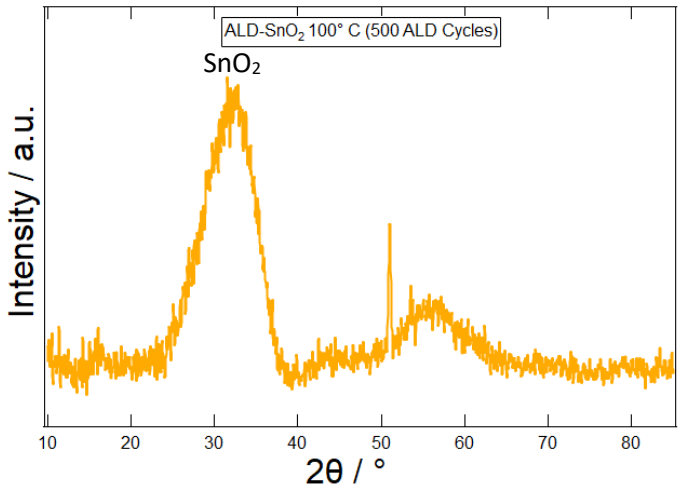

Figure A2. GiXRD pattern of 500 cycle ALD-SnO_2 grown on Si wafer at 100°C.

The deposition of ALD-SnO_2 films at 100 °C unveils intriguing structural properties when analyzed using grazing incidence X-ray diffraction (GIXRD). Through X-ray diffraction (XRD), it becomes evident that the film showcases a distinctive characteristic of an observable broad and weak peak centered around 32.6°. This peak signifies the film's structure, indicating the likelihood of a nano-crystalline arrangement at the given deposition temperature of 100 °C.

Morphology of Modified- PCBM Recipe

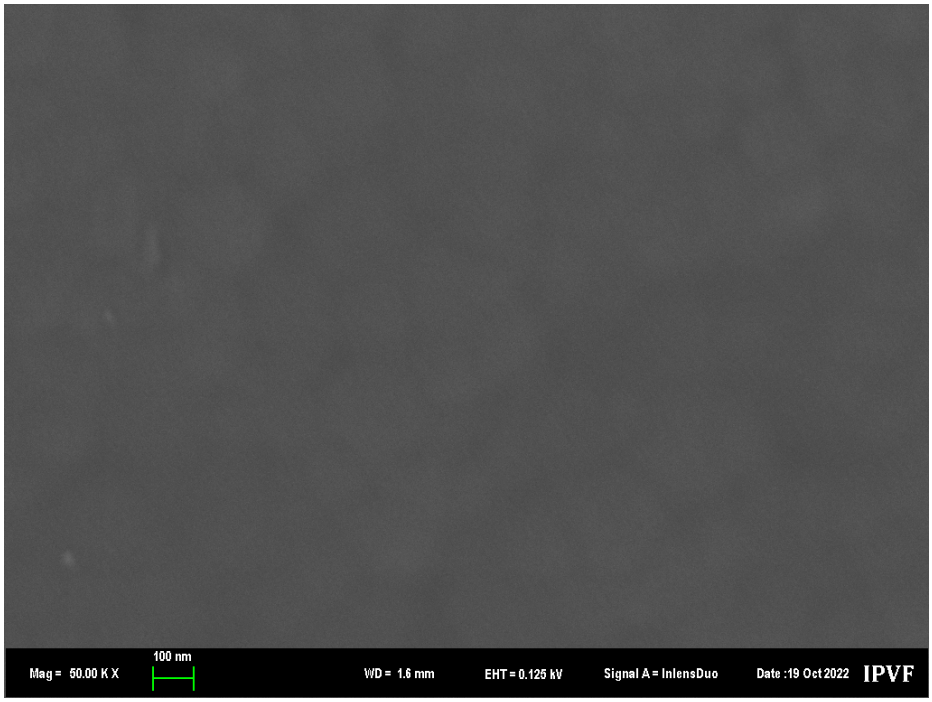

Figure A3. SEM images FTO/NiO/MHP / modified-PCBM.

HAXPES Survey Spectra

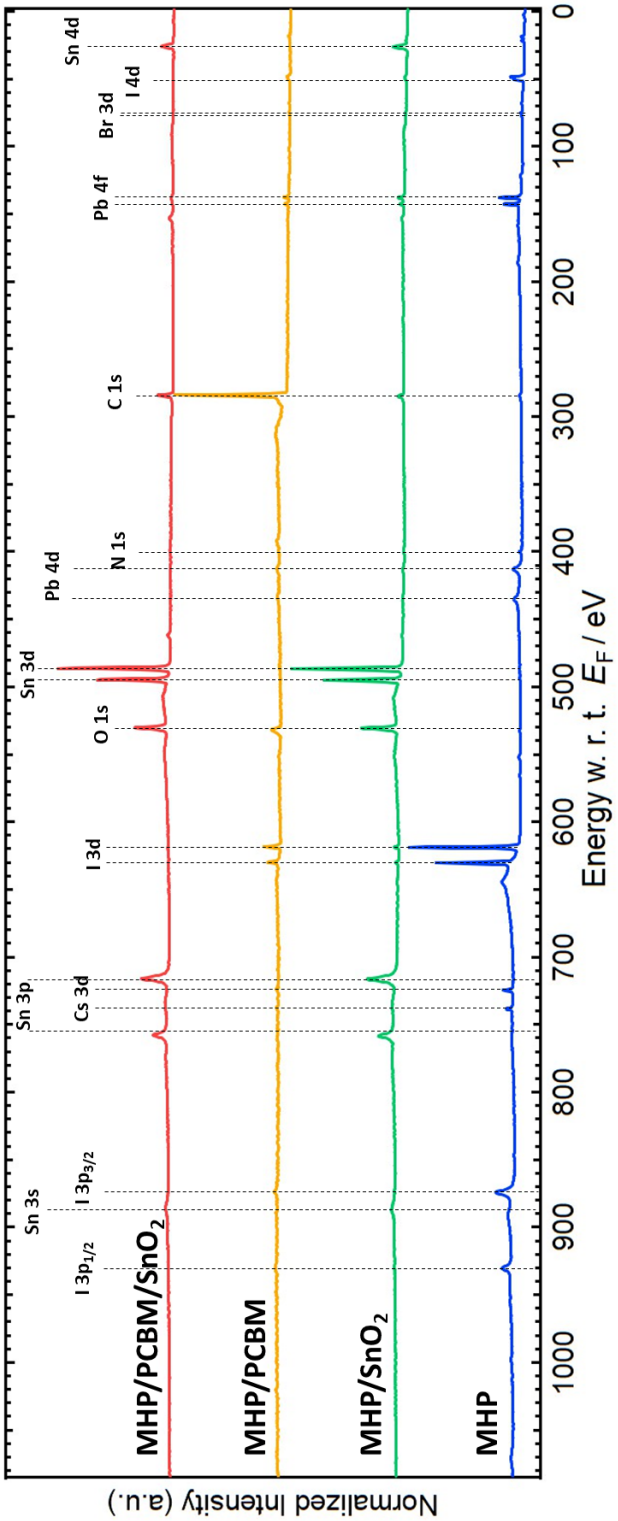

Figure A4. Survey spectra of MHP, MHP/SnO_2, MHP/PCBM, MHP/PCBM/SnO_2 samples measured using 2 keV excitation energy.

Chapter 4

Structural Properties of ALD-NiOx

To analyze the bulk structure of ALD-NiOx films grown on silicon wafer, GIXRD measurements are conducted. The NiOx film being investigated is extremely thin, measuring only 15nm in thickness. Figure A5 displays the XRD signature of the ALD-NiOx film. The diffractogram reveals distinct peak patterns, indicating that the film is composed of multiple crystalline grains. The presence of crystal planes with specific Miller indices, such as (111), (200), (220), and (311), suggests that the NiOx film is in the cubic phase.[6,7]

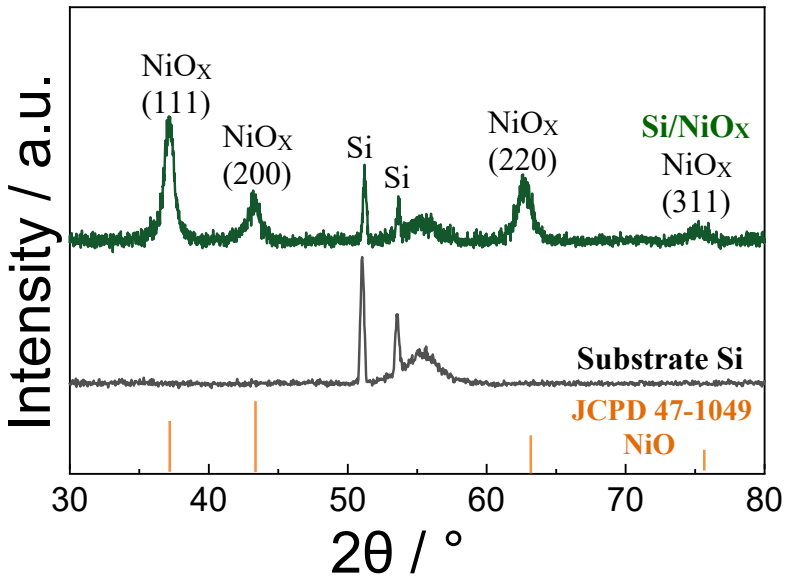

Figure A5. GiXRD pattern of 15nm ALD-NiO_X grown on Silicon wafer at 100°C.

XRD pattern of MHP with PTAA and NiO_X overlayer

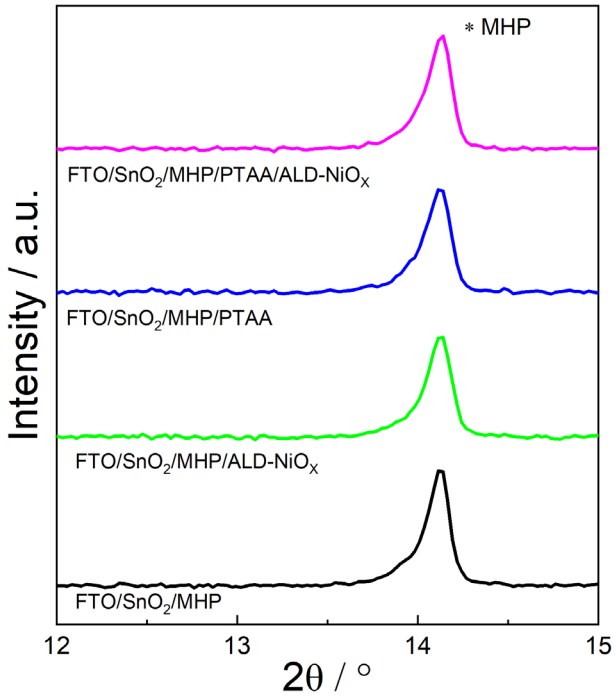

Figure A6. XRD pattern of double cation MHP film with and without ALD-NiO_X, PTAA, PTAA/ALD-NiO_X top layers.

Optical Bandgap of ALD-NiO_X

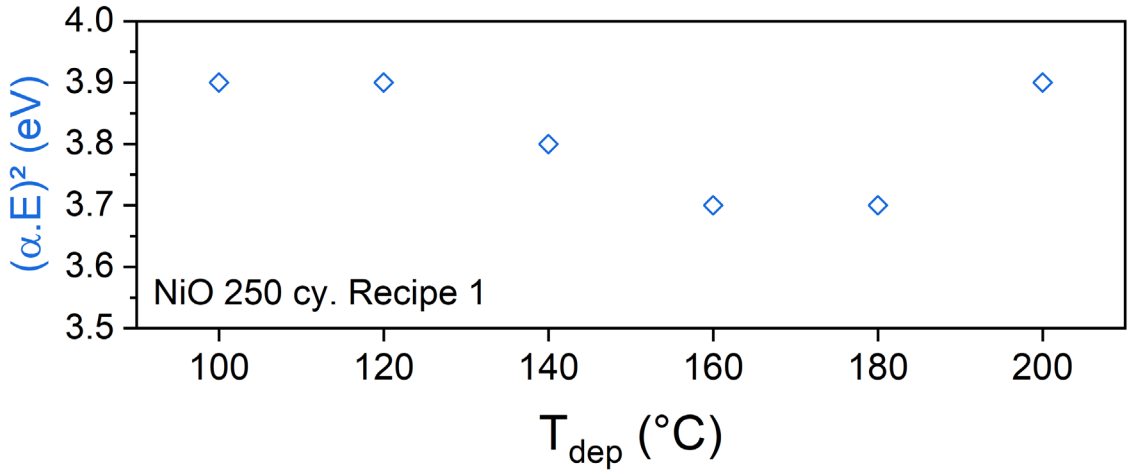

Figure A7. Optical bandgap of ALD NiO_X grown at different temperatures determined using Uv-Vis Spectroscopy.

Lab-based XPS plots

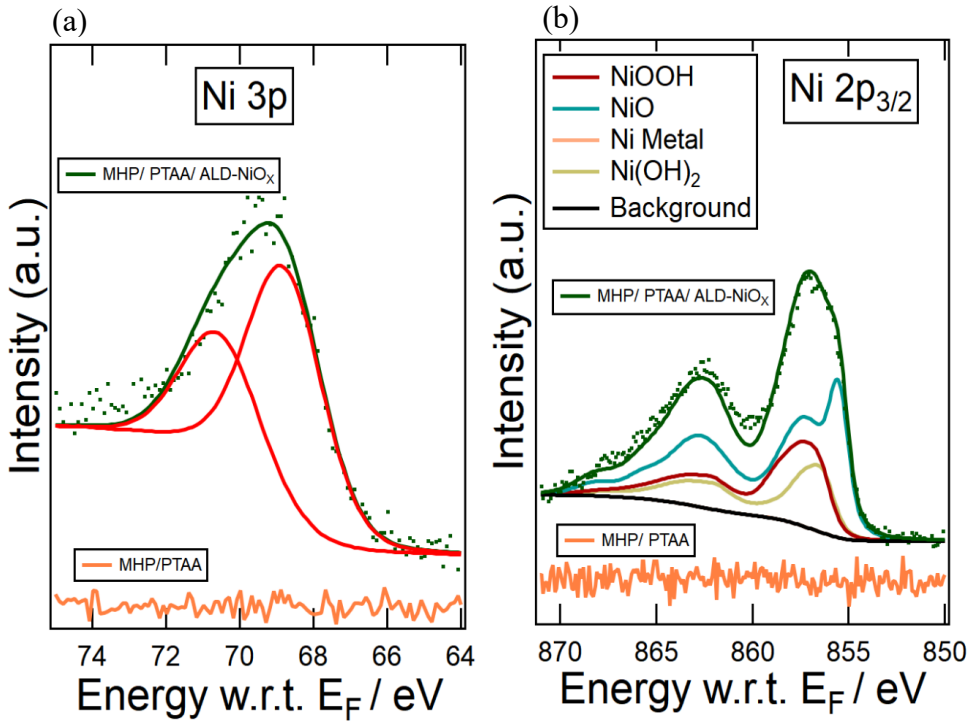

Figure A8. XPS spectra (Al-Kα 1486.7 eV) of FTO/CBD-SnO_2/MHP/PTAA (in orange color), and FTO/CBD-SnO_2/MHP/PTAA/ALD-NiO_X 125 ALD cycles (in dark-green color) (a) Ni 3p (b) Ni $2p_{3/2}$.

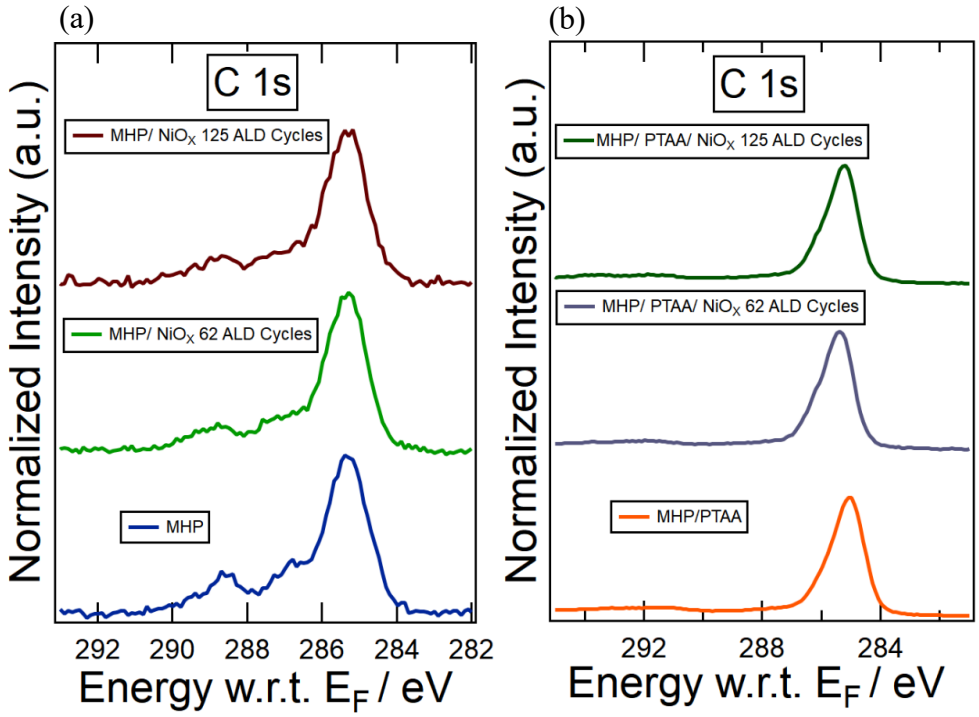

Figure A9. C 1s spectra using lab based XPS (Al-Kα 1486.7 eV) of (a) MHP vs MHP/ thin ALD-NiO_X vs MHP/thick ALD-NiO_X (b) MHP/PTAA vs MHP/PTAA/ thin ALD-NiO_X vs MHP/PTAA/thick ALD-NiO_X.

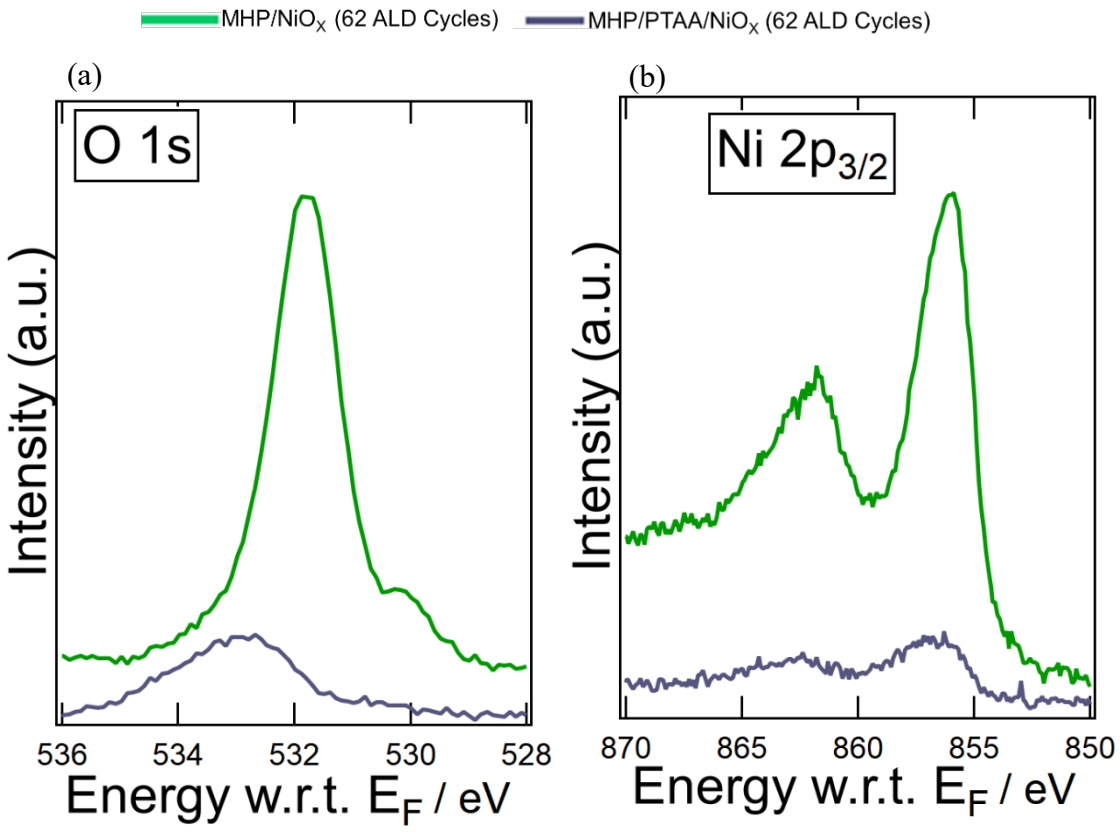

Figure A10. XPS spectra (Al-kα 1486.7 eV) of FTO/CBD-SnO_2/MHP/NiO_X 62 ALD cycles (in green color) and FTO/CBD-SnO_2/MHP/PTAA/ALD-NiO_X 62 ALD cycles (in blue color) (a) O 1s (b) Ni $2p_{3/2}$.

Synchrotron-based HAXPES plots

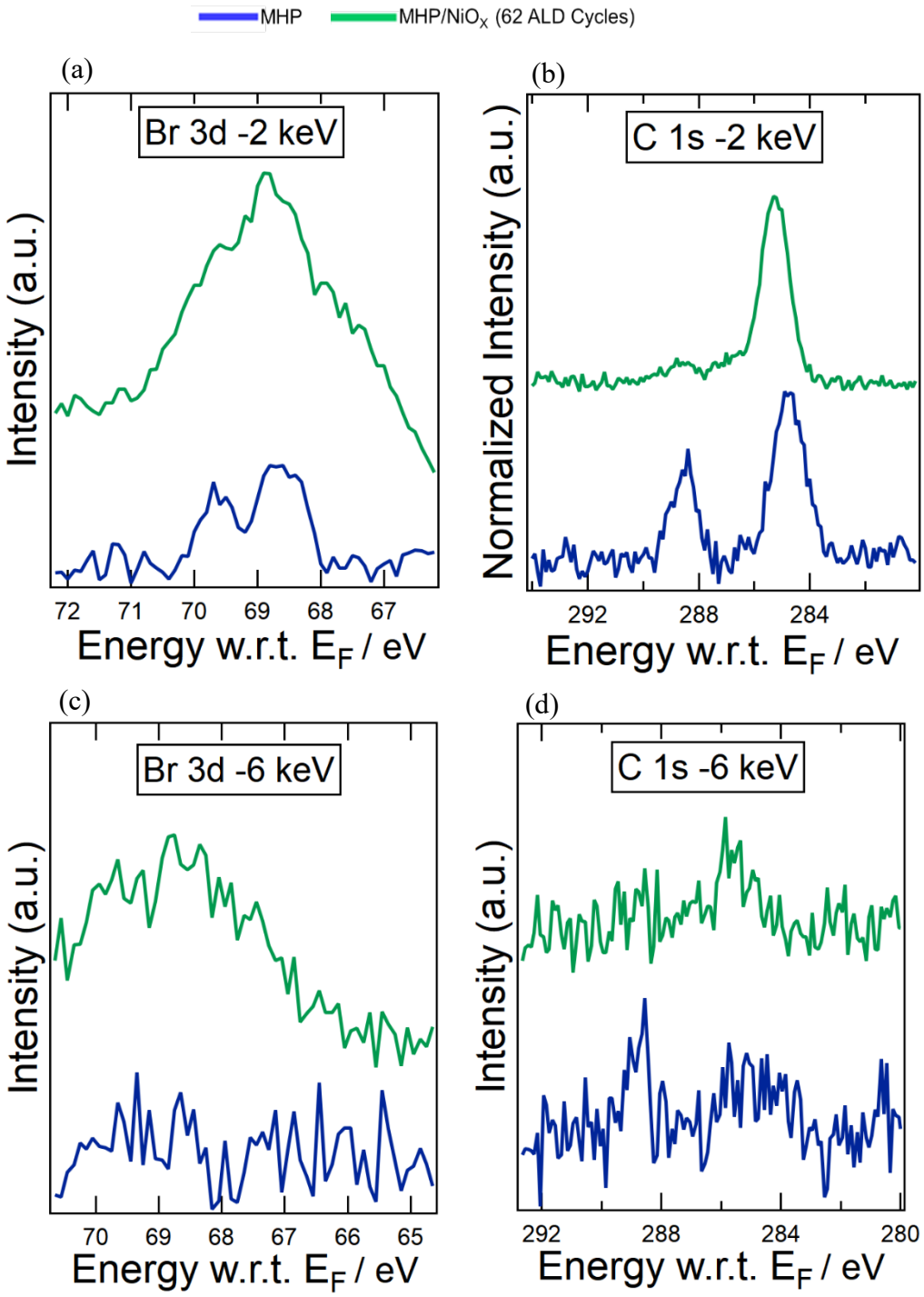

Figure A11. (a-d) HAXPES detail spectra of Br $3d_{5/2}$ and C 1s of double cation MHP without (blue spectra) and with (green spectra) ALD NiO_X top layers recorded with 2 and 6 keV excitation energy using Be filter.

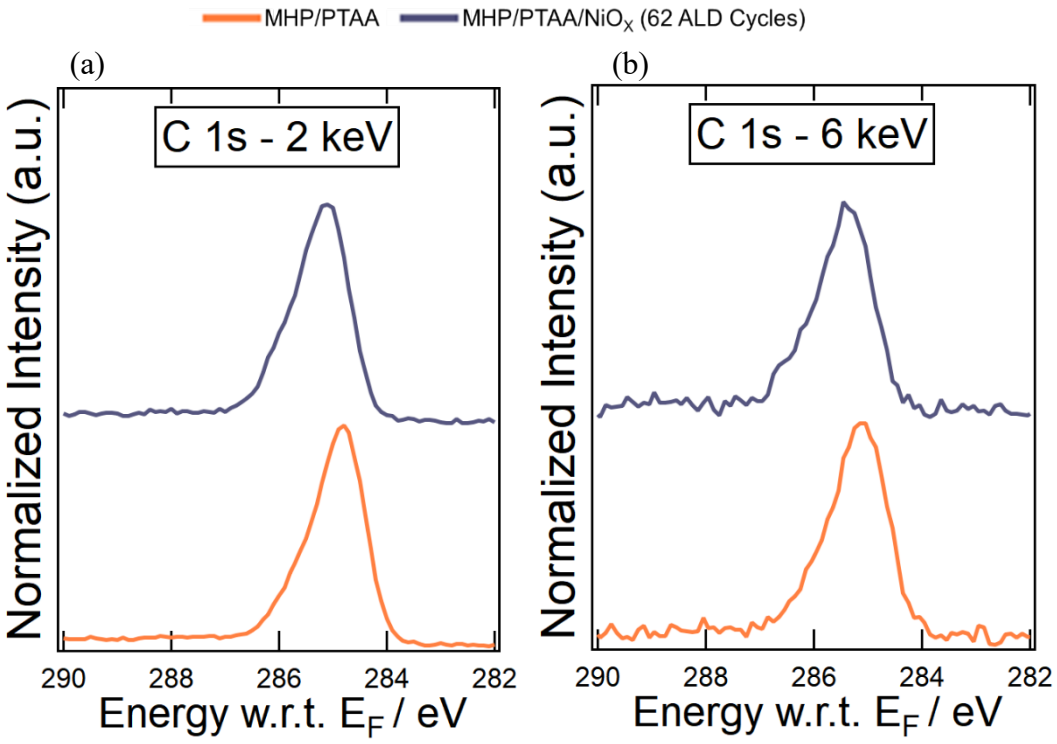

Figure A12. HAXPES detail spectra of C 1s of double cation MHP/PTAA without (orange spectra) and with (light blue spectra) ALD NiO_X top layers recorded with (a) 2 keV and (b) 6 keV excitation energy using Be filter.

Chapter 5

Synchrotron-based HAXPES plots

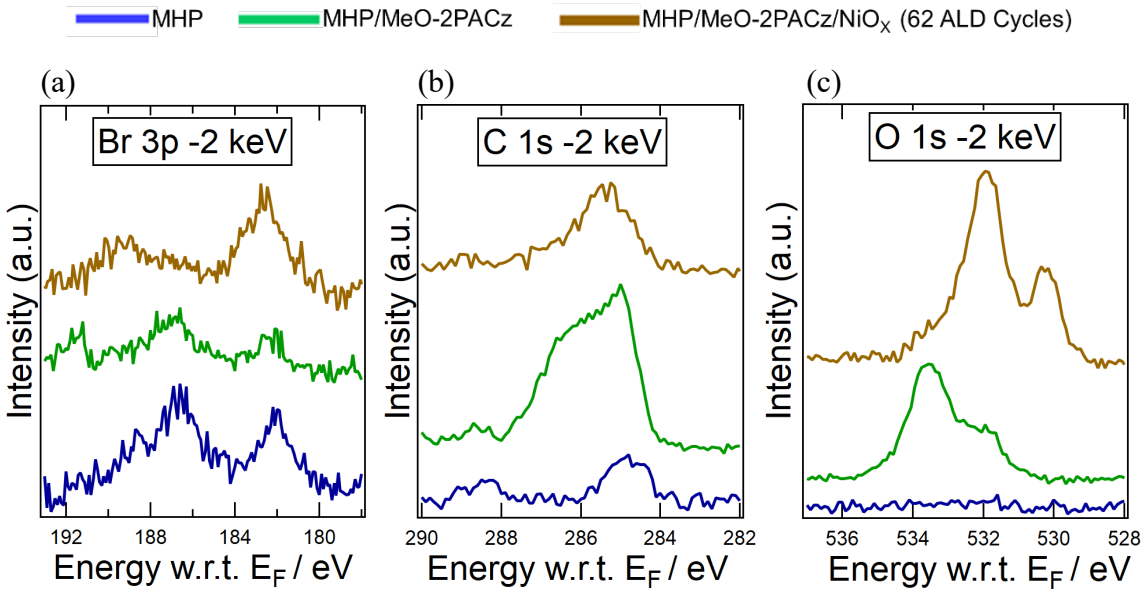

Figure A13. (a-g) HAXPES detail spectra (raw data) of Br 3p, C 1s, and O 1s of double cation MHP (blue spectra), MHP/MeO-2PACz (green spectra) and MHP/MeO-2PACz/ALD-NiO$_X$ (yellow spectra) layers recorded with 2 keV excitation energy using Be filter.

Résumé en Français

Dans un monde où la technologie domine la vie moderne et les économies, la demande énergétique et son impact environnemental sont devenus au centre des préoccupations. La forte dépendance aux sources d'énergie non renouvelables telles que le charbon et le gaz naturel a placé le monde au milieu d'une crise énergétique au cours des dernières années. De plus, l'utilisation intensive des sources d'énergie à base de combustibles fossiles a un impact sévère sur le climat en raison des émissions de gaz à effet de serre. Ces derniers ont été identifiées comme la cause principale du réchauffement climatique et du changement climatique. La recherche et le développement de technologies d'énergie renouvelable efficaces et rentables sont essentiels pour lutter contre le réchauffement climatique mondial.

Parmi les différentes technologies d'énergie renouvelable et propre, le photovoltaïque (PV) qui convertit directement la lumière du soleil en électricité est à l'avant-garde en raison de la quantité énorme d'énergie fournie par le soleil. Ces dernières années, des concepts novateurs tels que l'utilisation d'absorbeurs hybrides pérovskites organiques-inorganiques ont été développés. Les cellules solaires pérovskites (PSCs), décrites pour la première fois il y a presque 10 ans avec un rendement de 14,1 %, ont connu une avancée rapide avec un rendement certifié actuel de plus de 26 % en 2023. Cette amélioration extraordinaire de l'efficacité des PSC a été rendue possible grâce à une meilleure compréhension fondamentale des matériaux pérovskites et à une amélioration de l'ingénierie des interfaces. Cependant, il reste certains verrous au déploiement des PSC tels que l'industriabilité, et la stabilité à long terme des PSC qui est intrinsèquement affectée par ses interfaces. Par conséquent, l'ingénierie fine d'interfaces est cruciale pour améliorer la stabilité et l'efficacité de la technologie PV pérovskite.

La thèse de doctorat se concentre sur la mise en œuvre de couches de transport de charges en oxyde métallique fabriquée par la technique de dépôt de couche mince *Atomic Layer Deposition* (ALD), afin d'ingénierer les interfaces de la cellule solaire pérovskite. Ce type de conception d'interface vise non seulement à rendre le dispositif plus efficace, mais aussi à améliorer sa stabilité en formant une couche tampon protectrice. En effet, l'une des principales préoccupations concernant les PSC est leurs stabilités environnementale et thermique limitées, en particulier pour la pérovskite $MAPbI_3$ largement étudiée, mais aussi pour les variantes plus récentes mixant divers cations et ions halogénures. Dans ce contexte, la technique ALD est particulièrement prometteuse pour la croissance de couches compactes d'oxydes métalliques directement sur la pérovskite à basse température. L'oxyde compact peut également servir de couche protectrice contre les facteurs environnementaux externes ainsi que pour éviter la migration interne des ions.

Les précurseurs utilisés dans le processus ALD peuvent interagir chimiquement avec la surface de la pérovskite. Bien que cette nouvelle approche de conception d'interface soit prometteuse pour résoudre le problème de stabilité des technologies à base de pérovskites, le manque de compréhension précise des processus chimiques et physiques à l'interface de la pérovskite pendant les étapes ALD a constitué un obstacle à une utilisation efficace de cette approche et a donc nécessité des recherches fondamentales dédiées. Dans ce travail de recherche doctoral, je me concentre sur l'étude approfondie de la chimie, de la structure, de la morphologie et de l'alignement électronique des interfaces de pérovskite et d'oxyde métallique ALD en utilisant des techniques de caractérisation avancées, notamment la spectroscopie photoélectronique des rayons X, la spectroscopie photoélectronique des rayons X durs basée sur un synchrotron (utilisant des énergies de photon de 2 keV et 6 keV pour sonder différentes profondeurs de l'interface), la sonde Kelvin, la diffraction des rayons X et la microscopie électronique à balayage.

Dans le chapitre 3, l'interface entre une pérovskite halogénée métallique (MHP) et ALD-SnO_2 est étudié par spectroscopie photoélectronique des rayons X durs. Cette caractérisation avancée a fourni des informations importantes sur la formation de nouvelles espèces chimiques (sym-triazine, dihalogénures de plomb) à l'interface. Une analyse plus approfondie a été réalisée pour suivre la modification de l'alignement des bandes induite par la création de défauts d'interface. Les pics des niveaux de cœur Pb 4f, I 3d, N 1s et Cs 3d sont décalés à plus basse énergie de liaison lorsque la MHP est couverte de ALD-SnO_2, ce qui indique la présence d'une courbure ascendante des bandes à l'interface. Cette dernière agit comme une barrière électronique forte et est donc préjudiciable pour la PSC en fonctionnement. L'étude a été étendue à un système où une couche interfaciale de 40 nm de PCBM est déposé entre MHP et SnO_2. La couche PCBM ne protège pas complètement la MHP de l'exposition aux précurseurs ALD en raison de la présence de trous, comme le montre la signature du PbI_2 (basse intensité) observée par des mesures de diffraction des rayons X. Par conséquent, des réactions chimiques indésirables ont été observées à l'interface dans les deux cas, ce qui a eu un impact négatif sur les propriétés électroniques de l'interface. Enfin, pour résoudre ce problème, une recette alternative de dépôt PCBM a été utilisée et a permis d'améliorer le rendement des dispositifs PCBM/ALD-SnO_2 de 1 % à 10 % d'efficacité de conversion.

Le chapitre 4 traite de l'utilisation d'une couche de transport de trous ALD-NiO_X pour cellules solaires pérovskites en configuration n-i-p. Une analyse approfondie de l'interface, des caractéristiques des cellules solaires et de la stabilité opérationnelle a été réalisée dans ce chapitre. De plus, les techniques de spectroscopie photoélectronique des rayons X de laboratoire (LabXPS) et de spectroscopie photoélectronique des rayons X durs basée sur un synchrotron (HAXPES) ont été utilisées pour étudier en détail la chimie des interfaces de pérovskite et d'ALD-NiO_X. L'étude HAXPES a révélé l'émergence de nouvelles espèces chimiques à l'interface, en particulier des

composés d'azote et du bromure de plomb. Nous avons constaté que l'échantillon MHP/NiO_X présentait une évolution stœchiométrique avec des déficiences en iode, césium, azote et un excès de plomb. Nous avons également constaté que la MHP produite par ALD-NiO_X présentait une faible concentration de NiO pendant la croissance initiale (8-39%) et une forte concentration d'espèces d'hydroxyde et d'oxy-hydroxyde. Les concentrations élevées d'hydroxyde et d'oxy-hydroxyde sont préjudiciables à la stabilité de la MHP, car elles peuvent réagir rapidement avec la MHP, entraînant une dégradation rapide. Le film de NiOX cultivé sur MHP présentait des fonctions de travail extrêmement faibles (de l'ordre de 3,8 à 4,1) en raison de la forte contribution des hydroxyles, ce qui le rendait impropre à une utilisation en tant que couche de transport de trous (HTL).

Les travaux ont également été étendus à un système comportant une couche intermédiaire de poly(triaryl amine) (PTAA) de 20 nm entre la MHP et l'ALD-NiO_X. Il s'est avéré que la couche intermédiaire de PTTA empêchait le MHP d'interagir avec les précurseurs ALD-NiO_X. Cependant, la présence de trous d'épingle dans les films de PTAA n'inhibe pas complètement l'interaction entre le MHP et les précurseurs ALD. Les films ALD-NiOX sur PTAA avaient une concentration plus élevée de NiO dans la gamme de 61-74%, résultant en une fonction de travail plus élevée de 4,5-4,6 mesurée à l'aide d'une sonde kelvin. Lors de l'incorporation du PTAA/NiO_X dans les PSC, une cellule championne PCE de 16% a été enregistrée, et une amélioration significative de la stabilité opérationnelle dans des conditions ambiantes par rapport au dispositif à base de PTAA HTL a été observée en raison des propriétés compactes et de blocage des ions des oxydes ALD.

Le chapitre 5 décrit l'étude de l'efficacité de la couche intermédiaire de molécules à base d'acide phosphonique MeO-2PACz entre le MHP et l'ALD-NiO_X dans les PSC à configuration n-i-p. L'interface entre le MHP, le MeO-2PACz et l'ALD-NiO_X a été étudiée à l'aide d'une méthode HAXPES synchrotron sous une énergie d'excitation de 2 et 6 keV. Nous avons constaté la formation de nouvelles espèces chimiques (composé d'azote, bromure de plomb) à l'interface, ainsi que la modification de l'alignement des bandes induite par les défauts interfaciaux nouvellement créés. Les pics des niveaux centraux Pb 4f, I 3d, N 1s et Cs 3d se sont déplacés vers une énergie de liaison plus faible pour l'échantillon MHP/MeO-2PACz/ALD-NiO_X par comparaison avec l'échantillon MHP/MeO-2PACz. La présence de ces espèces défectueuses et la courbure des bandes sont également observés en présence d'une couche interfaciale de MeO-2PACz. Ceci indique que la couche de MeO-2PACz ne protège pas efficacement la couche de MHP de l'interaction avec les précurseurs ALD, vraisemblablement en raison de son extrême minceur (quelques nms) et sa nature non compacte. De plus, nous avons constaté que l'ALD-NiO_X déposé sur MeO-2PACz présentait une concentration élevée d'espèces hydroxyl et oxy-hydroxyl, qui sont nuisibles à la stabilité de la MHP, car elles peuvent réagir rapidement avec la MHP et provoquer sa dégradation rapide. Les dispositifs intégrant les couches double HTL MeO-2PACz/ALD-NiO_X ont une faible efficacité de

conversion (environ 3 %) en raison de la présence d'espèces défectueuses à l'interface, qui affectent le transport de trous et, par conséquent, le rendement.

En résumé, cette thèse de doctorat a montré que les précurseurs ALD interagissent chimiquement avec la MHP, modifiant l'interface, l'alignement électronique des bandes et impactant gravement les performances des cellules solaires pérovskites. Bien que le dépôt sans endommagement des matériaux ALD sur la MHP semble difficile, il reste encore un large spectre de solutions à explorer. En particulier, nous avons constaté que les précurseurs ALD organométalliques ont tendance à réagir avec les cations organiques de la MHP. Pour résoudre ce problème, une approche prometteuse consiste à développer des précurseurs organométalliques moins réactifs ou à utiliser des MHP inorganiques stables pour incorporer des oxydes ALD dans les cellules solaires pérovskites.

Une autre possibilité est l'utilisation d'une couche interfaciale appropriée, telle qu'une pérovskite bidimensionnelle (2D) entre la MHP et les films d'oxyde métallique ALD. Ceci est une solution viable pour protéger le matériau pérovskite de l'interaction directe avec les précurseurs ALD. Ces approches présentent un potentiel significatif pour préserver l'intégrité structurelle et les performances des MHP et peuvent contribuer à l'avancement et à l'optimisation des processus ALD pour les cellules solaires pérovskites.

ECOLE DOCTORALE

Titre: Étude de l'Interface des Couches de Transport de Charge en Oxyde Métallique basées sur Atomic Layer Deposition sur Pérovskite Halogénée Métallique.

Mots clés : Cellules solaires à pérovskite, Interfaces, Atomic Layer Deposition, Spectroscopie de Photoémission

Résumé : Les pérovskites halogénées métalliques (MHP) ont attiré l'attention des chercheurs depuis une dizaine d'années en raison de leur efficacité en tant qu'absorbeur dans les cellules solaires à pérovskite (PSC). Ces dernières atteignent aujourd'hui des efficacités de conversion de l'énergie solaire (PCE), au-delà de 25 %. Ces progrès rapides sont le fruit d'une compréhension fondamentale croissante des MHP et de l'amélioration des interfaces. Cependant, il reste certains verrous au déploiement des PSCs, la stabilité à long terme des PSC qui est intrinsèquement affectée par ses interfaces.

La thèse de doctorat se concentre sur la mise en œuvre d'une couche de transport de charge à base d'oxyde métallique déposée par la technique *Atomic Layer Deposition* (ALD) afin d'adapter les interfaces des PSC. Malgré les avantages de l'ALD et les nombreux travaux décrits dans la littérature, le dépôt d'oxydes métalliques directement sur la pérovskite n'a pas encore pu être réalisé sans endommager la couche de pérovskite sous-jacente. Le changement de propriétés physicochimiques et électroniques à l'interface de la pérovskite lors de l'exposition aux précurseurs ALD peut altérer le matériau et la fonctionnalité *in fine* du dispositif.

La première partie de ce manuscrit se concentre sur l'étude de l'interface entre l'absorbeur MHP et la couche de transport d'électrons ALD-SnO_2 par spectroscopie photoélectronique à rayons X durs basée sur le synchrotron (HAXPES). Elle a mis en évidence la formation de nouvelles espèces chimiques (composés d'azote, dihalides de plomb) et d'une courbure de bande spécifique à l'interface MHP/ALD-SnO_2 créant une couche de barrière électronique de ~400 meV, qui nuit aux performances de la PSC. En outre, l'introduction d'une fine couche intermédiaire d'ester méthylique de l'acide phényl-C61-butyrique (PCBM) entre le MHP et l'ALD-SnO_2 afin d'atténuer les effets du dépôt ALD est évaluée.

Le chapitre suivant examine les PSC de type n-i-p avec une couche intermédiaire ALD-NiO_X pour le transport des trous. La composition chimique des interfaces MHP/ALD-NiO_X a été analysée par XPS et HAXPES, ce qui a mis en évidence des composés azotés et des changements stœchiométriques (I, Cs, N, Pb), indiquant des défauts à l'interface dus aux interactions MHP-ALD-NiO_X. L'ajout d'une couche intermédiaire de 20 nm de poly(triaryl amine) (PTAA) a réduit les interactions MHP-ALD-NiO_X, et permis d'améliorer les performances et la stabilité des cellules. Le dernier chapitre examine l'utilisation de molécules à base d'acide phosphonique entre la MHP et l'ALD-NiO_X dans une architecture n-i-p afin d'éviter les réactions interfaciales indésirables.

Title: Interface Study of Atomic Layer Deposition based Metal Oxide Charge Transport Layer on Metal Halide Perovskite

Keywords: Perovskite solar cell, Interfaces, Atomic layer deposition, Photoemission spectroscopy

Abstract: In recent years, metal halide perovskite (MHP) solar cells have attracted immense attention among researchers due to the rapid advances in power conversion efficiency (PCE) beyond 25%. Such extraordinary improvement of PCE in perovskite solar cells (PSCs) was made in light of the growing fundamental understanding of MHPs and improved interface engineering. However, to this date, the long-term stability of PSCs, which is inherently affected by their interfaces, remains a key issue for widespread applications.

The Ph.D. thesis focuses on the implementation of atomic layer deposition (ALD)-based metal oxide charge transport layer to tailor the interfaces of perovskite solar cells. ALD grown compact metal oxide films have drawn immense attention for the fabrication of stable PSC. Despite the advantages of ALD, the deposition of metal oxides directly on bare perovskite has so far not been achieved without damaging the perovskite layer underneath. In addition, the changes to the physicochemical and electronic properties at the perovskite interface upon exposure to the ALD precursors can alter the material and hence device functionality.

The first part of the thesis focuses on synchrotron-based hard X-ray photoelectron spectroscopy (HAXPES) investigation of the interface between MHP absorber and ALD-SnO_2 electron transport layer. We found clear evidence for the formation of new chemical species (nitrogen compound, lead dihalides) and an upward band bending in the MHP and downward band bending in the SnO_2 towards the MHP/ALD-SnO_2 interface. The upward bending at the interface forms an electron barrier layer of ~400 meV, which is detrimental to the PSC performance. In addition, we assess the effectiveness of introducing a thin Phenyl-C61-butyric acid methyl ester (PCBM) interlayer between MHP and ALD-SnO_2 to mitigate the effects of ALD deposition.

The next chapter examines n-i-p perovskite solar cells with an ALD-NiO_X hole-transport interlayer. XPS and HAXPES were used to analyze the chemical composition of the perovskite and ALD-NiO_X interfaces, uncovering chemical defects, including nitrogen compounds, at the interface. The MHP/NiO_X sample showed stoichiometric changes, such as iodine, cesium, nitrogen deficiencies, and high lead content, indicating defects at the interface due to MHP-ALD-NiO_X interactions. Adding a 20 nm poly(triaryl amine) (PTAA) interlayer reduced MHP-ALD-NiO_X interactions, resulting in better cell performance and stability. The last chapter examines the use of a phosphonic acid-based molecule between MHP and ALD-NiO_X in an n-i-p architecture to prevent unwanted interfacial reactions.

Institut Polytechnique de Paris
91120 Palaiseau, France